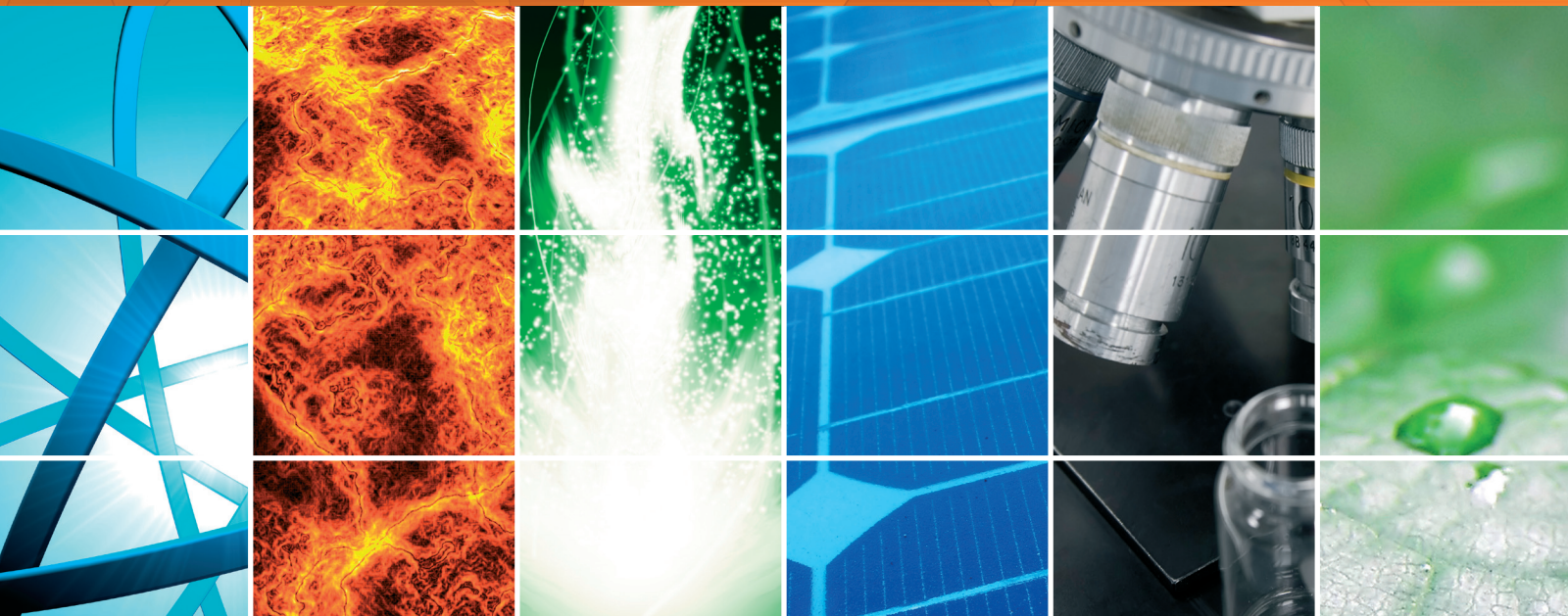


Innovative Applications of Advanced Solar Thermal Technologies Using Phase Change Materials

Lead Guest Editor: Ben Xu

Guest Editors: Juan Ordóñez, Zhonghao Rao, Xinhai Xu,
and Hamidreza Shabgard





Innovative Applications of Advanced Solar Thermal Technologies Using Phase Change Materials

Innovative Applications of Advanced Solar Thermal Technologies Using Phase Change Materials

Lead Guest Editor: Ben Xu

Guest Editors: Juan Ordonez, Zhonghao Rao, Xinhai Xu,
and Hamidreza Shabgard



Copyright © 2018 Hindawi. All rights reserved.

This is a special issue published in "International Journal of Photoenergy." All articles are open access articles distributed under the Creative Commons Attribution License, which permits unrestricted use, distribution, and reproduction in any medium, provided the original work is properly cited.

Editorial Board

M. S.A. Abdel-Mottaleb, Egypt
Angelo Albini, Italy
Alberto Álvarez-Gallegos, Mexico
Vincenzo Augugliaro, Italy
Detlef W. Bahnemann, Germany
Simona Binetti, Italy
Fabio Bisegna, Italy
Thomas M. Brown, Italy
Joaquim Carneiro, Portugal
Yatendra S. Chaudhary, India
Věra Cimrová, Czech Republic
Juan M. Coronado, Spain
P. Davide Cozzoli, Italy
Dionysios D. Dionysiou, USA
Abderrazek Douhal, Spain
Mahmoud M. El-Nahass, Egypt
Polycarpos Falaras, Greece
Chris Ferekides, USA
Paolo Fornasiero, Italy
Manuel Fuentes Conde, Spain

Germà Garcia-Belmonte, Spain
Elisa Isabel Garcia-Lopez, Italy
M. Ashraf Gondal, Saudi Arabia
Giulia Grancini, Switzerland
Pierluigi Guerriero, Italy
Michael D. Heagy, USA
Wing-Kei Ho, Hong Kong
Jürgen Hüpkens, Germany
Tariq Iqbal, Canada
Adel A. Ismail, Kuwait
Chun-Sheng Jiang, USA
Cooper H. Langford, Canada
Manuel Ignacio Maldonado, Spain
Dionissios Mantzavinos, Greece
Santolo Meo, Italy
Claudio Minero, Italy
Antoni Morawski, Poland
Fabrice Morlet-Savary, France
Mohammad Muneer, India
Maria da Graça P. Neves, Portugal

Tsuyoshi Ochiai, Japan
Kei Ohkubo, Japan
Leonardo Palmisano, Italy
Thierry Pauporté, France
Philippe Poggi, France
Francesco Riganti-Fulginei, Italy
Leonardo Sandrolini, Italy
Jinn Kong Sheu, Taiwan
Zofia Stasicka, Poland
Elias Stathatos, Greece
Jegadesan Subbiah, Australia
K. R. Justin Thomas, India
Nikolai V. Tkachenko, Finland
Ahmad Umar, Saudi Arabia
Thomas Unold, Germany
Mark van Der Auweraer, Belgium
Wilfried G.J.H.M. Van Sark, Netherlands
Xuxu Wang, China
Yanfa Yan, USA
Jiangbo Yu, USA

Contents

Innovative Applications of Advanced Solar Thermal Technologies Using Phase Change Materials

Ben Xu , Juan Ordonez, Zhonghao Rao , Xinhai Xu , and Hamidreza Shabgard
Editorial (2 pages), Article ID 5707264, Volume 2018 (2018)

A Parametric Investigation on Energy-Saving Effect of Solar Building Based on Double Phase Change Material Layer Wallboard

Xiaoxiao Tong  and Xingyao Xiong 
Research Article (8 pages), Article ID 1829298, Volume 2018 (2018)

Preliminary Estimate of Coriolis Force of Vapor Flow in Rotating Heat Pipes Based on Analytical Solution

Huanguang Wang  and Qi Yu
Research Article (12 pages), Article ID 8126318, Volume 2018 (2018)

Thermal Feature of a Modified Solar Phase Change Material Storage Wall System

Chenglong Luo , Lijie Xu , Jie Ji , Mengyin Liao, and Dan Sun
Research Article (8 pages), Article ID 6071589, Volume 2018 (2018)

Phase Distribution for Subcooled Flow Boiling in an Inclined Circular Tube

Wei Bao , JianJun Xu , TianZhou Xie, BingDe Chen, YanPing Huang, and DianChuan Xing
Research Article (10 pages), Article ID 7061826, Volume 2018 (2018)

Influence of Gas-Liquid Interface on Temperature Wave of Pulsating Heat Pipe

Ying Zhang, Zhiqiang Wang, Peisheng Li , Min Zhou, Boheng Dong, and Yanni Pan
Research Article (9 pages), Article ID 7492079, Volume 2018 (2018)

Preparation and Thermal Properties of Eutectic Hydrate Salt Phase Change Thermal Energy Storage Material

Lin Liang  and Xi Chen 
Research Article (9 pages), Article ID 6432047, Volume 2018 (2018)

Experimental Investigation on Thermal Management of Electric Vehicle Battery Module with Paraffin/Expanded Graphite Composite Phase Change Material

Jiangyun Zhang, Xinxi Li, Fengqi He, Jieshan He, Zhaoda Zhong, and Guoqing Zhang
Research Article (8 pages), Article ID 2929473, Volume 2017 (2018)

Numerical Simulation of Bubble Free Rise after Sudden Contraction Using the Front-Tracking Method

Ying Zhang, Min Lu, Wenqiang Shang, Zhen Xia, Liang Zeng, and Peisheng Li
Research Article (8 pages), Article ID 5128345, Volume 2017 (2018)

Study on the Instability of Two-Phase Flow in the Heat-Absorbing Tube of Trough Solar Collector

Ying Zhang, Peiyao Liu, Peisheng Li, Yue Chen, and Yanni Pan
Research Article (8 pages), Article ID 6547203, Volume 2017 (2018)



Predictive Power of Machine Learning for Optimizing Solar Water Heater Performance: The Potential Application of High-Throughput Screening

Hao Li, Zhijian Liu, Kejun Liu, and Zhien Zhang

Research Article (10 pages), Article ID 4194251, Volume 2017 (2018)

Determination of Performance Measuring Parameters of an Improved Dual Paraboloid Solar Cooker

Suhail Zaki Farooqui

Research Article (12 pages), Article ID 9459531, Volume 2017 (2018)

Editorial

Innovative Applications of Advanced Solar Thermal Technologies Using Phase Change Materials

Ben Xu ¹, **Juan Ordonez**,² **Zhonghao Rao** ³, **Xinhai Xu** ⁴ and **Hamidreza Shabgard**⁵

¹Department of Mechanical Engineering, The University of Texas Rio Grande Valley, Edinburg, TX 78539, USA

²Department of Mechanical Engineering, Florida State University, Tallahassee, FL 32306, USA

³School of Electrical and Power Engineering, China University of Mining and Technology, Xuzhou, Jiangsu 221116, China

⁴School of Mechanical Engineering and Automation, Harbin Institute of Technology, Shenzhen, Guangdong 518055, China

⁵Department of Aerospace and Mechanical Engineering, The University of Oklahoma, Norman, OK 73019, USA

Correspondence should be addressed to Ben Xu; ben.xu@utrgv.edu

Received 22 March 2018; Accepted 25 March 2018; Published 27 May 2018

Copyright © 2018 Ben Xu et al. This is an open access article distributed under the Creative Commons Attribution License, which permits unrestricted use, distribution, and reproduction in any medium, provided the original work is properly cited.

Recently, phase change material (PCM) have attracted a lot of attentions in energy storage and heating/cooling applications, because of its ability of storing more energy compared with the same amount of sensible storage material, but the intrinsically low thermal conductivity of PCM has restricted its broad applications; as a result, various heat transfer enhancement technologies have been developed [1]. Currently, PCMs have been widely applied in heating/cooling and heat recovery systems at low and medium temperature range (<200°C), but the integration of PCM with solar thermal energy is not well documented. Furthermore, most of the PCMs are not thermally or chemically stable at high or extremely high temperature (>200°C); as a result, it is critical to develop proper engineering ways to incorporate PCM at high temperature for solar thermal applications [2]. Currently, most of the solar thermal applications are in low and medium temperature range; limited information has been reported for high and extremely high-temperature applications due to the limitations of heat transfer fluid, especially for power energy [3].

This special issue is intended to address the integrated solutions using PCMs in various temperature ranges. It is of great interests for researchers and scientists in the fields of mechanical engineering, materials science/engineering, chemical engineering, environmental engineering, and so forth. A brief description and salient results of these papers are given below.

L. Liang and X. Chen prepared and tested a new cold storage phase change material eutectic hydrate salt by adding a nucleating agent and thickener. The physical properties were studied, and the experimental results showed that adding a nucleating agent can effectively improve the nucleation rate and nucleation stability.

H. Li et al. proposed a general design framework for solar water heater (SWH) design using a machine learning-based high-throughput screening (HTS) method, and they used the design of water-in-glass evacuated tube solar water heater (WGET-SWH) as an example; it is expected that this proposed design framework can cost effectively design and optimize a solar thermal system.

S. Z. Farooqui experimentally investigated the performance of an improved dual reflector foldable paraboloid solar cooker, along with its energy and exergy analysis. Their results indicated an average cooking power of 485 W, peak exergy gain of 60.53 W, quality factor of 0.077, and a high product of temperature difference gap at half peak power to peak power of 4364.33 W·K. The maximum exergy output power attained was 70 W, while maximum exergy efficiency was 8–10%.

Y. Zhang et al. had two papers discussing the applications of the front-tracking method (FTM) in the heat-absorbing tube of trough solar collector and pulsating heat pipe by considering the multiphase flow and heat transfer.

W. Bao et al. experimentally investigate the phase distribution of subcooled flow boiling in an inclined circular

tube, and they concluded that the phase distribution under the inclined condition is different from the phase distribution under the vertical condition; more specifically the profiles skewed highly for 90° and 45° direction in the tube cross-section, whereas the profile was also symmetrical at 0° direction.

J. Zhang et al. prepared and characterized the paraffin and EG composite phase change material (PCM), and the composite PCM have been applied in the 42110 LiFePO₄ battery module (48 V/10 Ah). The testing results indicated that the PCM cooling system can control the peak temperature under 42°C and balance the maximum temperature difference within 5°C. Even in extreme high-discharge pulse current process, the peak temperature can be controlled within 50°C.

H. Wang and Q. Yu studied the analytical solution of the vapor flow in rotating heat pipes based on the hypothesis of potential flow, and a specific rotating heat pipe was examined using three different boundary conditions: linear distribution, uniform but asymmetric distribution, and uniform and symmetric distribution of heat load; therefore, the flow field was calculated, and the Coriolis force is estimated.

C. Luo et al. investigated a novel solar PCM storage wall technology, which is a dual-channel and thermal-insulation-in-the-middle type solar PCM storage wall (MSPCMW) system. Basically, the system has four independent functions, passive solar heating, heat preservation, heat insulation, and passive cooling; therefore, this system can agilely cope with the requirements of climatization of buildings in different seasons, and therefore they experimentally analyzed the thermal feature of the system working in two different modes, summer and winter, respectively.

Acknowledgments

The authors would like to express their appreciation to all the authors and reviewers.

*Ben Xu
Juan Ordonez
Zhonghao Rao
Xinhai Xu
Hamidreza Shabgard*

References

- [1] M. Liu, W. Saman, and F. Bruno, "Review on storage materials and thermal performance enhancement techniques for high temperature phase change thermal storage systems," *Renewable and Sustainable Energy Reviews*, vol. 16, no. 4, pp. 2118–2132, 2012.
- [2] B. Xu, P. Li, and C. Chan, "Application of phase change materials for thermal energy storage in concentrated solar thermal power plants: a review to recent developments," *Applied Energy*, vol. 160, pp. 286–307, 2015.
- [3] J. Pereira da Cunha and P. Eames, "Thermal energy storage for low and medium temperature applications using phase change materials – a review," *Applied Energy*, vol. 177, pp. 227–238, 2016.

Research Article

A Parametric Investigation on Energy-Saving Effect of Solar Building Based on Double Phase Change Material Layer Wallboard

Xiaoxiao Tong ^{1,2} and Xingyao Xiong ³

¹Horticulture & Landscape College, Hunan Agricultural University, Changsha 410128, China

²School of Architecture & Design, China University of Mining and Technology, Xuzhou 221116, China

³Institute of Vegetables and Flowers, Chinese Academy of Agricultural Sciences, Beijing 100081, China

Correspondence should be addressed to Xingyao Xiong; xiongxingyao@126.com

Received 28 September 2017; Revised 5 December 2017; Accepted 18 April 2018; Published 27 May 2018

Academic Editor: Ben Xu

Copyright © 2018 Xiaoxiao Tong and Xingyao Xiong. This is an open access article distributed under the Creative Commons Attribution License, which permits unrestricted use, distribution, and reproduction in any medium, provided the original work is properly cited.

In order to further understand the thermal performance of the double phase change material (PCM) layer wallboard, the wallboard model was established and a comprehensively numerical parametric investigation was carried out. The variation laws of inner wall temperature rise and the heat flux transferred under different phase transition temperatures and thermal conductivities are presented in detail. The main results show that the temperature of the inside wall for case 2 can be reduced by about 1.5 K further compared to that for case 1. About 83% of the heat transferred from the outside is absorbed by the PCM layer in case 2. Reducing the phase transition temperature of the PCM layer can decrease the inside wall temperature to a certain extent in the period of high temperature. The utilization of double PCM layers shows much more performance compared to that of the single PCM layer case, and the temperature of the inside wall can be reduced by 2 K further.

1. Introduction

Energy demand has been increasing quickly with the development of economy. And the conventional fossil energy sources such as oil, coal, and gas are limited. Their use leads to climate changes and environmental pollution [1]. Building energy consumption has become a serious problem due to a large amount of energy that is consumed by the heating, ventilation, and air conditioning system of buildings every day. According to [2], about 40% of the world's total energy was used for buildings and more than 30% of the primary energy consumed in buildings is for the heating and air conditioning system. Therefore, some energy-saving and environment-friendly techniques have been investigated in recent years. Thermal energy storage techniques used in buildings to decrease the energy consumption were considered an effective way [3, 4]. Thermal energy storage can be divided into sensible heat storage, latent heat storage, and chemical energy storage. And among them, the latent heat storage has

received considerable attention in comparison with the other two methods attributed to the obvious advantages of latent heat storage using phase change material (PCM), like high energy storage density and narrow operating temperature range [5, 6]. Furthermore, PCM can store and release a large amount of latent heat during the process of melting and solidifying in its narrow phase transition range [7, 8].

In the past two decades, researches on the application of PCM in building energy conservation can be divided into two categories. One is combining the PCM with the active air conditional system where the PCM system serves as the heat source or cold source of the air conditioning system to increase the refrigerating efficiency or the heat efficiency [9, 10]. For instance, Tyagi et al. [11] designed and experimentally studied the thermal performance of a PCM-based building thermal management system for cool energy storage. The other is the usage in the passive heat insulation and preservation system, comprising the combination of PCM and building materials to obtain novel energy

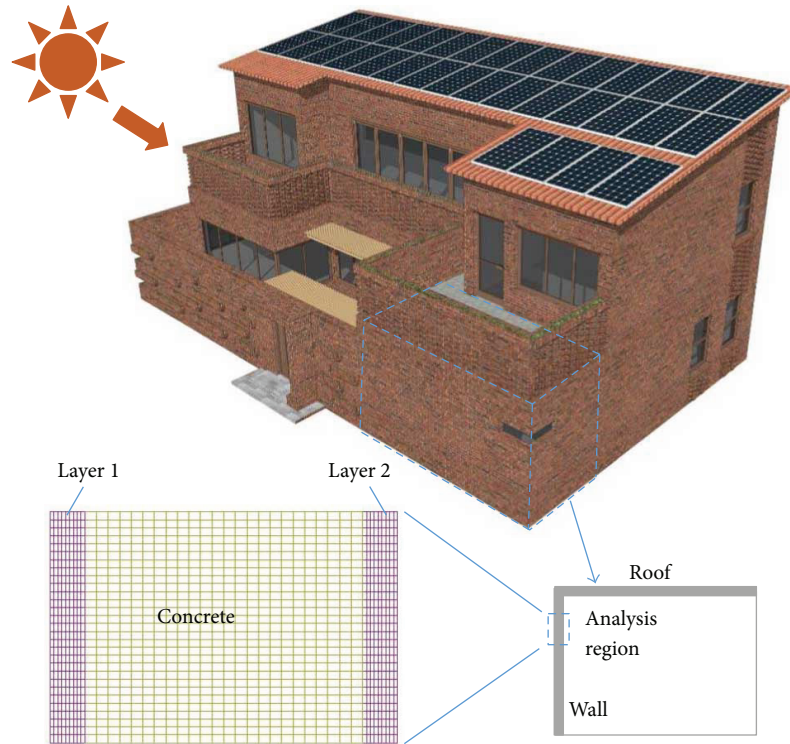


FIGURE 1: Schematics of the resident house and enlargement of the analysis region with structure mesh.

conservation building materials and directly inserting shape-stabilized PCM into the enclosure structure of the building [12–14]. The first category of PCM application needs to be considered early in the design process of the air conditioning system and also needs later maintenance. However, the second one is concentrated on the design of new building material, like coating material with phase change function, insulation wallboard, and brick with PCM encapsulated in it, and is a way to enhance the ability of the building itself to adapt to the climate. Therefore, it is widely of concern to scholars. Li et al. [15] compared the thermal performance of lightweight buildings with and without a PCM layer attached to the inside wallboard and found that the energy consumption to maintain comfortable temperature can be reduced by 40–70%. Ramakrishnan et al. [16] numerically investigated the thermal control effect of building fabrics integrated with PCM under extreme heatwave periods. The result shows that the indoor heat stress risks can be reduced effectively without the function of an air conditioner. Meanwhile, Thiele et al. [17] constructed a numerical model based on a modified admittance model to evaluate the thermal performance of building envelopes integrated with PCM whose result turns to agree well with that of the existing finite element simulations. Zhu et al. [18, 19] put forward a new structure of wallboards with double shape-stabilized PCM, proposed a related simplified dynamic model, and then used it to analyze energy performance of office building under different conditions. However, the model and related analysis are concentrated on the whole system and overall efficiency. The heat transfer process and the influence of the PCM parameters on the heat transfer law are also quite important for the actual design and need to be further understood.

In this paper, in order to further explore the heat transfer law and thermal performance of the double PCM layer wallboard put forward by Zhu et al. [18] under different conditions, the wallboard model was established and a comprehensively parametric numerical investigation was carried out. The variation law of temperature rise at the inner side of the wall and the heat flux transferred under different phase transition temperatures, thermal conductivities, and arrangements of PCMs are presented and discussed in detail in the following sections.

2. Model and Methodology

2.1. Model Description. Figure 1 shows the schematics of the resident house and enlargement of the analysis region with structure mesh. The performance of the wall determines the economic and energy-saving efficiency of the whole building to a great extent. Therefore, the wallboard is the key research object. The structure of the wallboard is presented in the enlarged view clearly. As shown in Figure 2, three cases of wallboard with different layer combinations were designed and compared. Case 1 represents the convection wallboard with insulation material only. The insulation layer outside is replaced by the PCM layer in case 2, and both insulation layers are replaced by PCM layers in case 3. The dimensions and thermo-physical properties of these two layers and the concrete can be seen in Table 1.

2.2. Numerical Simulation. With the development of computer technology, numerical study as an effective means of research involving design, analysis, and optimization is being developed quickly. In this exploration, commercial

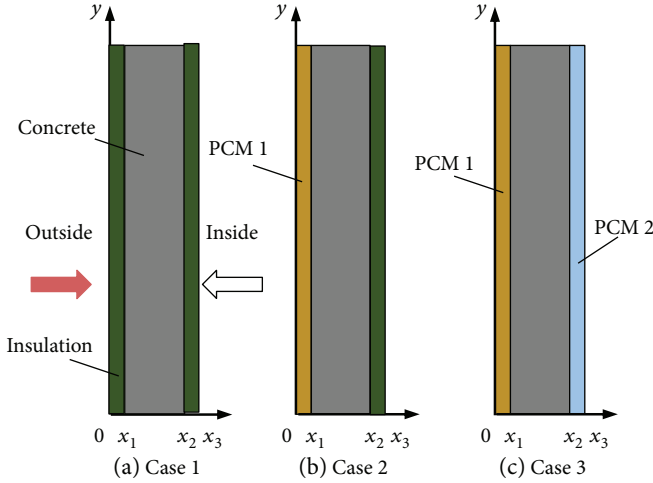


FIGURE 2: Schematics of the building wallboard with/without PCM.

computational fluid dynamics package, FLUENT 14.0, was utilized. The mesh density and the computational parameters such as time step and number of iterations per time step were evaluated by checking the dependency of the total heat transfer flux on models with various mesh quantities and different computational parameters. The time step was set to 10 seconds, and the number of iterations per time step was 50. The pressure-based 1st-order implicit algorithm for this unsteady problem was considered. Some assumptions were made in the following simulation work. The specific heat, the phase transition temperature, and the thermal conductivity of PCMs were constant. Also, the PCMs utilized were isotropic and homogenous. The volume change of the PCM during phase transition was ignored.

The energy conservation equation for the concrete region can be presented as follows:

$$\frac{\partial}{\partial \tau} (\rho_c c_{pc} t_c) = \nabla \cdot (\lambda_c \nabla t_c), \quad (1)$$

where ρ_c , c_{pc} , and λ_c are the density, heat capacity, and thermal conductivity of the concrete, respectively. The enthalpy-porosity model was adopted to model the phase changing process in this work. The liquid fraction is computed at each iteration, based on an enthalpy balance. The energy equation of PCM can be expressed as follows [20]:

$$\rho \frac{\partial H}{\partial \tau} = k \nabla^2 H + S, \quad H = H_0 + \Delta H,$$

$$H_0 = H_{\text{ref}} + \int_{T_{\text{ref}}}^T C_{p_{\text{pcm}}} dT, \quad C_{p_{\text{pcm}}} = \begin{cases} C_{p_{s_{\text{pcm}}}}, & T < T_m, \\ C_{p_{l_{\text{pcm}}}}, & T > T_m, \end{cases}$$

$$\Delta H = \beta \gamma, \quad \beta = \begin{cases} 0, & T < T_m, \\ 1, & T > T_m, \end{cases} \quad (2)$$

where H represents the total enthalpy of PCM, H_0 is the sensible enthalpy, ΔH is the latent heat, β is the liquid fraction, and T_m is the phase transition temperature.

$$q_s''(t) = \begin{cases} q_{s,\text{max}}'' \cos\left(\frac{\pi t}{43200} - \pi\right), & 6:00 \text{ am} \leq t \leq 6:00 \text{ pm}, \\ 0, & 6:00 \text{ pm} < t \leq 6:00 \text{ am}, \end{cases} \quad (3)$$

$$q_{\text{ave}}'' = \frac{\int q_s''(t) dt}{12 \times 3600} = \frac{\int q_{s,\text{max}}'' \cos\left(\frac{\pi t}{43200} - \pi\right) dt}{12 \times 3600} \quad (4)$$

$$= \frac{q_{s,\text{max}}'' \int \cos\left(\frac{\pi t}{43200} - \pi\right) dt}{12 \times 3600}.$$

The external boundary condition is based on the total solar radiation of the Xuzhou area, which can be seen in Figure 3 [21]. The average solar radiation (q_{ave}'') of the Xuzhou area in June is about 385.8 W/m^2 , and the maximum daily solar radiation can be observed through (4). Boundary conditions at the top and bottom of the model are thermal isolation. The sun radiation reaches the left side to heat the wall, and the convection heat transfer exists at the same time to cool the wall. But the heat flux and radiation cannot appear in the boundary condition at the same time to complete the numerical solution. Therefore, after simplification, the left boundary condition is time-dependent temperature boundary, which is described as follows:

$$x = 0,$$

$$-k \frac{\partial T}{\partial n} = T(\tau) = \Delta T_{\text{max}} + T_{\text{ini}} \sin\left(\frac{\pi t}{60000}\right). \quad (5)$$

The right side boundary conditions are mixed boundary conditions. The right side of the wall heats the air inside by radiation and convection synchronously, which can be described as follows:

$$x = x_3,$$

$$-k_i \frac{\partial T}{\partial n} = h_i (T_{\text{wi}} - T_{\text{ai}}) + \varepsilon \sigma (T_{\text{wi}}^4 - T_{\text{ai}}^4). \quad (6)$$

A parametric study was undertaken to investigate the influence of phase transition temperature of PCM and thermal conductivities of PCM and the thermal control effect of the double PCM layers compared to other two cases.

3. Result and Discussion

The aim of this work was to investigate a special kind of wallboard with two PCM layers attached both sides of the concrete wall for heat insulation and energy saving. Temperature variation of the outside wall with time in summer is exhibited in Figure 4. As the figure shows, the temperature of the outside wall increases to 325 K linearly with a relatively high rate of rise before 10:00 am, and the tendency of temperature rising gradually reduces from 10:00 am to 02:00 pm. The highest temperature of the outside wall in one solar day is up to about 338 K at 02:00 pm. After 02:00 pm, the temperature of the outside wall gradually decreases to 330 K (at 06:00 pm). This variation trend of the outside wall

TABLE 1: Thermo-physical properties of the wallboard materials [18].

Materials	c_p (kJ/kg \cdot °C)	λ (W/m \cdot °C)	ρ (kg/m 3)	L (kJ/kg)	T_m (°C)	D (m)
Concrete	0.8	2.1	2400	—	—	0.24
Insulation	2.0	0.2	850	—	—	0.03
PCM 1/PCM 2	2.0	0.1~2	850	200	26~29	0.03

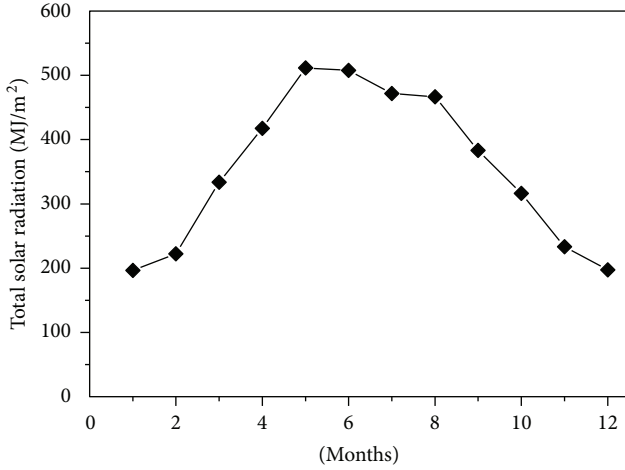


FIGURE 3: Total solar radiation of the Xuzhou area in different months.

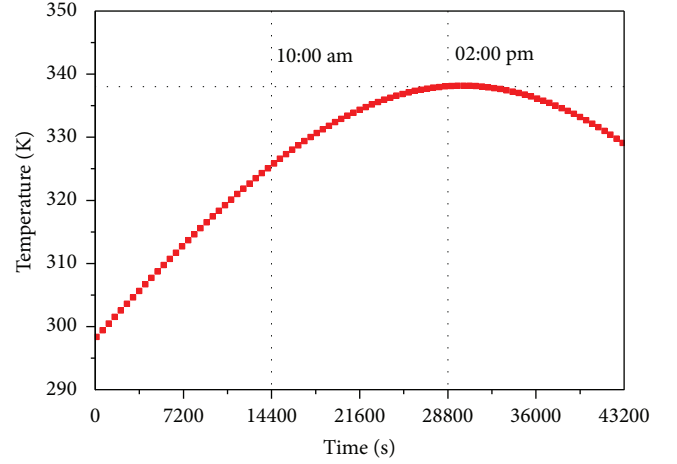


FIGURE 4: Temperature variation of the outside wall at different moments in summer.

temperature can reflect well the actual temperature condition of a solar day in the Xuzhou area in summer.

Figure 5 presents the temperature variation and the heat flux of the inside wall for different cases. As shown in Figure 5(a), the temperature of case 1 and case 2 has little change before 10:00 am, keeping a temperature of 299 K, and after 10:00 am, the temperature of case 1 gradually increases to 300 K, while that of case 2 has only little variation until 02:00 pm. After 02:00 pm, variation of temperature rising of case 1 has a significant improvement and case 2 starts a temperature rising with a similar tendency with that of case 1, and the temperatures of case 1 and case 2 are, respectively, 302 K and 300 K. As the wall is without any heat insulation layer or PCM layer, the temperature of the inside wall rises promptly after 09:00 am and finally rises to 312 K at 06:00 pm. In summary, the function of the insulation layer and PCM layer can both greatly retard the velocity of temperature diffusion, and the inside wall temperature can be decreased by more than 10 K. Case 2 has a certain advantage over case 1, which is attributed to the phase change endothermic behavior of the PCM layer. When the outside insulation layer was replaced by the PCM layer, the temperature of the inside wall can be reduced by about 1.5 K further. As shown in Figure 5(b), the heat flux is positive in the morning, indicating that the wall absorbs the air heat in the room, for the reason that the temperature of external air is set larger than the initial temperature of the wall in the simulation process. The heat flux of case 2 begins to turn negative, and the heat began to go through the wall completely until about 04:00 pm. It can be concluded from area C and area A in Figure 5(b) that the heat transferred into the indoor can be reduced about

98% by the function of the PCM layer and insulation layer. It can also be deduced that about 83% of the heat transferred from the outside is absorbed by the PCM layer through comparing area B and area C.

Figure 6 shows the temperature contours of the wallboard at 06:00 pm for three different cases obviously. The temperature distribution exhibits uniform gradient in the concrete wall case, in which the double layers are replaced by the concrete. It can be seen from case 1 and case 2 that the overall average temperature of the concrete wall in case 2 is obviously lower than that in case 1 for the reason that PCM can absorb large amount of latent heat under lower and stable temperature region, the heat transfer driving force and temperature difference are relatively weak, and less heat gets across the border to the concrete wall.

3.1. The Effect of Phase Transition Temperature of the PCM Layer. Figure 7 presents temperature variation and heat flux of the inside wall for case 2 under different phase transition temperatures (from 299.15 K to 302.15 K). As shown in Figure 7(a), the temperature under different phase transition times is identical before 10:00 am and after 04:00 pm. In the middle range of the solar day, the temperature difference under different phase transition temperatures increases firstly and then decreases. When time goes after 02:00 pm, the temperature difference under different phase transition temperatures decreases in contrast. The temperature of the inside wall under different phase transition temperatures is identical again at 04:00 pm, and the final identical temperature is about 301 K, increasing about 2.7 K. As shown in Figure 7(b), heat flux of the inside wall is also identical under

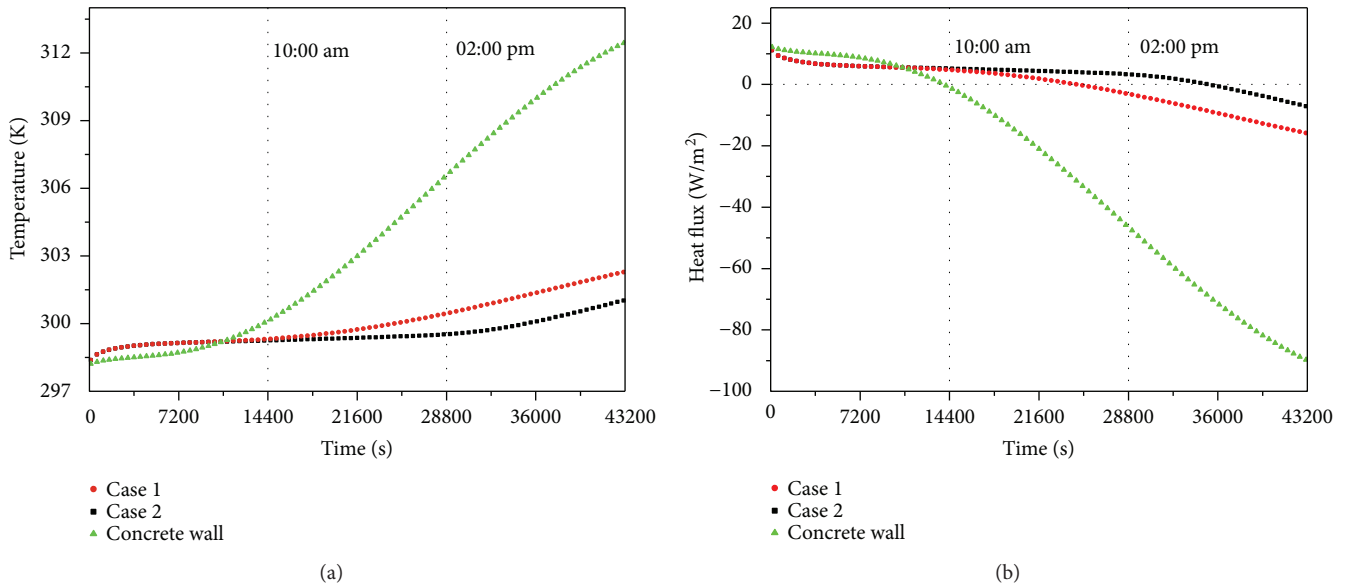


FIGURE 5: Temperature variation and heat flux of the inside wall under different cases.

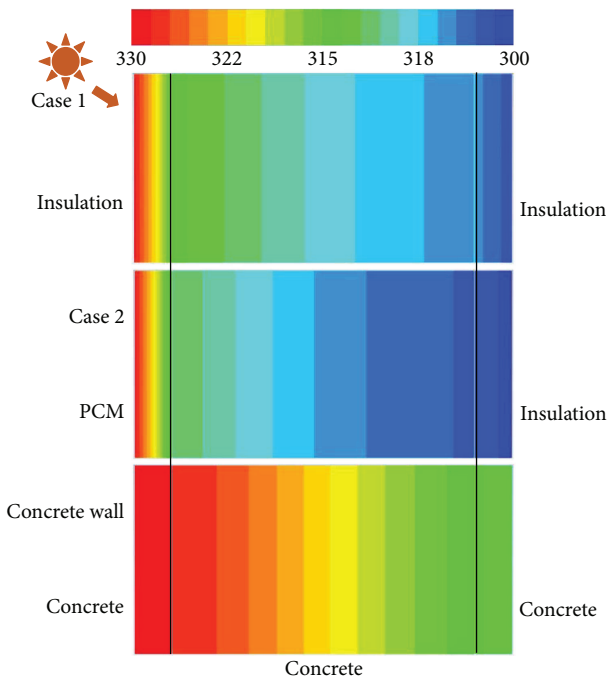


FIGURE 6: Temperature contour of the wallboard at 06:00 pm under different cases.

different transition temperatures before 10:00 am. When time is over 10:00 am, heat flux of the inside wall is higher under lower phase transition temperature, which is opposite to temperature. Heat flux of the inside wall under different phase transition temperatures is identical at the end. It can also be seen that heat flux decreases from 11.2 W/m^2 to -7 W/m^2 . Actually, heat flux decreases from 11.2 W/m^2 to 0 W/m^2 , and then it increases to 7 W/m^2 with the opposite heat transfer direction. In summary, reducing the phase transition temperature of the PCM layer can decrease the inside wall temperature to a certain degree in the middle period of

a solar day; however, the heat transferred into the indoor in the whole daytime is almost not affected by the phase transition temperature.

3.2. The Effect of Thermal Conductivity of PCM. Figure 8 exhibits the temperature variation and heat flux of the inside wall for case 2 under different thermal conductivities of PCM. As shown in Figure 8(a), the temperature of the inside wall has little change before 10:00 am, keeping a temperature of 299 K, though the thermal conductivity of PCM is changed. After 10:00 am, the temperature of the inside wall gradually increases and the final temperatures are 303.2 K, 305.4 K, and 307.4 K while the thermal conductivities of PCM are $0.4 \text{ W/(m}\cdot\text{K)}$, $0.8 \text{ W/(m}\cdot\text{K)}$, and $2 \text{ W/(m}\cdot\text{K)}$, respectively. As the thermal conductivity of PCM reaches $0.2 \text{ W/(m}\cdot\text{K)}$, the rising trend of the inside wall temperature becomes obvious after 02:00 pm, and the final temperature rises to 301 K. However, the temperature of the inside wall has little change during the whole solar day when the thermal conductivity of PCM is as low as $0.1 \text{ W/(m}\cdot\text{K)}$. It is obvious that decreasing the thermal conductivity of the PCM layer is beneficial to heat insulation and energy saving. Less heat can be transferred to the indoor. As shown in Figure 8(b), heat flux is almost stable around 5 W/m^2 and flows toward the outside before 10:00 am. And after 10:00 am, heat flux gradually reverses its direction and reaches about 22.5 W/m^2 , 37.9 W/m^2 , and 52.3 W/m^2 at 06:00 pm as the thermal conductivities of PCM are $0.4 \text{ W/(m}\cdot\text{K)}$, $0.8 \text{ W/(m}\cdot\text{K)}$, and $2 \text{ W/(m}\cdot\text{K)}$, respectively. Figure 9 shows the phase change ratio of the PCM layer for case 2 under different thermal conductivities. It can be found that when the thermal conductivity is $2 \text{ W/(m}\cdot\text{K)}$, the PCM melts entirely in almost 7200 s, while it takes 4.5 times longer to melt the PCM layer with a thermal conductivity of $0.1 \text{ W/(m}\cdot\text{K)}$.

3.3. The Effect of Double PCM Layers. In order to further increase the energy-saving capacity of the wallboard, the

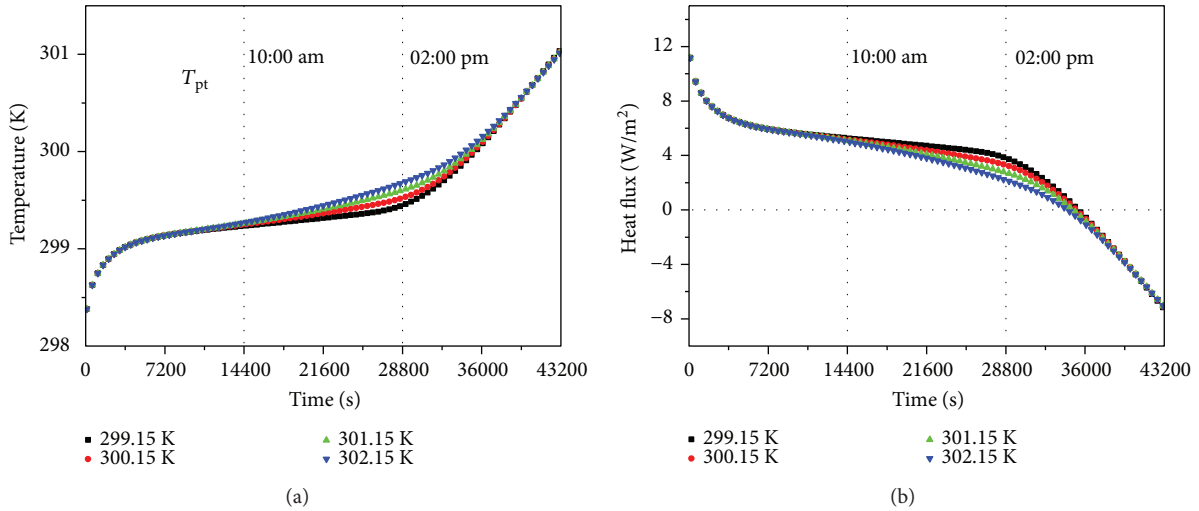


FIGURE 7: Temperature variation and heat flux of the inside wall for case 2 under different phase transition temperatures.

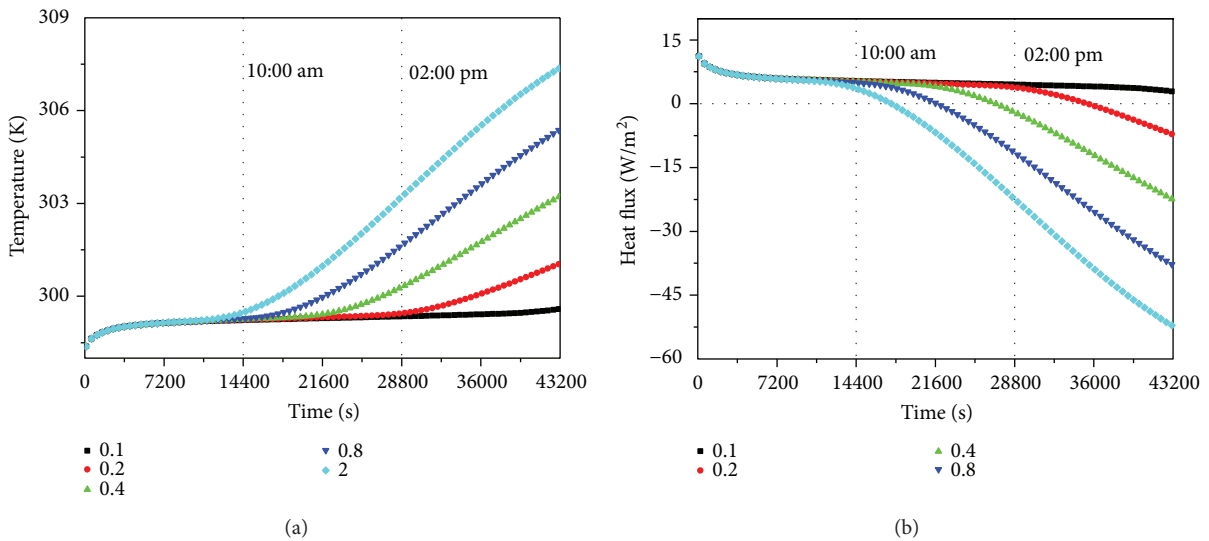


FIGURE 8: Temperature variation and heat flux of the inside wall for case 2 under different thermal conductivities of PCM.

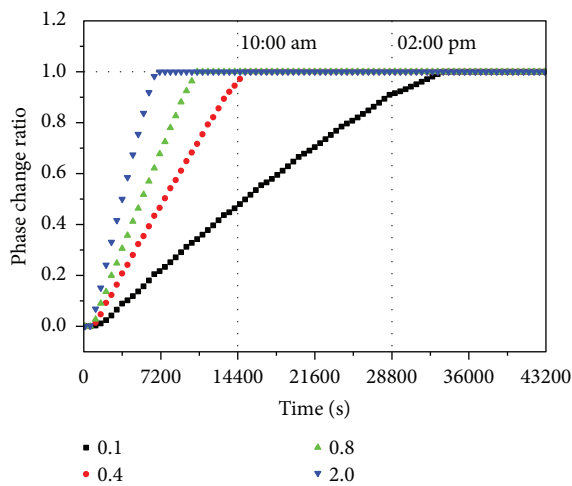


FIGURE 9: Phase change ratio of the PCM layer for case 2 under different thermal conductivities.

right insulation layer is also replaced by the PCM layer, and the PCM has the same thermal physical property as the left layer. Figure 10 presents the temperature variation and heat flux of the inside wall for case 3. It can be observed that the temperature curve for case 3 increases first and becomes stable almost the whole day. The temperature can be stabilized at about 299.15 K. The wallboard with double PCM layers shows much better thermal performance compared to the single PCM layer case, and the temperature of the inside wall can be reduced by 2 K further. The inner wall almost can exclude the interference from external environment. As shown in Figure 10(b), the heat flux for case 3 is positive in the whole daytime. The heat outside cannot be transferred to the indoor, which is the reason why the temperature of the inside wall can be stable. Figure 11 illustrates the phase change ratio of each PCM layer for case 3. The phase change ratio of PCM 1 is on the rise before 12:00 pm, but that of PCM 2 remains constant until 02:00 pm. It can be seen that PCM 1 just takes 21600 s to melt totally. However, the phase

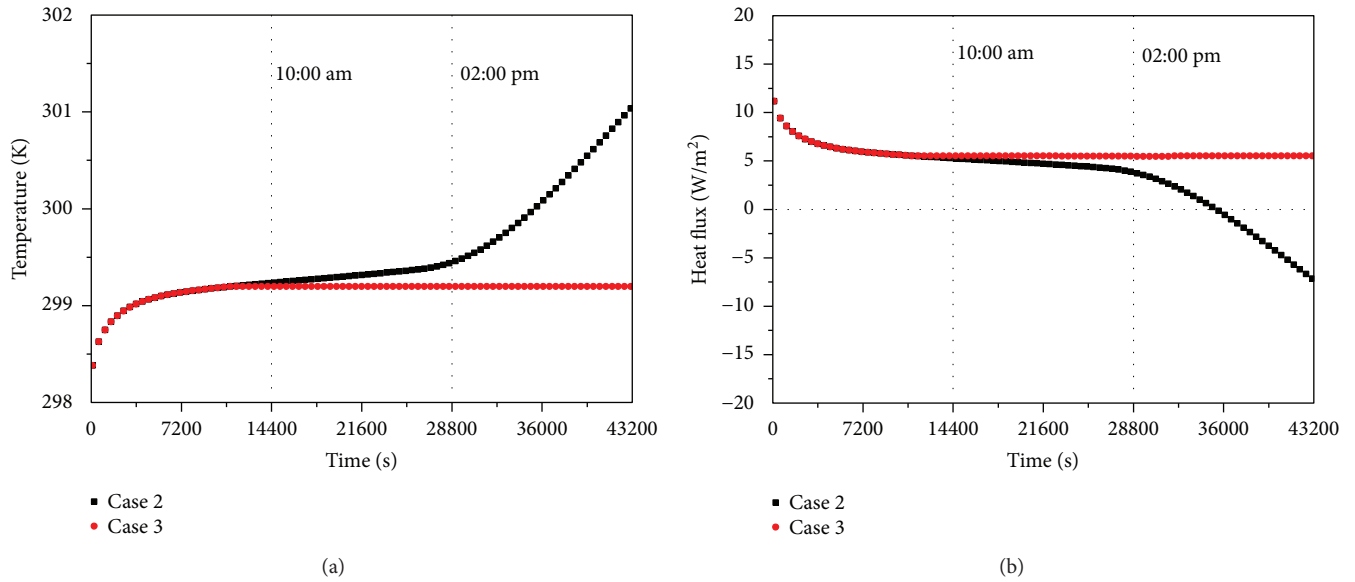


FIGURE 10: Temperature variation and heat flux of the inside wall for case 3.

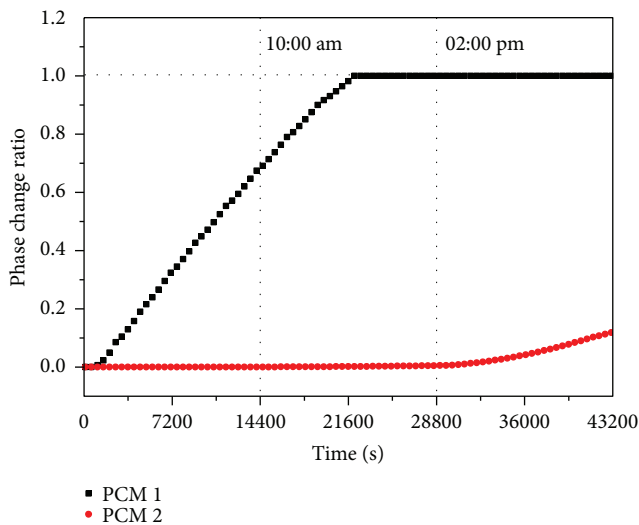


FIGURE 11: Phase change ratio of each PCM layer for case 3.

change ratio of PCM 2 is still under 0.2 at the end of the solar day.

4. Conclusion

In order to further understand the heat transfer law and thermal performance of the double PCM layer wallboard under different conditions, a comprehensively parametric numerical investigation was carried out. The variation law of temperature rise at the inner side of the wall and the heat flux flowed through under different phase transition temperatures, thermal conductivities, and arrangements of PCMs are presented and discussed in detail. The main conclusions can thus be summarized as follows:

- (1) The function of the insulation layer and PCM layer can both greatly retard the velocity of temperature

diffusion, and the inside wall temperature can be decreased by more than 10 K. About 83% of the heat transferred from the outside is absorbed by the PCM layer in case 2.

- (2) Reducing the phase transition temperature of the PCM layer can decrease the inside wall temperature to a certain degree in the period of high temperature. Increasing the thermal conductivity of the PCM layer is not beneficial to heat insulation and energy saving. More heat can be transferred to the indoor easily.
- (3) The utilization of the double PCM layer shows much more performance compared to that of the single PCM layer case, and the temperature of the inside wall can be reduced by 2 K further.

Nomenclature

T :	Temperature (K)
ΔT :	Temperature difference (K)
c_p :	Specific heat (J/(kg·K))
H :	Enthalpy (J kg ⁻¹)
ΔH :	Latent heat of PCM (J kg ⁻¹)
ΔT :	Temperature increase (K)
k :	Thermal conductivity (W/(m·K))
q :	Heat flux (W/m ²)
β :	Liquid volume fraction
τ :	Time (s)
ρ :	Density (kg/m ³)
ε :	Emissivity
σ :	Stefan-Boltzmann constant.

Subscripts

w:	Wall
wi:	Wall inside
a:	Air

ai: Air inside
 ini: Initial
 c: Concrete
 ave: Average
 ref: Reference
 m: Melting.

Acronyms

PCM: Phase change material.

Conflicts of Interest

The authors declare that there is no conflict of interest regarding the publication of this paper.

Acknowledgments

This work was supported by the National Natural Science Foundation of China (no. 51778611).

References

- [1] T. Qian, J. Li, X. Min, Y. Deng, W. Guan, and L. Ning, "Diatomite: a promising natural candidate as carrier material for low, middle and high temperature phase change material," *Energy Conversion and Management*, vol. 98, pp. 34–45, 2015.
- [2] Z. Chen, M. Qin, and J. Yang, "Synthesis and characteristics of hygroscopic phase change material: composite microencapsulated phase change material (MPCM) and diatomite," *Energy and Buildings*, vol. 106, pp. 175–182, 2015.
- [3] S. Karaman, A. Karaipekli, A. Sari, and A. Biçer, "Polyethylene glycol (PEG)/diatomite composite as a novel form-stable phase change material for thermal energy storage," *Solar Energy Materials and Solar Cells*, vol. 95, no. 7, pp. 1647–1653, 2011.
- [4] B. Xu and Z. Li, "Performance of novel thermal energy storage engineered cementitious composites incorporating a paraffin/diatomite composite phase change material," *Applied Energy*, vol. 121, pp. 114–122, 2014.
- [5] S.-G. Jeong, J. Jeon, O. Chung, S. Kim, and S. Kim, "Evaluation of PCM/diatomite composites using exfoliated graphite nanoplatelets (xGnP) to improve thermal properties," *Journal of Thermal Analysis and Calorimetry*, vol. 114, no. 2, pp. 689–698, 2013.
- [6] M. Li, H. Kao, Z. Wu, and J. Tan, "Study on preparation and thermal property of binary fatty acid and the binary fatty acids/diatomite composite phase change materials," *Applied Energy*, vol. 88, no. 5, pp. 1606–1612, 2011.
- [7] X. Fu, Z. Liu, Y. Xiao, J. Wang, and J. Lei, "Preparation and properties of lauric acid/diatomite composites as novel form-stable phase change materials for thermal energy storage," *Energy and Buildings*, vol. 104, pp. 244–249, 2015.
- [8] A. Sari and A. Karaipekli, "Fatty acid esters-based composite phase change materials for thermal energy storage in buildings," *Applied Thermal Engineering*, vol. 37, pp. 208–216, 2012.
- [9] F. Souayfane, F. Fardoun, and P.-H. Biwole, "Phase change materials (PCM) for cooling applications in buildings: a review," *Energy and Buildings*, vol. 129, pp. 396–431, 2016.
- [10] S. Ramakrishnan, X. Wang, M. Alam, J. Sanjayan, and J. Wilson, "Parametric analysis for performance enhancement of phase change materials in naturally ventilated buildings," *Energy and Buildings*, vol. 124, pp. 35–45, 2016.
- [11] V. V. Tyagi, D. Buddhi, R. Kothari, and S. K. Tyagi, "Phase change material (PCM) based thermal management system for cool energy storage application in building: an experimental study," *Energy and Buildings*, vol. 51, pp. 248–254, 2012.
- [12] D. Feldman, D. Banu, and D. W. Hawes, "Development and application of organic phase change mixtures in thermal storage gypsum wallboard," *Solar Energy Materials and Solar Cells*, vol. 36, no. 2, pp. 147–157, 1995.
- [13] M. Chung and J. Park, "An experimental study on the thermal performance of phase-change material and wood-plastic composites for building roofs," *Energies*, vol. 10, no. 2, p. 195, 2017.
- [14] J. Lei, K. Kumarasamy, K. T. Zingre, J. Yang, M. P. Wan, and E.-H. Yang, "Cool colored coating and phase change materials as complementary cooling strategies for building cooling load reduction in tropics," *Applied Energy*, vol. 190, pp. 57–63, 2017.
- [15] Y. Li, Y. Wang, X. Meng, W. Zhang, and E. Long, "Research on thermal performance improvement of lightweight buildings by integrating with phase change material under different climate conditions," *Science and Technology for the Built Environment*, vol. 23, no. 2, pp. 285–295, 2016.
- [16] S. Ramakrishnan, X. Wang, J. Sanjayan, and J. Wilson, "Thermal performance of buildings integrated with phase change materials to reduce heat stress risks during extreme heatwave events," *Applied Energy*, vol. 194, pp. 410–421, 2017.
- [17] A. M. Thiele, R. S. Liggett, G. Sant, and L. Pilon, "Simple thermal evaluation of building envelopes containing phase change materials using a modified admittance method," *Energy and Buildings*, vol. 145, pp. 238–250, 2017.
- [18] N. Zhu, P. Hu, and L. Xu, "A simplified dynamic model of double layers shape-stabilized phase change materials wallboards," *Energy and Buildings*, vol. 67, pp. 508–516, 2013.
- [19] N. Zhu, P. Liu, F. Liu, P. Hu, and M. Wu, "Energy performance of double shape-stabilized phase change materials wallboards in office building," *Applied Thermal Engineering*, vol. 105, pp. 180–188, 2016.
- [20] Z. Rao, S. Wang, and G. Zhang, "Simulation and experiment of thermal energy management with phase change material for ageing LiFePO₄ power battery," *Energy Conversion and Management*, vol. 52, no. 12, pp. 3408–3414, 2011.
- [21] L. Zhang, J. Liu, and R. Zhang, "Assessment of solar radiation condition in Xuzhou area," *Acta Agriculturae Jiangxi*, vol. 22, no. 3, pp. 114–117, 2010.

Research Article

Preliminary Estimate of Coriolis Force of Vapor Flow in Rotating Heat Pipes Based on Analytical Solution

Huanguang Wang  and Qi Yu

School of Electrical and Power Engineering, China University of Mining and Technology, Xuzhou 221116, China

Correspondence should be addressed to Huanguang Wang; whg2013@cumt.edu.cn

Received 25 August 2017; Revised 16 January 2018; Accepted 30 January 2018; Published 3 April 2018

Academic Editor: Ben Xu

Copyright © 2018 Huanguang Wang and Qi Yu. This is an open access article distributed under the Creative Commons Attribution License, which permits unrestricted use, distribution, and reproduction in any medium, provided the original work is properly cited.

In current theory models for rotating heat pipes, the temperature field of the vapor phase is often supposed to be homogenous, and as a result of such simplification, the experiment result of the heat transfer performance for high rotating speed has some discrepancy with that predicted by theory models. In this paper, the analytical solution of the vapor flow in rotating heat pipes was obtained on the hypothesis of potential flow and with the method of variable separation. A specific rotating heat pipe was examined under three kinds of boundary conditions: linear distribution, uniform but asymmetric distribution, and uniform as well as symmetric distribution of heat load. The flow field was calculated, the Coriolis force is estimated, and it is found that (1) for a rotating heat pipe with high speed or large heat load, it is necessary to consider the Coriolis force, as its magnitude can be that of the gravitational acceleration; (2) the maximum Coriolis force is located at the vapor-liquid interface at the evaporator and condenser sections, and the directions in these two sections are opposite; (3) the Coriolis force is closely related with working conditions and working fluids, and it decreased with working temperature and increased with the heat load; and (4) the maximum viscous shear stress is located at the adiabatic section.

1. Introduction

A rotating heat pipe is a special kind of heat pipe which rotates with the object it cools, and the liquid fluid in it flows back under the centrifugal force. The structure of a rotating heat pipe includes a cylindrical rotating heat pipe [1], a parallel axis rotating heat pipe [2, 3], a radial rotating heat pipe [4], a truncated cone rotating heat pipe [1], and an even fan-shaped rotating heat pipe [5]. On account of the stable and strong driving ability caused by the centrifugal force, the advantage of heat pipes to get more even temperature field can be brought into full play by rotating heat pipes, and an important application of it is the thermal and cold protection for rotary machines, such as generators [6], rotor of gas turbines [4, 5, 7], aeroengine nose cones [8–10], milling machines [11, 12], and drills [13]. For such equipment, due to friction, to electromagnetic induction, and to being heated or even cooled [8–10], the temperature of the rotating shaft, blade, or nose cone is often uneven, causing thermal stress [4], deformation, and even failure of the machine.

Thus, thermal and cold protection is required; however, there are some problems with the currently used thermal or cold protection method more or less, like economic or security ones, for instance, hydrogen cooling in generators [14] and film cooling in gas turbines. Therefore, the passive dredging thermal protection scheme of rotating heat pipes is now gradually revealing its advantage.

Current researches on rotating heat pipes contain two directions: experiment and numerical simulations, the former focuses on the relationship between thermal resistance and parameters like rotation speed and liquid charging rate, such as the research of Xie et al. [15], Ponnappan et al. [16], Song et al. [17], and so on. Ponnappan et al. [16] researched on the case of high rotation speed and found that the variation of thermal resistance was opposite to the result got by the Nusselt condensation model. While numerical simulation mainly studies on the four processes of evaporation, condensation, vapor flow, and liquid flow happened in the rotating heat pipe. According to recent researches, the thermal resistances in the four processes are of different

magnitudes. The resistance in the evaporation process is usually small and can be ignored, while for the condensation process, the modified Nusselt model is widely adopted which is now deemed as sophisticated, and when it comes to vapor and liquid flow, the vapor phase is usually simplified as a system with uniform temperature and pressure, and the interior boundary condition of the liquid flow can be set based on such hypothesis. Thus, liquid flow can be solved under different types of models, according to their dimensions. For example, Daniels and Al-Jumaily [18] and Uddina et al. [19] ignored the inertia term of the liquid phase and obtained its temperature distribution by the zero dimension model. Song et al. [17], Bertossi et al. [1], and Hassan and Harmand [2, 20] considered the liquid phase as a one-dimensional flow; Li et al. [21] treated it as a two-dimensional flow. However, to discuss the performance of the heat pipe clearly under different working conditions, the effect of the vapor phase should be taken into full consideration. Faghri et al. took full researches on who resolved originally the velocity field of the vapor phase in rotating heat pipes in [22] and who got the complex distribution of vapor phase parameters in high rotating speed. In their article, the effect of the radial Reynolds number Re_r on the vapor flow was intensively discussed, and it is found that when Re_r is small, the circumferential velocity is proportional to the radius and the field takes on the feature of plane flow; when the Re_r is large enough, the linear relationship between the circumferential velocity and the radius was broken, with the velocity becoming larger at the evaporation section and smaller at the condensation section, which indicated some circumferential forces existing and becoming obvious at high rotation speed, and it is just the Coriolis force. An Indian scholar, Solomon et al. [23], pointed out that vapor flow in the rotating heat pipe is affected by the Coriolis force to some extent, and this is the first literature to date pointing out the existence of the Coriolis force in rotating heat pipes.

In summary, it can be seen that vapor flow in a rotating heat pipe is very complicated, and its flow pattern has a significant impact on the whole performance of a rotating heat pipe; however, theoretical models aiming for rotating heat pipe simulating and mechanism revealing are insufficient. It is worth studying whether the heat transfer characteristics of a rotating heat pipe found by Ponnappan et al. at high rotation speed are affected by the vapor flow pattern, and the dynamics and thermodynamics law of vapor flow of a rotating heat pipe at high rotation speed or at high heat load is also needed to be further clarified. Thus, in this article, it is aimed to obtain the flow of vapor in rotating heat pipes by an analytical method based on the hypothesis of potential flow and especially explore the Coriolis force inflicted to the vapor phase.

2. Establishment of Physical Model for Calculation

For the sake of convenience of theoretical research and viability of the analytical method to get the solution of vapor flow, a two-dimensional rotating heat pipe model was established, which is also the mainstream model for rotating heat pipe research, and the structure of which is shown as the

following figure: the rotating heat pipe has a rotating shell which was installed on the object it cools, heat was sucked on the left side—the evaporator, and released on the right side—the condenser, and the middle part of the pipe corresponds to the adiabatic section. The liquid film is attached to the inner wall of the shell, under the function of the centrifugal force. It is advisable and reasonable to suppose that the centrifugal force is large enough, so the variation of the thickness of the liquid film along the direction of the axis can be neglected. The vapor phase flow is driven by the phase change at the liquid-vapor interface, which constitutes the boundary condition of the vapor phase flow. The length of the evaporator is denoted as l_1 , and the length of the condenser is denoted as l_2 . The heat flux at the evaporator is denoted as q_1 , and the heat flux at the condenser is denoted as q_2 . Accordingly, the velocity boundary condition of the vapor flow at the evaporator is denoted as u_1 , and that at the condenser is denoted as u_2 . For the sake of convenience, the inner diameter of the heat pipe is denoted as $2b$, and the radius of the liquid-vapor interface is denoted as a , so the thickness of the liquid film is $b-a$.

3. Mathematical Descriptions of the Model and Simplification of the Governing Equations

To solve the vapor flow in the physical model shown in Figure 1, it should be based on the NS functions coupled with the energy function and state function under rotating coordinates. In order to obtain the analytical solution, the flow of the vapor is supposed to be the potential flow; under which hypothesis, the above functions can be simplified to a great extent. The universal form of NS functions is the vector form, as shown below:

$$\rho \frac{d\vec{v}}{dt} = -\nabla p + \rho \vec{f} + \mu \nabla^2 \vec{v}. \quad (1)$$

This form is regardless with the coordinates, and for the case of rotating coordinates, which is a noninertial system, the function that the relative velocity \vec{v}_r satisfies has the same form as (1), with the difference of the mass force item, which can be expressed as

$$\rho \frac{d\vec{v}_r}{dt} = -\nabla p + \rho \vec{f} + \mu \nabla^2 \vec{v}_r, \quad (2)$$

$$\vec{f} = -2\vec{\omega} \times \vec{v}_r - \vec{\omega} \times (\vec{\omega} \times \vec{r}),$$

in which the mass force \vec{f} is an inertial force, the first item is the Coriolis force, and the second item is the centrifugal force. Between the two forces, the former is a nonpotential force and the direction of it is circumferential, while the latter is a potential force and the direction of it is radial. In most literatures, the Coriolis force is often neglected, and only the centrifugal force is taken into account, such treatment can make the model simple and, to some extent, can result in with acceptable accuracy. So firstly, the Coriolis force is also neglected by former researchers, and the mathematical model can be simplified accordingly, and then the estimation

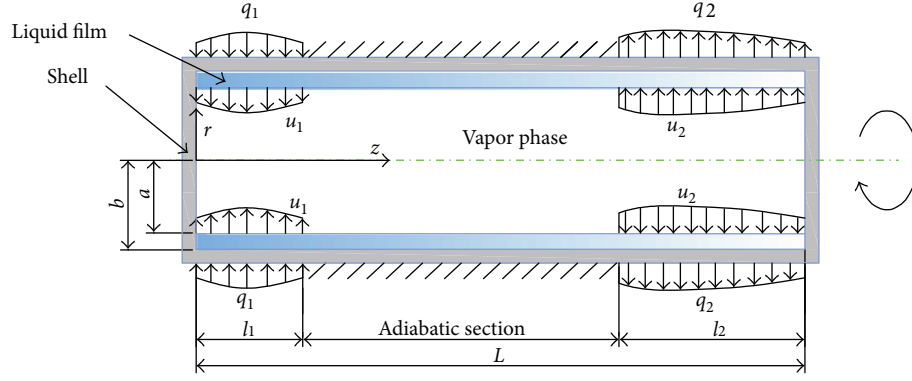


FIGURE 1: Physical model of the rotating heat pipe to be solved.

of the Coriolis force is carried out based on the obtained solution. For the potential hypothesis, the viscous item in (2) can be neglected, and therefore, the governing equations can be reduced into

$$\rho \frac{d\vec{v}_r}{dt} = -\nabla p - \rho \vec{\omega} \times (\vec{\omega} \times \vec{r}). \quad (3)$$

In summary, the hypothesis applied for this problem is listed below explicitly:

- (1) The flow is a two-dimensional plane flow, and the circumferential velocity is neglected.
- (2) The viscous items concerning the parameter viscosity are all neglected, so the flow is the potential flow.
- (3) The vapor phase is incompressible, and its state parameters are all saturated ones.
- (4) Estimation of the Coriolis force is based on the potential flow, but in the solving process, the Coriolis force is neglected, so that their coupling relationship is simplified.

So supposing the potential function of the velocity \vec{v}_r is denoted as ψ , then it should satisfy the Laplace function, as shown below:

$$\nabla^2 \psi = 0. \quad (4)$$

4. Solving the Velocity Field of the Vapor Phase

The calculating region of the mathematical problem above is written as

$$\begin{aligned} 0 \leq r \leq a, \\ 0 \leq z \leq L. \end{aligned} \quad (5)$$

The left boundary condition of the vapor flow is

$$\frac{\partial \psi}{\partial z} = 0, \quad z = 0. \quad (6)$$

And the right boundary condition is

$$\frac{\partial \psi}{\partial z} = 0, \quad z = L. \quad (7)$$

The boundary condition at the symmetry axis is

$$\frac{\partial \psi}{\partial r} = 0, \quad r = 0. \quad (8)$$

The boundary condition at the vapor-liquid interface is

$$\frac{\partial \psi}{\partial r} = \begin{cases} u_1, & 0 < z < z_1, \\ 0, & z_1 < z < z_2, \\ u_2, & z_2 < z < L, \end{cases} \quad r = a. \quad (9)$$

The notations z_1 and z_2 are defined as

$$\begin{aligned} z_1 &= l_1, \\ z_2 &= L - l_2. \end{aligned} \quad (10)$$

The governing equation (4) can be denoted below in rotating coordinates:

$$\frac{1}{r} \frac{\partial}{\partial r} \left(r \frac{\partial \psi}{\partial r} \right) + \frac{1}{r^2} \frac{\partial^2 \psi}{\partial \varphi^2} + \frac{\partial^2 \psi}{\partial z^2} = 0. \quad (11)$$

For the two-dimensional plane flow problem discussed in this paper, the second item in (11) can be neglected, and the governing equation can be turned as

$$\frac{1}{r} \frac{\partial \psi}{\partial r} + \frac{\partial^2 \psi}{\partial r^2} + \frac{\partial^2 \psi}{\partial z^2} = 0. \quad (12)$$

This equation can be solved by the variable separation method, and its analytical solution can be expressed in (13); the deduction process of which is illustrated in the appendix.

$$\psi = \sum_{m=1}^{+\infty} A_m \cos(\beta_m z) I_0(\beta_m r). \quad (13)$$

It is taken as the form of a series, in which β_m is the eigenvalues and can be calculated as below:

$$\beta_m = m\pi \frac{1}{L}, \quad m = 0, 1, 2, 3, \dots \quad (14)$$

A_m is the coefficient of each item in the series. $I_0(\beta_m r)$ is the zero-order modified Bessel function. The partial differentials of the function ψ to r and z are the two velocity solutions, u_r and u_z , which are shown below:

$$\begin{aligned} u_r &= \frac{\partial \psi}{\partial r} = \sum_{m=1}^{+\infty} A_m \cos(\beta_m z) I_1(\beta_m r) \beta_m, \\ u_z &= \frac{\partial \psi}{\partial z} = - \sum_{m=1}^{+\infty} A_m \sin(\beta_m z) I_0(\beta_m r) \beta_m. \end{aligned} \quad (15)$$

$$A_m = \frac{2}{I_1(\beta_m a) m \pi} \frac{1}{\beta_m} \left\{ -k_1 l_1 \sin(\beta_m l_1) - \frac{k_1}{\beta_m} [\cos(\beta_m l_1) - 1] - k_2 l_2 \sin(\beta_m z_2) - \frac{k_2}{\beta_m} [\cos(m\pi) - \cos(\beta_m z_2)] \right\}. \quad (17)$$

4.2. Uniform Distribution of the Boundary Radial Velocity. When the distribution of heat flux is uniform at the evaporation and condensation sections, the boundary condition of the radial velocity of the vapor flow is also uniform, and it can be described below:

$$\begin{aligned} u_1(z) &= -U_1, \quad 0 \leq z \leq z_1, \\ u_2(z) &= U_2, \quad z_2 \leq z \leq L. \end{aligned} \quad (18)$$

And the solution of the coefficients A_m is shown below:

$$A_m = - \frac{2}{I_1(\beta_m a) m \pi} \frac{1}{\beta_m} \{ U_1 [\sin(\beta_m l_1)] + U_2 [\sin(\beta_m z_2)] \}. \quad (19)$$

4.3. Uniform and Symmetric Distribution of the Boundary Radial Velocity. One special case of the uniform distribution of boundary condition is the symmetric case, in which the length of the evaporator and that of the condenser are equal and the magnitude of radial velocity U_1 and that of radial velocity U_2 are equal too, as shown below:

$$u_r(a) = \begin{cases} -U, & 0 \leq z \leq l_1, \\ 0, & l_1 \leq z \leq L - l_1, \\ U, & L - l_1 \leq z \leq L. \end{cases} \quad (20)$$

For this case, the solution of the coefficients is shown below, which means that the even terms are all zero.

$$A_m = \begin{cases} \frac{U}{\beta_m} \frac{-4 \sin(\beta_m l_1)}{I_1(\beta_m a) m \pi}, & \beta_m = (2k+1) \frac{\pi}{L}, \\ 0, & \beta_m = (2k) \frac{\pi}{L}. \end{cases} \quad (21)$$

The coefficient A_m is determined by the boundary condition (9), and for different boundary conditions, they have different values. The derivation process is illustrated in the appendix, and the results are shown below.

4.1. Linear Distribution of the Boundary Velocity. When the distribution of heat flux is linear, the boundary condition of the radial velocity of the vapor flow is linear, and it can be described as

$$\begin{aligned} u_1(z) &= -k_1 z, \quad 0 \leq z \leq l_1, \\ u_2(z) &= k_2 (L - z), \quad z_2 \leq z \leq L. \end{aligned} \quad (16)$$

And the solution of the coefficients A_m is shown below:

So the final solution of the velocity potential can be expressed as

$$\psi = \sum_{k=0}^{+\infty} \frac{-4U}{\beta_k} \frac{I_0[\beta_k r]}{I_1[\beta_k a]} \frac{\cos(\beta_k z) \sin(\beta_k l_1)}{(2k+1)\pi}, \quad \beta_k = (2k+1) \frac{\pi}{L}. \quad (22)$$

And the velocities u_r and u_z can be expressed as

$$\begin{aligned} u_r &= \frac{\partial \psi}{\partial r} = \sum_{k=0}^{+\infty} -4U \frac{I_1[\beta_k r]}{I_1[\beta_k a]} \frac{\cos(\beta_k z) \sin(\beta_k l_1)}{(2k+1)\pi}, \quad \beta_k = (2k+1) \frac{\pi}{L}, \\ u_z &= \frac{\partial \psi}{\partial z} = \sum_{k=0}^{+\infty} 4U \frac{I_0[\beta_k r]}{I_1[\beta_k a]} \frac{\sin(\beta_k z) \sin(\beta_k l_1)}{(2k+1)\pi}, \quad \beta_k = (2k+1) \frac{\pi}{L}. \end{aligned} \quad (23)$$

5. Results and Discussion

5.1. The Potential Solution of the Flow Field for Three Cases of Boundary Condition. Directed by the analytical solution obtained above, a specific heat pipe was calculated; the structure parameters of which were set as follows: the length L is 200 mm, the inner diameter of the heap pipe is 40 mm, and the thickness of the liquid film is 4 mm. In order to compare the influence of boundary condition on the distribution of vapor flow, especially the Coriolis force, three cases for different heat loads are calculated which are (1) uniform as well as symmetric distribution, (2) linear distribution, and (3) uniform but asymmetric distribution of heat load.

The calculated flow field for case (1) is drawn as Figure 2, in which the velocity field of the liquid film is also exhibited, which is obtained with the same method as the vapor flow. In this case, the length of the evaporator and that of the condenser are both 40 mm. In the figure, the black lines denote the streamline; the vectors denote the direction and the magnitude of the velocity at each point, while the colored lines

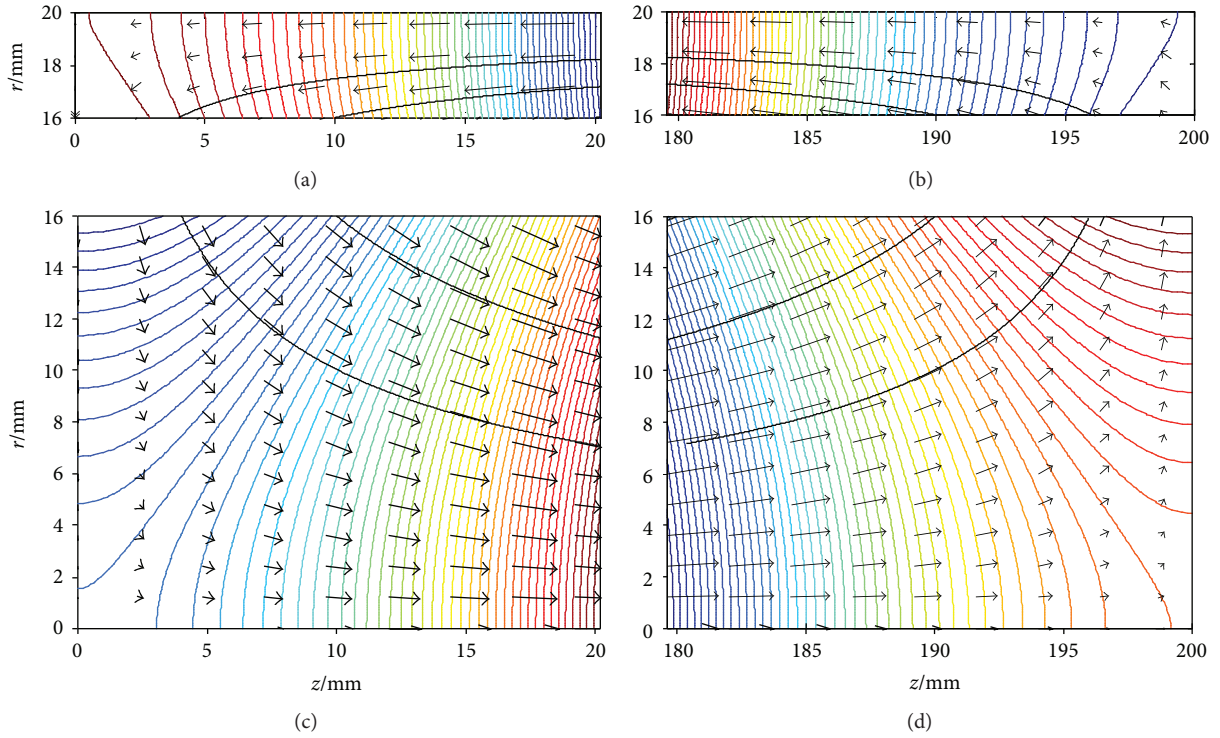


FIGURE 2: Potential solution of the flow field for the case with uniform and symmetric boundary condition. (a) Liquid film at the evaporator. (b) Liquid film at the condenser. (c) Vapor phase at the evaporator. (d) Vapor phase at the condenser.

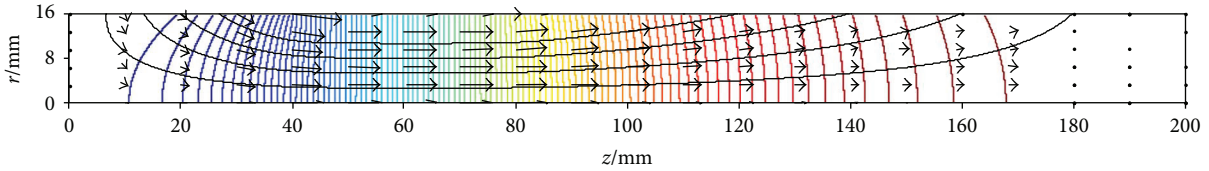


FIGURE 3: Potential solution of the flow field for the case with linear boundary condition.

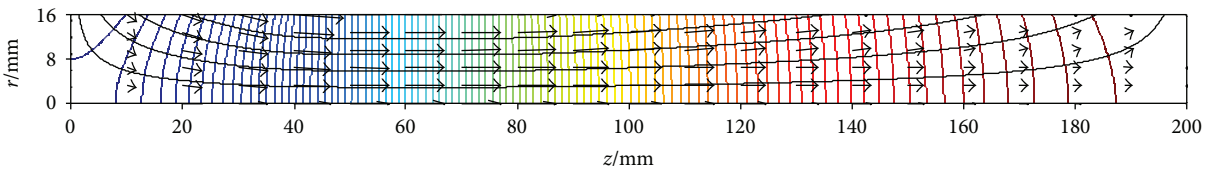


FIGURE 4: Potential solution of the flow field for the case with uniform but asymmetric boundary condition.

stand for the contour line of the velocity potential. In the figure, subfigure (a) corresponds to the velocity field of the liquid film at the evaporator; subfigure (b) corresponds to the velocity field of the liquid film at the condenser section; subfigure (c) corresponds to the velocity field of the vapor phase at the evaporator; and subfigure (d) corresponds to the velocity fields of the vapor phase at the condenser section.

Figure 3 exhibits the wholesome vapor flow field of the rotating heat pipe for the boundary condition as case 2, in which the heat load at the evaporator and the condenser is linearly distributed. The length of the evaporator is 40 mm, and along the axial direction of z , the heat source at the evaporator increases linearly; the length of the condenser is

120 mm, and along the axial direction of z , the heat sink at the condenser decreases linearly.

Figure 4 exhibits the wholesome vapor flow field of the rotating heat pipe for the boundary condition as case 3, in which the heat load at the evaporator and the condenser is uniformly distributed. The length of the evaporator is 40 mm, and the length of the condenser is 120 mm. As the length of the evaporator and that of the condenser are not identical, therefore, the magnitudes of the heat load as well as the boundary velocity at both sides are not equal.

5.2. Discussion of the Coriolis Force. Once the solution of the velocity field is obtained, the Coriolis force can be discussed,

which is closely related with the radial velocity, and is calculated by the following:

$$f_c = 2u_r\omega. \quad (24)$$

In the equation, f_c denotes the Coriolis force per unit mass, so its dimension is that of acceleration, m/s^2 , u_r denotes the radial velocity of the working fluid, and ω denotes the absolute angular velocity relative to the ground; as the flow is supposed to be a plane flow, it is equal to the angular velocity of the shell. It can be deduced that the Coriolis force is proportional to the rotating speed of the rotating heat pipe, but it is also noticeable that when the circumferential velocity is taken into account, the angular velocity of the working fluid and that of the shell are not equal, which is just the result of the Coriolis force.

In this article, a specific working condition is calculated, in which the rotating speed n is 3000 rpm, the structure parameters are the same as that discussed above, the working fluid is R134a, which is a common refrigerant, and the working temperature of the vapor phase T is 50°C, so its calculating parameters are presented in Table 1.

The heat load conditions are also set for three cases as before; for the uniform distribution cases, the heat source is set to be 5 W/cm², and for the linear distribution case, its total heat load is set to be equal to the other two cases. The distribution of the Coriolis force along the axial direction is exhibited in Figure 5. In this figure, subfigure (a) exhibits the distribution of the Coriolis force in the vapor phase in the case with linear distribution of heat load; subfigure (b) exhibits the distribution of the Coriolis force in the vapor phase in the case with uniform but asymmetric distribution of heat load; and subfigures (c) and (d) exhibit the distribution of the Coriolis force in the vapor phase and the liquid film in the case with uniform and symmetric distribution of heat load.

It can be seen that the direction of the Coriolis force at the evaporator and that at the condenser are different, the Coriolis force at the adiabatic section is negligible, and as the radial coordinates increase, the magnitude of the Coriolis force increases, so the maximum value of the Coriolis force is located at the interface of the liquid-vapor phase. And it can also be observed that the magnitude of the maximum Coriolis is that of the gravitational acceleration g . As the rotating velocity 3000 rpm is a typical value, such as the dynamos and steam turbines in power plants and the heat load is not an extreme value, it is reasonable to consider the Coriolis force in rotating heat pipes. From subfigures (c) and (d), it can also be concluded that the Coriolis force in the vapor phase is much larger than that in the liquid phase and, in the liquid phase, the Coriolis force can be negligible.

Figure 6 exhibits the distribution of the Coriolis force along the radial direction. In this figure, subfigure (a) exhibits the distribution of the Coriolis force in the vapor phase in the case with a linear distribution of heat load; subfigure (b) exhibits the distribution of the Coriolis force in the vapor phase in the case with uniform but asymmetric distribution of heat load.

TABLE 1: Calculating parameters for the specific case.

Parameter/unit	Value	Parameter/unit	Value
$T/^\circ\text{C}$	50	n/rpm	3000
$h_{fg}/\text{kJ/kg}$	151.82	$U_r/\text{m/s}$	0.005
$\rho_v/\text{kg/m}^3$	66.27	$q/\text{W/cm}^2$	5

In this figure, $z = 30$ mm is located at the evaporator section, $z = 50$ mm is located at the adiabatic section, $z = 160$ mm is located at the condenser section, and $z = 45$ mm is located at the boundary of the evaporator section and the adiabatic section. It can be seen that, at the most region of the evaporator and the condenser sections, the relationship between the Coriolis force and the radial coordinate is nearly linear, and the more uniform the boundary condition is, the stronger the linearity is. But it is also noticeable that this solution is based on a two-dimensional plane flow; if the circumferential velocity is taken into consideration, further investigation into the degree of this linearity is needed.

The magnitude of the Coriolis force is influenced by working conditions such as the heat load q and the working temperature of the vapor phase T . What is more, it has a great relationship with the working fluid itself. Figure 7 exhibits the maximum Coriolis forces at different working conditions for two specific working fluids: R134a (a) and water (b), and boundary condition distribution for both working fluids is as case (1): uniform and symmetric.

From Figure 7, it can be seen that the magnitude of the Coriolis force decreases with working temperature and increases with the heat load. It can also be found that the Coriolis force is larger when the working fluid is water, compared with R134a. As the heat loads calculated are possible ones, it can be concluded that it is possible for the Coriolis force to be 1~10 times the gravitational acceleration.

5.3. *Viscous Shear Stress at the Interface.* From the obtained axial velocity, the shear stress can be discussed. Because of the potential flow, hypothesis neglects the viscous items in the governing equation, so at the interface of the liquid and vapor phases, the calculated velocity cannot be continuous, as shown in Figure 8.

From this figure, the viscous shear stress can be evaluated by the axial velocity difference of the vapor and liquid phases across the interface. Subfigure (a) corresponds to the case of linear distribution boundary condition, and subfigure (b) corresponds to the case of the uniform but asymmetric distribution boundary condition. The total heat loads for the two cases are equal, and the heat flux of the evaporator for uniform distribution case is 5 W/cm². For the two cases, the length of the evaporator and that of the condenser are identical, which means that $z = 30$ mm is located at the evaporator section, $z = 45$ mm is located at the adiabatic section, and $z = 140$ mm and $z = 160$ mm are located at the condenser section. It can be seen that the axial velocity of the liquid phase is approximately zero and the maximum axial velocity difference is located at the adiabatic section. So the viscous

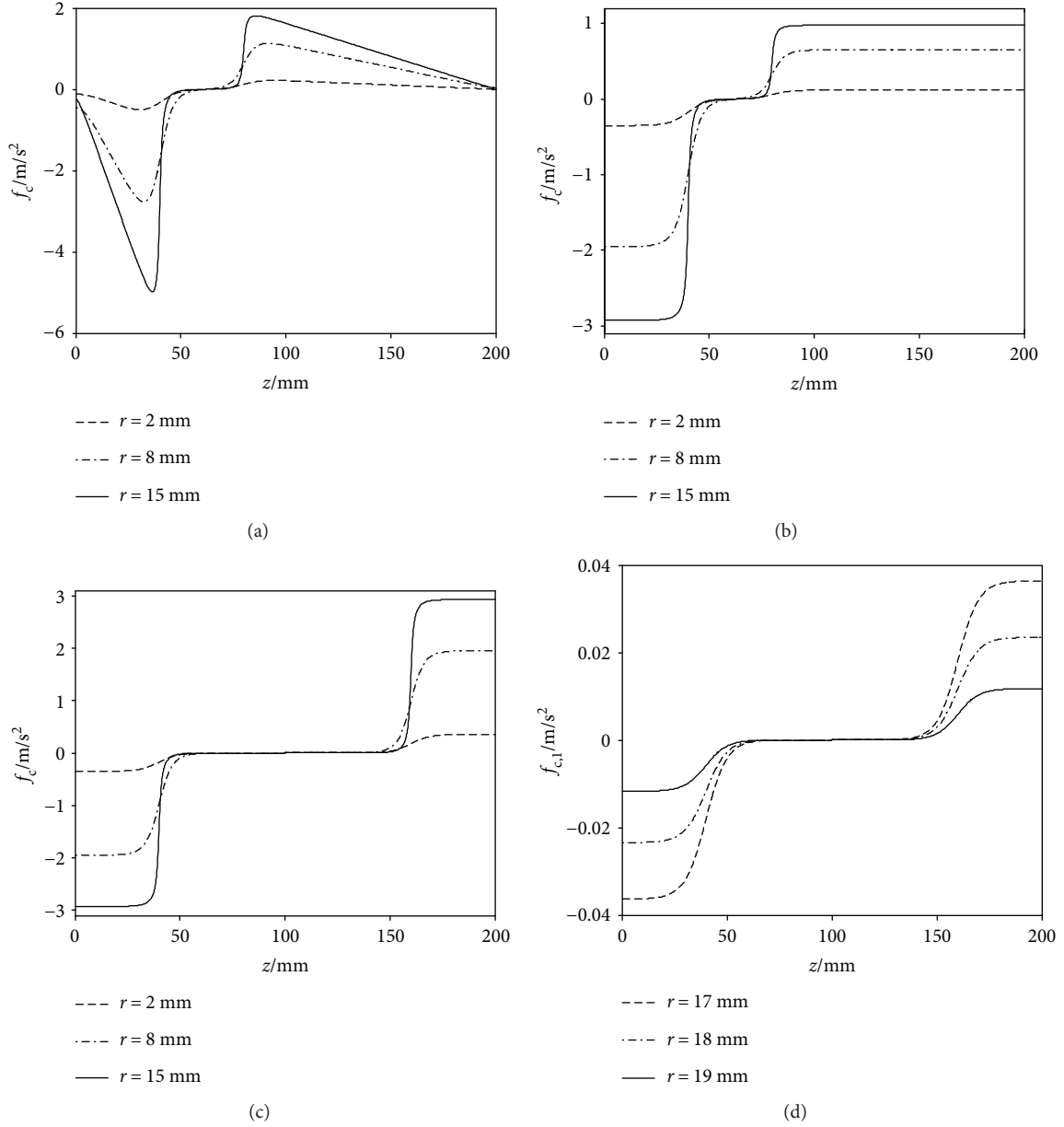


FIGURE 5: Distribution of the Coriolis force along the axial direction for different cases. (a) Distribution in vapor for case 2. (b) Distribution in vapor for case 3. (c) Distribution in vapor for case 1. (d) Distribution in liquid film for case 1.

shear stress at this region needs to be further investigated based on a more accurate model, in which the viscous items should be taken into account.

It can be deduced that if the nonslip boundary condition is considered, the gradient of the axial velocity along the axial direction will shift a lot, so according to the continuity equation, which is written below, the gradient of the radial velocity along the radial direction will shift a lot, and the linearity relationship between the Coriolis force and the radial direction indicated by the potential flow solution will change, and a more exact relationship needs to be explored.

$$\frac{\partial u_r}{\partial r} + \frac{\partial u_z}{\partial z} = 0. \quad (25)$$

6. Conclusions and Outlooks

The analytical solution of the vapor flow in rotating heat pipes was obtained in the hypothesis of potential flow and with the method of variable separation, which is a solution of a series form. A specific rotating heat pipe was examined under the three kinds of boundary conditions: linear distribution, uniform but asymmetric distribution, and uniform as well as symmetric distribution of heat load. The flow field was calculated, and the Coriolis force is estimated for different boundary conditions, different working fluids, and different working conditions, and the following conclusions were arrived:

- (1) When neglecting the Coriolis force and the viscous item in the governing equations, it is viable to obtain

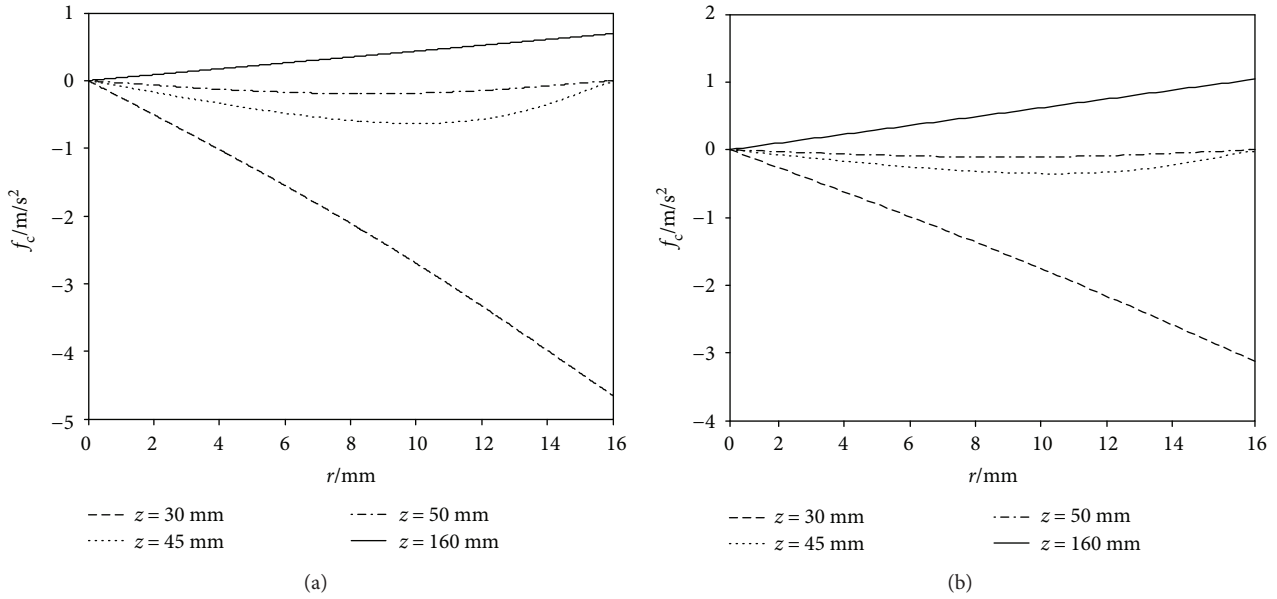


FIGURE 6: Distribution of the Coriolis force along the radial direction for different cases. (a) Distribution in vapor for case 2. (b) Distribution in vapor for case 3.

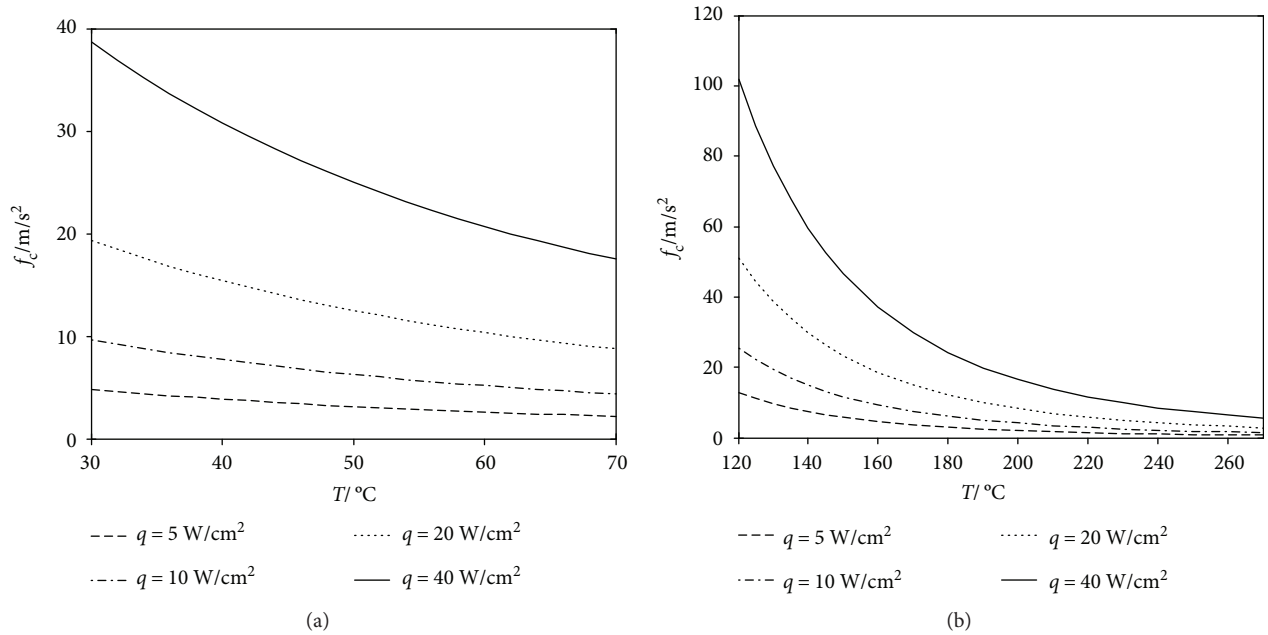


FIGURE 7: The maximum Coriolis force at different working conditions for different working fluids. (a) For working fluid R134a. (b) For working fluid water.

- the analytical solution of the working fluid flow, especially for the vapor phase, with the method of variable separation, and such method is applicable for any cases of heat load distribution.
- (2) The magnitude of the Coriolis force can be that of the gravitational acceleration; for rotating heat pipes with high speed and large heat load, the Coriolis force needs to be considered.
- (3) Along the axial direction, the maximum Coriolis force is located at the vapor-liquid interface at the evaporator and condenser sections, and the directions of the Coriolis force at these two sections are opposite, while at the adiabatic section, the Coriolis force is negligible.
- (4) The Coriolis force is closely related with working conditions and working fluids, and it decreased

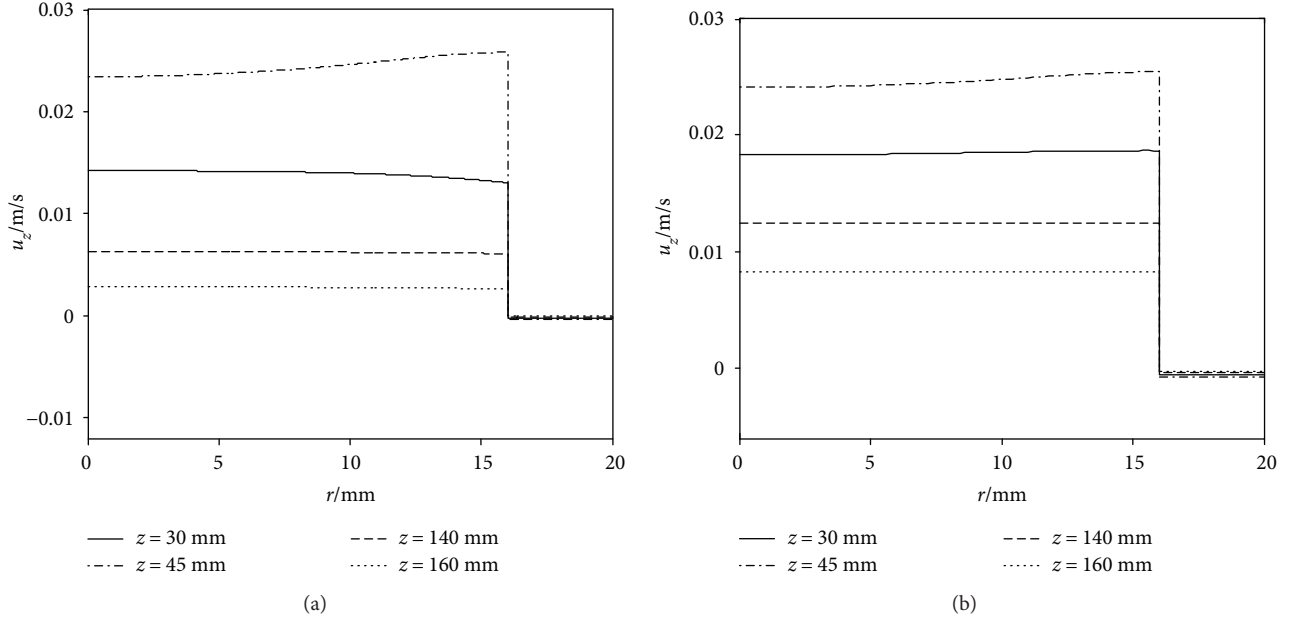


FIGURE 8: Distribution of axial velocity along the radial direction for different cases. (a) Distribution for linear boundary condition. (b) Distribution for uniform but asymmetric boundary condition.

with working temperature and increased with the heat load.

- (5) The influence range of the viscous force can be estimated according to the axial velocity difference of the vapor phase and the liquid phase across the interface, and the maximum viscous shear stress is located at the adiabatic section.

6.1. Outlooks. As the Coriolis force can result in the circumferential velocity, it can be inferred that the flow can take on circumferential shift, both in the evaporator section and in the condenser section. As the directions of the Coriolis force are opposite in the two sections, the circumferential velocity is also opposite. So the mutual interaction of the distribution of the circumferential velocity and the Coriolis force as well as the viscous shear stress are needed to be further clarified.

Appendix

A. Deduction of the Series Form Solution

A.1. General Solution of the Velocity Potential Solution. For the governing equation of the velocity potential function (12), it is supposed that its solution can be expressed as

$$\psi = R(r)Z(z). \quad (\text{A.1})$$

Substituting it into function (12), it is obtained that

$$\frac{1}{r}Z\frac{dR}{dr} + Z\frac{d^2R}{dr^2} + R\frac{d^2Z}{dz^2} = 0. \quad (\text{A.2})$$

Dividing it with equation $\psi = ZR$, it is obtained that

$$\frac{1}{r}\frac{dR}{dr} + \frac{d^2R}{Rdr^2} + \frac{d^2Z}{Zdz^2} = 0. \quad (\text{A.3})$$

If this equation is always satisfied regardless of any variables, then it can be supposed that

$$\frac{1}{r}\frac{dR}{dr} + \frac{d^2R}{Rdr^2} = -\frac{d^2Z}{Zdz^2} = \beta^2. \quad (\text{A.4})$$

And for the function Z , the following function should be satisfied:

$$\frac{d^2Z}{dz^2} + \beta^2 Z = 0. \quad (\text{A.5})$$

And the boundary conditions are shown below:

$$\begin{aligned} \frac{dZ}{dz} &= 0, & z &= 0, \\ \frac{dZ}{dz} &= 0, & z &= L. \end{aligned} \quad (\text{A.6})$$

The solution to the above problem is a solution system, which can all be written as the form

$$Z = \cos(\beta_m z), \quad (\text{A.7})$$

in which the eigenvalue β_m is

$$\beta_m = \frac{m\pi}{L}, \quad m = 0, 1, 2, 3, \dots \quad (\text{A.8})$$

While for function R , it satisfies the function below:

$$\frac{d^2R}{dr^2} + \frac{1}{r}\frac{dR}{dr} - \beta^2 R = 0. \quad (\text{A.9})$$

This function is a zero-order modified Bessel equation, and its boundary conditions are shown below:

$$\left. \frac{dR}{dr} \right|_0 = 0, \quad (\text{A.10})$$

$$\left. \frac{dR}{dr} \right|_a = \begin{cases} u_1, & 0 < z < z_1, \\ 0, & z_1 < z < z_2, \\ u_2, & z_2 < z < L. \end{cases} \quad (\text{A.11})$$

According to boundary condition (A-10), it is convenient to express the solution of R as shown below:

$$R = I_0(\beta_m r), \quad (\text{A.12})$$

where the notation I_0 stands for the first kind zero-order modified Bessel function. And thus, the solution of the problem discussed in this article can be expressed as a series:

$$\psi = \sum_{m=0}^{+\infty} A_m \cos(\beta_m z) I_0(\beta_m r), \quad (\text{A.13})$$

where the notation A_m is a series of coefficient to be determined.

A.2. Settlement of the Coefficients A_m for a Given Boundary Condition. Once the expression of the velocity potential has been obtained, the velocity field can be deduced by the partial difference of ψ to the two coordinate variables, r and z , and the expression of the radial velocity u_r and the axial velocity u_z can be written as follows:

$$u_r = \frac{\partial \psi}{\partial r} = \sum_{m=1}^{+\infty} A_m \cos(\beta_m z) \beta_m I_0'[\beta_m r], \quad (\text{A.14})$$

$$u_z = \frac{\partial \psi}{\partial z} = - \sum_{m=1}^{+\infty} A_m \sin(\beta_m z) \beta_m I_0[\beta_m r]. \quad (\text{A.15})$$

And the coefficient A_m can be determined based on radial velocity expression (A.14) by the orthogonal integral method, which takes into account boundary condition (A.11) and multiplies function (A.7) to the two sides of (A.14) and then makes integral at the boundary $r = a$, so the left side became

$$J_{\text{left}} = \int_0^L \frac{\partial \psi}{\partial r} \cos(\beta_m z) dz = \int_0^{z_1} u_1 \cos(\beta_m z) dz + \int_{z_2}^L u_2 \cos(\beta_m z) dz. \quad (\text{A.16})$$

The symbol J_{left} stands for the integral above, and by integration by parts, it can be transformed into the following form:

$$J_{\text{left}} = \frac{1}{\beta_m} \left[u_1(z_1) \sin(\beta_m z_1) - u_2(z_2) \sin(\beta_m z_2) - \int_0^{z_1} \sin(\beta_m z) du_1 - \int_{z_2}^L \sin(\beta_m z) du_1 \right]. \quad (\text{A.17})$$

The specific expression is determined by the specific expression u_1 and u_2 . For the linear distribution of boundary condition (A.11), as shown in (16), the expression of (A.17) can be obtained as shown below:

$$J_{\text{left}} = \frac{1}{\beta_m} \left\{ -[k_1 l_1 \sin(\beta_m l_1) + k_2 l_2 \sin(\beta_m z_2)] - \frac{k_1}{\beta_m} [\cos(\beta_m l_1) - 1] - \frac{k_2}{\beta_m} \cos(m\pi) + \frac{k_2}{\beta_m} \cos(\beta_m z_2) \right\}. \quad (\text{A.18})$$

For the uniform distribution of boundary condition (A.11), as shown in (18), expression (A.17) can be written as

$$J_{\text{left}} = -\frac{U_1}{\beta_m} [\sin(\beta_m l_1)] - \frac{U_2}{\beta_m} [\sin(\beta_m z_2)]. \quad (\text{A.19})$$

For the uniform and symmetric distribution of boundary condition (A.11), as shown in (20), expression (A.17) can be written as

$$J_{\text{left}} = \begin{cases} -2 \frac{U}{\beta_m} \sin(\beta_m l_1), & \beta_m = (2k+1) \frac{\pi}{L}, \\ 0, & \beta_m = (2k) \frac{\pi}{L}. \end{cases} \quad (\text{A.20})$$

The orthogonal integral to the right side of (A.14) can be expressed as

$$J_{\text{right}} = \int_0^L \sum_{m=1}^{+\infty} A_m \cos(\beta_m z) \beta_m I_0'[\beta_m a] \cos(\beta_m z) dz. \quad (\text{A.21})$$

And its result is shown below, which is universal and regardless of the specific form of boundary condition (A.11).

$$J_{\text{right}} = \frac{1}{2} A_m I_0'(\beta_m a) m\pi. \quad (\text{A.22})$$

The two sides of the orthogonal integral are equal, so the coefficient A_m can be obtained, as shown below:

$$A_m = \frac{2J_L}{I_1(\beta_m a) m\pi}. \quad (\text{A.23})$$

In the expression above, the derivative of the zero-order modified Bessel function I_0' is substituted by I_1 , which is the first-order modified Bessel function and is just the derivative of the zero-order modified Bessel

function. The above equation is applicable for cases when $m > 0$, while for $m = 0$, the first term in (A.13) is

$$A_0 \cos(0) I_0[0] = A_0. \quad (\text{A.24})$$

This item is a constant but cannot be settled by the method of orthogonal integral to the partial difference of the potential function, so its value is unknown. But for the problem we care, this constant has no influence on the settlement of the velocity field, because it can be eliminated by derivation. So for the sake of simplicity, its value is given as 0. So the solution of velocity potential (A.13) can be rewritten as

$$\psi = \sum_{m=1}^{+\infty} A_m \cos(\beta_m z) I_0(\beta_m r). \quad (\text{A.25})$$

Nomenclature

Denotation/unit:	Physical meaning
a/mm :	Radius of the vapor-liquid interface
$A_m/\text{m}^2/\text{s}$:	Coefficients of each item in the solution series
b/mm :	Inner radius of the shell
$f_c/\text{m}/\text{s}^2$:	Coriolis force per unit mass
$h_{fg}/\text{kJ}/\text{kg}$:	Latent heat of evaporation
I_0 :	The zero-order modified Bessel function
I_1 :	The first-order modified Bessel function
k_1/s^{-1} :	Coefficient of linear velocity boundary condition at the evaporator
k_2/s^{-1} :	Coefficient of linear velocity boundary condition at the condenser
L/mm :	Length of the rotating heat pipe
l_1/mm :	Length of the evaporator
l_2/mm :	Length of the condenser
m :	Serial number of each item in the solution series
n/rpm :	Rotating speed of the heat pipe
p/Pa :	Pressure of the working fluid
$q_1/\text{W}/\text{cm}^2$:	Heat load at the evaporator
$q_2/\text{W}/\text{cm}^2$:	Heat load at the condenser
r/mm :	Radial coordinate
R :	Separated function about r
$T/\text{K}(\text{°C})$:	Working temperature of the vapor phase
$u_1/\text{m}/\text{s}$:	Velocity boundary condition at the evaporator
$U_1/\text{m}/\text{s}$:	Uniformly distributed velocity boundary condition at the evaporator
$u_2/\text{m}/\text{s}$:	Velocity boundary condition at the condenser
$U_2/\text{m}/\text{s}$:	Uniformly distributed velocity boundary condition at the evaporator
$u_r/\text{m}/\text{s}$:	Radial velocity solution
$u_z/\text{m}/\text{s}$:	Axial velocity solution
z/mm :	Axial coordinate
Z :	Separated function about z
β_m :	Eigenvalues of the solution
$\psi/\text{m}^2/\text{s}$:	Velocity potential
ω/s^{-1} :	Angular velocity
$\rho_v/\text{kg}/\text{m}^3$:	Density of the vapor phase.

Conflicts of Interest

The authors declare that there is no conflict of interest regarding the publication of this paper.

Acknowledgment

This project is supported by the Fundamental Research Funds for the Central Universities, China (Grant no. 2014QNB07) and Basic Research Project of Natural Science Foundation of Jiangsu Province (BK20170280).

References

- [1] R. Bertossi, N. Guilhem, V. Ayel, C. Romestant, and Y. Bertin, "Modeling of heat and mass transfer in the liquid film of rotating heat pipes," *International Journal of Thermal Sciences*, vol. 52, pp. 40–49, 2012.
- [2] H. Hassan and S. Harmand, "Effect of operating parameters on the heat transfer and liquid film thickness of revolving heat pipe," *Heat Transfer Engineering*, vol. 38, no. 5, pp. 538–548, 2017.
- [3] Y. H. Yau and Y. C. Foo, "Comparative study on evaporator heat transfer characteristics of revolving heat pipes filled with R134a, R22 and R410a," *International Communications in Heat and Mass Transfer*, vol. 38, no. 2, pp. 202–211, 2011.
- [4] S. Ding and B. Luo, "Control of stress in aeroengine turbine disk using radially rotating heat pipe," *Journal of Thermophysics and Heat Transfer*, vol. 28, no. 3, pp. 428–439, 2014.
- [5] B. Reding and Y. Cao, "Sector rotating heat pipe with interconnected branches and reservoir for turbomachinery cooling," *Journal of Heat Transfer*, vol. 139, no. 1, article 014503, 2016.
- [6] R. Ponnappan and J. E. Leland, "Rotating heat pipe for high speed motor/generator cooling," *SAE Transactions*, vol. 1, pp. 167–172, 1998.
- [7] Y. Cao and J. Ling, "Performance simulations of a gas turbine disk-blade assembly employing miniature radially rotating heat pipes," *Journal of Heat Transfer*, vol. 134, article 051016, no. 5, p. 7, 2012.
- [8] S. Gilchrist, D. Ewing, and C. Y. Ching, "On the design of an aero-engine nose cone anti-icing system using a rotating heat pipe," *Journal of Thermal Science and Engineering Applications*, vol. 1, article 022002, no. 2, p. 11, 2009.
- [9] W. Lian, W. Chang, and Y. Xuan, "Numerical investigation on flow and thermal features of a rotating heat pipe," *Applied Thermal Engineering*, vol. 101, pp. 92–100, 2016.
- [10] W. Lian and Y. Xuan, "Experimental investigation on a novel aero-engine nose cone anti-icing system," *Applied Thermal Engineering*, vol. 121, pp. 1011–1021, 2017.
- [11] J. Chen, Y. Fu, Z. Gu, H. Shen, and Q. He, "Study on heat transfer of a rotating heat pipe cooling system in dry abrasive-milling," *Applied Thermal Engineering*, vol. 115, pp. 736–743, 2017.
- [12] K. Ma, H. J. Xu, and Y. C. Fu, "The effect of a rotating heat pipe in a brazed diamond grinding wheel on grinding temperature," *Key Engineering Materials*, vol. 416, pp. 274–278, 2009.
- [13] T. C. Jen, G. Gutierrez, S. Eapen et al., "Investigation of heat pipe cooling in drilling applications. Part 1: preliminary numerical analysis and verification," *International Journal of Machine Tools and Manufacture*, vol. 42, no. 5, pp. 643–652, 2002.

- [14] I. D. Anikina, V. V. Sergeev, N. T. Amosov, and M. G. Luchko, "Use of heat pumps in turbogenerator hydrogen cooling systems at thermal power plant," *International Journal of Hydrogen Energy*, vol. 42, no. 1, pp. 636–642, 2016.
- [15] M. Xie, Z. Xue, W. Qu, and W. Li, "Experimental investigation of heat transfer performance of rotating heat pipe," *Procedia Engineering*, vol. 99, pp. 746–751, 2015.
- [16] R. Ponnappan, Q. He, and J. E. Leland, "Test results of water and methanol high-speed rotating heat pipes," *Journal of Thermophysics and Heat Transfer*, vol. 12, no. 3, pp. 391–397, 1998.
- [17] F. Song, D. Ewing, and C. Y. Ching, "Fluid flow and heat transfer model for high-speed rotating heat pipes," *International Journal of Heat and Mass Transfer*, vol. 46, no. 23, pp. 4393–4401, 2003.
- [18] T. C. Daniels and F. K. Al-Jumaily, "Investigations of the factors affecting the performance of a rotating heat pipe," *International Journal of Heat and Mass Transfer*, vol. 18, no. 7-8, pp. 961–973, 1975.
- [19] Z. Uddin, S. Harmand, and S. Ahmed, "Computational modeling of heat transfer in rotating heat pipes using nanofluids: a numerical study using PSO," *International Journal of Thermal Sciences*, vol. 112, pp. 44–54, 2017.
- [20] H. Hassan and S. Harmand, "Effect of using nanofluids on the performance of rotating heat pipe," *Applied Mathematical Modelling*, vol. 39, no. 15, pp. 4445–4462, 2015.
- [21] H. M. Li, C. Y. Liu, and M. Damodaran, "Analytical study of the flow and heat transfer in a rotating heat pipe," *Heat Recovery Systems and CHP*, vol. 13, no. 2, pp. 115–122, 1993.
- [22] A. Faghri, S. Gogineni, and S. Thomas, "Vapor flow analysis of an axially rotating heat pipe," *International Journal of Heat and Mass Transfer*, vol. 36, no. 9, pp. 2293–2303, 1993.
- [23] A. Solomon, N. Arun, K. Shukla, and B. Pillai, "Steady state performance of a rotating heat pipe," in *46th AIAA Aerospace Sciences Meeting and Exhibit*, Reno, Nevada, January 2008.

Research Article

Thermal Feature of a Modified Solar Phase Change Material Storage Wall System

Chenglong Luo ¹, Lijie Xu ², Jie Ji ², Mengyin Liao,¹ and Dan Sun¹

¹Institute of Energy Research, Jiangxi Academy of Sciences, Nanchang 330096, China

²Department of Thermal Science and Energy Engineering, University of Science and Technology of China, Hefei 230027, China

Correspondence should be addressed to Chenglong Luo; xxlong@ustc.edu and Jie Ji; jjie@ustc.edu.cn

Received 25 August 2017; Accepted 11 January 2018; Published 29 March 2018

Academic Editor: Zhonghao Rao

Copyright © 2018 Chenglong Luo et al. This is an open access article distributed under the Creative Commons Attribution License, which permits unrestricted use, distribution, and reproduction in any medium, provided the original work is properly cited.

This work is to study a novel solar PCM storage wall technology, that is, a dual-channel and thermal-insulation-in-the-middle type solar PCM storage wall (MSPCMW) system. The system has the following four independent functions, passive solar heating, heat preservation, heat insulation, and passive cooling, and it can agilely cope with the requirements of climatization of buildings in different seasons throughout the year and is exactly suitable for building in regions characterized by hot summer and cold winter. The present work experimentally analyzes thermal feature of the system working in summer and winter modes, respectively.

1. Introduction

The application of solar energy in buildings to reduce the final energy consumption of conventional energy is an important approach to develop a low-carbon society. The way the phase change material (PCM) provides indirect heat storage is related to energy absorption, which turns into latent heat instead of self-temperature rise. Phase change material (PCM) has strengths of small volume, low temperature, and high heat storage. Therefore, it is a good and efficient heat storage material to be used in building climatization. Hence, the investigation of applying the combination of PCM storage technology and solar energy technology to energy efficient building emerges and receives more and more attention.

Focusing on reducing energy consumption for space heating in building, much work has been done to study and use Trombe wall system which is a high-efficiency simple structure that does not require maintenance [1]. Although this system has been well developed, hurdles remain such as the low annual utilization rate in places with hot and lengthy summer and the often suffering problem of summer overheating [2, 3]. Therefore, its broad application, improvement, and development have been implemented in the decades since it was proposed. Jie et al. [4, 5] made a lot

of efforts on investigation of a PV-Trombe wall system. Koyunbaba et al. [6] proposed a BIPV Trombe wall model by computational fluid dynamics (CFD) analysis. The three-dimensional model for the shutter structure of Trombe wall was established in [7], and the comparison with experimental data and an optimal design scheme were conducted. But there are a few research work for the combination of Trombe wall technology and PCM envelope structure.

With regard to the combination of solar energy application technology and PCM envelope structure, current researches and discussions mainly focus on PCM floor [8], PCM wall [9–12], and PCM roof [13, 14]. Soares et al. [15] demonstrated that the approach of combining solar energy utilization technology and PCM envelope structure can effectively reduce the room temperature fluctuation in solar energy building caused by lack of solar energy during the night or uncertain weather, thus enhancing the in-room thermal comfort. However, some large areas of China are characterized by hot summers and cold winters and usually require more than three months of air conditioning cooling. In winter, buildings need heating/heat preservation, while in summer they need heat cooling/insulation. Since solar energy is a thermal energy, it can be used conveniently for building heating in winter, but it can also cause overheating and heavy load of air conditioner in summer. Thus, in regions with hot

summers and cold winters, current solar PCM storage technology cannot fully satisfy the application requirements.

Based upon the analysis above, a former work proposed a novel solar PCM storage wall technology that combines Trombe-wall-like technology and phase change material storage technology, that is, a dual-channel and thermal-insulation-in-the-middle type solar PCM storage wall (MSPCMW) system [16]. This system has the following four independent functions: passive heating, heat preservation, heat insulation, and passive cooling. Therefore, it can easily cope with the requirements of different seasons throughout the year when applied to buildings in regions with hot summers and cold winters. To deeply experimentally analyze thermal feature of the system working in summer and winter modes, respectively, temperature variation and distribution of PCM plates, insulated absorbing plate, and air channels are studied by comparison of temperature difference between the monitoring nodes in the present work.

2. Principles of MSPCMW System and Experiment Introduction

MSPCMW system is a combination of Trombe-wall-like technology and phase change material storage technology. A schematic of the system is shown in Figure 1, mainly consisting of a MSPCMW module and a hot-box room with indoor upper and lower vents. The module includes PCM wall, thermal insulation layer, interior and exterior flow channels, heat-absorbing aluminum plate covered by selective absorption coating, indoor upper and lower vents, outdoor upper and lower vents, insulation layer upper and lower vents, glass cover board, and frame. Heat-absorbing aluminum plate and thermal insulation layer are combined as insulated absorbing plate. The structure in which interior and exterior flow channels are separated by thermal insulation layer differs from the single-channel structure of conventional Trombe wall system. The detailed operation modes and functions are as follows:

Summer mode: (a) Heat insulation mode: in summer's daytime, when building needs thermal insulation protection, the indoor and middle layer upper and lower vents are closed, while the outdoor ones are kept opened. Ambient wind pressure together with thermosiphon pressure would form a circular flow between the exterior channel and the outdoor air that takes the solar energy absorbed by aluminum plate back to the environment. Meanwhile, the thermal insulation layer prevents heat conduction into the room, reducing building's absorption of solar energy. (b) Passive cooling mode: when building needs insulation protection, such as summer's night, the indoor upper and lower vents are shut while the middle layer and outdoor ones are kept opened. Under the action of ambient wind pressure, the formed circular flow among the interior channel, the exterior channel, and the outdoor cool air can cool down the PCM wall, reducing indoor air temperature and storing PCM wall's cold energy.

Winter mode: (a) Solar passive heating function: in winter daytime, when building needs heating, the outdoor upper and lower vents of system close, the middle layer ones

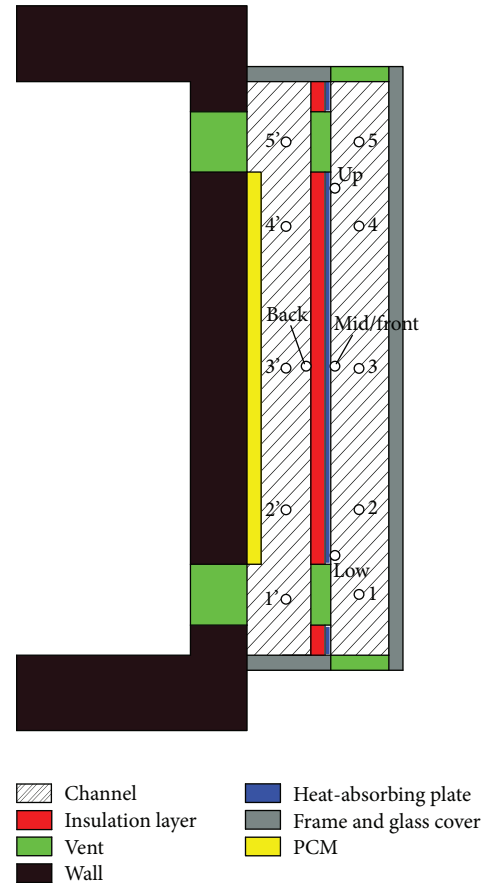


FIGURE 1: The structural principle of the proposed system and the arrangement diagram of thermocouples.

open, and the indoor ones can open/close to implement the interactive adjustment between the indoor temperature rise rate and the stored heat amount of PCM. Aluminum absorbing plate heats up the air of exterior flow channel by absorbing solar radiation irradiated on it. Among the air in the exterior channel, the interior channel, and indoor, the natural circulation due to thermosiphon occurs and induces circular exchange, heating up PCM wall and indoor air, eventually achieving the solar passive heating in building. (b) Heat preservation function: in winter nights, when the building needs heat preservation, the indoor, outdoor, and middle layer upper and lower vents all close, and PCM wall transfers the heat stored during daytime into the room via heat conduction to its neighboring building wall. In addition, the thermal insulation layer composed of insulation material can block the heat loss toward outdoor as much as possible.

The experimental test of the system was carried out on a comparative hot-box test platform located in Hefei City, Anhui Province, characterized by hot summer and cold winter zones. The test system included two hot-box rooms. The experimental room was the hot-box room installed with MSPCMW module, and the other one was the reference room. PCM wall was made by orderly laying and pasting 11 PCM plates on the building's south-facing wall using thermal silicone grease. Each plate measured $0.45\text{ m} \times 0.3\text{ m} \times 0.01\text{ m}$

(L, W, and H). Figure 2 presents the array pattern of PCM plates and monitoring point distribution of thermocouples. The plate was wrapped in aluminum and plated with anticorrosive coating. Its interior components are crystalline hydrate and organic PCM; thus, it benefits from both phase change materials of hydrate and organic matter.

Copper-constantan thermocouple with ice-point compensation (accuracy of $\pm 0.2^\circ\text{C}$) measures the temperature of experimental system. Five thermocouples are arranged in the interior air channel and the exterior air channel, respectively. Three thermocouples are placed on heat-absorbing aluminum plate, and one is on the back of the insulation layer (shown in Figure 1). There are 5 thermocouples placed on internal surfaces (bonding with the south wall surface) of the middle PCM plates (plates 1, 2, and 3). The locations of measuring points are referred to as circular marks in Figure 2. As shown, three monitoring points are evenly arranged on PCM plate 2 along vertical direction, and the other two are, respectively, positioned in the center of PCM plates 1 and 3. The measuring system also includes ambient temperature measurement and total solar radiation intensity of south-facing vertical surface obtained by TBQ-2 pyranometer. All temperature data and radiation data are collected in real time by Agilent 34970A data collector.

3. Results and Discussions

3.1. Summer Mode. The summer tests were conducted during August 28–30, 2016, in which the outdoor vents were kept opened while the indoor vents were kept closed; the middle layer vents were shut during daytime and opened during the night, and the switching time was around 7:00 and 17:30.

3.1.1. Temperature Variation and Distribution of PCM Plates. Figure 3 shows comparison of interior side temperature difference between centers of the upper, middle, and lower PCM boards. T_{B-E} is the temperature difference between nodes B and E, and T_{D-B} is the temperature difference between nodes D and B, which are shown in Figure 2. To reduce noise in experimental data, each of the variation curve is processed based on the smooth regression analysis method as well as the following curves. As is given, during the three-day continued test, the temperature of the upper position was higher than that of the lower position most of the time. But about 0–8 o'clock each day, the temperature difference was relatively small. Besides, according to the smooth regression analysis, it shows that T_{B-E} had two evident peaks and only one peak showed in T_{D-B} contrastively. For example, in the second day, the two extrema of T_{B-E} were, respectively, 3.0°C and 3.1°C , reached at 12:00 and 19:34, respectively, meanwhile the only extremum of T_{D-B} was 4.1°C , reached at 11:28.

Figure 4 shows the temperature difference between the three nodes on the middle of PCM plate 2, shown as A, B, and C in Figure 2. T_{B-C} is the temperature difference between nodes B and C, and T_{A-B} is the temperature difference between nodes A and B. As shown during the three-day test, similar to the situation shown in Figure 3, the temperature



FIGURE 2: Arrangement diagram of PCM plate array and thermocouples.

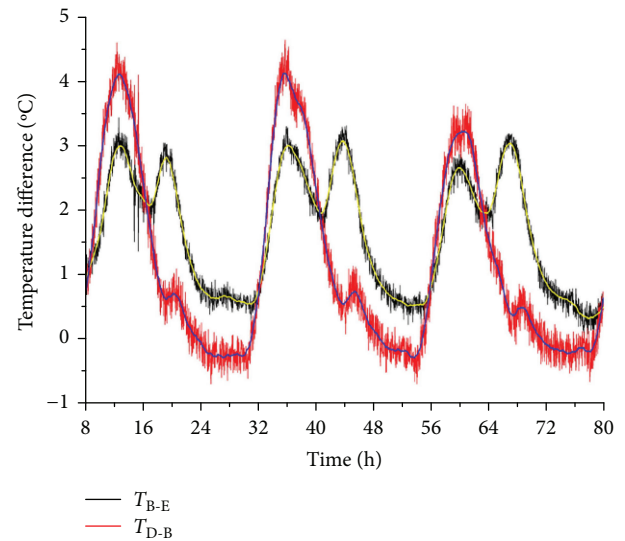


FIGURE 3: Comparison of the interior side temperature difference between the upper, middle, and lower PCM boards.

difference presented the behavior of daily fluctuation, lower position's temperature was higher than the upper position's, and temperature difference also became small during 0–8 o'clock. Otherwise, both T_{A-B} and T_{B-C} showed only one peak during daytime, and T_{B-C} became negligible at night. Also, take the second day for example, extremum of T_{A-B} was 1.4°C , reached at 11:20, meanwhile extremum of T_{B-C} was 2.3°C , reached at 14:26. It shows that the peak value of T_{B-C} had a delay phenomenon compared with that of T_{A-B} .

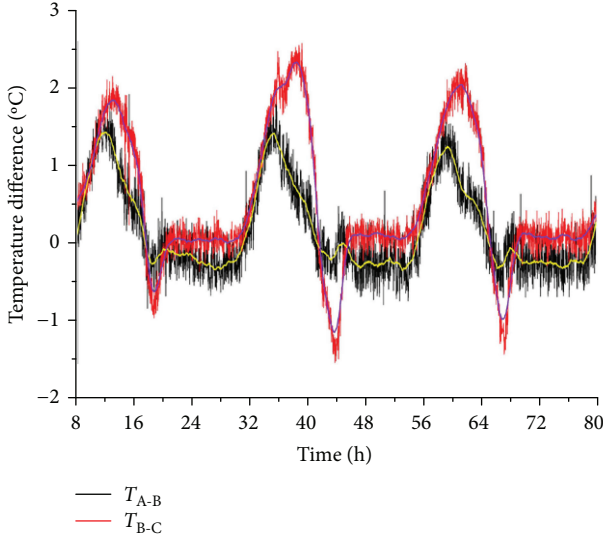


FIGURE 4: Temperature variation comparison for the nodes at the internal surface of center PCM.

3.1.2. Temperature Variation and Distribution of Insulated Absorbing Plate. Figure 5 represents the temperature difference between the upper, middle, and lower heat-absorbing aluminum plate and back of the insulation layer. T_{up-mid} is the temperature difference between nodes “up” and “mid,” $T_{mid-low}$ is the temperature difference between nodes “mid” and “low,” and $T_{front-back}$ is the temperature difference between nodes “front” and “back,” which are shown in Figure 1. As shown during the three-day test, T_{up-mid} rose till the peak and decreased during daytime. Then at night, T_{up-mid} maintained 0°C . The variation trend of $T_{mid-low}$ is similar to T_{up-mid} . The result demonstrates that the 3-day experiment’s data was repetitive and that the temperature of the upper position on heat absorber was higher than that of the lower position during daytime. Otherwise, $T_{front-back}$ had a trough, which was different from T_{up-mid} and $T_{mid-low}$. After we opened the middle layer vents, wind from the ambient came into the interior air channel and cooled the PCM, and the PCM started releasing heat. The back temperature of the insulation board would rise. For example, in the third day, the detailed data is shown in Table 1.

3.1.3. Temperature Variation and Distribution of Air Channels. Figure 6 shows variations of temperature difference between nodes of exterior air channel. There are 5 nodes at exterior air channel, which are shown in Figure 1. As shown, the temperature difference between exterior air channel was irregular, mostly because it was easily influenced by the ambient air when the outdoor vents were opened in summer. Also, take the third day for example, the detailed data is shown in Table 2.

Figure 7 shows variations of temperature difference between nodes of interior air channel. There are 5 nodes at interior air channel, which are shown in Figure 1. Different from the exterior air channel, the temperature difference of interior air channel was regular; in most time of the second day, for example, the maximum temperature difference

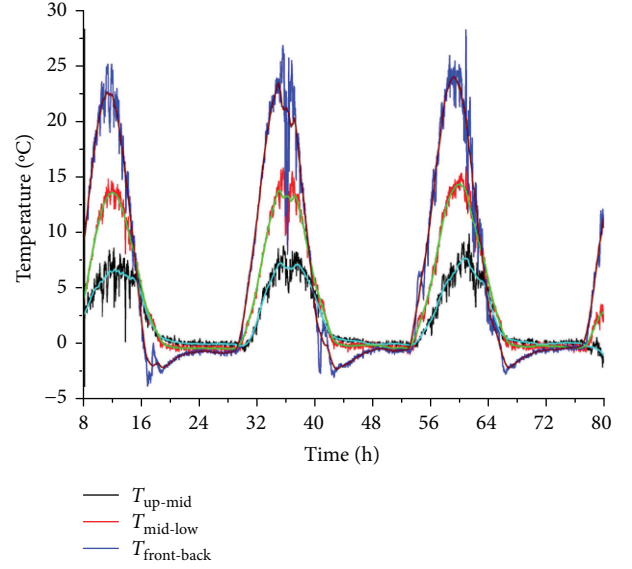


FIGURE 5: Temperature difference between the upper, middle, and lower heat-absorbing aluminum plates and back of the insulation layer.

TABLE 1: Summarized result of temperature difference between the upper, middle, and lower of heat-absorbing aluminum plate and back of the insulation layer.

	Max	Time to reach max	Min	Time to reach min	Average
T_{up-mid}	7.8°C	12:36	-0.1°C	5:08	2.2°C
$T_{mid-low}$	14.5°C	12:08	-0.4°C	2:48	4.1°C
$T_{front-back}$	24.2°C	11:12	-2.2°C	18:52	6.0°C

increased with height. Besides that, the minimum and average values of $T_{5'-4'}$, $T_{4'-3'}$, $T_{3'-2'}$, and $T_{2'-1'}$ were relatively close. The data is listed in Table 3.

3.2. Winter Mode. Similarly, 2-day continuous experimental tests of winter were conducted from 9:00 on Dec. 15 to 9:00 on Dec. 17 in 2015, during which the outdoor vents were kept shut; the middle layer vents and the indoor vents were kept opened during daytime and shut during night, and the switching time was around 8:00 and 17:00.

3.2.1. Temperature Variation and Distribution of PCM Plates. Figure 8 shows variations of temperature difference between the centers of PCM plates 1, 2, and 3 in winter mode. Despite the complex variation trend, most of the time in the 2-day test, the upper position’s temperature is higher than that of the lower position’s. For convenience, the data of the second day was chosen for analysis. According to the smooth regression analysis, T_{D-B} was approximately 0 during 0–8 o’clock. And T_{D-B} reflected an upward trend and reached the extremum value of 5.4°C at 10:20. Then, a slight decrease appeared, reached the extremum value of 3.5°C at 11:27,

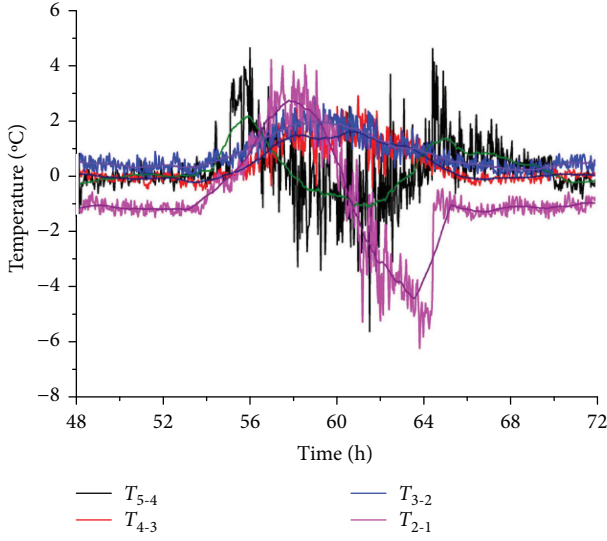


FIGURE 6: Temperature difference between the nodes of the exterior air channel.

TABLE 2: Summarized result of temperature difference between nodes of the exterior air channel.

	Max	Time to reach max	Min	Time to reach min	Average
T_{5-4}	2.2°C	7:54	-1.2°C	13:26	0.2°C
T_{4-3}	1.6°C	12:34	-0.3°C	5:24	0.4°C
T_{3-2}	2°C	11:08	0.2°C	20:08	0.8°C

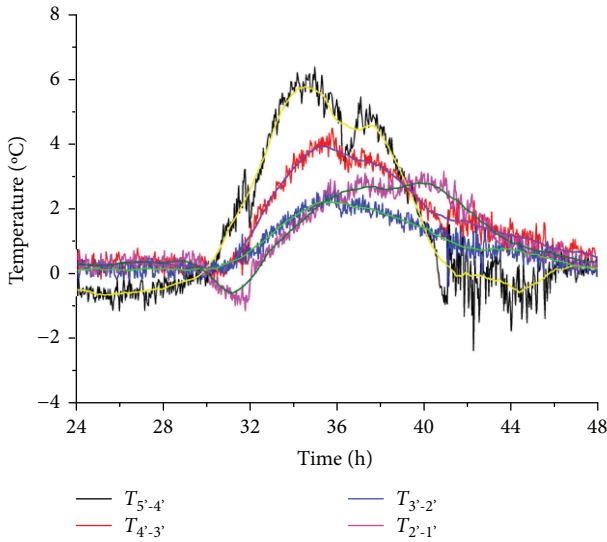


FIGURE 7: Temperature difference between the nodes of the interior air channel.

and kept rising till the extremum value reached 8.9°C at 15:25. Then, the temperature difference decreased again and reached the extremum value of -1.5°C at 18:28 and kept rising again till the extremum value reached 7.9°C at 23:04. Finally, at night, T_{D-B} maintained 0°C again similar as the

TABLE 3: Summarized result of temperature difference between nodes of the interior channel.

	Max	Time to reach max	Min	Time to reach min	Average
T_{5-4}	5.8°C	10:30	-0.7°C	1:14	1.5°C
T_{4-3}	4.0°C	11:24	0.2°C	6:08	1.6°C
T_{3-2}	2.2°C	11:17	0.1°C	5:01	0.9°C
T_{2-1}	2.8°C	15:44	-0.6°C	7:06	1.1°C

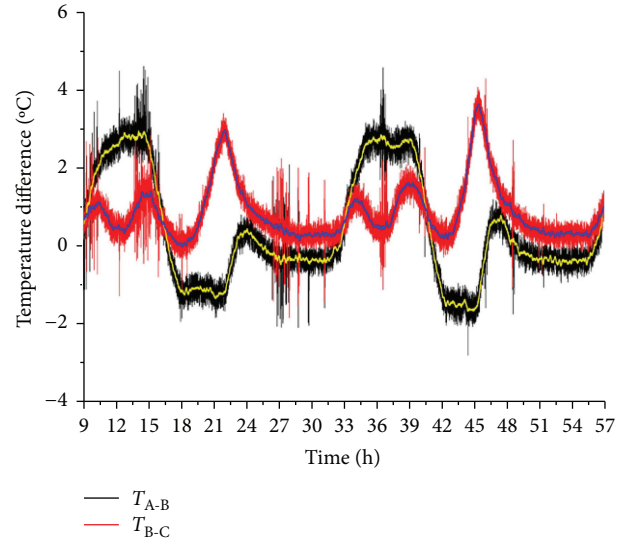


FIGURE 8: Temperature variation comparison for the nodes on the internal surface of center PCM.

first day. Its first peak occurred because till 10:20 in the second day, the top board started the phase change process. Heat absorbed from the channel changed into latent heat, so temperature difference will be diminished. The phase change time difference between panels D and B was between 10:20 and 11:27. Then, after reaching the temperature difference of 8.9°C at 15:25, T_{D-B} reached under 0°C because position B changed phase firstly that means releasing heat without temperature decrease. Then, T_{D-B} rose again because position D started the phase change process. Then, finally, temperature difference tends to be 0°C at night. T_{B-E} showed similar trends, which are only some differences between the extremum values and appear times.

Figure 9 shows temperature difference of the internal surface of the middle PCM plate 2. As shown, in the second day, during 0–8 o'clock on that day, average T_{B-C} was 0.4°C. Then, T_{B-C} rose at the peak temperature of 1.2°C at 10:00, fell off and maintained the average temperature of 0.5°C, then went up again and reached the extremum value of 1.6°C at 15:00. And it fell off again and reached extremum value of 1.6°C at 18:33 and went up again at the max temperature of 3.7°C in 21:26. Then, at night, T_{B-C} decreased to average temperature of 0.4°C again. The variation trend of T_{B-C} is similar to T_{D-B} in Figure 3. As for T_{A-B} , the average value was -0.3°C during

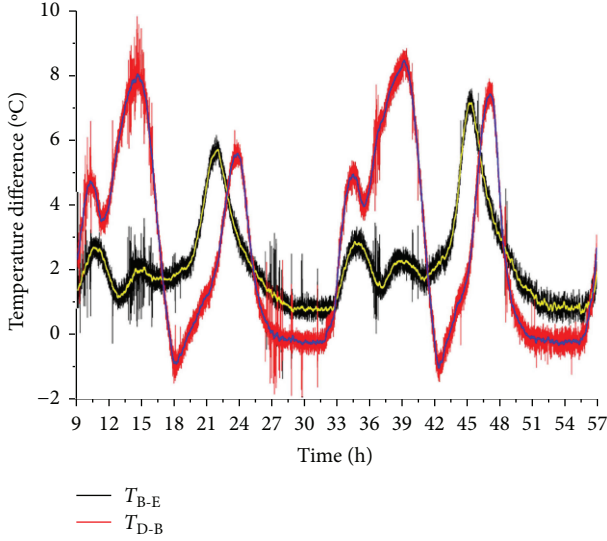


FIGURE 9: Comparison of the interior side temperature difference between the upper, middle, and lower PCM boards.

0–8 o'clock on the second day. Then, T_{A-B} rose and reached a new balance of 2.7°C during 11–16 o'clock approximately. After that, T_{A-B} started decreasing and kept an average temperature of -1.5°C during 18–21 o'clock roughly. And it rose at the peak temperature of 0.8°C in 23:27, then finally decreased at the average temperature of 0.23°C at night. The complex variation trends of T_{A-B} and T_{B-C} both indicate the melting and freezing processes that did not occur synchronously at the different positions along vertical direction even for a single PCM plate.

3.2.2. Temperature Variation and Distribution of Insulated Absorbing Plate. Figure 10 shows temperature difference between the upper, middle, and lower heat-absorbing aluminum plates and back of the insulation layer. As is given, during the two-day test, $T_{\text{front-back}}$ was higher than that in the summer mode. On the one hand, the insulation layer prevented an amount of heat from the front. On the other hand, in the winter mode, the outdoor vents were closed, so the temperature of heat-absorbing aluminum plate was very high. The temperature of the upper position on heat-absorbing aluminum plate was higher than that of the lower position during daytime, which was similar to that of the summer mode. The particular data is listed in Table 4.

3.2.3. Temperature Variation and Distribution of Air Channels. Figure 11 shows variations of temperature difference between nodes of exterior air channel. As shown, the upper position's temperature of exterior air channel was higher than that of the lower position's. Temperature difference became high during daytime, and at night, it was approximately 0°C . Other data is listed in Table 5.

Figure 12 shows variations of temperature difference between nodes of interior air channel. As shown, T_{5-4}' was higher than others during daytime and this situation was also different from summer mode. In winter, the middle layer vents were both opened during daytime, and high

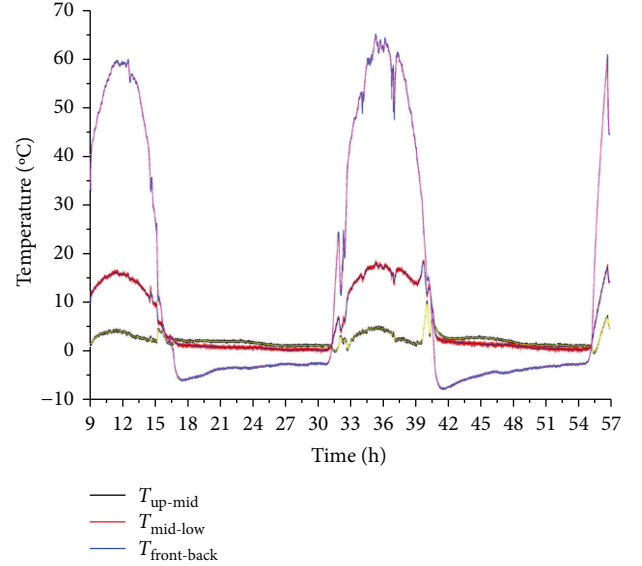


FIGURE 10: Temperature difference between the upper, middle, and lower heat-absorbing aluminum plates and back of the insulation layer.

TABLE 4: Summarized result of temperature difference between the upper, middle, and lower heat-absorbing aluminum plate and back of the insulation layer.

	Max	Time to reach max	Min	Time to reach min	Average
$T_{\text{up-mid}}$	10.2°C	16:06	-0.6°C	7:36	2.2°C
$T_{\text{mid-low}}$	18.6°C	15:45	-0.7°C	6:20	5.8°C
$T_{\text{front-back}}$	65.6°C	11:22	-8.3°C	17:30	14.5°C

temperature air mixed at the top of the channel, so the temperature would be much higher at the lower position in the interior channel. The detailed data is shown in Table 6.

4. Conclusions

This paper proposes a novel solar PCM storage wall technology, that is, a dual-channel and thermal-insulation-in-the-middle type solar PCM storage wall (MSPCMW) system. By tests on a hot-box test platform, experimental tests and analyses are conducted on the system, respectively, operating in summer and winter modes. By comparison of temperature difference between the monitoring points on surfaces of PCM plates along vertical direction, temperature variation and distribution of PCM plates are studied. The following conclusions are obtained:

- (1) Temperature variation and distribution of PCM plates: (a) In summer mode, during 0–8 o'clock every day, the temperature differences between centers of the upper, middle, and lower PCM plates were all relatively small. T_{B-E} had two evident peaks; meanwhile, only one peak showed in T_{D-B} during the rest of the time. Also, the temperature differences between the upper, middle, and lower positions on the middle

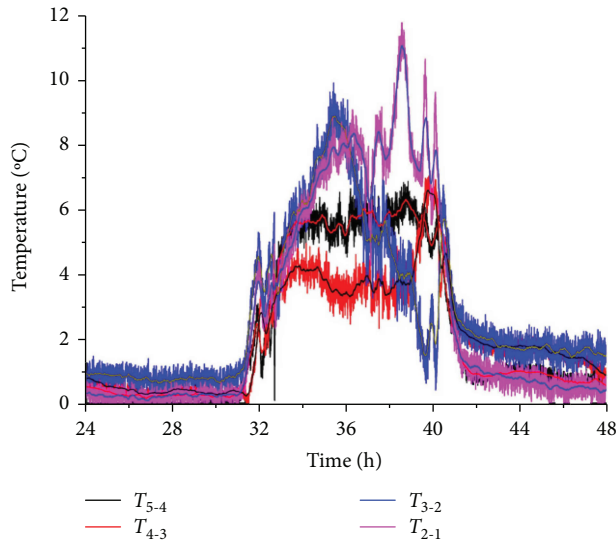


FIGURE 11: Temperature difference between the nodes of the exterior air channel.

TABLE 5: Summarized result of temperature difference between nodes of the exterior air channel.

	Max	Time to reach max	Min	Time to reach min	Average
T_{5-4}	6.4°C	14:44	0.15°C	2:45	2.4°C
T_{4-3}	6.7°C	15:46	0.22°C	7:22	2.2°C
T_{3-2}	9.0°C	11:28	0.6°C	3:20	2.9°C
T_{2-1}	11.3°C	14:33	0.1°C	2:49	2.9°C

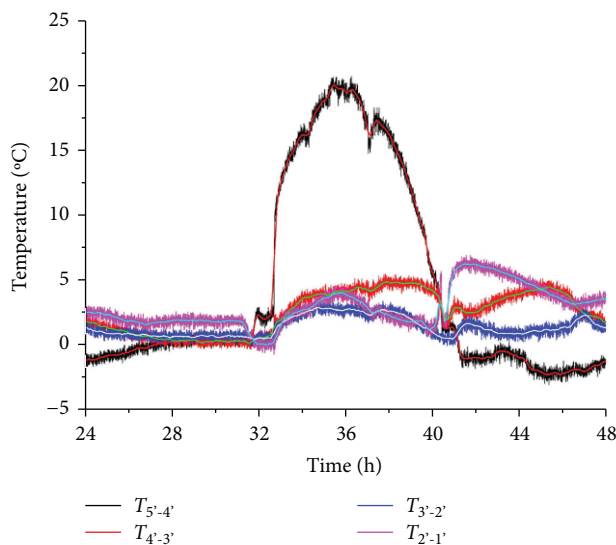


FIGURE 12: Temperature difference between the nodes of the interior air channel.

PCM plate became small during 0–8 o'clock; even the value of T_{B-C} became negative at night; and distinctively, both T_{A-B} and T_{B-C} showed only one peak

TABLE 6: Summarized result of temperature difference between nodes of the interior air channel.

	Max	Time to reach max	Min	Time to reach min	Average
$T_{5-4'}$	20.1°C	12:14	-3.2°C	21:24	4.4°C
$T_{4-3'}$	5.4°C	13:48	-0.5°C	7:36	2.4°C
$T_{3-2'}$	3.3°C	11:06	-0.3°C	16:54	1.2°C
$T_{2-1'}$	6.8°C	17:42	-0.9°C	8:36	2.8°C

during daytime. (b) In winter mode, both T_{B-E} and T_{D-B} had numerous peaks each day during the 2-day continuous experimental tests, and the peak phenomena represented there were obvious time difference of melting process between the upper and lower positions. T_{B-C} showed the same trend as T_{B-E} , and T_{A-B} showed three obvious peaks. Their differences showed that melting and freezing processes did not occur synchronously at the different positions along vertical direction even for a single PCM plate.

- (2) Temperature variation and distribution of insulated absorbing plate: Both in summer and winter modes, the temperature of the upper position on heat absorber was higher than that of the lower position during daytime, while in winter mode, $T_{\text{front-back}}$ was higher than that in summer mode.
- (3) Temperature variation and distribution of air channels: (a) In summer mode, the temperature difference between exterior air channel was irregular, while the temperature difference of interior air channel was regular, that is, the maximum temperature difference increased with height. (b) In winter mode, air temperature distribution in exterior and interior air channels had a similar feature with that of the upper position's air temperature which was higher than that of the lower position's. Besides, in interior air channel temperature, difference between the top position and the adjacent position was much higher than that in others during daytime and this situation was also different from summer mode.

Conflicts of Interest

The authors declare that there is no conflict of interest regarding the publication of this paper.

Acknowledgments

This study was sponsored by (1) the National Science Foundation of China (NSFC), Project no. 51408278, (2) the National Science Foundation of China (NSFC), Project no. 51366004, and (3) the Jiangxi Provincial Key Technology R&D Program, China, Project no. 20141BBE50041.

References

- [1] A. Akbarzadeh, W. W. S. Charters, and D. A. Lesslie, "Thermocirculation characteristics of a Trombe wall passive test cell," *Solar Energy*, vol. 28, no. 6, pp. 461–468, 1982.
- [2] G. Gan, "A parametric study of Trombe walls for passive cooling of buildings," *Energy and Buildings*, vol. 27, no. 1, pp. 37–43, 1998.
- [3] G. S. Yakubu, "The reality of living in passive solar homes: a user-experience study," *Renewable Energy*, vol. 8, no. 1–4, pp. 177–181, 1996.
- [4] J. Jie, Y. Hua, H. Wei, P. Gang, L. Jianping, and J. Bin, "Modeling of a novel Trombe wall with PV cells," *Building and Environment*, vol. 42, no. 3, pp. 1544–1552, 2007.
- [5] J. Jie, Y. Hua, P. Gang, and L. Jianping, "Study of PV-Trombe wall installed in a fenestrated room with heat storage," *Applied Thermal Engineering*, vol. 27, no. 8–9, pp. 1507–1515, 2007.
- [6] B. K. Koyunbaba, Z. Yilmaz, and K. Ulgen, "An approach for energy modeling of a building integrated photovoltaic (BIPV) Trombe wall system," *Energy and Buildings*, vol. 67, pp. 680–688, 2013.
- [7] X. Hong, W. He, Z. Hu, C. Wang, and J. Ji, "Three-dimensional simulation on the thermal performance of a novel Trombe wall with venetian blind structure," *Energy and Buildings*, vol. 89, pp. 32–38, 2015.
- [8] X. Xu, Y. Zhang, K. Lin, H. Di, and R. Yang, "Modeling and simulation on the thermal performance of shape-stabilized phase change material floor used in passive solar buildings," *Energy and Buildings*, vol. 37, no. 10, pp. 1084–1091, 2005.
- [9] K. Peippo, P. Kauranen, and P. D. Lund, "A multicomponent PCM wall optimized for passive solar heating," *Energy and Buildings*, vol. 17, no. 4, pp. 259–270, 1991.
- [10] C. Zhang, Y. Chen, L. Wu, and M. Shi, "Thermal response of brick wall filled with phase change materials (PCM) under fluctuating outdoor temperatures," *Energy and Buildings*, vol. 43, no. 12, pp. 3514–3520, 2011.
- [11] Y. A. Kara and A. Kurnuç, "Performance of coupled novel triple glass unit and PCM wall," *Applied Thermal Engineering*, vol. 35, pp. 243–246, 2012.
- [12] Y. Zhang, K. Lin, Y. Jiang, and G. Zhou, "Thermal storage and nonlinear heat-transfer characteristics of PCM wallboard," *Energy and Buildings*, vol. 40, no. 9, pp. 1771–1779, 2008.
- [13] H. J. Alqallaf and E. M. Alawadhi, "Concrete roof with cylindrical holes containing PCM to reduce the heat gain," *Energy and Buildings*, vol. 61, pp. 73–80, 2013.
- [14] A. Pasupathy, L. Athanasius, R. Velraj, and R. V. Seeniraj, "Experimental investigation and numerical simulation analysis on the thermal performance of a building roof incorporating phase change material (PCM) for thermal management," *Applied Thermal Engineering*, vol. 28, no. 5–6, pp. 556–565, 2008.
- [15] N. Soares, J. J. Costa, A. R. Gaspar, and P. Santos, "Review of passive PCM latent heat thermal energy storage systems towards buildings' energy efficiency," *Energy and Buildings*, vol. 59, pp. 82–103, 2013.
- [16] C. Luo, L. Xu, J. Ji, M. Liao, and D. Sun, "Experimental study of a modified solar phase change material storage wall system," *Energy*, vol. 128, pp. 224–231, 2017.

Research Article

Phase Distribution for Subcooled Flow Boiling in an Inclined Circular Tube

Wei Bao , JianJun Xu , TianZhou Xie, BingDe Chen, YanPing Huang, and DianChuan Xing

CNNC Key Laboratory on Nuclear Reactor Thermal Hydraulics Technology, Nuclear Power Institute of China, Chengdu 610041, China

Correspondence should be addressed to JianJun Xu; xujun2000@sohu.com

Received 28 September 2017; Revised 6 December 2017; Accepted 4 January 2018; Published 15 March 2018

Academic Editor: Zhonghao Rao

Copyright © 2018 Wei Bao et al. This is an open access article distributed under the Creative Commons Attribution License, which permits unrestricted use, distribution, and reproduction in any medium, provided the original work is properly cited.

An experimental investigation of phase distribution for subcooled flow boiling in an inclined circular tube (i.d. 24 mm) was conducted in this paper. The local interfacial parameters were measured by a double-sensor optical fiber probe, and the measurements were performed on three different directions in the inclined tube cross section. The experiment shows that the phase distribution under the inclined condition is different from the phase distribution under the vertical condition. The profiles skewed highly for 90° and 45° direction in the tube cross section, whereas the profile was also symmetrical at 0° direction. These results can be explained by the fact that buoyancy caused the bubbles to move toward the top of the tube cross section under inclined condition. In addition, the typical distributions were also influenced by the inclination angles.

1. Introduction

Subcooled flow boiling often appears in industrial fields, such as nuclear reactors, chemical plants, and some engineering systems. With the deepening of the research on the two-phase flow and boiling heat transfer, it has been found that distribution of the local interfacial parameter has an important influence on the flow and heat transfer characteristics of the two-phase flow, and the capability to predict the local void distribution in subcooled flow boiling is of great importance for the safety of boiling water reactor. Meanwhile, the establishment and development of the two-fluid model also require the verification with the experimental data of the local interfacial parameters. Therefore, the study on the phase distribution characteristics of the subcooled flow boiling is of great significance to the understanding of the mechanism of two-phase flow and heat transfer.

The local void fraction and interfacial area concentration (IAC) is the basic parameter determining the structure of the two-phase flow. In order to obtain a more reliable interfacial area transport equation, some experiments for the phase distribution of local parameters in two-phase flow are

indispensable. Over the past few years, a large number of the experiments regarding gas-liquid bubbly flow have been performed [1–8]. Revankar and Ishii [9] observed that the local IAC appears as a wall-peak profile in a vertical tube. In studies by Hibiki and Ishii [10], Hibiki et al. [11], and Shen et al. [12], four kinds of typical profiles of local interfacial parameters including wall peak, core peak, intermediate peak, and transition have been found in the studies.

A large number of the experiments regarding subcooled flow boiling have been performed. Some tasks for different geometrical channels have been already conducted by the previous investigators. Sekoguchi et al. [13] have used the single-sensor conductivity probe to measure both radial and axial distributions of local fraction under a subcooled boiling condition in a circular tube. Garnier et al. [14] performed the measurements of local interfacial parameters in R-12 subcooled flow boiling in a vertical channel with two-sensor optical probe; meanwhile, it is found that void fraction profiles in the experiment are concave profile, convex profile, and two-peak profile. Sun [15] reported the radial distributions of local void fraction and bubble frequency in the low-mass flux subcooled flow boiling. For vertical

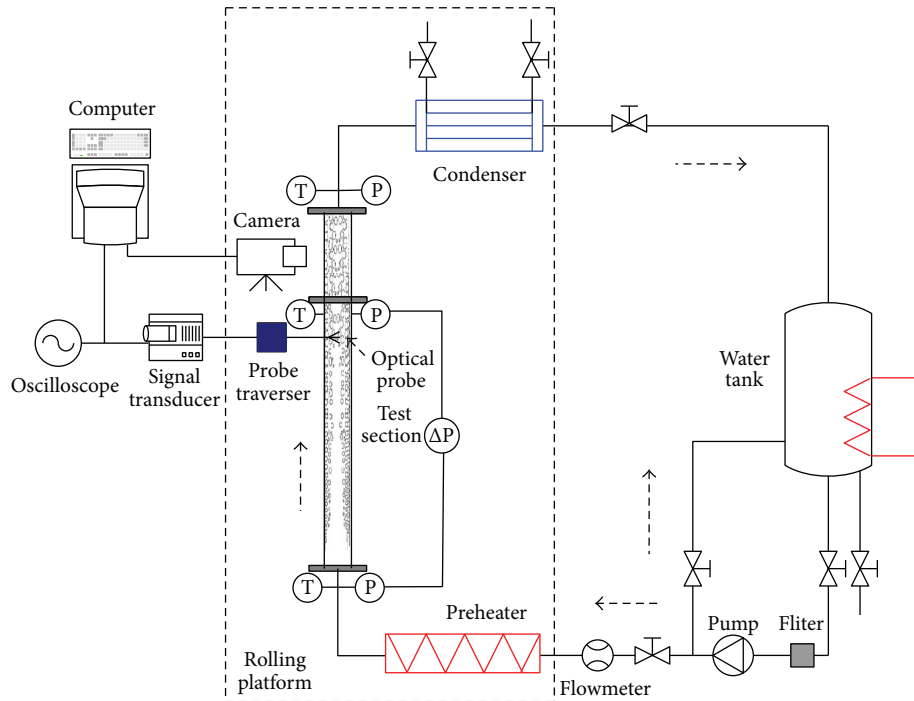


FIGURE 1: Schematic diagram of test loop.

annulus channel, Hasan et al. [16] and Roy and Velidandla [17] measured local void fraction, gas velocity, and bubble diameter in R-113 boiling flow. Recently, it has been presented in the studies of Situ et al. [18], Lee et al. [19], and Yun et al. [20] that local measurements of void fraction, bubble diameter, interfacial velocity, and liquid velocity in subcooled flow boiling were performed in annulus channel. Besides, some double-sensor conductivity probes were used for the measurements of the local interfacial parameters at three or more axial locations.

The above studies are mainly focused on the local interfacial characteristics of two-phase flow under the vertical condition. Inclined condition extensively occurred in the field of ship industry and chemical engineering. The trend of developing applications for ocean environments has attracted growing interests on two-phase flow under inclined condition. Therefore, the flow pattern, void fraction, and pressure drop of two-phase flow in inclined tubes have been studied extensively [21–25]. However, only very few literatures have focused on the local interfacial parameter distribution under inclined condition. Spindler and Hahne [26] have investigated the void fraction and bubble frequency profiles of adiabatic two-phase flow in an inclined tube with the method of optical fiber probe. Recently, Xing et al. [27] have researched the radial distribution of interfacial parameters for air-water bubbly flow in a circular tube under inclined condition with the double-sensor optical fiber probe. Only one-dimensional distribution of the local interfacial parameter in inclined bubbly flow has been experimentally studied in the previous task. Among all of the existing experiments measured along single direction of cross section in an inclined tube, the asymmetrical distributions of local parameters have been found in these experiments.

However, the measurement of multiple directions can fully reflect the three-dimensional distribution characteristics. It is regrettable that few studies aim at the phase distribution in different directions under inclined condition. Recently, Bao et al. [28] measured local interfacial parameters for subcooled flow boiling in an inclined circular tube. It is required not only by the profile for one chord of tube cross section but also by some profiles for other direction in the cross section, for it better gains the physical insight into the distribution characteristics of subcooled flow boiling under inclined condition. From this point of view, this experimental study aims to investigate the phase distribution of subcooled flow boiling in inclined circular tube under different directions.

2. Material and Methods

2.1. Experimental Loop. A schematic of the experimental loop used for this study is shown in Figure 1. The experimental system has been introduced by previous work [28]. As can be seen in Figure 1, the preheater, condenser, test section, optical probe, and probe traverser are mounted onto the rolling platform and the other apparatus are on the floor. The two parts of the test loop are connected with flexible pipe. The deionized water is stored in a tank, and the non-condensable gas in the water is removed by a heater. The water is circulated by the drive of the pump. Two regulated valves were installed separately on the bypass, and the test branch controls the flow rate through the test section. A direct electrical-heating preheater is used to regulate the liquid temperature at the inlet of the heated test section. The uniform heat flux is provided by the 80 kW DC power supply. Two-phase mixture flowing out of the test section is chilled by a condenser. The test section is a circular tube with

an inner diameter of 24 mm and a heated length of 1000 mm. There are two parts in this section. One is the heated section made of stainless steel, and the other one is the visual section made of quartz glass.

The volumetric flow rate was measured with a venturi flowmeter and the accuracy of flow measurement was $\pm 2\%$ of the full-scale flow. Two test gauges with accuracy of $\pm 0.1\%$ were installed to measure the pressure at the inlet and outlet of the test section. The pressure drop across the inlet and outlet of the heated section was measured with the pressure differential pressure transmitters of range 0~0.2 MPa with accuracy of $\pm 0.1\%$ of full-scale pressure drop. Some N-type thermocouples were used to measure fluid temperatures at the inlet and outlet of the heated test section. A typical uncertainty associated with temperature measurement was $\pm 1^\circ\text{C}$. The heat flux to the heated test section was obtained by measuring the current into the test section and the voltage drop across the heater. The electrical current was measured using a digital multimeter, and the voltage was measured using a multirange voltmeter. Maximum uncertainty in power measurement was $\pm 1\%$ of measured power. The heat loss to the ambient is estimated from the sensible heat that is gained by the fluid for single-phase heat transfer conditions.

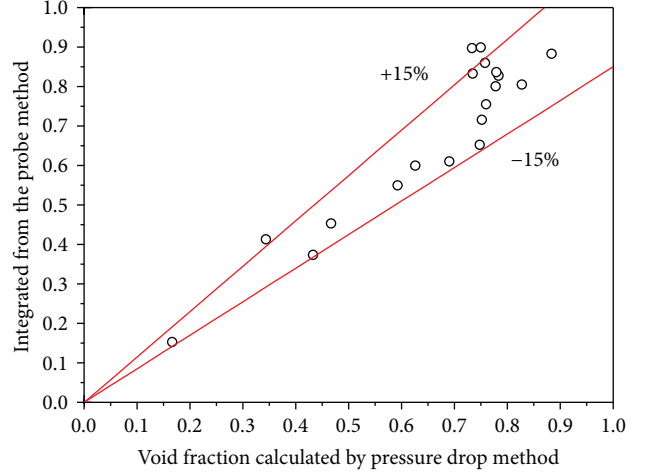
2.2. Optical Probe System. To quantify the complicated local interfacial characteristic in subcooled flow boiling, a double-sensor optical fiber probe was applied to measure the local interfacial parameters. A signal processor generated high- or low-voltage signal corresponding to the vapor and liquid phases around the probe tip, with each pulse representing a bubble hitting the sensor tip. The double-sensor probe consists of two independent sensors, the two sensor tips space 0.7 mm along the main flow direction and upstream one is called the front sensor. The location of the optical probe was at axial position of $40D$ ($D = 24$ mm) distance from the entrance. The optical probe can move with the drive of a probe traverse with 0.02 mm resolution. For inclined condition, the probe was traversed in $r/R = -0.95 \sim 0.95$ to obtain the radial profiles of local parameters; r and R are the radial distance from the center and the inner radius of the heated tube, respectively.

Based on the signal from the two-sensor probe, local void fraction and bubble frequency are calculated by the signals of the front sensor. Local void fraction is equal to the ratio of all of the bubble-dwelling time measured by the front sensor to the total sampling time (T), which can be expressed by

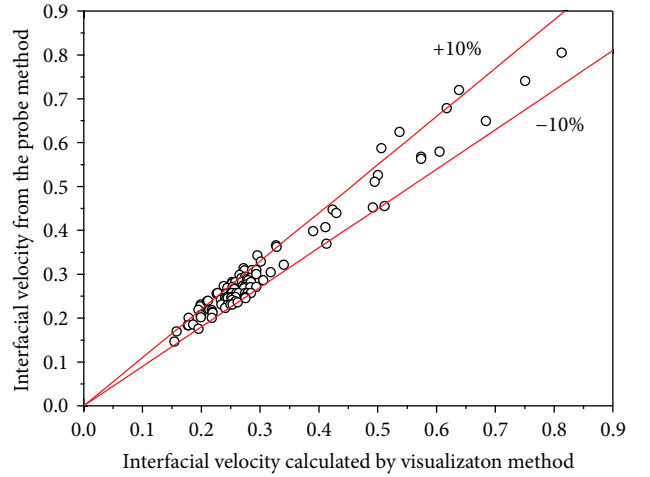
$$\alpha = \frac{\sum (t_j - t_{j-1})}{T} = \frac{\sum \Delta t_j}{T}. \quad (1)$$

Local bubble frequency is equal to the ratio of the bubble numbers (N) passing through the front fiber tip in the measurement time to the total sampling time,

$$f_b = \frac{N}{T}. \quad (2)$$



(a)



(b)

FIGURE 2: Uncertainty of the two-sensor optical probe: (a) void fraction; (b) interfacial velocity.

The interfacial velocity parallel to the flow direction can be simply calculated from the distance between the two sensor tips and the time difference, and it can be expressed as

$$v_i = \frac{\Delta s}{\Delta t_{kl}}. \quad (3)$$

Local IAC calculated by the method of Wu and Ishii [29], who considered the effect of bubble lateral motions on the IAC measured,

$$\alpha_i = \frac{2N_b}{\Delta s \Delta T} \left[2 + \left(\frac{v'_b}{v_b} \right)^{2.25} \right] \frac{\sum_j (\Delta t_j)}{N_b - N_{\text{miss}}}. \quad (4)$$

ΔT , N_b , N_{miss} , and v'_b/v_b denote the sampling time, the total numbers detected by the front sensor, the number of the missed bubbles, and the relative bubble velocity fluctuation, respectively. The missed bubbles referred to those are touched by the front sensor but not by the rear sensor, or those pass the rear sensor ahead of the front sensor due to

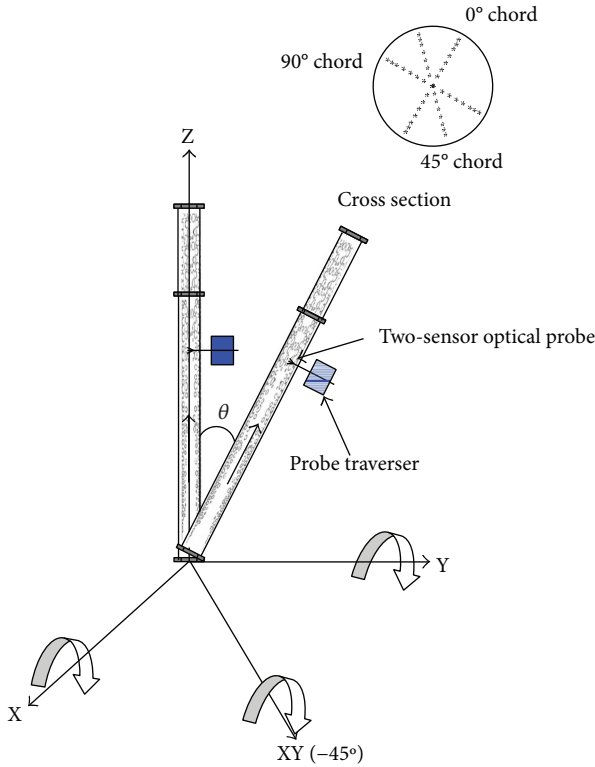


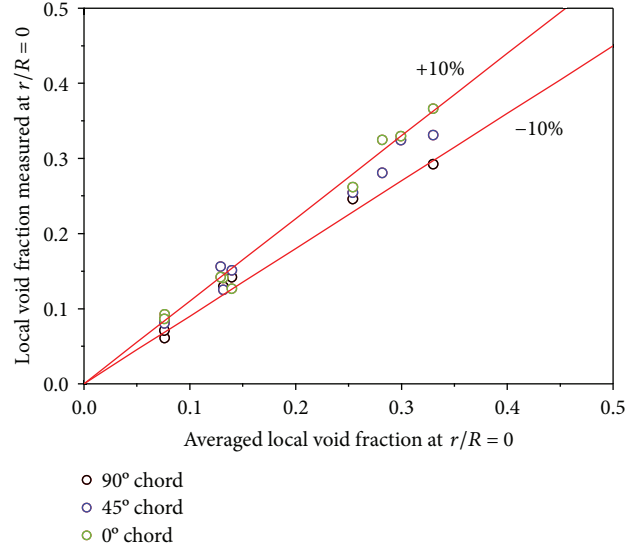
FIGURE 3: Diagram of test section under vertical and inclined condition.

bubble lateral motions. They also reported the relative bubble velocity fluctuation.

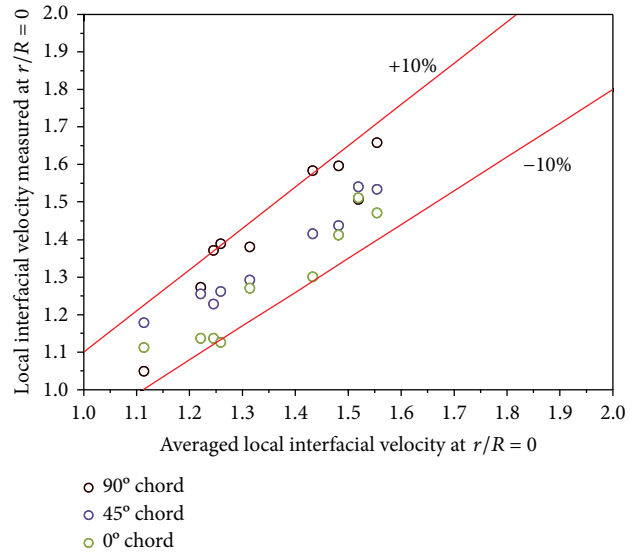
It can be seen from Figure 2 that the probe measurement results show good agreement with the void fraction calculated by pressure drop method, and the maximum relative error is less than 15%. It is also found that the maximum relative error between the local interfacial velocities measured by probe and that by the visualization method is less than 10%.

2.3. Experimental Methods. The measurement method named multiangle between the direction of motion and the measuring is used in the experiment, which can obtain the local interfacial parameters in different directions of the inclined tube cross section. As shown in Figure 3, the inclination angle can be adjusted between $\theta = 0^\circ$ (vertical) and $\theta = 30^\circ$; in addition, the test tube can incline through different directions with the help of the moveable platform. As a result, according to the angle between the two directions of inclination axis and probe measurement, three chords (0° , 45° , and 90° chord) of different directions in the tube cross section can be measured under the inclined condition. $\beta = 90^\circ$ means that the measuring direction is perpendicular to the inclination axis direction, and $\beta = 0^\circ$ means that the measuring direction is parallel to the inclination axis direction; $r = 0$ corresponds to the channel center, whereas $r/R > 0$ and $r/R < 0$ represent the lower and upper half part of inclined cross section of tube, respectively.

Figure 4 shows the measurement repeatability of the two-sensor probe at $r/R = 0$ for the three chords in the



(a)



(b)

FIGURE 4: Repeatability of the two-sensor optical probe measurement at $r/R = 0$: (a) void fraction; (b) interfacial velocity.

tube cross section. It has also been found that the local void fraction and local interfacial velocity are similar regardless of the measurement chord when the tube inclined for any axis. To sum up, it clearly indicates that the multiangle measurement method is reasonable.

3. Results and Discussion

3.1. The Characteristics of Phase Distribution for Subcooled Flow Boiling under the Inclined Condition. Figure 5 clearly shows the characteristics of the phase distributions of subcooled flow boiling under inclined condition. As presented in the figures, local void distribution for inclined condition is quite different from that for vertical condition, and the phase distribution profiles are not symmetrical in inclined tube. Moreover, the different distribution profiles occurred

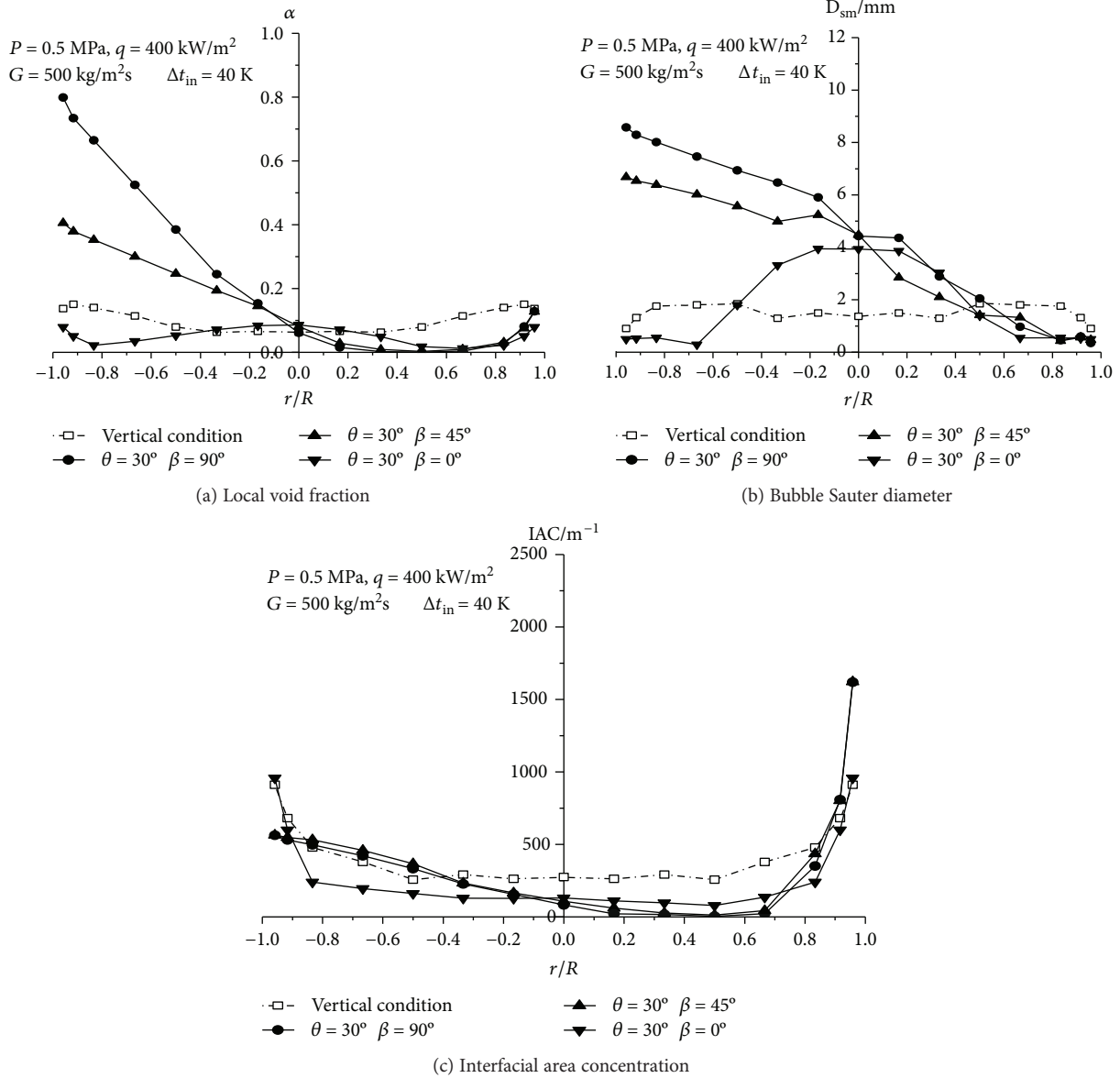


FIGURE 5: Phase distribution of subcooled flow boiling under inclined condition.

in three measured directions. That is to say, the profile of local interfacial parameters highly skewed at 90° chord and 45° chord, while the profile is still symmetrical at 0° chord. These results can be explained by the fact that buoyancy caused the bubbles to move toward the upper side of inclined tube and congregate. Owing to the lateral migration and polymerization of bubbles onto the upper wall of the channel, the peak value of the local void fraction appears in the $r/R = -1$ position of the inclined channel; in addition, the largest bubble Sauter diameter appears in this position as well. Because of the increase of the bubble size, the IAC is smaller than that under the static condition, which indicates that the heat transfer ability between the liquid and vapour phase at the top of the inclined channel becomes weaker. As the bubbles emerge from the heated wall, there are still some bubbles at the bottom of the inclined channel ($r/R = 1$). As we can see in the picture, the local void

fraction and bubble size at the bottom of the flow path are less affected by the inclination. Meanwhile, due to the migration of large bubbles to the top of the tube, the IAC can be larger than that under static condition, which indicates that the heat transfer between the liquid and vapour phase at the bottom of the inclined channel is becoming stronger.

3.2. The Influence of the Inclination Angle on the Phase Distribution for Subcooled Flow Boiling. According to the analysis above, the phase distribution on the direction of $\beta = 90^\circ$ and $\beta = 45^\circ$ is similar, and the phase distribution on the direction of $\beta = 0^\circ$ is still symmetrical. As follows, the analysis of phase distribution characteristics on the directions of $\beta = 90^\circ$ and $\beta = 0^\circ$ has been conducted, respectively.

3.2.1. The Characteristics of the Phase Distribution on the Direction of $\beta = 90^\circ$ in Cross Section. Figures 6–8 shows the

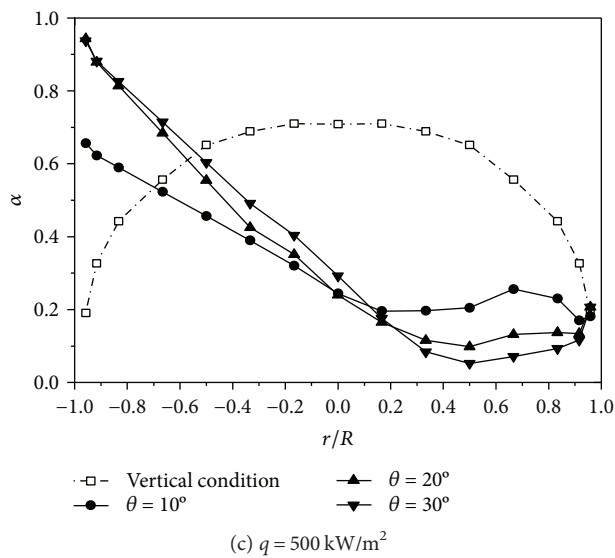
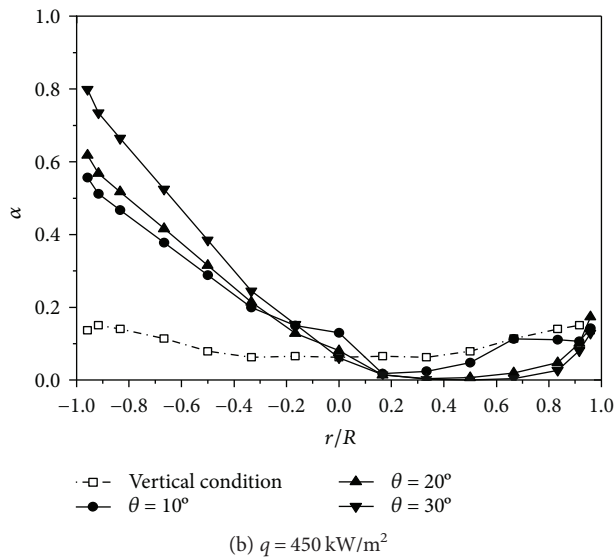
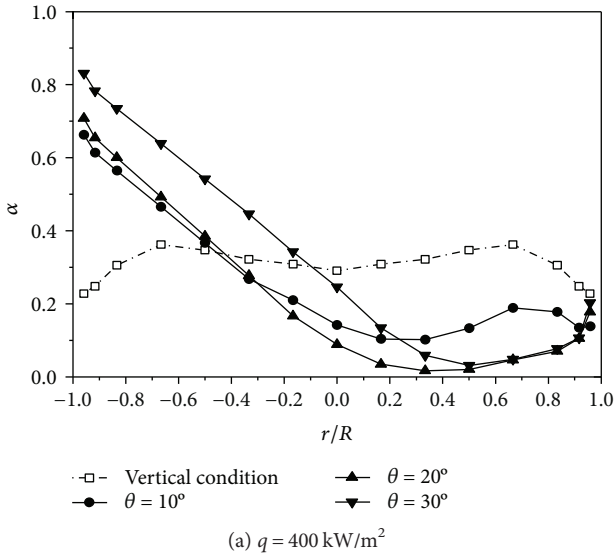


FIGURE 6: Inclusion angle effect on the local void fraction on the direction of $\beta = 90^\circ$ in cross section ($P = 0.5 \text{ MPa}$, $G = 500 \text{ kg/m}^2 \text{ s}$).

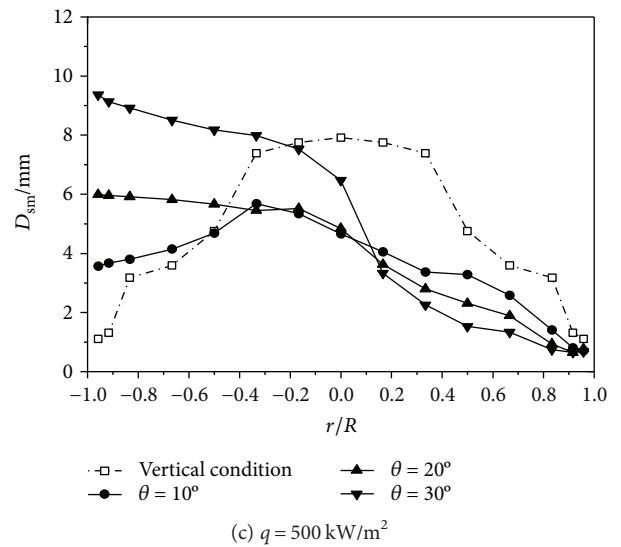
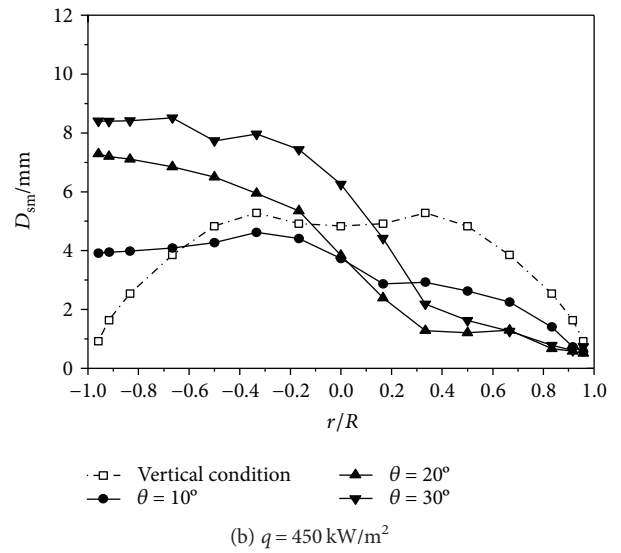
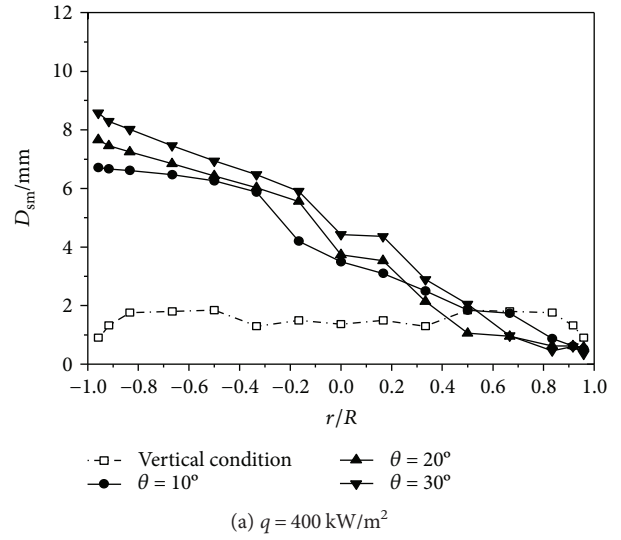


FIGURE 7: Inclusion angle effect on the bubble Sauter diameter on the direction of $\beta = 90^\circ$ in cross section ($P = 0.5 \text{ MPa}$, $G = 500 \text{ kg/m}^2 \text{ s}$).

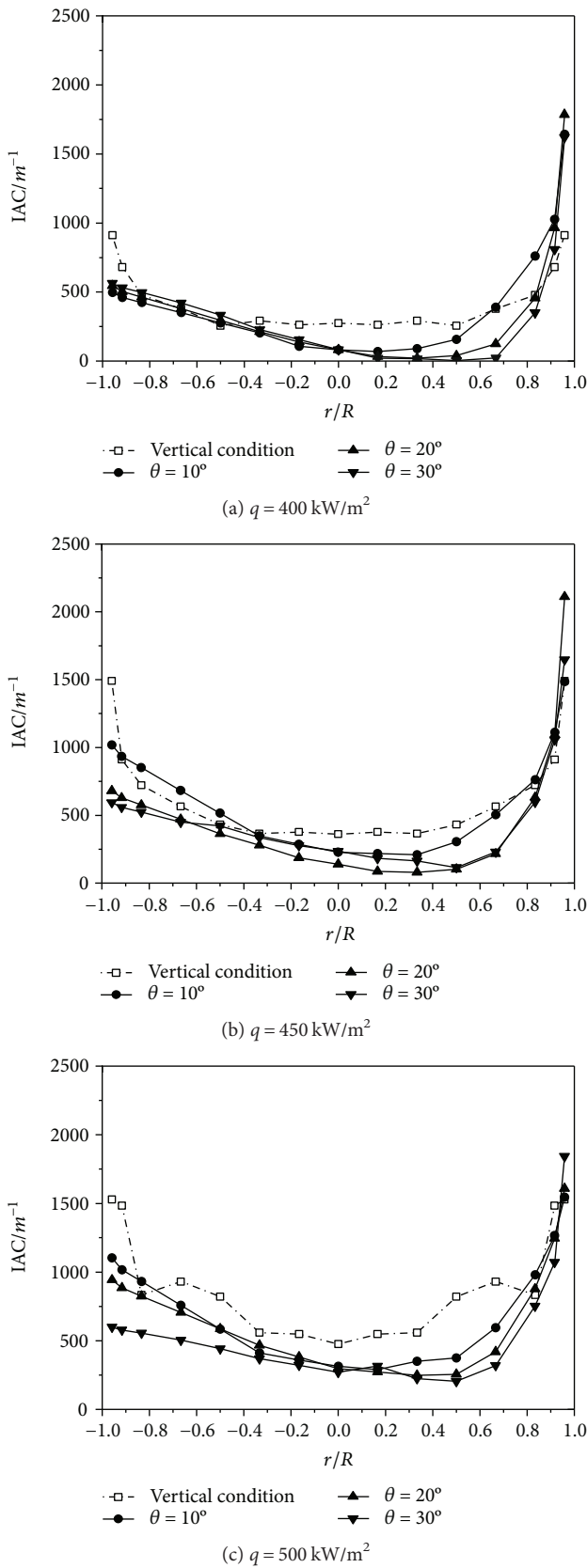


FIGURE 8: Inclination angle effect on the interfacial area concentration on the direction of $\beta = 90^\circ$ in cross section ($P = 0.5 \text{ MPa}$, $G = 500 \text{ kg/m}^2 \text{ s}$).

influence of the inclination angle on the deviation of local void fraction, bubble size, and IAC on the direction of $\beta = 90^\circ$. As we can see, with the increasing of the inclination angle, deviation of local void fraction, bubble size, and IAC, the peak value of local void fraction increases on the top of tube; meanwhile, the bubble Sauter diameter of also raises but IAC decreases slightly. This can be explained by the reason that the radial part of buoyancy increases with the rising of the inclination angle. Hence, it results in more bubble aggregation on the top of the flow channel and the uneven phase distribution of the subcooled flow boiling under inclined condition exacerbates.

It can be seen in Figure 6 that the peak value near the location where $r/R = -1$ increases as the inclination angle increases, while it becomes weakened near the $r/R = 0.8$ and the inclination angles will affect the typical distributions in some degree. When heat flux $q = 400 \text{ kW/m}^2$, the local void core peak profile changes into intermediate peak profile as the inclination angle increases at the lower half part of the inclined tube. Even in the case of 30° for an inclination angle, the peak near the lower side will disappear, when the heat flux is lower and the wall peak profile occurred. It is also found that local void fraction at $r/R = -1$ was independent of the inclination angle. The reason is the bubble generation controlled by the heat surface in subcooled flow boiling.

The local bubble Sauter diameter profile is illustrated in Figure 7. As clearly reported in some literature, the lift force pushes the small bubbles toward the wall in vertical upward flow, while the direction of lift force is reversed when the bubble diameter exceeds the threshold size. Different from vertical flow, the buoyancy force has a radial component normal to the tube axis. For large size bubbles, the direction of force is the same as the lift force in the lower part of the tube while it reverses to the lift force in the upper part of the tube. Therefore, large bubbles moved to the upper part of the tube and congregate. For small size bubbles, more of them moved to the upside resulting from the direction of F which reversed to the lift force in the lower part of tube.

Figure 8 shows typical profiles of the measured local IAC; there is an approximately symmetrical profile for inclined condition. Local IAC explicitly decreased near the upper side at 90° direction when heat flux was high when compared with that for vertical condition. This explains that IAC is proportional to void fraction, but inversely proportional to bubble size. And it causes the decrease of IAC in this region with the aforementioned bubbles near the upper side of the inclined tube becoming larger.

3.2.2. *The Characteristics of the Phase Distribution on the Direction of $\beta = 0^\circ$ in Cross Section.* Figure 9–11 shows the influence of the inclination angle on the local void fraction, bubble size, and IAC on the direction of $\beta = 0^\circ$ in the flow channel. It can be clearly seen that the profile of phase distribution still maintains symmetrical. In addition, the influence of the inclination angle on the phase distribution in this direction is also of vital significance.

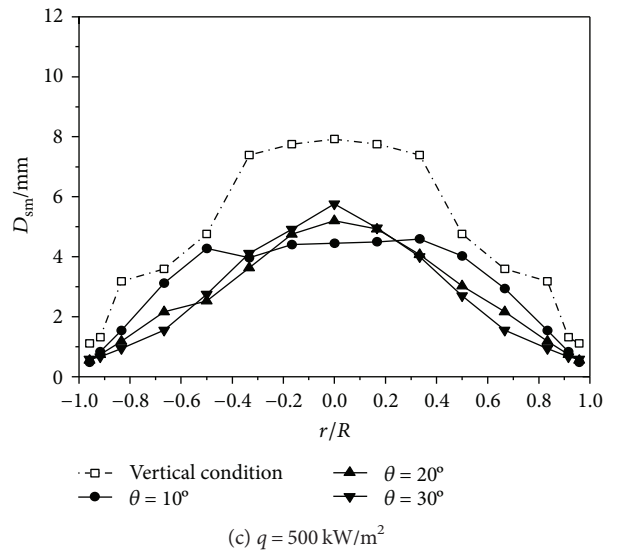
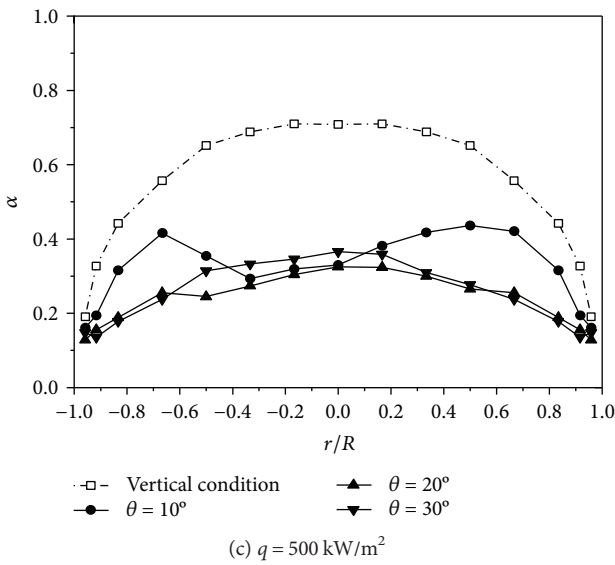
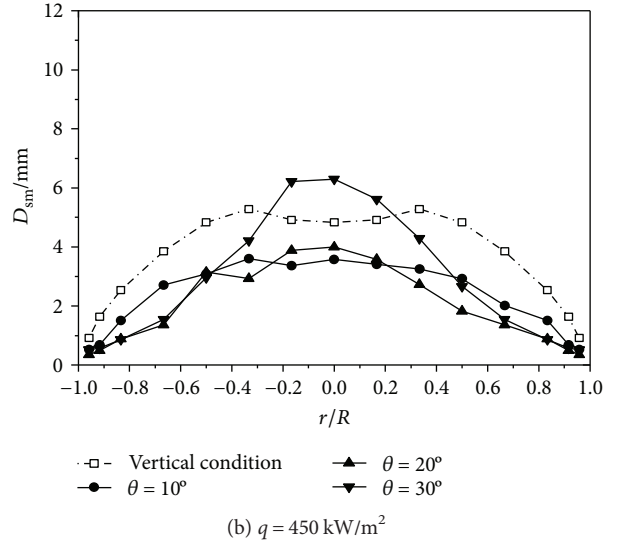
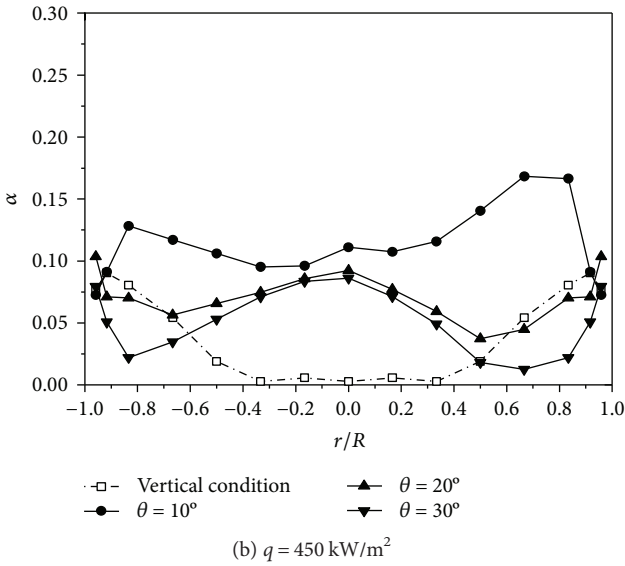
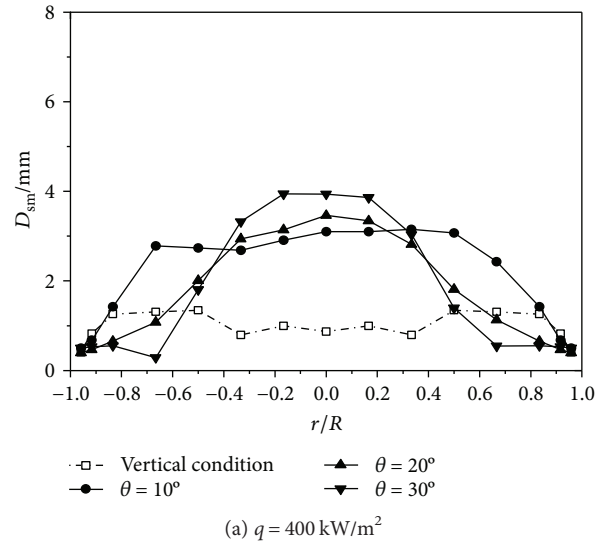
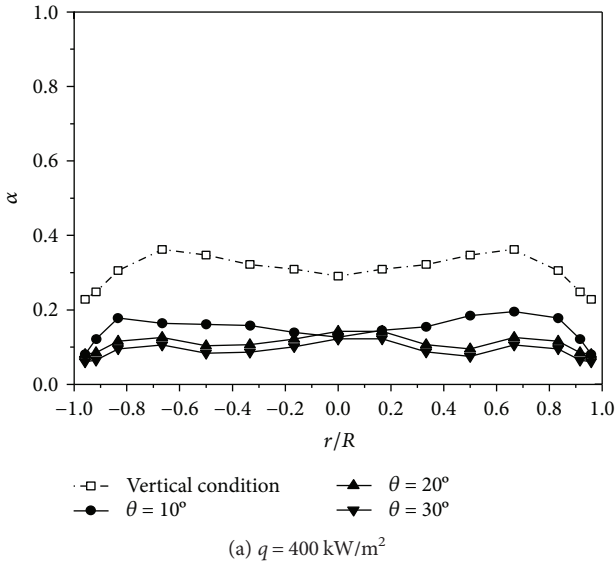


FIGURE 9: Inclination angle effect on the local void fraction on the direction of $\beta = 0^\circ$ in cross section ($P = 0.5 \text{ MPa}$, $G = 500 \text{ kg/m}^2 \text{ s}$).

FIGURE 10: Inclination angle effect on the bubble Sauter diameter on the direction of $\beta = 0^\circ$ in cross section ($P = 0.5 \text{ MPa}$, $G = 500 \text{ kg/m}^2 \text{ s}$).

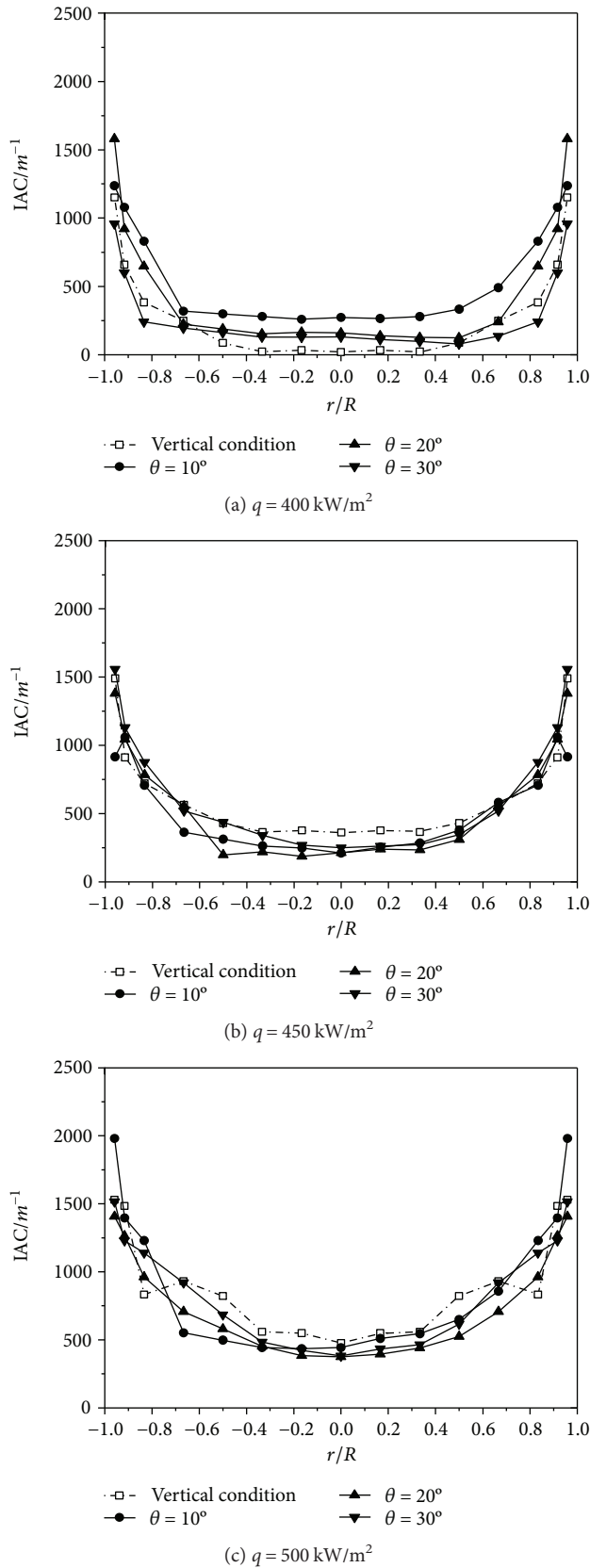


FIGURE 11: Inclination angle effect on the interfacial area concentration on the direction of $\beta = 0^\circ$ in cross section ($P = 0.5 \text{ MPa}$, $G = 500 \text{ kg/m}^2 \text{ s}$).

Figure 9 shows the local void fraction distribution under different inclination angles. When the heat flux is $q = 400 \text{ kW/m}^2$, the bubbles rise along the radial direction under inclined condition. With the increase of the inclination angles, the near-wall peak gradually disappeared. Meanwhile, the local void fraction in the channel center is larger than that under the condition of vertical. As the heat flux increases, the local void fraction distribution on the direction of $\beta = 0^\circ$ is more uneven. From Figure 10, it can be seen that the size of the bubble in the inclined channel is mainly the core-peak distribution. The inclination angle has little influence on the size of the bubble near the wall. With the increase of the inclination angle, the bubble size increases as well. Figure 11 shows that the inclination angle has little influence on the IAC on the direction of $\beta = 0^\circ$ due to the reason that more large bubbles occur and gather onto the top of tube when the heat flux increases.

4. Conclusions

In this paper, local interfacial characteristics in subcooled flow boiling were investigated under vertical and inclined conditions. For vertical upward subcooled flow boilings, the local interfacial parameters presented three kinds of distribution types, including wall peak, core peak, and intermediate peak. As it is expected, the phase distribution under the inclined condition is different from the phase distribution under the vertical condition. The profiles skewed highly for 90° and 45° chord of tube cross section, whereas the profile was also symmetrical at 0° chord. These results can be explained by the fact that buoyancy caused the bubbles to move toward the top of the tube cross section under inclined condition. In addition, the typical distributions were also influenced by the inclination angles.

Nomenclature

a_i :	Local interfacial area concentration ($1/\text{m}$)
D :	Tube diameter (mm)
D_{sm} :	Local bubble Sauter mean diameter (mm)
f_b :	Local bubble frequency (Hz)
F_{bl} :	Radial component for buoyancy force
G :	Mass flux ($\text{kg/m}^2 \text{ s}$)
N_b :	Bubble number of sampling
N_{miss} :	Missed bubble number of sampling
P :	Pressure (MPa)
q :	Heat flux ($\text{kW/m}^2 \text{ s}$)
R :	Tube radius (mm)
r :	Radial position for probe measurement (mm)
v_i :	Local interfacial velocity (m/s)
ΔT :	Sampling time(s)/subcooling degree($^\circ\text{C}$).

Greek Symbols

α :	Local void fraction
Δs :	Distance between two sensor tips (m)
Δt_j :	Time delay for j th interface (s)
Δt_{kl} :	Time delay between the front and rear sensor (s)
ΔT_{in} :	Inlet temperature.

Conflicts of Interest

The authors declare that they have no conflicts of interest.

Acknowledgments

This work is supported by the National Natural Science Foundation of China under Grant nos. 11475161 and 11505176.

References

- [1] M. Higuchi and T. Saito, "Quantitative characterizations of long-period fluctuations in a large-diameter bubble column based on point-wise void fraction measurements," *Chemical Engineering Journal*, vol. 160, no. 1, pp. 284–292, 2010.
- [2] S. L. Kiambi, H. K. Kiriamiti, and A. Kumar, "Characterization of two phase flows in chemical engineering reactors," *Flow Measurement and Instrumentation*, vol. 22, no. 4, pp. 265–271, 2011.
- [3] T. Hibiki and M. Ishii, "Interfacial area concentration of bubbly flow systems," *Chemical Engineering Science*, vol. 57, no. 18, pp. 3967–3977, 2002.
- [4] K. Sun, M. Zhang, and X. Chen, "Local measurement of gas-liquid bubbly flow with a double-sensor probe," *Chinese Journal of Chemical Engineering*, vol. 8, pp. 33–40, 2000.
- [5] X. Shen and K. Mishima, "Two-phase phase distribution in a vertical large diameter pipe," *International Journal of Heat and Mass Transfer*, vol. 48, no. 1, pp. 211–225, 2005.
- [6] X. Shen, Y. Saito, K. Mishima, and H. Nakamura, "A study on the characteristics of upward air-water two-phase flow in a large diameter pipe," *Experimental Thermal and Fluid Science*, vol. 31, no. 1, pp. 21–36, 2006.
- [7] S. Kim, M. Ishii, Q. Wu, D. McCreary, and S. G. Beus, "Interfacial structures of confined air-water two-phase bubbly flow," *Experimental Thermal and Fluid Science*, vol. 26, no. 5, pp. 461–472, 2002.
- [8] X. D. Sun, T. R. Smith, S. Kim, M. Ishii, and J. Uhle, "Interfacial area of bubbly flow in a relatively large diameter pipe," *Experimental Thermal and Fluid Science*, vol. 27, no. 1, pp. 97–109, 2002.
- [9] S. T. Revankar and M. Ishii, "Local interfacial area measurement in bubbly flow," *International Journal of Heat and Mass Transfer*, vol. 35, no. 4, pp. 913–925, 1992.
- [10] T. Hibiki and M. Ishii, "Experimental study on interfacial area transport in bubbly two-phase flows," *International Journal of Heat and Mass Transfer*, vol. 42, no. 16, pp. 3019–3035, 1999.
- [11] T. Hibiki, M. Ishii, and Z. Xiao, "Axial interfacial area transport of vertical bubbly flows," *International Journal of Heat and Mass Transfer*, vol. 44, no. 10, pp. 1869–1888, 2001.
- [12] X. Z. Shen, R. Matsui, K. Mishima, and H. Nakamura, "Distribution parameter and drift velocity for two-phase flow in a large diameter pipe," *Nuclear Engineering and Design*, vol. 240, no. 12, pp. 3991–4000, 2010.
- [13] K. Sekoguchi, H. Fukui, and Y. Sato, "Flow boiling in subcooled and low quality regions heat transfer and local void fraction," in *Proceedings of Fifth International Heat Transfer Conference*, vol. 4, pp. 180–184, Tokyo, Japan, 1974.
- [14] J. Garnier, E. Manon, and G. Cubizolles, "Local measurements on flow boiling of refrigerant 12 in a vertical tube," *Multiphase Science and Technology*, vol. 13, no. 1-2, p. 111, 2001.
- [15] Q. Sun, *Phase Distribution for Low Mass Flux Subcooled Boiling Flow [Ph. D Thesis]*, Tsinghua University, 2004.
- [16] A. Hasan, R. P. Roy, and S. P. Kalra, "Some measurements in subcooled flow boiling of refrigerant-113," *Journal of Heat Transfer*, vol. 113, no. 1, p. 216, 1991.
- [17] R. P. Roy and V. Velidandla, "Local measurements in the two-phase region of turbulent subcooled boiling flow," *Journal of Heat Transfer*, vol. 116, no. 3, p. 660, 1994.
- [18] R. Situ, T. Hibiki, X. D. Sun, Y. Mi, and M. Ishii, "Axial development of subcooled boiling flow in an internally heated annulus," *Experiments in Fluids*, vol. 37, no. 4, pp. 589–603, 2004.
- [19] T. Lee, R. Situ, T. Hibiki, H. Park, M. Ishii, and M. Mori, "Axial developments of interfacial area and void concentration profiles in subcooled boiling flow of water," *International Journal of Heat and Mass Transfer*, vol. 52, no. 1-2, pp. 473–487, 2009.
- [20] B. J. Yun, B. U. Bae, D. J. Euh, G. C. Park, and C. H. Song, "Characteristics of the local bubble parameters of a subcooled boiling flow in an annulus," *Nuclear Engineering and Design*, vol. 240, no. 9, pp. 2295–2303, 2010.
- [21] J. G. Jing, M. Y. Zhang, and X. J. Chen, "A study on flow pattern transitions for gas-liquid two-phase upward flow in an inclined tube," *Journal of Xi'an Jiaotong University*, vol. 28, pp. 143–150, 1994.
- [22] S. Wongwises and M. Pipathattakul, "Flow pattern, pressure drop and void fraction of two-phase gas-liquid flow in an inclined narrow annular channel," *Experimental Thermal and Fluid Science*, vol. 30, no. 4, pp. 345–354, 2006.
- [23] J. Y. Xu, Y. X. Wu, Z. H. Shi, L. Y. Lao, and D. H. Li, "Studies on two-phase co-current air non-Newtonian shear-thinning fluid flows in inclined smooth pipes," *International Journal of Multiphase Flow*, vol. 33, no. 9, pp. 948–969, 2007.
- [24] V. Hernandez-Perez, *Gas-Liquid Two-Phase Flow in Inclined Pipes [Ph. D Thesis]*, The University of Nottingham, 2008.
- [25] A. Abdulahi, L. Abdulkareem, S. Sharaf, M. Abdulkadir, V. Hernandez Perez, and B. J. Azzopardi, "Investigating the effect of pipe inclination on two-phase gas-liquid flows using advanced instrumentation," in *The 8th Thermal Engineering Joint Conference (AJTEC2011)*, Honolulu, HI, USA, March, 2011.
- [26] K. Spindler and E. Hahne, "An experimental study of the void fraction distribution in adiabatic water-air two-phase flows in an inclined tube," *International Journal of Thermal Sciences*, vol. 38, no. 4, pp. 305–314, 1999.
- [27] D. Xing, C. Yan, L. Sun, J. Liu, and B. Sun, "Experimental study of interfacial parameter distributions in upward bubbly flow under vertical and inclined conditions," *Experimental Thermal and Fluid Science*, vol. 47, pp. 117–125, 2013.
- [28] W. Bao, B. D. Chen, J. J. Xu, T. Z. Xie, D. C. Xing, and Y. P. Huang, "Experimental study on the local interfacial characteristic of subcooled flow boiling under inclined condition," in *23rd International Conference on Nuclear Engineering*, Chiba, Japan, 2015.
- [29] Q. Wu and M. Ishii, "Sensitivity study on double-sensor conductivity probe for the measurement of interfacial area concentration in bubbly flow," *International Journal of Multiphase Flow*, vol. 25, no. 1, pp. 155–173, 1999.

Research Article

Influence of Gas-Liquid Interface on Temperature Wave of Pulsating Heat Pipe

Ying Zhang, Zhiqiang Wang, Peisheng Li , Min Zhou, Boheng Dong, and Yanni Pan

College of Mechanical and Electrical Engineering, Nanchang University, Nanchang 330031, China

Correspondence should be addressed to Peisheng Li; ncudns1995z@163.com

Received 31 August 2017; Revised 22 December 2017; Accepted 11 January 2018; Published 11 March 2018

Academic Editor: Xinhai Xu

Copyright © 2018 Ying Zhang et al. This is an open access article distributed under the Creative Commons Attribution License, which permits unrestricted use, distribution, and reproduction in any medium, provided the original work is properly cited.

The influence of the interface on the amplitude and phase of the temperature wave and the relationship between the attenuation of the temperature wave and the gas-liquid two-phase physical parameters are studied during the operation of the pulsating heat pipe. The numerical simulation shows that the existence of the phase interface changes the direction of the temperature gradient during the propagation of the temperature wave, which increases the additional “thermal resistance.” The relative size of the gas-liquid two-phase thermal conductivity affects the propagation direction of heat flow at phase interface directly. The blockage of the gas plug causes hysteresis in the phase of the temperature wave, the relative size of the gas-liquid two-phase temperature coefficient will gradually increase the phase of the temperature wave, and the time when the heat flow reaches the peak value is also advanced. The attenuation of the temperature wave is almost irrelevant to the absolute value of the density, heat capacity, and thermal conductivity of the gas-liquid two phases, and the ratio of the thermal conductivity of the gas-liquid two phases is related. When the temperature of the heat pipe was changed, the difference of heat storage ability between gas and liquid will lead to the phenomenon of heat reflux and becomes more pronounced with the increases of the temperature wave.

1. Introduction

Pulsating heat pipe (PHP) is an efficient and energy-saving heat exchanger element [1, 2]. Solar collectors are the main equipment of solar energy equipment, and the combination with PHP can improve the heat transfer efficiency [3]. When using a PHP as a thermal management tool [4], the temperature of the heat management object changes frequently [5, 6], whose temperature and power vary constantly as the working load changes. Whether the PHP can respond quickly to such a temperature change is extremely important for heat management. Therefore, as the core component of solar collector, solar heat pipe plays an important role in collecting heat and safety of the collector [7]. The flow characteristics of the working fluid in the pulsating heat pipe determine the operating mechanism and heat transfer characteristics of the PHP, so the study of the flow law is the basis of the theoretical analysis and the establishment of the mathematical model [8]. The pulsating heat pipe undergoes complex gas-liquid flow patterns and transitions such as bubble flow, plunger flow, annular/semiannular flow

during the start-up phase as well as the alternating cycles between the annular flow of the initial circulation stage and plunger flow in the tube [9]. Jiansheng et al. [10] use the numerical simulation method to demonstrate that different flow patterns can reduce the heat transfer resistance and enhance the heat transfer capacity in the PHP starting and running. In order to evaluate the heat transfer performance of the PHP accurately, it is necessary to examine the radial heat transfer, evaporation heat transfer, and condensation heat transfer of the working medium and the wall [11]. Kim et al. [12] studied the effect of the temperature pulsation at the evaporating section and the condensate section on the performance of heat pipe, it was found that the sensible heat transfer in the heat transfer mode of the PHP was dominant, and the oscillation frequency of the liquid slug decreases with the increase of the frequency and amplitude of the wall temperature with the periodic pulsation, and the heat transfer performance of the PHP depends on the intensity of the pulsation [13]. Zhang et al. [14] studied the effects of variable bend, number of the liquid slug and the air slug, and the amplitude and frequency of the oscillating flow in the PHP;

the result showed that the influence of the liquid slug and the air slug was small when the number of bends was less than 5, and the amplitude and frequency of the oscillating will increase with the increase of the filling rate. In addition, by studying the movement of gas slug and liquid slug in U tube, it is found that the amplitude and frequency of pulsation of gas slug and liquid slug increase with the increase of temperature difference between evaporation section and condensation section [15].

However, scholars mainly focus on the overall heat dissipation of PHP, and the research on the flow characteristics of the working fluid in PHP is less. As measuring and controlling the temperature in the experiment are difficult, and many factors affect the flow pattern, it is difficult to obtain a stable flow pattern in PHP. Therefore, this paper constructs a phase interface containing a gas slug in a rectangular area and simulates the related phenomena under the condition of low power start and power change. Since any continuous periodic fluctuation curve can be superimposed with multiple sine or cosine functions [16, 17], a sinusoidal temperature is added at one end of the rectangle. The influence of temperature fluctuation on the operation of PHP is analyzed by studying the variation of heat flow and heat flux as well as the amplitude and phase of temperature wave.

2. Computational Model and Numerical Method

2.1. Computational Model. According to the working state of PHP, a computational domain of gas-liquid interface is constructed. Since the time of the movement of the air slug is much shorter than the time of the temperature changes in the steady state of the PHP, it is assumed that the air slug remains stationary during the temperature propagation in order to facilitate the study. As shown in Figure 1, the area of the computational domain is 2 mm × 1 mm. The upper boundary and lower boundary are solid boundary, and the left boundary and the right boundary are the pressure boundary. The coordinates of points 1, 2, and 3 are $x=0.4$ mm, $y=-0.5$ mm; $x=0.743$ mm, $y=-0.5$ mm; and $x=1.6$ mm, $y=0.5$ mm (located in front of the gas slug, inside the gas slug, and behind the gas slug).

2.2. Numerical Methods. In this paper, the VOF model is adopted, and the control equation is shown as follows:

(1) Continuity equation:

$$\frac{\partial \rho}{\partial t} + \frac{\partial}{\partial x_i}(\rho u_i) = 0. \quad (1)$$

(2) Momentum conservation equation:

$$\frac{\partial}{\partial t}(\rho u_i) + \frac{\partial}{\partial x_i}(\rho u_i u_j) = -\frac{\partial p}{\partial x_i} + \frac{\partial \omega_{ij}}{\partial x_j} + \rho g_i + S_N, \quad (2)$$

wherein P is the pressure, g_i is the volume force in the i direction, and S_N is the source term which is a continuum surface force term.

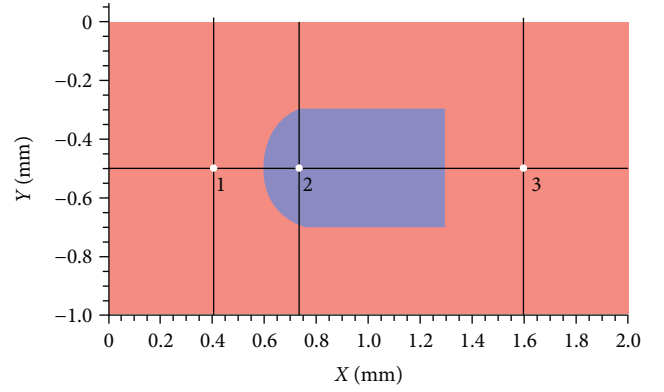


FIGURE 1: Computational model (the light area is the liquid phase area, and the dark area is the gas phase area).

The stress tensor is shown below:

$$\omega_{ij} = u \left(\frac{\partial u_i}{\partial x_j} + \frac{\partial u_j}{\partial x_i} \right) - \frac{2}{3} \frac{\partial u_i}{\partial x_i} \delta. \quad (3)$$

(3) The energy equation:

$$\frac{\partial(\rho T)}{\partial t} + \text{div}(\rho u T) = \text{div} \left(\frac{\lambda}{c} \text{grad } T \right) + S_T. \quad (4)$$

Taken as the microelement at the interface, which is assumed that its physical parameters are equal, the equation of heat conduction can be expressed by the following formula [18]:

$$\frac{\partial T}{\partial t} = \frac{\lambda}{\rho c} \left(\frac{\partial^2 T}{\partial x^2} + \frac{\partial^2 T}{\partial y^2} \right), \quad (5)$$

wherein T is the temperature, t is the time, λ is the thermal conductivity, c represents the heat capacity at constant pressure, and S_T is viscous dissipation term.

In this paper, the liquid phase is the main phase, and the volume fraction of liquid phase is obtained by the following equation:

$$\varphi_L = 1 - \varphi_G, \quad (6)$$

wherein φ_L is the volume fraction of liquid phase; φ_G is the volume fraction of gas phase. And φ_G is obtained by the following formula:

$$\frac{\partial}{\partial t}(\rho_g \varphi_g) + \Delta(\rho_g \varphi_g u_g) = 0. \quad (7)$$

The computational model shown in Figure 1 is divided into unstructured meshes. After completing the grid independence check, the total number of grids adopted was 21980. In this paper, Ansys16.0 Fluent is used to solve the model control equation. Initially, the left boundary temperature is 300 K, the right boundary using the first type of boundary conditions is 300 K constantly, and the upper and lower boundaries are set to be adiabatic and solid boundary.

The UDF file on the left border was imported with a period of 5100 s and a sine temperature waveform with an amplitude of 100 K. The simulation parameters used in this paper are given in Table 1, and assume that these parameters do not change with temperature. Because the scale of the model is very small, the internal gas-liquid two-phase flow belongs to the typical confined laminar flow; therefore, the basic laminar flow model is used in the simulation, and the pressure field and velocity field are coupled in the solution. The PISO method is introduced, which includes the near correction and the skewness correction. In this paper, the residual convergence criterion of each parameter in the flow field is 10^{-5} .

3. Results Analysis

3.1. The Influence of Phase Interface on Heat Flow. The existence of phase interface changes the direction of propagation of temperature. Initially, the temperature gradient in the Y direction is almost zero, and the isotherm is approximately parallel to the y -axis. When the temperature propagates near the phase interface, as shown in Figures 2(a)–2(c), there is no temperature change in the flow field without the interface, a temperature gradient in the Y direction is generated near the arc phase interface, and the central normal of phase interface is symmetrical axis and is symmetrically distributed on both sides. In the area near the center of the curved interface, the temperature gradient is not obvious due to the fact that the upper and lower heat flows are almost simultaneous. In contrast to Figures 2(b) and 2(c), it can be found that the direction of the temperature gradient is related to the thermal conductivity of the gas-liquid two phases. When the thermal conductivity of the liquid phase is greater than that of the gas phase, the direction of the temperature gradient is outward. When the thermal conductivity of the liquid phase is less than that of the gas phase, the direction of the temperature gradient is inward.

The propagation of thermal waves is similar to that of electromagnetic waves, when passing through propagation medium of different density, both the reflection and the refraction occur, the ratios of reflection and refraction are determined by the thermal conductivity of the two phases. Similar to the Kirchhoff law, heat flow always flows in the direction of less thermal resistance. When the heat flow passes through the phase interface, its orientation is related to the relative thermal conductivity of the internal and external materials at the interphase interface and always tends to the material with large thermal conductivity. Figures 3(a) and 3(b) are corresponding to physical parameters of Figures 2(b) and 2(c), respectively. In combination with Figures 2 and 3, it is found that when the thermal conductivity of the gas is less than that of the liquid phase, the temperature gradient near the interface is outward and the heat flow passes through the gas slug inward. When the thermal conductivity of the gas is larger than that of the liquid phase, the temperature gradient near the interface is inward, and the heat flow passes around the gas slug outward.

3.2. Influence of Phase Interface on Phase and Amplitude of Temperature Wave

3.2.1. Influence of Phase Interface on Temperature Wave Phase. The attenuation degree of temperature wave is different in the different area of gas-liquid, and the change of the temperature wave phase may advance or lag. When the period of temperature wave is large, the change of the temperature wave is not obvious in the informal state, whether it changes its physical parameter or position coordinate, and the phase of all the positions in the computational domain is almost the same. When the period of the temperature wave is small, the apparent irregular state can be seen, and the phases in different positions of the computational domain are obviously different.

For the sake of study, the abscissa of the case b in Figure 4(a) is reduced by a factor of 15, the periods of case b and case e are 100 s and 5 s, respectively. In Figure 4, A-I represents the case A of position I. As shown in case e, by comparing curves e-1 and e-2, it can be found that the phase lag of the temperature wave in the gas phase is about 20% along the x -axis, the time after reaching the highest temperature is delayed, and the amplitude of the temperature wave is also reduced by 30%.

Figure 4(b) shows the change of the phase of the temperature wave with or without phase interface. Case e and case I are selected, y is -0.5 mm, and the values of x were different (as shown in the model 1, 2, and 3 points). It can be seen from the figure that the presence of the phase interface changes the phase of the temperature wave. Compared with several sets of curves, it is found that the phase of the curve without phase interface is ahead of the temperature wave curve with phase interface before the temperature wave propagates to the phase interface. With the increase of the x -coordinate, the temperature wave with phase interface will gradually advance the temperature wave without phase interface. This is mainly because the thermal diffusion coefficient of the liquid phase is substantially the same in the front of the gas slug, but the obstruction of the gas slug causes the heat flow in the local area close to the phase interface to be reduced. Therefore, the temperature of this region peaks faster than that of the region with the phase interface. Behind the phase interface, the thermal diffusivity of gas is greater than the liquid, so the change of the temperature of the gas phase is faster than that of the liquid phase, resulting in the temperature of the region with phase interface peaks faster than that of the region without the phase interface. The phase advance and hysteresis have great influence on the propagation of temperature. This is because the process of starting and running of the whole heat pipe has always been the alternate change of gas-liquid phase. The existence of phase interface is bound to affect the speed of temperature propagation.

3.2.2. Influence of Phase Interface on the Amplitude of Temperature Wave. It is significant to understand the change of the temperature of the gas-liquid two-phase working fluid in the heat pipe by studying the attenuation of the temperature wave when the temperature of the outer wall of the heat pipe changes. Figure 5 shows the attenuation curve of the

TABLE 1: Physical property of input temperature wave under different working conditions.

Period	$\lambda_{\text{gas}} (\text{W/m} \cdot ^\circ\text{C})$	$\lambda_{\text{liquid}} (\text{W/m} \cdot ^\circ\text{C})$	$\rho_{\text{liquid}} (\text{g/m}^3)$	$C_{\text{gas}} (\text{J/kg} \cdot \text{K})$	$\rho_{\text{gas}} (\text{g/m}^3)$	$C_{\text{liquid}} (\text{J/kg} \cdot \text{K})$	Curvature (m^{-1})	Thermal		Case	$\lambda\Delta$	$A\Delta_{\text{liquid}} (\text{K})$	$A\Delta_{\text{gas}} (\text{K})$	Positive heat flux peak (W/m^2)	Negative heat flux peak (W/m^2)
								diffusion coefficient of gas (m^2/s)	diffusion coefficient of liquid (m^2/s)						
100	2.42	6	1	418	200	1006.43	0.2	1.20227E-05	0.014354067	a	2.479339	-76.9401	-118.4243	537262	-3421
100	0.0242	0.6	1000	4182	1.225	1006.43	0.2	1.96289E-05	1.43472E-07	b	24.79339	-54.1293	-136.5001	53319	-6358
100	0.0242	0.06	100	4182	1.225	1006.43	0.2	1.96289E-05	1.43472E-07	c	2.479339	-77.3138	-118.6228	—	—
100	0.0242	0.06	1000	4182	1.225	1006.43	0.2	1.96289E-05	1.43472E-07	d	2.479339	-77.3147	-118.6212	—	—
5	0.0242	0.6	1000	4182	1.225	1006.43	0.2	4.72384E-05	1.43472E-07	e	24.79339	-69.4986	-140.8545	207836	-145931
100	242	0.6	1000	4182	1.225	1006.43	0.2	0.196288883	1.43472E-07	f	0.002479	-181.6578	-44.4312	—	—
100	0.242	0.6	998.2	4182	1.225	1006.43	0.2	0.000196289	1.43472E-07	g	2.479339	-77.2963	-118.6027	—	—
100	0.242	0.6	1000	4182	1.225	1006.43	0.2	0.000196289	1.43472E-07	h	2.479339	-77.2933	-118.5876	59011	-5426
100	2.42	0.6	1000	4182	1.225	1006.43	0.2	0.000196289	1.43472E-07	i	0.247934	-142.0084	-69.1189	76499	-4367
100	0.0242	0.6	1000	4182	1.225	1006.43	0.2	4.72384E-06	1.43472E-07	i	24.79339	-100.7039	-100.0572	66164	-6202
15	0.0242	0.6	1000	4182	1.225	1006.43	0.2	4.72384E-06	1.43472E-07	k	24.79339	-61.4455	-141.9224	122696	-74977
5	0.0242	0.6	1000	4182	1.225	1006.43	0.2	4.72384E-06	1.43472E-07	l	24.79339	-92.7734	-85.5599	—	—

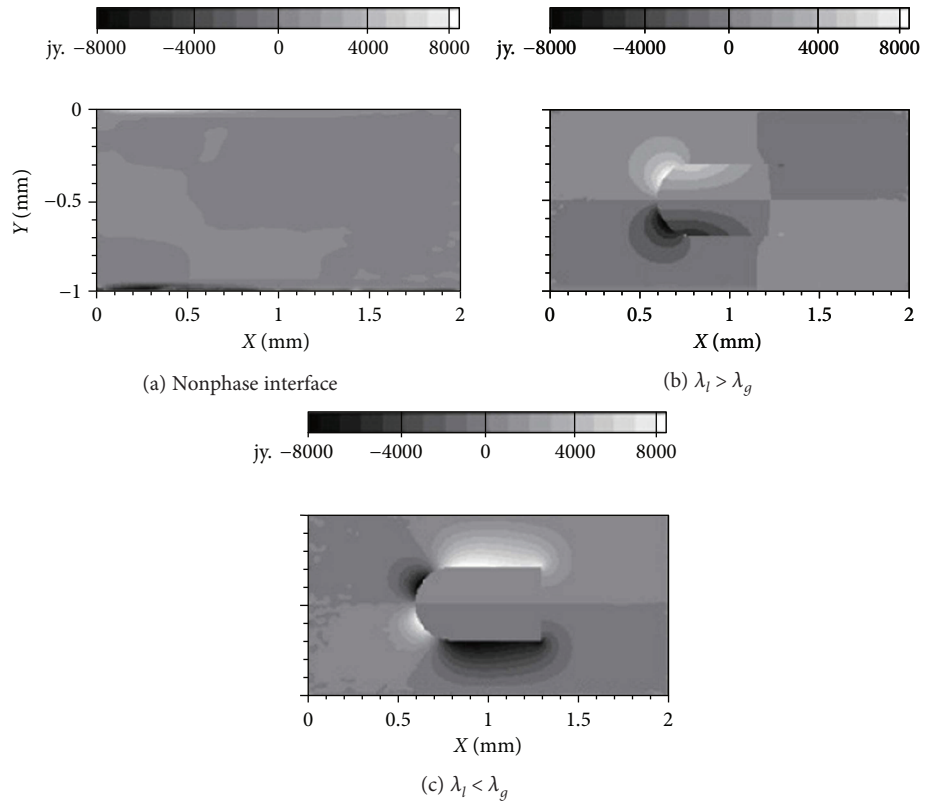


FIGURE 2: Temperature gradient diagram of Y direction with or without phase interface.

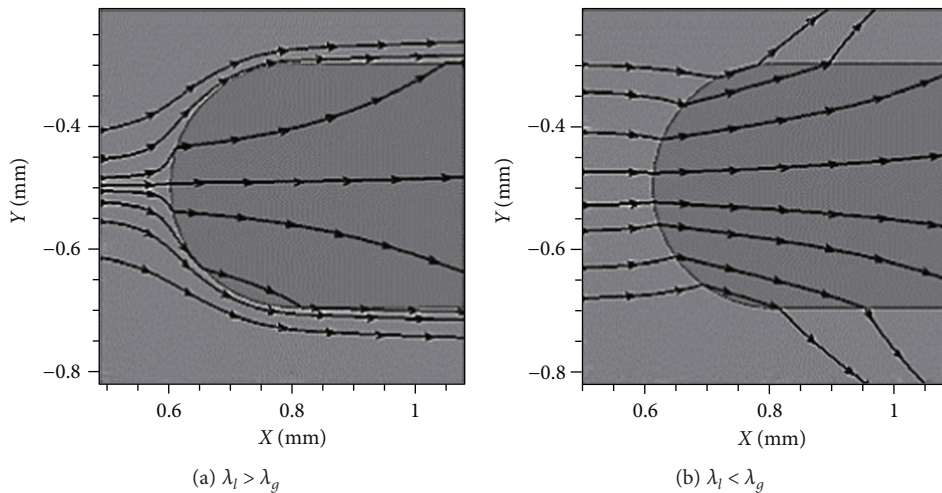


FIGURE 3: Vector diagram of heat flow through a phase interface (the light-colored area is the liquid phase, and the dark area is the gas phase).

amplitude of the temperature wave on the axis of the air plug in different working conditions. It can be found that the curvature of the curve will change obviously near the position of the phase interface, and this position is located in the front of the interface. Before and after the curvature changes, the temperature wave in each condition attenuates by approximately equal attenuation coefficient. In the gas phase section, since the heat flow is no longer propagating in the original direction, the attenuation coefficient of the gas phase section is significantly smaller than the temperature attenuation

coefficient of the liquid phase section, regardless of whether the thermal conductivity of the gas phase is larger or smaller than that of the liquid phase. At the same time, it can be seen from Figure 5 that the attenuation coefficient of case b is the smallest and the attenuation coefficient of the case f is the largest. However, the attenuation curves of a, c, d, and k are almost coincident. Combined with Table 1, it can be concluded that the temperature attenuation coefficient has nothing to do with the density and the heat capacity of the material and is also not significantly related to the value of

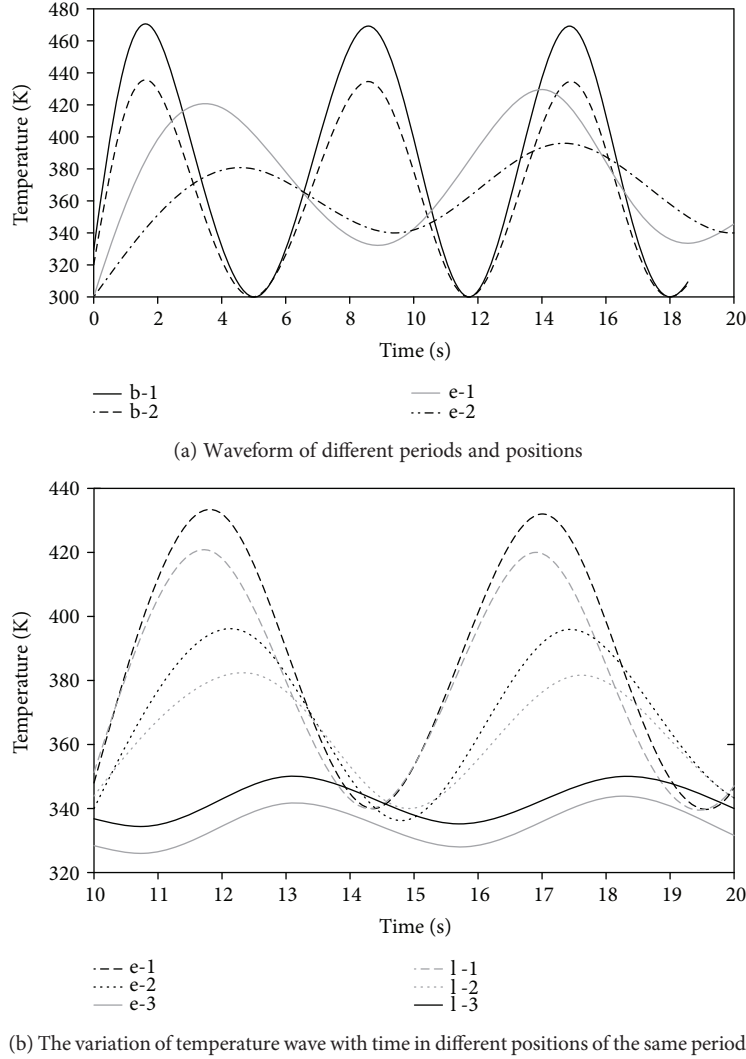


FIGURE 4: Curves of waveform versus time.

the thermal conductivity of the material, considering that the difference in thermal conductivity could lead to the direction of the heat flow change at the phase interface. There defines a new variable $\lambda_{\Delta} = \lambda_l / \lambda_g$ which is used to investigate the attenuation of a temperature wave in a heat pipe. Table 1 shows the λ_{Δ} and A_{Δ} for some of the conditions. As can be seen from the table, A_{Δ} and λ_{Δ} are significantly related. Before the attenuation coefficient changes, the correlation coefficient of the two variables can be calculated by the correlation formula:

$$\rho_{\lambda_{\Delta}, A_{\Delta}} = \frac{\text{COV}(\lambda_{\Delta}, A_{\Delta})}{\sqrt{D(\lambda_{\Delta})} \sqrt{D(A_{\Delta})}}, \quad (8)$$

wherein $\text{COV}(\lambda_{\Delta}, A_{\Delta})$ is the covariance of λ_{Δ} and A_{Δ} and $\sqrt{D(\lambda_{\Delta})}$ and $\sqrt{D(A_{\Delta})}$ are the mean square deviations of λ_{Δ} and A_{Δ} , respectively. Substituting the experimental data can obtain that the correlations in the liquid phase area are 0.6414 and 0.673, respectively, which is strongly correlated.

After the curvature changes obviously, the correlation coefficient becomes -0.6714 , but it remains strong correlation. As the experimental data increases, the correlation coefficient will be closer to 1. Then, it is found that A_{Δ} and λ_{Δ} are approximately logarithmic function by fitting the two sets of data, and the confidence of the fitting is 97%. In the liquid phase section, the base number of logarithm is less than 1, and in the gas phase section, the logarithmic base is greater than 1, the relationship between the specific function as follows:

$$\begin{aligned} A_{\Delta} &= 4.989 \times \log_{3/2}(x) + 97.97 \text{ (gas)}, \\ A_{\Delta} &= 5.625 \times \log_{2/3}(x) + 99.68 \text{ (liquid)}. \end{aligned} \quad (9)$$

Figure 6 is a curve of the attenuation coefficient of the gas phase and the liquid region with the coefficient of thermal conductivity. In the liquid region, the attenuation coefficient A_{Δ} decreases with the increase of liquid-gas ratio λ_{Δ} , and the rate of change is gradually reduced, finally stabilized near a

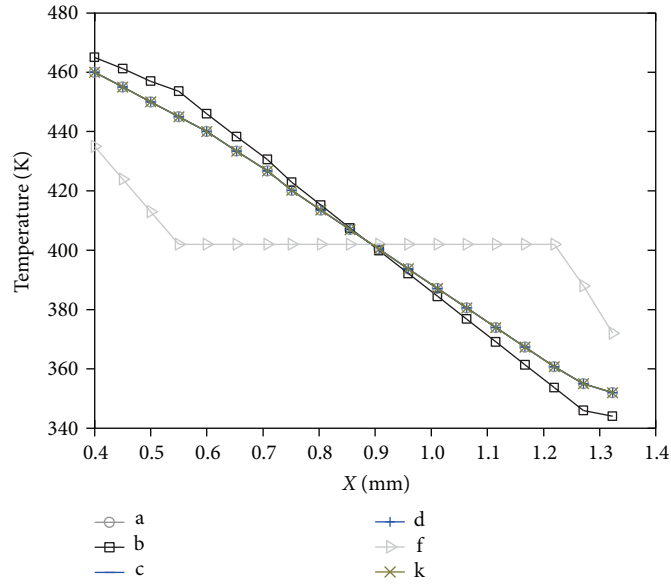


FIGURE 5: Attenuation curve of temperature wave on the central axis of gas slug under different working conditions (the two vertical dashed lines whose location is 0.6 mm and 1.3 mm, resp., indicate the phase interface positions).

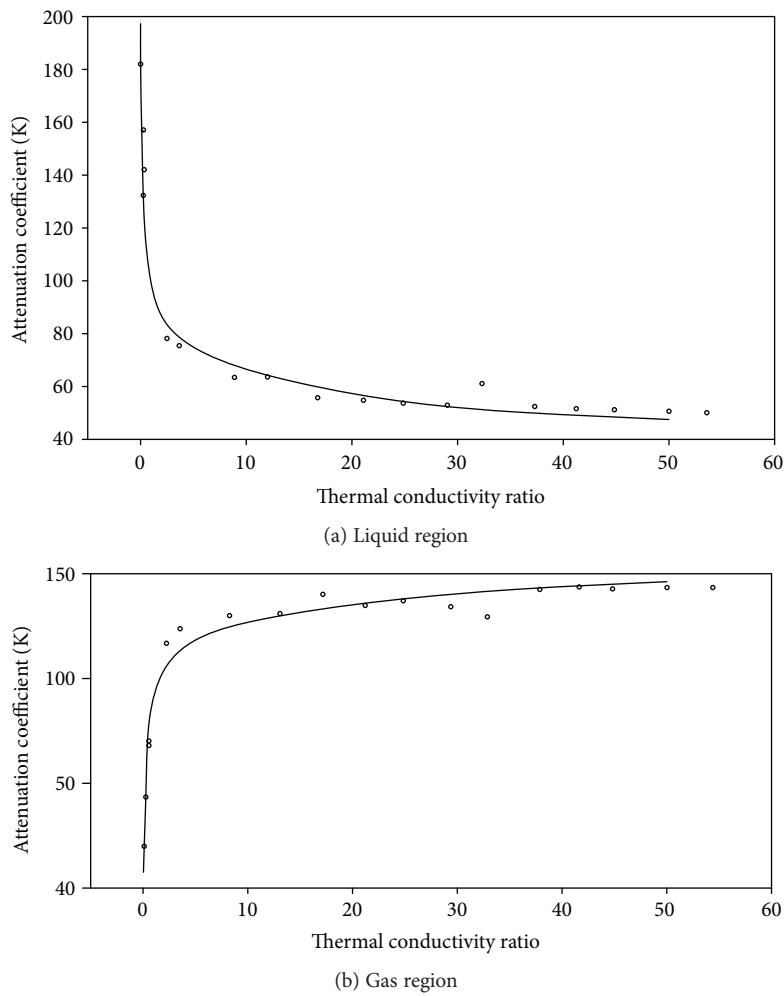


FIGURE 6: Curve of attenuation coefficient versus thermal conductivity ratio.

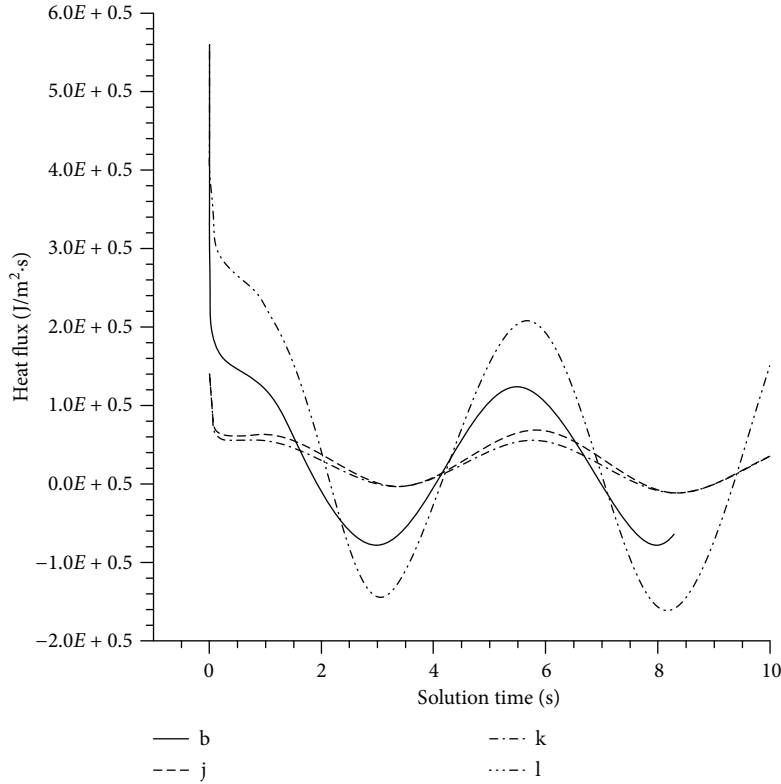


FIGURE 7: The variation of heat flux with time under different frequencies.

certain value, which is stable near 52 K in this simulation. However, in the gas region, the attenuation coefficient increases with the increase of λ_{Δ} . Similar to the liquid section, the A_{Δ} eventually stabilized near 142 K.

3.2.3. Influence of Phase Interface on Heat Flux Density. The heat flux is an important indicator of the working state of the heat pipe, and the effect of the phase interface on the heat flux is directly related to the normal and efficient operation of the PHP. Near the left wall, the heat flux is almost equal; therefore, a point near the centerline of the left wall is used to characterize the heat flow in the whole flow field. Figure 7 shows the variation of the heat flux with time under different frequency conditions. Because there mainly research the influence of negative heat flux and in order to make a more intuitive comparison, the abscissa of the period 100 s and 15 s is reduced by 10 times and 3 times, respectively. It can be found that due to the delay of the internal temperature change, the heat flow in the opposite direction will occur when the wall temperature drops, which is detrimental to the work of the PHP. By comparing case b and case j, it can be found that the presence of phase interface makes this situation more serious and will also decrease the heat flow peak in the positive direction. By comparing the temperature and heat flux curves at different frequencies, the higher the frequency is, the higher the peak values of heat flow in the positive and negative directions are. There defines a parameter Φ to measure the intensity of the opposite direction heat flux density. And the greater the absolute value of Φ is, the

greater the intensity of the opposite direction heat flux density is. Φ is defined as follows:

$$\Phi = \frac{q_2}{q_1 - q_2}, \quad (10)$$

wherein q_1 is the heat flux density of positive direction and q_2 is the heat flux density of opposite direction. Under the same conditions of other physical parameters, when the periods are 5 s, 15 s, and 100 s, the values of Φ are -2.35 , -1.571 , and -0.13539 , respectively. It can be found that the frequency of temperature change is high, which is unfavorable to heat pipe heat transfer, that is in line with Kim's research [5]. In the process of starting the heat pipe, the appearance of the two phase is inevitable, so it is necessary to suppress the intensity of the heat flux in the opposite direction.

4. Conclusions

In this paper, the influence of the phase boundary in a pulsating heat pipe on the characteristics of temperature wave is simulated and the following conclusions are obtained:

- (1) The phase interface changes the propagation direction of the temperature gradient. The propagation direction of heat flux is also changed due to the different thermal conductivity of the gas-liquid two phases. When the thermal conductivity of gas phase is greater than that of liquid phase, the temperature gradient is

inward at the phase interface, and the heat flow goes outward to bypass the slug. When the thermal conductivity of the gas phase is smaller than the liquid phase, the opposite is true.

- (2) Because of the blocking effect of the gas slug, the temperature wave causes phase advance or hysteresis near the phase interface. It can be found that the phase lag of the temperature wave in the gas phase is about 20% along the x -axis.
- (3) In the liquid region, the A_{Δ} decreases with the decrease of the λ_{Δ} , and the rate of change is gradually decreased, the A_{Δ} tends to stabilize near 52 K. But in the gas phase, it is just the opposite, and the A_{Δ} tends to stabilize near 142 K eventually.
- (4) Because of the delay of the temperature response in the PHP, the phenomenon of thermal reflux is easy to occur when the temperature changes suddenly. In the process of the operation of the PHP, the phase interface will aggravate this phenomenon. And with the increase of the frequency of temperature change, the greater the heat flux in the negative direction is, the worse the heat transfer effect becomes.

Conflicts of Interest

The authors declare that there is no conflict of interest regarding the publication of this paper.

Authors' Contributions

Professor Ying Zhang is the first author.

Acknowledgments

This paper is supported by the National Natural Science Foundation of China (11562011).

References

- [1] D. Haiyan and H. Guo, "Application of heat pipe in solar water heater," *Chemical Progress*, vol. 3, pp. 390–394, 2008.
- [2] Z. Deng, Y. Zheng, X. Liu, B. Zhu, and Y. Chen, "Experimental study on thermal performance of an anti-gravity pulsating heat pipe and its application on heat recovery utilization," *Applied Thermal Engineering*, vol. 125, pp. 1368–1378, 2017.
- [3] C. Chuanbao, "Oscillating heat pipe research and its application in solar collectors," *North China Electric Power University*, 2009.
- [4] J. L. Xu, Y. X. Li, and T. N. Wong, "High speed flow visualization of a closed loop pulsating heat pipe," *International Journal of Heat and Mass Transfer*, vol. 48, no. 16, pp. 3338–3351, 2005.
- [5] K. S. Kim, M. H. Won, J. W. Kim, and B. J. Back, "Heat pipe cooling technology for desktop PC CPU," *Applied Thermal Engineering*, vol. 23, no. 9, pp. 1137–1144, 2003.
- [6] K. Gi, S. Maezawa, Y. Kojima, and N. Yamazaki, "CPU cooling of notebook PC by oscillating heat pipe," in *Proceedings of 11th International Heat Pipe Conference*, pp. 166–169, Tokyo, Japan, 1999.
- [7] Q. Huang, "Experimental study on the startup performance of solar heat pipe," *Beijing University of Technology*, 2009.
- [8] L. Jingtao, L. Zhihong, and H. Zhenxing, "Flow pattern and the flow direction analysis of the pulsating heat pipe," *Thermal Power Engineering*, vol. 24, no. 3, pp. 347–351, 2009.
- [9] L. Xiangdong and H. Yingli, "The oscillating heat pipe in closed cycle two-phase flow numerical simulation," *Southeast University*, vol. 39, no. 5, pp. 961–965, 2009.
- [10] W. Jiansheng, W. Zhenchuan, and L. Meijun, "Thermal performance of pulsating heat pipes with different heating patterns," *Applied Thermal Engineering*, vol. 64, no. 1-2, pp. 209–212, 2014.
- [11] H. Tingting, "The effect of hydrophilic and hydrophobic properties on the transmission properties of pulsating heat pipes," *Dalian University of Technology*, 2014.
- [12] S. Kim, Y. Zhang, and J. Choi, "Effects of fluctuations of heating and cooling section temperatures on performance of a pulsating heat pipe," *Applied Thermal Engineering*, vol. 58, no. 1-2, pp. 42–51, 2013.
- [13] T. Hao, X. Ma, Z. Lan, and Y. Zheng, "Experimental study on liquid slug liquid film deposition in superhydrophilic pulsating heat pipe," *Journal of Engineering Thermophysics*, vol. 1, pp. 168–171, 2015.
- [14] Y. Zhang, A. Faghri, and M. B. Shafii, "Analysis of liquid–vapor pulsating flow in a U-shaped miniature tube," *International Journal of Heat and Mass Transfer*, vol. 45, no. 12, pp. 2501–2508, 2002.
- [15] AIAA, "Oscillatory flow in pulsating heat pipes with arbitrary number of turns," *Journal of Thermophysics & Heat Transfer*, vol. 17, no. 3, pp. 340–347, 2003.
- [16] X. Zhang, Z. Ren, and F. Mei, *Heat transfer theory*, vol. 75, China Architecture and Building Press, Beijing, 2007.
- [17] Q. Yueping, S. Huaitao, W. Jiansong, and D. Zhanyuan, "Analysis of the temperature of the surrounding rock periodic boundary finite volume method," *Coal Society*, vol. 40, no. 7, pp. 1541–1549, 2015.
- [18] S. Yang and W. Tao, *Heat Transfer*, Higher Education Press, 2011.

Research Article

Preparation and Thermal Properties of Eutectic Hydrate Salt Phase Change Thermal Energy Storage Material

Lin Liang  and Xi Chen 

School of Electrical and Power Engineering, China University of Mining and Technology, Xuzhou 221116, China

Correspondence should be addressed to Lin Liang; lianglin@cumt.edu.cn

Received 28 July 2017; Accepted 10 January 2018; Published 26 February 2018

Academic Editor: Hamidreza Shabgard

Copyright © 2018 Lin Liang and Xi Chen. This is an open access article distributed under the Creative Commons Attribution License, which permits unrestricted use, distribution, and reproduction in any medium, provided the original work is properly cited.

In this study, a new cold storage phase change material eutectic hydrate salt ($K_2HPO_4 \cdot 3H_2O - NaH_2PO_4 \cdot 2H_2O - Na_2S_2O_3 \cdot 5H_2O$) was prepared, modified, and tested. The modification was performed by adding a nucleating agent and thickener. The physical properties such as viscosity, surface tension, cold storage characteristics, supercooling, and the stability during freeze-thaw cycles were studied. Results show that the use of nucleating agents, such as sodium tetraborate, sodium fluoride, and nanoparticles, are effective. The solidification temperature and latent heat of these materials which was added with 0, 3, and 5 wt% thickeners were -11.9 , -10.6 , and $-14.8^\circ C$ and 127.2, 118.6, 82.56 J/g, respectively. Adding a nucleating agent can effectively improve the nucleation rate and nucleation stability. Furthermore, increasing viscosity has a positive impact on the solidification rate, supercooling, and the stability during freeze-thaw cycles.

1. Introduction

The development of cities is accompanied by huge energy consumption; people have gradually realized that the energy storage technology has very good ability to improve this situation, which can effectively improve the energy utilization ratio and reduce losses. Phase change material (PCM) is an effective latent heat thermal storage material. It has been widely used as a thermal functional material in thermal and cold energy storage fields, like solar energy storage [1], industrial waste heat utilization [2], building heating and air conditioning [3], thermal management of mobile devices [4], and so on. All of these are aimed at realizing the conversion of energy beyond the restriction of time and space. Thus, the study of PCM is of great significance for energy storage [5]. PCM can be mainly divided into two categories of organic and inorganic. However, organic PCMs such as paraffin wax [6] and some organic compounds [7] are poor in low thermal conductivity and have flammability, which greatly limits the application of PCMs [8]. Therefore, the study of inorganic PCM has attracted much attention of researchers.

Salt hydrates [8] as an inorganic PCM have an advantage in higher heat storage capacity, suitable cold storage temperature [9], nonflammable, and so on. Thus, it would be more suitable and safer than organic PCM in energy storage application especially cryogenic storage. The traditional ice storage and water storage cannot reach the temperature of low-temperature cold storage. The temperature requirement of low cold storage is between -20 and $-30^\circ C$, and the high-temperature cold storage is between 0 and $4^\circ C$. However, the ice storage and water storage systems can only reach $0^\circ C$, which cannot meet requirements of low-temperature application. Adding inorganic salts in the water can ensure that the amount of phase change latent heat almost unchanged and reduce the phase change temperature of cool storage material at the same time. Compound salts can not only further reduce the melting point of solidification but also optimize and modify the overall physical properties of certain materials. Many researchers have studied the compounded eutectic hydrate salt to achieve more suitable phase change temperature and better cold storage performance. Li et al. [10] have studied the preparation, characterization, and modification of a new phase change material $CaCl_2 \cdot 6H_2O - MgCl_2 \cdot 6H_2O$ eutectic

hydrate salt. As a result, its phase change temperature and latent heat are 21.4°C and 102.3 J/g, respectively. Liu et al. [11] studied the energy storage characteristics of a novel binary hydrated salt by means of SEM, XRD, and DSC techniques. It was concluded that the phase transition temperature was 27.3°C, the degree of supercooling was 3.67°C, and the enthalpy of phase transition was 220.2 J/g. Efimova et al. [12] proposed a ternary hydrated salt mixture suitable for use in air conditioning systems and carried out the thermal analysis. It was concluded that the material has a melting temperature of 18–21°C and an enthalpy of fusion of 110 kJ/kg. However, different from organic PCM [13], inorganic PCM such as salt hydrates has a significant supercooling [14, 15] and relatively poor stability, which greatly limit the life of phase change material and energy storage performance. In general, methods that can be used to effectively enhance the stability of the material are additions of the thickener [16], nucleating agent [17, 18], microencapsulation [19] or nanocomposite modification [20], and so on. Tyagi [21] et al. studied the supercooling behavior of $\text{CaCl}_2 \cdot 6\text{H}_2\text{O}$ and the effect of pH value, which indicates that the supercooling of PCM can be removed or decreased by adjusting the pH value. Bilen et al. [22] studied the modification of $\text{CaCl}_2 \cdot 6\text{H}_2\text{O}$ PCM system and selected different nucleating agents. Pilar et al. [23] used SrCO_3 and $\text{Sr}(\text{OH})_2$ as nucleating agents for $\text{MgCl}_2 \cdot 6\text{H}_2\text{O}$; the results show that the addition of 1 wt% SrCO_3 and 0.5 wt% $\text{Sr}(\text{OH})_2$ almost fully suppress the supercooling and improve the performance of this PCM system. For phase separation, Wang et al. [24] studied the thermal stability of a novel eutectic ternary system by placing the salt mixture in an argon atmosphere with a constant heating rate. In order to determine the accurate upper limit of the working temperature of the ternary salt, Sharma et al. [25] used a differential scanning calorimeter to carry out 1500 times melting and freezing cycles to study the changes in thermal properties of thermal energy storage materials. At present, the inorganic salt hydrate phase change cold storage materials have a good application prospect in refrigerator energy-saving field.

It can be seen above that most of the research on hydrated salt cold storage has focused on the development of energy storage materials for air conditioning. There is a lack of research on the energy storage materials with phase change temperature below 0°C. Otherwise, it is a meaningful attempt to study the improvement of supercooling and cycle stability of ternary eutectic system from the point of fluid viscosity and different nucleating agents added. In this paper, firstly, a $\text{K}_2\text{HPO}_4 \cdot 3\text{H}_2\text{O} - \text{NaH}_2\text{PO}_4 \cdot 2\text{H}_2\text{O} - \text{Na}_2\text{S}_2\text{O}_3 \cdot 5\text{H}_2\text{O}$ ternary salt system was prepared, modified, and synthesized. Then the contrast experimental method, step cooling method, and DSC technology were proceeded to investigate the thermal storage property and solidification behavior of eutectic hydrate when adding different amounts of nucleating agent and thickener.

2. Materials and Experimental Methods

2.1. Preparation of Hydrated Salt-Based PCMs. Preparation of hydrated salt phase change material (HSPCM) is the major key step to ensure the performance of PCM in cold storage

application. The proper mixing and stabilization are required in order to achieve stable HSPCM. In the present study, deionized water (DI water) as the base PCM; sodium dihydrogen phosphate dihydrate, dipotassium hydrogen phosphate trihydrate, and sodium thiosulfate pentahydrate as hydrated salts; nanoactivated carbon, sodium tetraborate, and sodium fluoride as nucleating agents; polyethylene glycol 400 as a dispersant; and sodium alginate as a thickener were used to prepare the HSPCM. The used materials are listed in Table 1. After a large number of experimental analysis, the hydrated salts with the same mass ratio (6 wt%) were mixed with DI water by a magnetic stirrer (MVP22-1) for 10 min to make the mixed solution system uniform. Before using the nanoparticle as a nucleating agent, the solution needs to be adjusted to weak alkaline by 10 wt% NaOH, followed by being mixed with nanoparticles and dispersant through magnetic stirring for 10 min. Afterwards, this mixture was ultrasonicated for 60 min at a frequency of 40 kHz and another 20 min stirring to make the nanoparticles dispersed as evenly as possible. The preparation process of nanocomposite hydrated salts is shown in Figure 1. The nanocomposite fluid can be considered accessible when it is observed that the formulated nanofluid undergoes no visual sedimentation over time.

2.2. Experimental Setup. Table 2 shows the uncertainty to measure results caused by experimental equipment. Figure 2 shows the schematic of the experimental setup to conduct the studies during the solidification of the HSPCM. The cooling chamber of 0.108 m³ has the cooling ability to freeze 5 kg reagent from 25°C to -18°C in 24 hours. In the first experiment, the temperatures were measured by the armored thermocouple (T-Type) floating at the same location in the containers filled with reagents. The signal of temperature was monitored continuously for every 10 s, and the experiment was continued until the PCM completely solidified. When measuring the percentage of solidification, three samples of different viscosity were put in a square container with a small thickness. On the upper surface, the square container was divided into a grid scale, and then the three samples were put into the cooling bath during the first trial. The solidified mass was calculated by observing the grid value change of the solid area from the initial state of the liquid PCMs. The thermal properties of eutectic mixtures were obtained by using a differential scanning calorimeter (DSC, NETZSCH 200F3). The surface tension was tested by a surface tension meter (BZY-1). The step cooling analysis method was employed to examine the values of supercooling. In addition, the thermal stability was measured by the freeze-thaw cycles test, which was performed in three containers with a volume of 150 ml. The hydrated salt PCM mixture was cycled repeatedly through 20, 30, and 50 times within a freezer. Temperature data acquisition system was used to study the supercooling change after several freeze-thaw processes. The weighing of drug used a high precision electronic balance with an accuracy of ±0.002 g. All the armored thermocouples are connected to a data logger of Agilent 34970A to store the continuous data generated during the experiments.

TABLE 1: Experimental materials.

Experimental materials	Purity	Application
Sodium dihydrogen phosphate dihydrate ($\text{NaH}_2\text{PO}_4 \cdot 2\text{H}_2\text{O}$)	AR	Hydrated salt
Sodium alginate	CP	Thickener
Sodium thiosulfate pentahydrate ($\text{Na}_2\text{S}_2\text{O}_3 \cdot 5\text{H}_2\text{O}$)	AR	Hydrated salt
Dipotassium hydrogen phosphate trihydrate phosphate ($\text{K}_2\text{HPO}_4 \cdot 3\text{H}_2\text{O}$)	AR	Hydrated salt
Nanoactivated carbon (100 nm, heat treatment)	AR	Nucleating agent
Sodium tetraborate	AR	Nucleating agent
Polyethylene glycol 400	AR	Dispersant
Sodium fluoride	AR	Nucleating agent

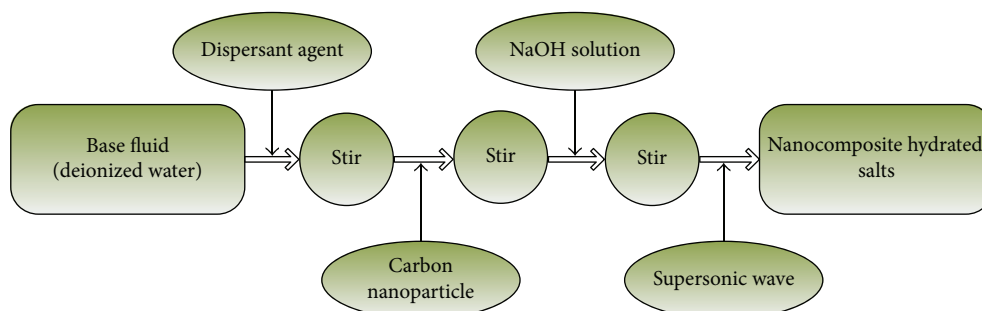


FIGURE 1: Nanocomposite PCM preparation flow chart.

TABLE 2: Result uncertainty analysis of experimental equipment.

Measured quantities	Deviation
Latent heat	± 6 kJ/kg
Mass	± 0.002 g
Temperature data logger	$\pm 0.06\%$
Volume (10 ml, 20 ml)	± 0.06 ml
Volume (100 ml)	± 0.02 ml
Thermocouple	$\pm 1.0\%$
Surface tension	± 0.01 mN/m
Viscosity	$\pm 2\%$ mps

3. Results and Discussion

3.1. The Thermal Performance of Salt Hydrate PCM. In order to assess the effect of thickener concentration on onset/end temperature and phase change heat absorption capacity during the phase change process, the thermal analysis was conducted in different cases of 0, 3, and 5 wt% sodium alginates, while the latent heat of melting process and onset/end temperature was measured with a differential scanning calorimeter (DSC), using measuring temperature range from -25 to 5°C and constant heating rates of $2\text{ K}\cdot\text{min}^{-1}$. In the process of measurement, the temperature of the material rises constantly, and the heat flux of the sample was measured continuously. The heat flux is proportional to the instantaneous specific heat of the material. Melting phase change enthalpy was calculated through the area of the

endothermic peak in the DSC picture. In addition, the specific heat, heating rate (dH_m/dt), phase change enthalpy, and specific heat satisfy certain relationships as follows:

$$\frac{dH_m}{dt} = m \cdot C_p \cdot \frac{dT}{dt}, \quad (1)$$

$$C_p = \frac{H_p}{\Delta t},$$

where H_m , H_p , C_p , m , T , and Δt represent the heat flux, melting phase change enthalpy, specific heat, sample mass, and the temperature difference, respectively, between the beginning and end of the melting process and time interval.

Figure 3 shows the DSC heat absorption curves of three eutectic hydrate salt nitrates with 0, 3, and 5 wt% thickeners separately. It is obviously seen that the onset and end temperature of the absorption peak become higher with the increase of the viscosity when the mass fraction is 3%. After that, with more thickener added, there is a substantial reduction with the durative increase of the viscosity. Through comparing the three samples, it was easily seen that several microparticles from the industrial sodium alginate scattered in the solution that may have the function of improving the solidification point in the case of low viscosity. However, when the fluid viscosity is increasing, the solidification point decreased adversely; the impact of microparticles gradually disappeared. Furthermore, the height of the absorption peak and the phase change enthalpy reached the maximum without the thickener and gradually decreased after adding the thickener. This is because the fluid viscosity affects the

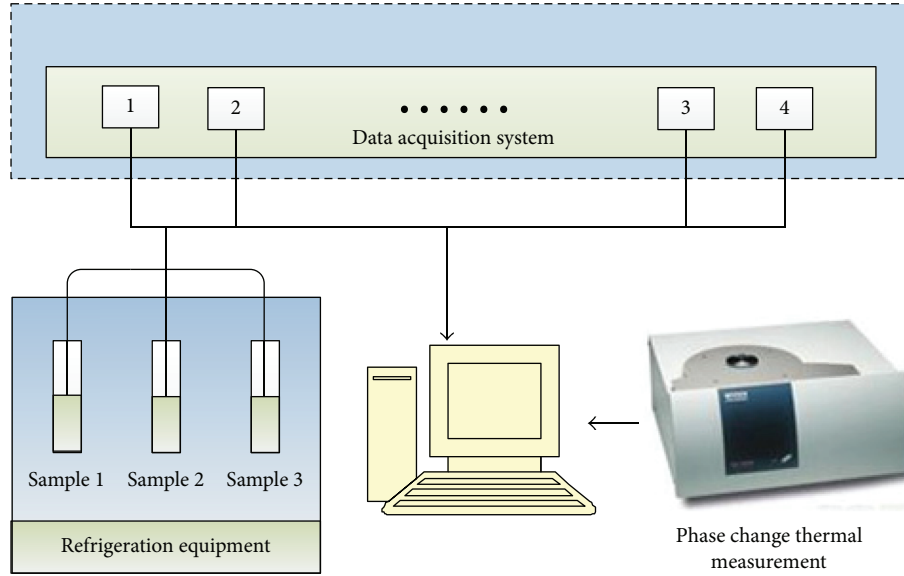


FIGURE 2: Schematic diagram of the experimental system.

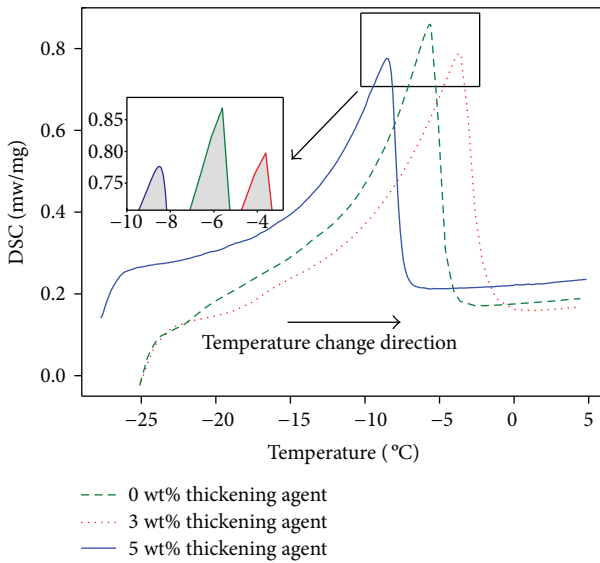


FIGURE 3: DSC curves of eutectic hydrate salt with three different amount of thickening agent.

convective heat transfer performance within the fluid. When the viscosity of the fluid increases, the effect of the microconvection of the fluid and the particles which can enhance heat conduction is gradually suppressed.

From Table 3, it is clearly observed that the onset temperature of the three samples is -11.9 , -10.6 , and -14.8°C while the end temperature is -4.6 , -2.3 , and -7.5°C separately. The peak temperature of the three sample is -5.0 , -2.4 , and -8.3°C in turn. By calculating the DSC phase change area which is divided by the phase change DSC curve and the onset/end baseline, it is concluded that the phase change enthalpies of the three samples are 127.2 , 118.6 , and 82.56J/g , respectively. Compared with similar studies [9], this material has an edge in storage ability.

TABLE 3: DSC measurements.

Data items	Thickener (wt%)		
	0	3	5
Area (J/g)	82.56	118.6	127.2
Peak sample temperature ($^\circ\text{C}$)	-8.3	-2.4	-5.0
Onset temperature ($^\circ\text{C}$)	-14.8	-10.6	-11.9
End temperature ($^\circ\text{C}$)	-7.5	-2.3	-4.6

TABLE 4: Melting latent heat of water and three samples.

Material	Melting latent heat (kJ/kg)
Ice	335
Hydrated salt with 0 wt% thickener added	127.2
Hydrated salt with 3 wt% thickener added	118.6
Hydrated salt with 5 wt% thickener added	82.56

Table 4 shows the melting latent heat change of the three samples with different additions of the thickener. It is not difficult to find that the melting latent heat of cold storage materials was reduced by 62%, 64.6%, and 75.3% as compared with ice. The increase of viscosity will reduce the heat absorption amount, thereby affecting the cold storage ability. Therefore, the thickener needs to be controlled in a suitable amount.

3.2. The Nucleation and Supercooling Characteristics of Hydrated Salt PCM. Supercooling is a process closely related to the crystallization process. Before the temperature returns to the original freezing point, the liquid solidifies below its normal freezing point and continues to decrease until complete solidification. When the degree of supercooling increased, the degree of the deviation from the equilibrium

state has risen, and the critical dimension of the ice core and the formation energy also decrease dramatically, which ultimately increases the probability of forming the nucleus. Calculating the absolute degree of supercooling following relation was used to measure the thermal storage performance of materials:

$$T_{sc} = T_m - T_s, \quad (2)$$

where T_{sc} , T_m , and T_s represent the supercooling degree, melting point, and solidification temperatures, respectively.

The supercooling degree was measured by temperature change curves during the cooling process by putting a thermocouple at the three sample's center separately. During the solidification and crystallization process, the general liquid crystal is divided into the stable region (noncrystalline), substable region, and unstable region as shown below in Figure 4. Crystallization phenomenon only occurred in the unstable area. The viscosity and temperature change of the inorganic hydrated salt are both important factors which affect the nucleation.

Figure 5 shows four hydrated salts of different viscosities without adding the nucleating agent. The three-step cooling curve of ternary hydrate salt solution with different viscosities can be obtained to observe the supercooling. Comparing the four curves, the recovery process after the reduction of the temperature curve gradually decreases during the solidification process with the increase of the viscosity, which can consider that the supercooling is gradually reduced. This is because the increase in liquid viscosity will affect the diffusion of the fluid, reducing the driving force of crystallization, and thus, the supercooling is suppressed. Therefore, increasing the fluid viscosity will not only reduce the latent heat of phase transformation but also improve the stability of the phase transition and reduce the degree of supercooling. When the inorganic PCM is applied to the practical application, the viscosity should be appropriately increased to find a middle value of the best performance.

3.3. The Physical Characteristics of Hydrated Salt PCM. In this experiment, the characteristics of the fluid itself were significantly changed with a constant increase in viscosity. From Table 5, we can find that ternary hydrate salt itself is more viscous than water whose viscosity is 2.04, 6.3, and 8.77 mpa·s, respectively. The viscosity of three solutions with 1.5, 2.5, and 3 wt% nucleating agent added was changed by adding a thickener. Results show that the salt solution with higher viscosity has a relatively lower degree of supercooling.

Figure 6 shows that the degree of supercooling is almost eliminated with the thickener and nucleating agent added simultaneously. It was seen that both the nucleating agent and the thickener have a dampening effect on supercooling. However, the amount of thickener should not be too much; otherwise, the heat capacity will drop dramatically; this is not economical. Therefore, rationally, selecting the amount of nucleating agent and thickener is improving the cold storage performance of inorganic solution better.

Figure 7 shows the mass fraction solidified at various time intervals during the solidification process with 0, 3, and 5 wt% thickeners added, respectively. Solidification time is

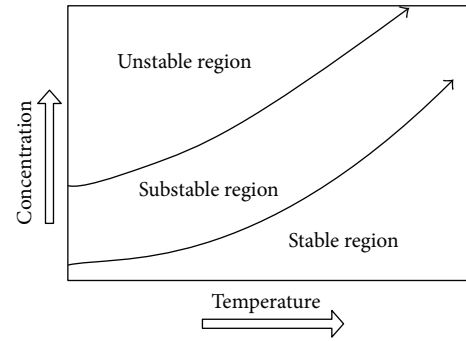


FIGURE 4: Supersaturation and super solubility curves of the solution.

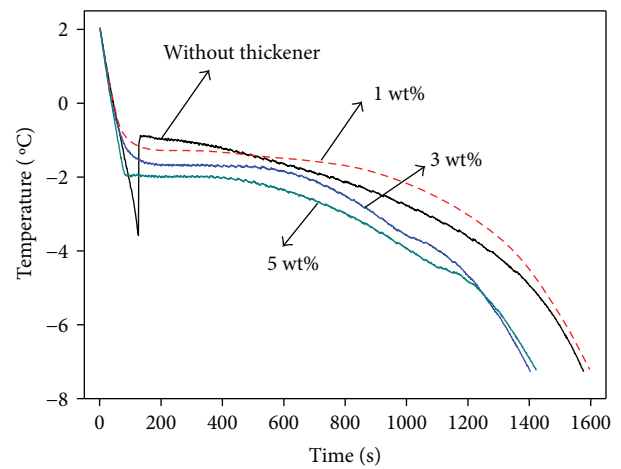


FIGURE 5: Step cooling curves of adding 1, 3, and 5 wt% thickeners in the solution without the nucleating agent.

TABLE 5: Viscosity of water and hydrated salts.

Material	Viscosity (mpa·s)
Ice	1
Hydrated salt with 0 wt% thickener added	2.04
Hydrated salt with 3 wt% thickener added	6.3
Hydrated salt with 5 wt% thickener added	8.77

also an important parameter which was used to measure the response time of a cold storage system. Under the same phase change enthalpy and time, storage medium which reached a higher percentage of solidification earlier has the quality to start next phase change circulation quickly, so as to improve the energy storage efficiency. It has been noted from Figure 7 that the solidification started about 40 minutes later from the start of the experiment and the hydrated salts with 5 wt% thickener appear crystal firstly, followed by the sample with 3 wt% thickener added. The above two samples began to appear crystal almost at the same time, only the sample without thickener crystallized slower which started at about 50–55 minutes. The crystallization rate of the three samples was also different in the solidification process. From

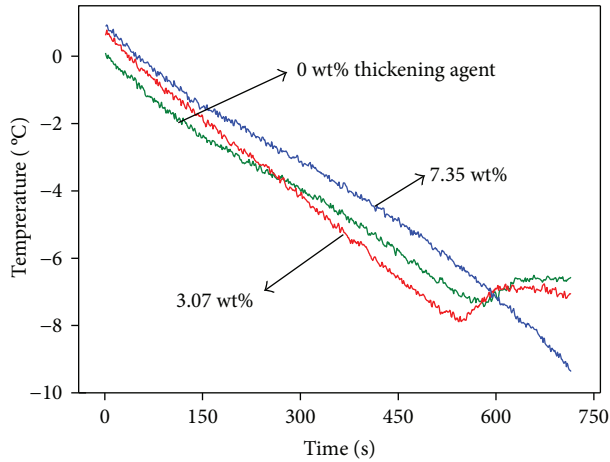


FIGURE 6: Step cooling curves of adding 0, 3.12, and 7.46 wt% thickeners and 2.5 wt% nucleating agent in the solution.

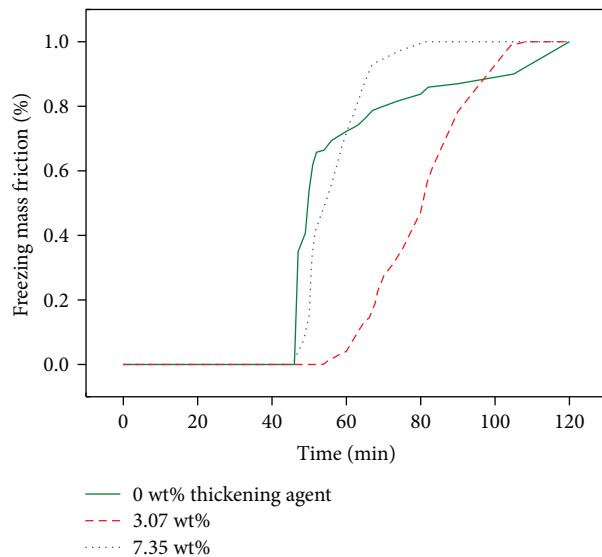


FIGURE 7: Solidification mass fraction curve of three samples with different nucleating agents added.

45 to 50 minutes, the sample with 3 wt% and 5 wt% thickeners added had the similar crystallization rate. However, the crystallization rate of the sample without adding a thickener was obviously slowed down while the rate of the other two samples kept stable all the time. Finally, the time of the complete solidification of these three samples was about 120, 100, and 75 minutes, respectively. It can be concluded that the increase of the viscosity of the cold storage fluid can effectively shorten the time of the complete solidification of the material. This is because the solidified PCM offers increasing thermal resistance between the solidified PCM and the surrounding heat transfer fluid as the freezing front moves away from the surface. From the previous conclusion, it is drawn that viscosity has the same effect on the storage capacity of phase change materials, so the viscosity selection should ensure both the storage capacity and the solidification rate at a right value.

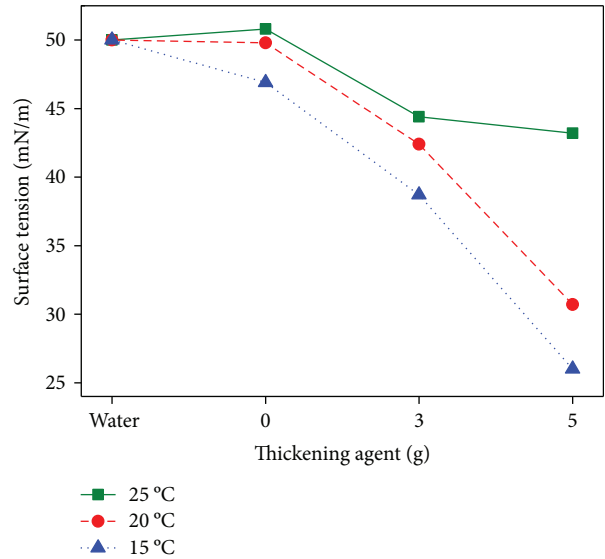


FIGURE 8: Surface tension of three samples within three different temperatures.

The viscosity of the hydrated salt affects not only the internal thermophysical properties of the fluid but also the properties of the fluid surface. Figure 8 shows the variation of surface tension change of hydrated salts and single water. It was found that the surface tension of hydrated salt is lower than that of the water, and the surface tension decreases as the viscosity increases gradually. This is due to the fluid with larger viscosity which has higher surface shrinkage resistance. In addition, the effect of temperature on the surface tension is very obvious; the surface tension decreases with the increase of temperature. This is because the increase of liquid temperature leads to the increase of molecular internal energy and the decrease of interaction force between molecules. Owing to the surface tension which originates from the attraction between molecules on the surface of the liquid, the decrease of attractive force leads to the decrease of surface tension.

3.4. The Influence of Different Nucleating Agents to Hydrated Salt PCM. In the above test, it was found that the supercooling phenomenon is a serious defect of the inorganic phase change material. Through many studies of the nucleation mechanism, it is proved that the supercooling also improved effectively by adding a nucleating agent. According to the crystal nucleation theory, for homogeneous nucleation process, the formation of the crystal needs to be larger than the critical size of the particles, but for heterogeneous nucleation, the surface affinity should also be considered [26]. Nevertheless, the effective crystallization depends on the value of the surface free energy. The aim of adding nucleation agent in the solution is to increase the surface affinity or to reduce the critical dimension so that the surface free energy is reduced. From Figure 9(c), it was discovered that the degree of supercooling ranges from about 3°C to 1.5°C as the mass fraction of $\text{Na}_2\text{B}_4\text{O}_7 \cdot 10\text{H}_2\text{O}$ increases from 1.5 wt% to 3 wt%. Therefore, sodium tetraborate is an ideal agent for

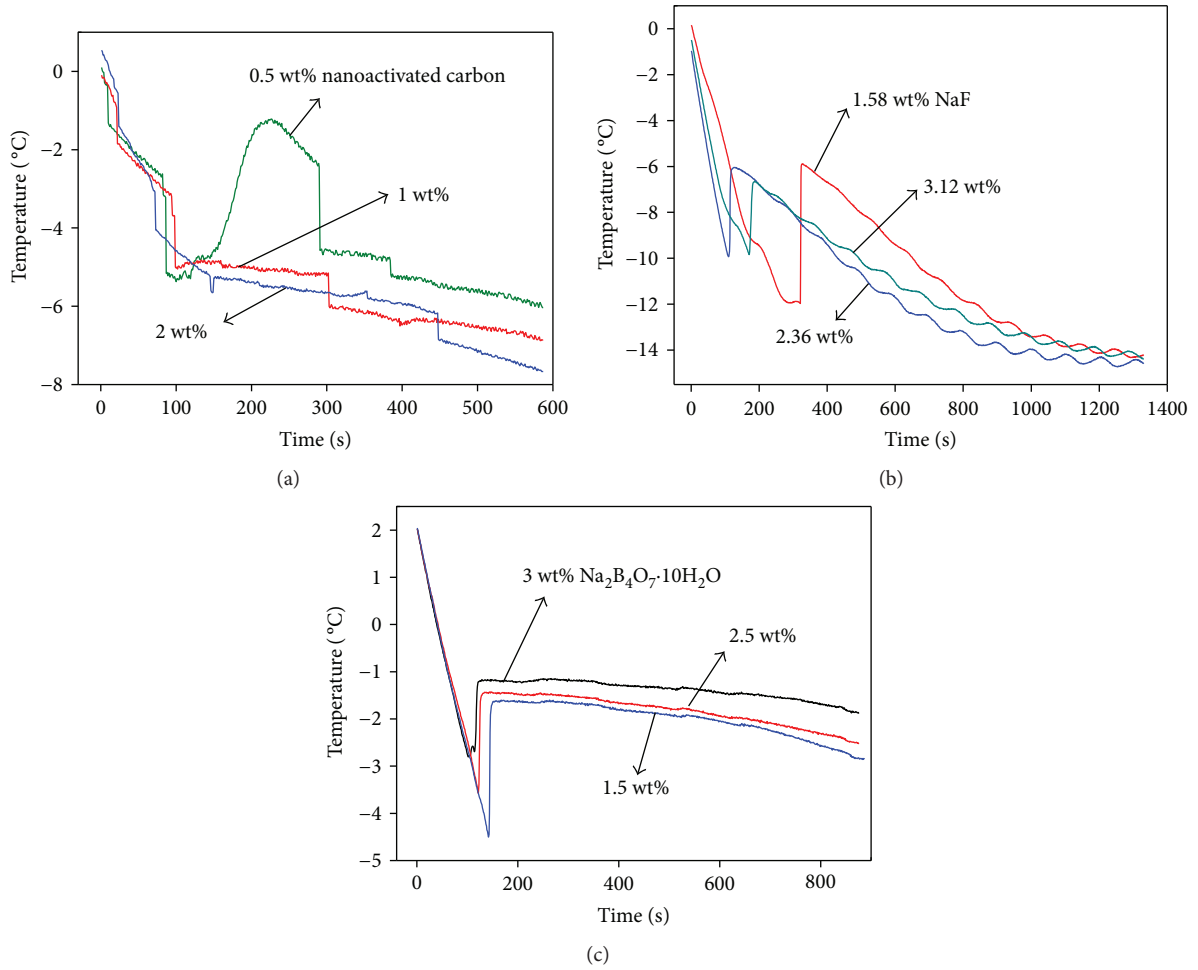


FIGURE 9: (a), (b), and (c) represent step cooling curves of adding three different kinds of nucleating agent (nanoactivated carbon, NaF, and $\text{Na}_2\text{B}_4\text{O}_7 \cdot 10\text{H}_2\text{O}$) in ternary eutectic hydrate salts without a thickener.

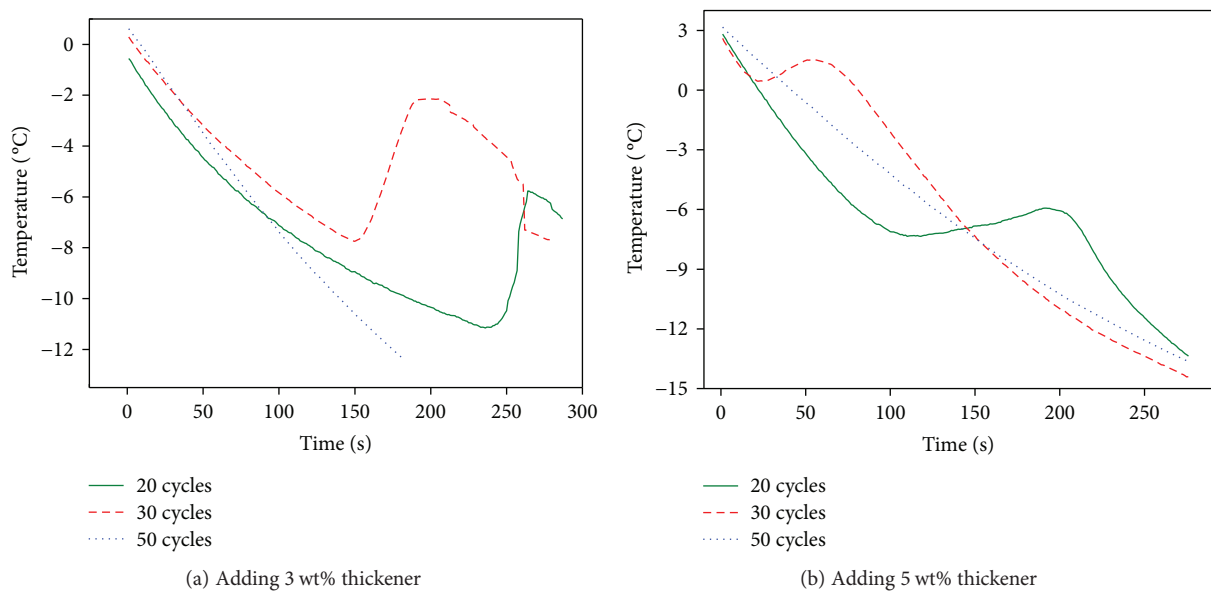


FIGURE 10: (a) and (b) represent the change of step cooling temperature curve after 20, 30, and 50 freeze-thaw cycles.

the inhibition of the supercooling. In order to further study the influence of nucleating agent on inorganic phase change materials, two other nucleating agents were chosen and three different proportioning were selected to add to the HSPCMs. In Figure 9(a), 0.5, 1, and 2 wt% nanoactivated carbon particles with a particle size of 100 nm were separately added into the ternary eutectic hydrate salts. It was seen that the addition of 0.5 wt% particles cannot inhibit the supercooling obviously. With the increase of the content of nanoparticles, the degree of supercooling is almost zero. Through the analysis of Figure 9(b), the amount of nucleating agent NaF added is 1.5, 2.5, and 3 wt%; when the 3 wt% NaF is added, the degree of supercooling is almost half of that of 1.5 wt% and the total supercooling degree is reduced to about 3°C, so the effect is remarkable. Then, increasing the content of the same kind of nucleating agent, the effect almost remains unchanged, compared to the result curve of the three nucleating agents. It is found that an excessive dose of the nucleating agent does little influence to the inhibition of supercooling and these three different nucleating agents all reduced the supercooling significantly. Adding inorganic salt, hydrated salt and nanoparticles all contribute to the nonhomogeneous nucleation.

3.5. Thermal Cycling Test of Hydrated Salt PCM. When using a cold storage material, life span is an important factor to measure the stability. In this experiment, adding a thickener in inorganic hydrated salt is an effective method to enhance the working life of materials and prevent phase separation phenomenon. The salt solution which was added 3 wt% and 5 wt% thickeners still maintained good stability, and there was no obvious phase separation phenomenon. However, a thin layer of crystal at the bottom after about 10 times of freeze-thaw cycles in the salt solution without a thickener appeared. As the freeze-thaw cycles continue, crystal thickness was increased, which severely affected the cold storage characteristics of the salt solution. After stirring or heating, the sample changed back to its initial state and no rapid degradation or irreversibility was observed. Therefore, to avoid the shortcoming of the phase separation mentioned above, the mixture can be stabilized by adding a thickener.

Figure 10 shows that the HSPCMs showed better stability as the number of freeze-thaw cycles increased. The cooling curve changed from an undulating curve into a smooth decline gradually after 50 or more cycles. The performance of the phase change material was more stable, and the supercooling phenomenon will also be reduced gradually. PCM is easier to crystallize than never to solidify due to the residual crystal which is not completely melted during the last process which will reduce the required energy of the next crystallization process during freeze-thaw cycles.

4. Conclusions

This experimental study was conducted on the preparation, modification, and characterization of a new ternary eutectic of inorganic salt hydrate phase change materials with 0, 3, and 5 wt% thickeners added into salt hydrate solution, and the effect of viscosity and nucleating agents on the

thermophysical properties and cold storage ability of PCM was measured by DSC and temperature acquisition system. The results of this study can be summarized as follows:

- (1) The increase of the viscosity will reduce the phase change enthalpy, which reduces the storage capacity. Meanwhile, the phase stability, supercooling, and phase separation will be significantly improved.
- (2) NaF, $\text{Na}_2\text{B}_4\text{O}_7 \cdot 10\text{H}_2\text{O}$, and nanoactivated carbon were all proved to be effective nucleating agents. With the increasing content of a nucleating agent, the degree of cooling can be obviously reduced or even eliminated.
- (3) During the stability test of the inorganic material, the supercooling of inorganic materials will become smaller after 20, 30, and 50 freeze-thaw cycles.

Nomenclature

T_{sc} :	The degree of supercooling
H_m :	Heat flux
H_p :	Melting phase change enthalpy
T_m :	The melting point temperature
T_s :	The freezing point temperature
AR:	Analytically pure reagent
CP:	Chemically pure reagent
DI:	Deionized water
PCM:	Phase change materials
HSPCM:	Hydrated salt-based PCMs
STA:	Simultaneous thermal analyzer
XRD:	X-ray diffraction
DSC:	Differential scanning calorimeter.

Conflicts of Interest

The authors declare that they have no conflicts of interest.

Acknowledgments

This work is financially supported by the Fundamental Research Funds for the Central Universities (Grant no. 2014QNB05).

References

- [1] W. Su, J. Darkwa, and G. Kokogiannakis, "Development of microencapsulated phase change material for solar thermal energy storage," *Applied Thermal Engineering*, vol. 112, pp. 1205–1212, 2017.
- [2] Z. Huang, Z. Luo, X. Gao, X. Fang, Y. Fang, and Z. Zhang, "Investigations on the thermal stability, long-term reliability of LiNO_3/KCl -expanded graphite composite as industrial waste heat storage material and its corrosion properties with metals," *Applied Energy*, vol. 188, pp. 521–528, 2017.
- [3] X. Q. Zhai, X. L. Wang, T. Wang, and R. Z. Wang, "A review on phase change cold storage in air-conditioning system: materials and applications," *Renewable and Sustainable Energy Reviews*, vol. 22, pp. 108–120, 2013.

- [4] C.-V. Hémerly, F. Pra, J.-F. Robin, and P. Marty, "Experimental performances of a battery thermal management system using a phase change material," *Journal of Power Sources*, vol. 270, pp. 349–358, 2014.
- [5] J. P. da Cunha and P. Eames, "Thermal energy storage for low and medium temperature applications using phase change materials – a review," *Applied Energy*, vol. 177, pp. 227–238, 2016.
- [6] R. Yang, H. Xu, and Y. Zhang, "Preparation, physical property and thermal physical property of phase change microcapsule slurry and phase change emulsion," *Solar Energy Materials and Solar Cells*, vol. 80, no. 4, pp. 405–416, 2003.
- [7] S. Behzadi and M. M. Farid, "Long term thermal stability of organic PCMs," *Applied Energy*, vol. 122, pp. 11–16, 2014.
- [8] F. Souayfane, F. Fardoun, and P.-H. Biwole, "Phase change materials (PCM) for cooling applications in buildings: a review," *Energy and Buildings*, vol. 129, pp. 396–431, 2016.
- [9] N. Pflieger, M. Braun, M. Eck, and T. Bauer, "Assessment of novel inorganic storage medium with low melting point," *Energy Procedia*, vol. 69, pp. 988–996, 2015.
- [10] G. Li, B. B. Zhang, X. Li, Y. Zhou, Q. G. Sun, and Q. Yun, "The preparation, characterization and modification of a new phase change material: $\text{CaCl}_2 \cdot 6\text{H}_2\text{O}$ – $\text{MgCl}_2 \cdot 6\text{H}_2\text{O}$ eutectic hydrate salt," *Solar Energy Materials and Solar Cells*, vol. 126, pp. 51–55, 2014.
- [11] Y. Liu and Y. Yang, "Preparation and thermal properties of $\text{Na}_2\text{CO}_3 \cdot 10\text{H}_2\text{O}$ – $\text{Na}_2\text{HPO}_4 \cdot 12\text{H}_2\text{O}$ eutectic hydrate salt as a novel phase change material for energy storage," *Applied Thermal Engineering*, vol. 112, pp. 606–609, 2017.
- [12] A. Efimova, S. Pinnau, M. Mischke, C. Breikopf, M. Ruck, and P. Schmidt, "Development of salt hydrate eutectics as latent heat storage for air conditioning and cooling," *Thermochimica Acta*, vol. 575, pp. 276–278, 2014.
- [13] M. Li, H. Kao, Z. Wu, and J. Tan, "Study on preparation and thermal property of binary fatty acid and the binary fatty acids/diatomite composite phase change materials," *Applied Energy*, vol. 88, no. 5, pp. 1606–1612, 2011.
- [14] A. Safari, R. Saidur, F. A. Sulaiman, Y. Xu, and J. Dong, "A review on supercooling of phase change materials in thermal energy storage systems," *Renewable and Sustainable Energy Reviews*, vol. 70, pp. 905–919, 2017.
- [15] R. Al-Shannaq, J. Kurdi, S. Al-Muhtaseb, M. Dickinson, and M. Farid, "Supercooling elimination of phase change materials (PCMs) microcapsules," *Energy*, vol. 87, pp. 654–662, 2015.
- [16] X. Li, Y. Zhou, H. G. Nian et al., "Preparation and thermal energy storage studies of $\text{CH}_3\text{COONa} \cdot 3\text{H}_2\text{O}$ – KCl composites salt system with enhanced phase change performance," *Applied Thermal Engineering*, vol. 102, pp. 708–715, 2016.
- [17] P. Chandrasekaran, M. Cheralathan, V. Kumaresan, and R. Velraj, "Solidification behavior of water based nanofluid phase change material with a nucleating agent for cool thermal storage system," *International Journal of Refrigeration*, vol. 41, pp. 157–163, 2014.
- [18] R. Androsch, A. Monami, and J. Kucera, "Effect of an alpha-phase nucleating agent on the crystallization kinetics of a propylene/ethylene random copolymer at largely different supercooling," *Journal of Crystal Growth*, vol. 408, pp. 91–96, 2014.
- [19] F. Cao and B. Yang, "Supercooling suppression of microencapsulated phase change materials by optimizing shell composition and structure," *Applied Energy*, vol. 113, pp. 1512–1518, 2014.
- [20] Y. D. Liu, J. Q. Wang, C. J. Su, S. C. Geng, Y. K. Gao, and Q. G. Peng, "Nucleation rate and supercooling degree of water-based graphene oxide nanofluids," *Applied Thermal Engineering*, vol. 115, pp. 1226–1236, 2017.
- [21] V. V. Tyagi, S. C. Kaushik, A. K. Pandey, and S. K. Tyagi, "Experimental study of the supercooling and pH behavior of a typical phase change material for thermal energy storage," *Indian Journal of Pure & Applied Physics*, vol. 49, pp. 117–125, 2011.
- [22] K. Bilen, F. Takgil, and K. Kaygusuz, "Thermal energy storage behavior of $\text{CaCl}_2 \cdot 6\text{H}_2\text{O}$ during melting and solidification," *Energy Sources, Part A: Recovery, Utilization, and Environmental Effects*, vol. 30, no. 9, pp. 775–787, 2008.
- [23] R. Pilar, L. Svoboda, P. Honcova, and L. Oravova, "Study of magnesium chloride hexahydrate as heat storage material," *Thermochimica Acta*, vol. 546, pp. 81–86, 2012.
- [24] T. Wang, D. Mantha, and R. G. Reddy, "Novel high thermal stability LiF – Na_2CO_3 – K_2CO_3 eutectic ternary system for thermal energy storage applications," *Solar Energy Materials and Solar Cells*, vol. 140, pp. 366–375, 2015.
- [25] R. K. Sharma, P. Ganesan, V. V. Tyagi, and T. M. I. Mahlia, "Accelerated thermal cycle and chemical stability testing of polyethylene glycol (PEG) 6000 for solar thermal energy storage," *Solar Energy Materials and Solar Cells*, vol. 147, pp. 235–239, 2016.
- [26] A. Mariaux and M. Rappaz, "Influence of anisotropy on heterogeneous nucleation," *Acta Materialia*, vol. 59, no. 3, pp. 927–933, 2011.

Research Article

Experimental Investigation on Thermal Management of Electric Vehicle Battery Module with Paraffin/Expanded Graphite Composite Phase Change Material

Jiangyun Zhang, Xinxi Li, Fengqi He, Jieshan He, Zhaoda Zhong, and Guoqing Zhang

School of Materials and Energy, Guangdong University of Technology, Guangzhou, Guangdong 510006, China

Correspondence should be addressed to Xinxi Li; pkdlxx@163.com

Received 5 September 2017; Revised 31 October 2017; Accepted 19 November 2017; Published 31 December 2017

Academic Editor: Hamidreza Shabgard

Copyright © 2017 Jiangyun Zhang et al. This is an open access article distributed under the Creative Commons Attribution License, which permits unrestricted use, distribution, and reproduction in any medium, provided the original work is properly cited.

The temperature has to be controlled adequately to maintain the electric vehicles (EVs) within a safety range. Using paraffin as the heat dissipation source to control the temperature rise is developed. And the expanded graphite (EG) is applied to improve the thermal conductivity. In this study, the paraffin and EG composite phase change material (PCM) was prepared and characterized. And then, the composite PCM have been applied in the 42110 LiFePO₄ battery module (48 V/10 Ah) for experimental research. Different discharge rate and pulse experiments were carried out at various working conditions, including room temperature (25°C), high temperature (35°C), and low temperature (−20°C). Furthermore, in order to obtain the practical loading test data, a battery pack with the similar specifications by 2S*2P with PCM-based modules were installed in the EVs for various practical road experiments including the flat ground, 5°, 10°, and 20° slope. Testing results indicated that the PCM cooling system can control the peak temperature under 42°C and balance the maximum temperature difference within 5°C. Even in extreme high-discharge pulse current process, peak temperature can be controlled within 50°C. The aforementioned results exhibit that PCM cooling in battery thermal management has promising advantages over traditional air cooling.

1. Introduction

EVs have received universal eyes owing to their unique advantages over traditional vehicles in energy efficiency and emission reduction [1–3]. The temperature and its distribution have essential effects on the battery properties [4–6]. Such overheating and inhomogeneous temperature distribution frequently result in the module's premature failure earlier and life span degradation during practical operation process [7–9]. Especially in harsh working conditions, catastrophic destruction, such as fire and explosion, even thermal runaway will occur [10–12]. It is well known that the max temperature of cells must be strictly controlled within 55°C. Also, the ΔT must be maintained below 5°C by means of effective thermal management systems [13, 14]. Therefore, selecting an appropriate heat dissipation system is of critical importance for power battery modules [15, 16]. At present,

traditional air cooling [17–19] cannot transfer the heat generated from batteries quickly with the increasing module capacity and specifications. Although the liquid cooling [20, 21] method has a better heat dissipation effect, some disadvantages include complicated system, difficult maintenance, and high cost. In recent years, a novel thermal management with the PCM cooling system was proposed as an ideal substitute to the abovementioned traditional patterns [22–24].

PCM cooling technology is able to maintain the operating temperature of cells at a relatively constant temperature range, absorbing/releasing abundant heat during change of phase. The solution can make the temperature within the optimal range, managing uniform temperature distribution, especially in the extreme environment. Zhao et al. [25] summarized different kinds of thermal management methods and obtained the conclusion that PCM heat dissipation

technology is very promising for battery management systems. Karimi et al. [26] had an experimental study of a cylindrical lithium-ion battery thermal management using PCM composites and found that the metal matrix-PCM composite decreases the max ΔT between battery surface and PCM composite by up to 70%. The thermal management with LiFePO₄ battery pack at high temperature using a composite of PCMs and aluminum wire mesh plates was investigated by Azizi and Sadrameli [27], which displayed that the maximum surface temperature of battery was reduced by 19%, 21%, and 26% at 1C, 2C, and 3C discharge rate, respectively. Wilke et al. [27] had an experiment about preventing thermal runaway propagation in lithium-ion battery packs using a phase change composite material and got that the use of PCC (phase change composite) lowers the max temperature experienced by neighboring cells by 60°C or more. As a widely used organic phase change material, paraffin has many advantages, including high-phase change latent heat, wide melting point range, stable thermal performance, easy molding in solid state, generally not disappear phase separation phenomenon, and low corrosion and cost. Nevertheless, the thermal performance of low conductivity restricts the use of PCM-based cooling systems in subsequent application. In this paper, as a porous high thermal conductive material, expanded graphite is used to improve the thermal conductivity of materials. At present, most research about various battery thermal management systems are limited to the laboratory experiments under different working conditions, few practical loading tests are conducted according to the real driving road operation.

In this paper, a completely novel PCM-based cooling system, for 42110 cylindrical LiFePO₄ battery pack (96 V/20 Ah), has been introduced and developed herein. The battery pack made-up of four battery modules (48 V/10 Ah) by 2 series 2 parallel with the same technical parameters was carried out for practical pure electric vehicle (EV) loading experiments. The EV, with 96 V/150 Ah lead-acid power batteries, was assembled into lithium-ion battery pack (96 V/20 Ah). Various road conditions were conducted for evaluating the heat dissipation and temperature uniform distribution, including flat ground, 5-degree, 10-degree, and 20-degree slope. The composite PCM was prepared and its thermophysical performance was tested, including the thermal conductivity coefficient, latent heat, and thermalgravimetric (TG). Relevant experimental results indicated that cooling effect of PCM heat dissipation technology had more advantages over traditional air natural cooled, which showed PCM cooling system had a bright future for thermal management in the power battery module.

2. Experimental Setup

2.1. Composite Material Preparation and Characterization. Composite PCM was obtained by a physically mixing method. Firstly, industrial-grade paraffin (melting point from 35 to 40°C) was used. Expandable graphite with an average particle size (150 μm) and expansion ratio (220 mL g⁻¹) was obtained from Qingdao Bai Xing Graphite Co., Ltd. Secondly, EG was obtained by heating the expandable graphite

at 800°C for 60 s in a muffle furnace. PA was heated to 80°C. EG was added to the completely melting PA at a mass ratio of 4:1 with continuous mechanical stirring. Finally, through the hot-compaction process in a mold, a composite PCM module was fabricated with an overall dimension of 228.25 mm (length) × 142.34 mm (width) × 110 mm (height). The 42110 cylindrical cells were inserted into the 15 holes uniformly distributed on the PCM module, each with a diameter of 42.5 mm and height of 110 mm. The construction and fabrication of the PCM module were provided in Figure 1. Detailed preparation process of the composite material was described in our group previous research [28].

The microstructure of the composite PCMs was tested by a scanning electron microscope (SEM, Hitachi S-3400 N, Japan). The thermal conductivity was observed by an LFA447 NanoFlash™ system (range 0.1–2000 W · m⁻¹ · K⁻¹, accuracy ±5%, repeatability ±3%). The latent heat was measured using a Differential Scanning Calorimeter (HS-DSC-101B, HESON Instrument Inc., Shanghai).

2.2. Battery Module Construction. Figure 2 described the battery module assemble process. There were 15 holes with a diameter of 42.3 mm on the composite PCM module, in which 15 commercial 42110 Li-ion batteries (3.2 V/10 Ah) with symmetric distribution of T-type thermocouples were placed (layout of thermocouples were showed in Figure 3). All the cells were electrically connected in 15S1P configuration electric connection (15 cells in series and 1 string in parallel) by nickel pieces. Finally, the module technical parameters were shown in Table 1.

Technical specifications of the power battery module are provided in Table 1.

2.3. Design of the Experiment System. The experiment facilities are summarized in Figure 3. The constant-current sources (YK-AD12015, 120 V/15A, 1800 W) were used for module charging. DC electric load (M9718, 240 V/150A, 6000 W) was provided for constant-current discharging and acquiring current and voltage data during the discharge process. The temperature inspection instrument was used for collecting temperature data real-time.

2.4. Module Laboratory Testing. The PCM battery module was tested at a constant room temperature of 29°C. T-type thermocouples (OMEGA type SMPW-T-M) were placed inside the module to measure the battery surface temperature. During the experiment, the battery module was subjected to the following charge protocol: galvanostatic mode at 0.5C rate with a voltage cutoff limit of 59.0 V and then a potentiostatic mode until the current drops to 0A. After the charging process, adequate equilibration time was left for cooling the module to ambient temperature. Subsequently, the battery module was discharged at specified rates including 2.0C and 4.5C, respectively. Meanwhile, pulse experiment with high discharge current was conducted.

2.5. Pack Loading Testing. A battery pack (96 V/20 Ah) included one as-assembled PCM module and three air cooling modules in 2 series * 2 parallel with the same specifications. Four modules were placed in symmetrical

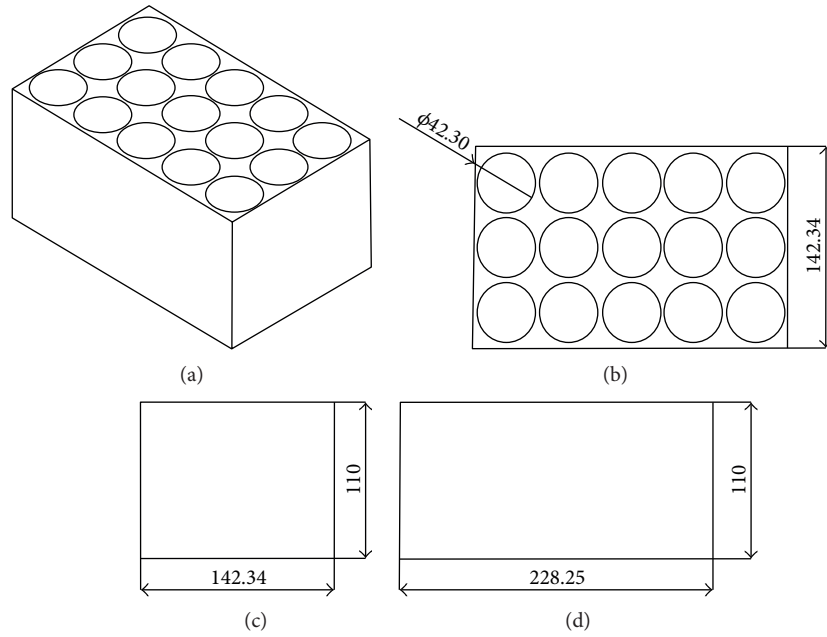


FIGURE 1: The battery module sizes with PCM. (a) The whole structure: (b) top view, (c) left view, and (d) front view.

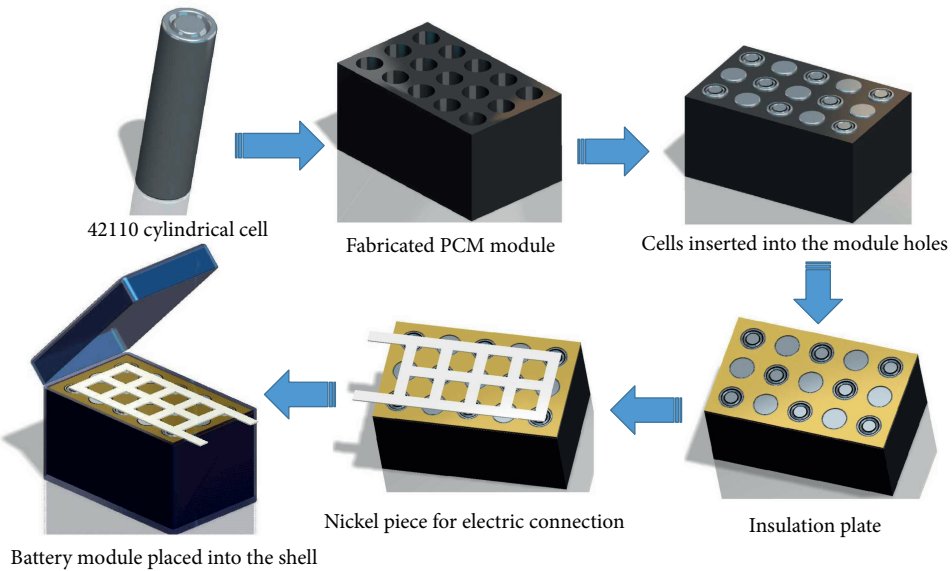


FIGURE 2: The battery module assembly process.

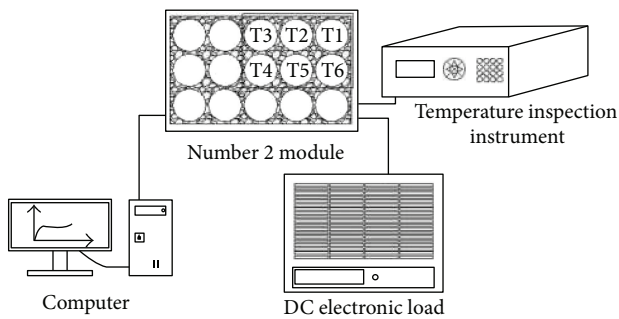


FIGURE 3: The sketch measurement experiment systems of battery module with PCM cooling.

TABLE 1: Battery module specifications.

Name	Parameters
Cell type	IFR42110LiFePO ₄
Module nominal voltage (V)	48
Module nominal capacity (Ah)	10
Max discharge current (A)	50
Max charge current (A)	10
Operating temperature range (°C)	-20~60
Charging temperature range (°C)	0~45

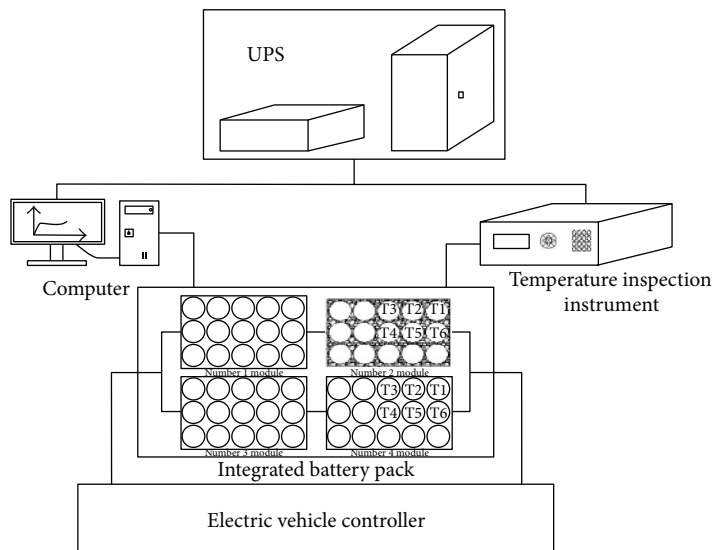


FIGURE 4: An illustration of the loading test setup.

distribution; therefore, one-quarter of both the PCM and air-cooled module were selected for collecting the temperature real-time. The pack was connected with the electric vehicle controller through 175A 600 V industrial plugs. Uninterruptible power supply (UPS) was used for providing the electric power to the temperature inspection instrument and the computer. The UPS with two lead-acid (12 V/38 Ah) battery modules in series was backup style which means that the host and its power are connected separately by communication signal wires. The loading test experiment setup scheme was shown in Figure 4. (Number 1, number 3, and number 4 battery modules designed with air-cooled scheme, number 2 module designed with PCM-based cooling, all with the same technical parameters. T4 stood for the cell temperature located in the module middle, and T1 represented the cell temperature located in the module edge.)

3. Results and Discussion

3.1. Characterization of Composite PCMs. DSC results of pure paraffin (PA) and paraffin/EG composite were shown in Figure 5. After adding EG, the latent heat of paraffin/EG composite decreased from 200.64 J/g to 147.61 J/g. In addition, the melting points of PA and PA/EG composite were 41.5 and 40.4°C, respectively, which is consistent with the melting point variations tendency of PA/EG composite proposed by Radhakrishnan and Gubbins [29, 30].

Thermal conductivity coefficient of composite ranging from 35°C to 50°C with 5°C interval was shown in Figure 6. Testing data indicated that the thermal conductivity came to the highest at 40°C (nearly close to the melting point 41.5°C), which was $3.084 \text{ W} \cdot \text{m}^{-1} \cdot \text{k}^{-1}$, almost 12 times larger than that of pure paraffin ($0.26 \text{ W} \cdot \text{m}^{-1} \cdot \text{k}^{-1}$). Above results could be owed to the EG high thermal conductivity. Figure 7 compared the mass changing trend with the temperature of pure PA and PA/EG composite named TG curves. Linear slope of PA was greatly higher than that of PA/EG composite.

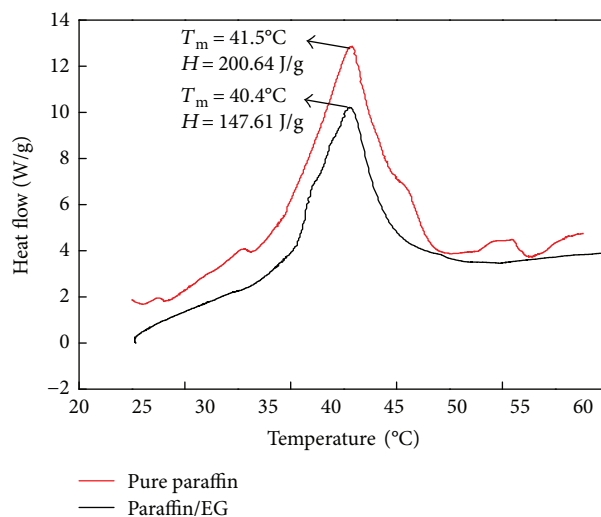


FIGURE 5: The comparison of latent heat between pure PA and PA/EG composite PCM.

The PA volatilization temperature was 100°C (PA nearly 100% volatilized), and the composite was 250°C (PA nearly 100% volatilized). The addition of EG can effectively delayed the paraffin volatilizing temperature and make the TG curve more smooth. Therefore, expanded graphite not only obviously improves the thermal stability but also decrease the volatilizing rate effectively.

3.2. Comparison of Heat Dissipation Performance

3.2.1. Constant-Current Discharge Test Results of PCM Cooling Module. The battery module was discharged at 2.0C and 4.5C, respectively, under room temperature condition (29°C). Comparisons of the experimental data were shown in Figure 8. Meanwhile, the module was tested at

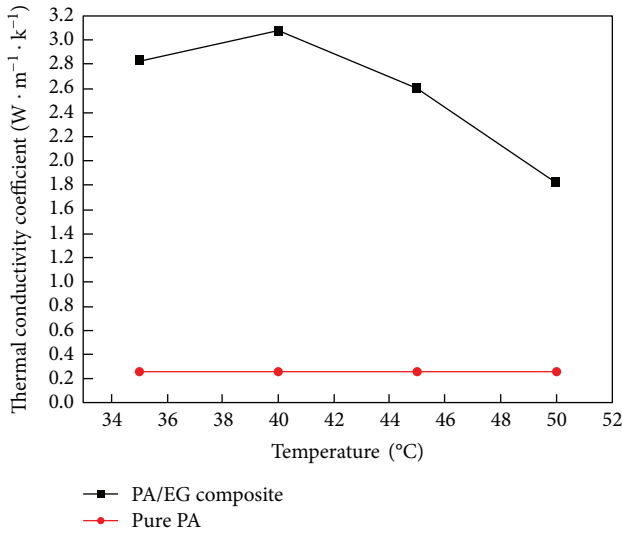


FIGURE 6: Thermal conductivity analysis between pure PA and PA/EG composite PCM.

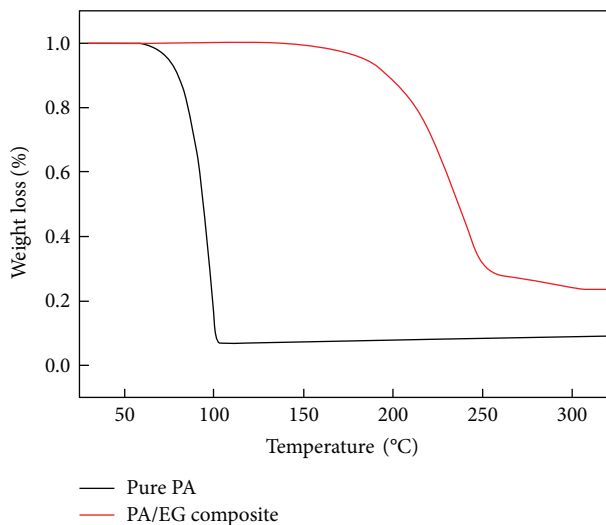


FIGURE 7: TG curves of pure PA and PA/EG composite PCM.

different discharge rates under low temperature (-20°C) and relatively high temperature (35°C) condition, respectively.

Figure 8 indicated number 4 cell temperature at 2.0C and 4.5C discharge rate came to 35.8 and 40.58°C , respectively, which indicated the core temperature came to the highest. Additionally, the above maximum temperature value is nearly closed to the PCM melting point and the max ΔT for 2.0C and 4.5C is 0.41°C and 3.05°C , respectively (which is significantly less than 5°C), which showed more excellent temperature uniform distribution. At 3C discharge rate, the room temperature, high temperature, and low temperature reached 37.61°C , 38.23°C , and 32.38°C , respectively, which revealed that high temperature was higher at 1.64% and 18.06% compared to that of the room and low-temperature condition. The test data indicated that PCM cooling system can control the max temperature well below 42°C and accompany with excellent distribution, which means that the peak

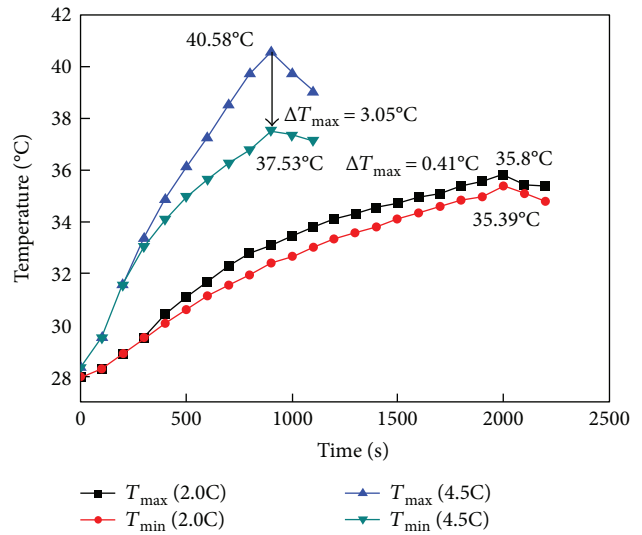


FIGURE 8: The T_{max} and T_{min} comparisons of battery module with PCM cooling at 2C and 4.5C, respectively (T_{max} meant number 4 cell; T_{min} meant number 1 cell).

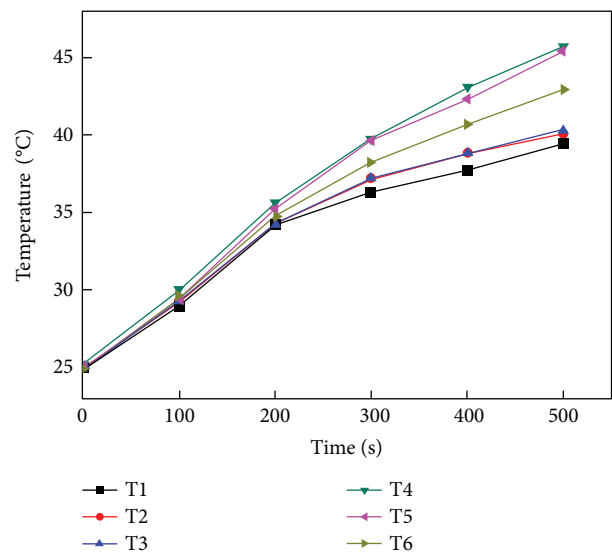


FIGURE 9: Temperature test results of pulse discharge experiments.

ΔT can be managed within 5°C . Therefore, the PCM cooling effect can satisfy the heat dissipation requirement, while maintaining the max temperature and keeping the temperature difference within the safety range.

3.2.2. *Pulse Test with High Discharge Current.* Pulse experiments were conducted in order to test the PCM cooling battery module, accompanied with the temperature instantaneous change and discharge performance. Detailed test stage was as follows: (a) charge state: galvanostatic mode at 0.5C rate with a voltage cutoff limit of 59.0V and then a potentiostatic mode until the current descended to 0A. (b) Hold stage: 1.5 h. (c) Pulse discharge stage: The module was discharged under a constant current of 10.0C for 10s, then hold for 10s, next discharge at 4.5C for 5s, then the rest for

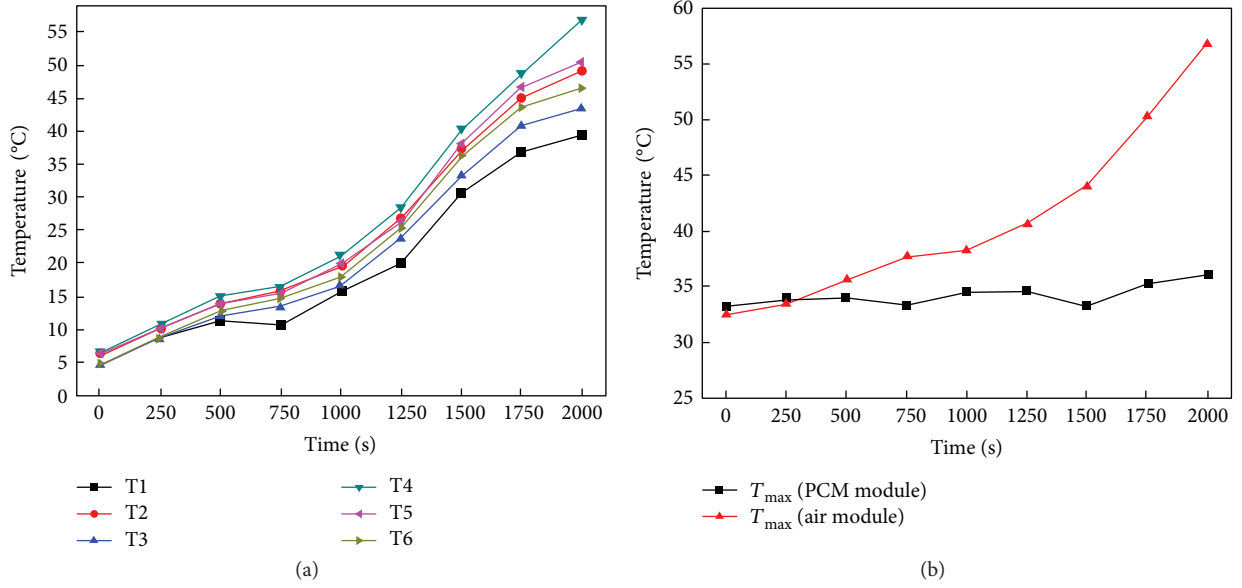


FIGURE 10: Pack testing results on the flat ground. (a) Temperature curve of the air-cooled module. (b) The T_{max} comparison of test data between the air cooling module and PCM cooling module. (T_{max} meant number 4 cell).

TABLE 2: Comparison of experimental results.

Road condition	T_{max} (°C) (PCM)	T_{min} (°C) (PCM)	ΔT_{max} (°C) (PCM)	T_{max} (°C) (air-cooled)	T_{min} (°C) (air-cooled)	ΔT_{max} (°C) (air-cooled)
Ground	35.1	31.8	3.3	56.8	49.3	7.5
5° slope	36.87	33.75	3.12	39.6	33.5	6.2
10° slope	36.38	35.1	1.28	42.25	36.2	6.05
20° slope	36.5	34.5	2.0	44.8	38	6.8

10 s. All the test period was 475 s. (d) Hold stage: 1.0 h. Test data was present in Figure 9.

Figure 9 Indicates the max temperature (number 4 cell) of the module core location reaches 45.65°C which is managed within 50°C in extreme instantaneous high discharge rate condition owing to PCM cooling technology participation. The minimum data (number 1 cell) of the module edge location reached to 39.44°C. Even discharged under the 10.0C high current pulse condition, the max temperature can still be controlled within the 50°C, which showed superior temperature instantaneous change ability.

3.3. Loading Test Results and Discussion

3.3.1. Driving Test Results on the Ground. One-quarter of the module was regarded as the research object according to the symmetry principle. Experiments were processed on the fixed road A, and the results were taken from the average of three-times experiments. Air-cooled module temperature data was obtained in Figure 10(a). The comparison of the max temperature curves between air-cooled and PCM cooling modules was displayed in Figure 10(b).

In Figure 10(b), the red curve indicated the max temperature with pure air cooling module comes to 56.8°C, which presented a rapidly increasing tendency. In contrast, the

black curve revealed the max temperature with the PCM cooling module can reach to 36°C and decreases by 57.7%, which displayed a slowly increasing tendency. Therefore, the battery module with the PCM cooling system can improve the thermal management effectively.

3.3.2. Data Analysis on Different Road Conditions. Comparisons of test results on different road conditions are shown in Table 2.

Table 2 shows that peak temperature and its difference of the air cooling module is always higher than that of the PCM cooling module. The max temperature of the air-cooling module on the ground reaches 56.8°C which has exceeded 55°C with 7.5°C peak ΔT and will have a heavy influence on the battery electric chemistry performance. Therefore, the cooling effect of the PCM system is far superior that of air cooling.

4. Conclusions

The paraffin and EG composite PCM were applied to battery modules for thermal management in this study. Thermal performance, including latent heat, thermal conductivity, and TG curves of PA/EG composite were carried out, respectively. The 42110 LiFePO₄ battery module (48 V/10 Ah) is investigated at different discharge rates under

various conditions. Simultaneously, practical loading work under different road conditions was processed. The conclusions were summarized based on the experimental results as follows:

- (1) The composite thermal conductivity reached $3.084 \text{ W} \cdot \text{m}^{-1} \cdot \text{K}^{-1}$ at 40°C , as the max value, which was nearly 12 times higher than that of PA. Also, the composite volatilization temperature was delayed to 250°C with more smooth TG curve owing to EG participation and the thermal stability was greatly improved. The latent heat of the PA/EG composite came to 147.61 J/g , which was 35.9% lower than that of PA. Also, the melting point of PA/EG composite showed a decreasing tendency.
- (2) Peak temperature gradually increased with the rise of discharge rates under each condition. On one hand, the results showed that the max temperature and its peak difference of the module could be controlled within 42°C and 5°C under constant-current discharge condition, respectively. On the other hand, even in extreme 10.0C pulse discharge rate, peak temperature is always controlled within 50°C which can meet the heat dissipation demand. The heat dissipation was greatly improved by the PCM cooling system which exhibited excellent temperature controlling and temperature balance ability.
- (3) Loading test data showed the max temperature and its peak difference of PCM cooling were always lower than that of the air-cooling module, which revealed that the PCM cooling can exhibit excellent thermal management for battery modules.

Conflicts of Interest

The authors declare that there are no conflicts of interest regarding the publication of this paper. The authors confirm that the mentioned received funding in the Acknowledgments section did not lead to any conflict of interests regarding the publication of this manuscript.

Acknowledgments

This work is supported by the Science and Technology Planning Project of Guangdong Province, China (2014B010128001), South Wisdom Valley Innovative Research Team Program (2015CXTD07), Scientific and Technological Project of Administration of Quality and Technology Supervision of Guangdong Province (2015PJ03), Science and Technology Application Research and Development Projects of Guangdong Province, China (2015B010135010), and Science and Technology Plan Projects of Guangdong Province, China (2016B090918015).

References

- [1] Q. C. Wang, Z. H. Rao, Y. T. Huo, and S. F. Wang, "Thermal performance of phase change material/oscillating heat pipe-based battery thermal management system," *International Journal of Thermal Sciences*, vol. 102, pp. 9–16, 2016.
- [2] W. X. Wu, X. Q. Yang, G. Q. Zhang, K. Chen, and S. F. Wang, "Experimental investigation on the thermal performance of heat pipe-assisted phase change material based battery thermal management system," *Energy Conversion and Management*, vol. 138, pp. 486–492, 2017.
- [3] T. Yuksel, S. Litster, V. Viswanathan, and J. J. Michalek, "Plug-in hybrid electric vehicle LiFePO_4 battery life implications of thermal management, driving conditions, and regional climate," *Journal of Power Sources*, vol. 338, pp. 49–64, 2017.
- [4] F. C. Wu and Z. H. Rao, "The lattice Boltzmann investigation of natural convection for nanofluid based battery thermal management," *Journal of Applied Thermal Engineering*, vol. 115, pp. 659–669, 2017.
- [5] S. Shi, Y. Xie, M. Li et al., "Non-steady experimental investigation on an integrated thermal management system for power battery with phase change materials," *Energy Conversion and Management*, vol. 138, pp. 84–96, 2017.
- [6] A. Hussain, C. Y. Tso, and C. Y. Chao, "Experimental investigation of a passive thermal management system for high-powered lithium ion batteries using nickel foam-paraffin composite," *Energy*, vol. 115, Part 1, pp. 209–218, 2016.
- [7] D. Chen, J. Jiang, G. H. Kim, C. Yang, and A. Pesaran, "Comparison of different cooling methods for lithium ion battery cells," *Applied Thermal Engineering*, vol. 94, pp. 846–854, 2016.
- [8] S. Basu, K. S. Hariharan, S. M. Kolake, T. Song, D. K. Sohn, and T. Yeo, "Coupled electrochemical thermal modeling of a novel Li-ion battery pack thermal management system," *Applied Energy*, vol. 181, pp. 1–13, 2016.
- [9] Z. Qian, Y. Li, and Z. Rao, "Thermal performance of lithium-ion battery thermal management system by using mini-channel cooling," *Energy Conversion and Management*, vol. 126, pp. 622–631, 2016.
- [10] J. Qu, J. T. Zhao, and Z. H. Rao, "Experimental investigation on the thermal performance of three-dimensional oscillating heat pipe," *International Journal of Heat and Mass Transfer*, vol. 109, pp. 589–600, 2017.
- [11] C. Z. Liu, Z. Y. Ma, J. T. Wang, Y. M. Li, and Z. H. Rao, "Experimental research on flow and heat transfer characteristics of latent functional thermal fluid with microencapsulated phase change materials," *International Journal of Heat and Mass Transfer*, vol. 115, Part A, pp. 737–742, 2017.
- [12] Z. H. Rao, Z. Qian, Y. Kuang, and Y. M. Li, "Thermal performance of liquid cooling based thermal management system for cylindrical lithium-ion battery module with variable contact surface," *Applied Thermal Engineering*, vol. 123, pp. 1514–1522, 2017.
- [13] Y. Lv, X. Yang, X. Li, G. Zhang, Z. Wang, and C. Yang, "Experimental study on a novel battery thermal management technology based on low density polyethylene-enhanced composite PCMs coupled with low fins," *Applied Energy*, vol. 178, pp. 376–382, 2016.
- [14] M. Alipanah and X. Li, "Numerical studies of lithium-ion battery thermal management systems using phase change materials and metal foams," *International Journal of Heat and Mass Transfer*, vol. 102, pp. 1159–1168, 2016.
- [15] C. Zheng, F. Geng, and Z. Rao, "Proton mobility and thermal conductivities of fuel cell polymer membranes: molecular dynamics simulation," *Computational Materials Science*, vol. 132, pp. 55–61, 2017.

- [16] S. K. Mohammadian, S. M. Rassoulinejad-Mousavi, and Y. Zhang, "Thermal management improvement of an air-cooled high-power lithium-ion battery by embedding metal foam," *Journal of Power Sources*, vol. 296, pp. 305–313, 2015.
- [17] Z. Lu, X. Z. Meng, L. C. Wei, W. Y. Hu, L. Y. Zhang, and L. W. Jin, "Thermal management of densely-packed EV battery with forced air cooling strategies," *Energy Procedia*, vol. 88, pp. 682–688, 2016.
- [18] L. H. Saw, Y. Ye, A. A. Tay, W. T. Chong, S. H. Kuan, and M. C. Yew, "Computational fluid dynamic and thermal analysis of lithium-ion battery pack with air-cooling," *Applied Energy*, vol. 177, pp. 783–792, 2016.
- [19] W. Tong, K. Somasundaram, E. Birgersson, A. S. Mujumdar, and C. Yap, "Thermo-electrochemical model for forced convection air cooling of a lithium-ion battery module," *Applied Thermal Engineering*, vol. 99, pp. 672–682, 2016.
- [20] X. H. Yang, S. C. Tan, and J. Liu, "Thermal management of Li-ion battery with liquid metal," *Energy Conversion and Management*, vol. 117, pp. 577–585, 2016.
- [21] Y. Azizi and S. M. Sadrameli, "Thermal management of a LiFePO₄ battery pack at high temperature environment using a composite of phase change materials and aluminum wire mesh plates," *Energy Conversion and Management*, vol. 128, pp. 294–302, 2016.
- [22] W. Wu, G. Zhang, X. Ke, X. Yang, Z. Wang, and C. Liu, "Preparation and thermal conductivity enhancement of composite phase change materials for electronic thermal management," *Energy Conversion and Management*, vol. 101, pp. 278–284, 2015.
- [23] T. Nomura, C. Zhu, S. Nan, K. Tabuchi, S. Wang, and T. Akiyama, "High thermal conductivity phase change composite with a metal-stabilized carbon-fiber network," *Applied Energy*, vol. 179, pp. 1–6, 2016.
- [24] C. J. Lan, J. Xu, Y. Qiao, and Y. B. Ma, "Thermal management for high power lithium-ion battery by minichannel aluminum tubes," *Applied Thermal Engineering*, vol. 101, pp. 284–292, 2016.
- [25] J. T. Zhao, P. Z. Lv, and Z. H. Rao, "Experimental study on the thermal management performance of phase change material coupled with heat pipe for cylindrical power battery pack," *Experimental Thermal and Fluid Science*, vol. 82, pp. 182–188, 2017.
- [26] G. Karimi, M. Azizi, and A. Babapoor, "Experimental study of a cylindrical lithium ion battery thermal management using phase change material composites," *Journal of Energy Storage*, vol. 8, pp. 168–174, 2016.
- [27] S. Wilke, B. Schweitzer, S. Khateeb, and S. Al-Hallaj, "Preventing thermal runaway propagation in lithium ion battery packs using a phase change composite material: an experimental study," *Journal of Power Sources*, vol. 340, pp. 51–59, 2017.
- [28] W. X. Wu, X. Q. Yang, and G. Q. Zhang, "An experimental study of thermal management system using copper mesh-enhanced composite phase change materials for power battery pack," *Energy*, vol. 113, pp. 909–916, 2016.
- [29] R. Radhakrishnan and K. E. Gubbins, "Free energy studies of freezing in slit pores: an order-parameter approach using Monte Carlo simulation," *Molecular Physics*, vol. 96, no. 8, pp. 1249–1267, 1999.
- [30] R. Radhakrishnan, K. E. Gubbins, A. Watanabe, and K. Kaneko, "Freezing of simple fluids in microporous activated carbon fibers: comparison of simulation and experiment," *Journal of Chemical Physics*, vol. 111, no. 19, pp. 9058–9067, 1999.

Research Article

Numerical Simulation of Bubble Free Rise after Sudden Contraction Using the Front-Tracking Method

Ying Zhang,¹ Min Lu,¹ Wenqiang Shang,¹ Zhen Xia,¹ Liang Zeng,¹ and Peisheng Li^{1,2}

¹*School of Mechanical and Electrical Engineering, Nanchang University, Nanchang, Jiangxi 330031, China*

²*Shangrao Normal College, Shangrao, Jiangxi 334001, China*

Correspondence should be addressed to Peisheng Li; ncudns1995z@163.com

Received 29 July 2017; Revised 7 September 2017; Accepted 11 September 2017; Published 24 October 2017

Academic Editor: Ben Xu

Copyright © 2017 Ying Zhang et al. This is an open access article distributed under the Creative Commons Attribution License, which permits unrestricted use, distribution, and reproduction in any medium, provided the original work is properly cited.

Based on the front-tracking method (FTM), the movement of a single bubble that rose freely in a transverse ridged tube was simulated to analyze the influence of a contractive channel on the movement of bubbles. The influence of a symmetric contractive channel on the shape, speed, and trajectory of the bubbles was analyzed by contrasting the movement with bubbles in a noncontractive channel. As the research indicates, the bubbles became more flat when they move close to the contractive section of the channel, and the bubbles become less flat when passing through the contractive section. This effect becomes more obvious with an increase in the contractive degree of the channel. The symmetric contractive channel can make the bubbles first decelerate and later accelerate, and this effect is deeply affected by Reynolds number (Re) and Eötvös number (Eo).

1. Introduction

The corrugated tube has been the focus of scholars because the internal structure of the pipe can disturb the movement of the fluid and increase the surface area of the pipe; thereby, it can increase the heat transfer of the pipe. So it is widely used in various fields such as the solar hot water system because there are a number of solar collector tube and heat transfer tubes in this system. In order to improve the heat absorption and heat transfer efficiency, different types of corrugated tubes have been studied. Vicente et al. [1] studied heat transfer of the threaded pipe under different sizes by experimentation, he shows the guidelines to choose which roughness geometry offers the best performance for specific flow conditions. García et al. [2] analyzed the thermal-hydraulic behavior of three types of enhancement technique based on artificial roughness, and the results show that shape of the artificial roughness exerts a greater influence on the pressure drop characteristics than on the heat transfer augmentation. Saha [3] has studied the pressure drop characteristics of pipe with internal transverse rib turbulators on two opposite surfaces and with wire-coil inserts.

Pethkool et al. [4] experimentally studied the heat transfer performance of helically corrugated tube and got the empirical formula. Kareem et al. [5] studied the three-start spirally corrugated tube by experiment and simulation, he said that this geometry with a creative spiral corrugation profile can improve the heat transfer significantly with reasonable increase in friction factor. It is obvious that scholars have made a lot of research on corrugated tubes in different structural forms and got some good results. However, most of these studies have been studied for the effects of different pipe shapes on heat transfer and pressure drop with a single fluid, while the study of multiphase flow in the tube has been rarely reported.

In practical cases, such as solar collectors and heat exchangers, the temperature of water in the tube is generally higher than the natural temperature. The gas in the water will be released and the bubbles will form. The interaction of the bubble with the contraction structure can also cause negligible disturbance to the flow in the pipe and affect its heat transfer. Therefore, we believe that the study of bubble flow in the corrugated tube has a certain reference value for improving the heat transfer of the heat exchanger, reducing

the pressure drop of the helically corrugated tube and obtaining the empirical formula of thermal performance.

The method of numerical simulation of bubble motion has been well developed [6–11]. In order to describe the movement characteristics of the bubbles in the corrugated tube intuitively, it is convenient to study it with the simulation method. FTM is a classic method used in numerical simulations that has been widely used in multiphase analyses [12–14]. It can accurately capture the complex topological changes of the moving interface, and it is very important in tracking the phase interface during the research process of multiphase flow.

Therefore, in this paper, the FTM was used to simulate the free rise of a single bubble in the transverse ridged tube. However, the cross-sectional shape of the transverse ridged tube is not a regular rectangle like an ordinary pipe, so we set the contraction channel by modifying the boundary position. And we analyzed the coupling effect between the bubble and the solid wall of the channel and studied the influences of sudden contraction on the shape, velocity, and trajectory of the bubble. It is hoped that the analysis of the flow field under coupling effect between the bubble and the solid wall of the channel will provide a theoretical help for the design of the heat transfer pipe in a solar hot water system, so that the internal flow of the transverse ridged tube can be more reasonable and achieve better heat transfer effect.

2. Mathematical Model, Numerical Methods, and Physical Model

2.1. Tracking and Processing the N-S Equations at the Phase Interface. The surface tension is concentrated on the interface when the control equation is applied to the whole calculation area. We consider introducing a source term and is applied by multiplying the volume force and the δ function. The δ function is nonzero only on the interface. Using the amendments above, the two-dimensional incompressible flow momentum equation can be expressed as

$$\frac{\partial}{\partial t}(\rho \mathbf{u}) + \nabla \cdot (\rho \mathbf{u} \mathbf{u}) = -\nabla p + \rho \mathbf{g} + \nabla \cdot \mu (\nabla \mathbf{u} + \nabla \mathbf{u}^T) + \int_s \sigma \kappa n \delta(x - x^f) ds, \quad (1)$$

where $\delta(x - x^f)$ is the two-dimensional Dirac function, x^f is the position of the surface, the integral is along the interface S , n is the interface normal, σ is the interface tension coefficient, κ is the secondary interface average curvature, and ρ and μ are noncontinuous density field and viscosity field.

To solve the equation above, we split (4) and remove the pressure introducing the temporary speed \mathbf{u}^* . Thus, an equation containing only the \mathbf{A} convection term and the \mathbf{D} diffusion term is obtained:

$$\frac{\mathbf{u}^* - \mathbf{u}^n}{\Delta t} = -\mathbf{A}^n + \mathbf{g} + \frac{1}{\rho^n} \mathbf{D}^n. \quad (2)$$

By solving the equation, we obtain the temporary velocity field without pressure, and then add the pressure term to obtain the general velocity discrete equation:

$$\frac{\mathbf{u}^{n+1} - \mathbf{u}^*}{\Delta t} = -\frac{\nabla_h p}{\rho^n}. \quad (3)$$

In the formula, ∇_h is a discrete form of the Hamiltonian operator whose step size is h and because of the speed it needs to meet the discrete form of mass conservation:

$$\nabla_h \mathbf{u}^{n+1} = 0. \quad (4)$$

Then the pressure Poisson equation is obtained:

$$\nabla_h \cdot \left(\frac{1}{\rho^n} \nabla_h p \right) = \frac{1}{\Delta t} \nabla_h \cdot \mathbf{u}^*. \quad (5)$$

The CSF (continuous surface force method) method given by Brackbill [15] was used to calculate the surface tension.

$$F_\sigma = \int_s \left[\sigma(T) \kappa n + \frac{\partial \sigma(T)}{\partial(s)} t \right] (x - x^f) ds. \quad (6)$$

Take the surface tension on the unit line to study, for the two-dimensional flow is

$$\kappa n = \frac{\partial \mathbf{t}}{\partial s}. \quad (7)$$

Get the surface tension on the unit interface element:

$$\delta F_\sigma^l = \int_{\Delta s} \left(\sigma \frac{\partial \mathbf{t}}{\partial s} + \frac{\partial \sigma(T)}{\partial(s)} t \right) ds = (\sigma \mathbf{t})_{l+1/2} - (\sigma \mathbf{t})_{l-1/2}. \quad (8)$$

Here, \mathbf{t} is the tangent vector on the interface.

2.2. Reconstruction of Density and Viscosity. For immiscible and incompressible fluids, the fluid maintains its characteristics at both sides of the interface, so there is a step in the physical properties at the interface. When the interface moves, the density and viscosity distribution of the interface also change, so the Heaviside function is introduced as an indicator to characterize the change:

$$H(\varphi) = \begin{cases} 1, & \varphi > \alpha \\ \frac{1}{2} \left(1 + \frac{\varphi}{\alpha} + \frac{1}{\pi} \left(\frac{\pi \varphi}{\alpha} \right) \right), & \|\varphi\| \leq \alpha \\ 0, & \varphi < -\alpha, \end{cases} \quad (9)$$

where φ is the distance from the given point to the interface, and 2α is the absolute value of the thickness of the transition zone between the two fluids. So the density and viscosity distribution is

$$\psi(\varphi) = H(\varphi) \psi_1 + (1 - H(\varphi)) \psi_2. \quad (10)$$

Here, ψ_1, ψ_2 are the density and viscosity of the two fluids.

2.3. Interface Movement. The moving interface is typically combined with a fixed mesh, and the information exchange between the interface and the grid is achieved by the area weight function. With the bilinear interpolation method,

the abrupt change density and the surface tension of the interface are changed from the interface to the fixed grid. Finally, we use a simple first-order time integral to obtain the interface position of the next time.

$$x_f^{(n+1)} = x_f^n + \Delta t \mathbf{u}_f^n. \quad (11)$$

Here, x_f^n is the position of surface and \mathbf{u} is velocity.

2.4. Physical Model. In the actual production industry, the geometric conditions of the contractive channel are varied, and to facilitate the research, only the unit shown in Figure 1 is extracted as the object of this paper and the upper and lower borders are set to periodic boundary conditions to satisfy the structure of the transverse ridged tube. Since the three-dimensional model will spend much time, so we use the two-dimensional model. The contractive ratio is defined as $E = L/M$ and is used to describe the contractive degree. D is the diameter of the bubble.

Re is defined as

$$Re = \frac{\rho_l u D}{\nu_l}. \quad (12)$$

Eo is defined as

$$Eo = \frac{\rho_l g D^2}{\sigma}. \quad (13)$$

Mo is defined as

$$Mo = \frac{(\rho_l - \rho_g) g \nu_l^4}{\sigma^3 \rho_l^2}. \quad (14)$$

Here, ρ_l is the density of liquid phase, ν_l is the viscosity of liquid phase, σ is the coefficient of the surface tension, ρ_g is the density of the gas phase, and g is the acceleration due to gravity.

2.5. Initial Conditions. Given $D/L = 0.2$, the center coordinates of the bubble are $(0.5L, 0.5L)$. In this paper, the ratio of the two-phase density is 5:1, and the wetting condition (contact angle effect) is not considered. The calculating area is the 12 rectangular region, and the grid resolution is 256×512 (including the contraction region, which is not involved in the calculation). The X direction was defined using a no-slip boundary condition, and the Y direction was defined using periodic boundary conditions. All the results in this paper are simulated in two-dimensional space.

3. Calculation Results and Discussion

Hua and Lou simulated several typical bubble morphology in Bhaga and Weber [16] with a two-dimensional model, and they compared the Re number between the experiment and simulation and results from simulations agree with those of experiments very well within 10% difference. So, we simulated one of the case ($Eo = 116$, $Re = 13.95$) from Hua and Lou [12] and the result is shown in Figure 2. We can find that

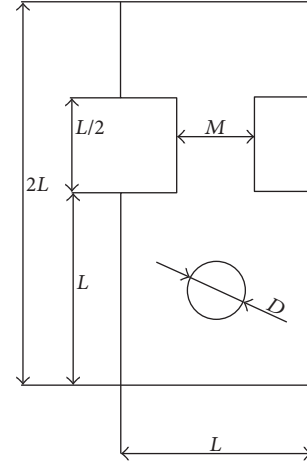


FIGURE 1: Physical model.

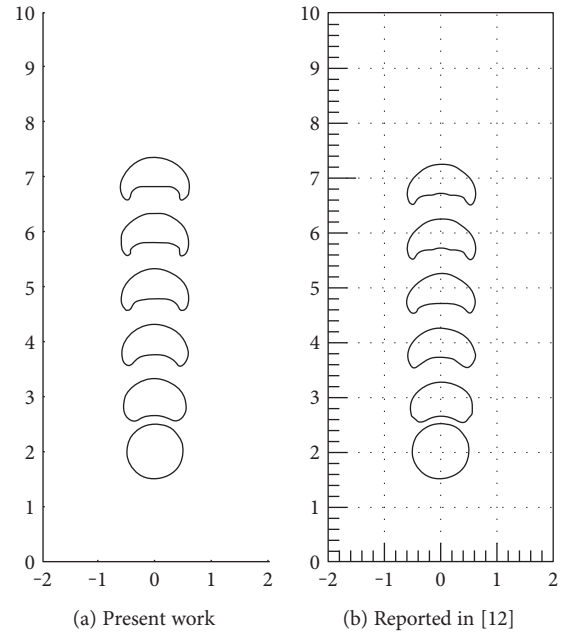


FIGURE 2: The evolution of a rising bubble with $Eo = 116$ and $Re = 13.95$.

the results of our model are very close to the result reported in [12].

In the process of numerical simulation, the grid density has a significant effect on the calculation results. In order to ensure that there is no correlation between the grid density and the calculated results, we have carried out the four cases of the grid density of 64×128 , 128×256 , 256×512 , 512×1024 to simulate the bubble rises in the contractive channel and we extract the position of bubble centroid at different time. The results are shown in Figure 3. It can be seen that the difference between the numerical results is not large at different grid densities. The calculation results of the other three cases are very close except that the grid density is 64×128 . To meet the accuracy of the calculation results

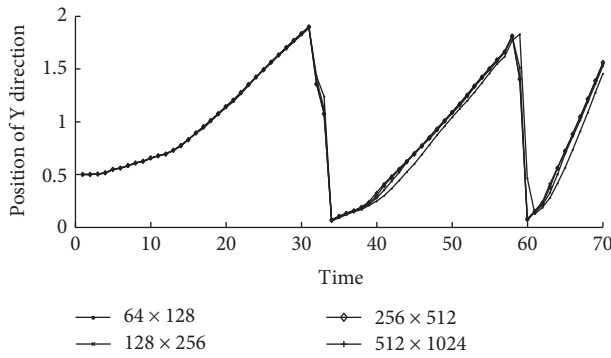


FIGURE 3: Grid convergence test.

and to save the calculation time as much as possible, we select the 256×512 grid density to calculate the object of our study.

4. Effect of a Symmetric Contractive Channel on Bubble Deformation

In this part, we primarily analyze the effect of the symmetric contractive channel on the bubble's deformation. Figure 4 shows the movements of bubbles with a contractive ratio of 1, 1.18, 1.45, 1.88, 2.2, 2.67, 4.57, and 16 under the same situation ($Re = 28.2$, $Eo = 16$, and $Mo = 0.01$). In the noncontractive channel ($E = 1$), the bubble changes from circular into a hat, and then, its shape becomes stable.

Because the contractive degree is small ($E = 1.18, 1.45$), the deformation of the bubble in this channel does not differ significantly from a bubble in the noncontractive channel. When the contractive ratio is 1.88, 2.2, 2.67, and 4.57 and before entering into the contractive portion of the channel, the shape of the bubble is more flat compared with the shape of bubbles in the noncontractive channel. Even when the contractive ratio is greater ($E = 2.67, 4.57$), the bubble becomes wider than that section of the contraction. When the bubble just enters the contractive portion of the channel, the middle portion of the bubble is raised up. When the bubbles enter into the contractive portion of the channel, the distance of the vertical wall on both sides of the bubble becomes smaller, and the shape of the bubble is not as flat as before. When the contractive ratio is 16, the bubble cannot pass through the contraction, and its shape becomes more flat.

To analyze the deformation of the bubble more directly, the deformation of the bubble was measured using the aspect ratio. Figure 5 shows the variation of aspect ratio with the centroid height of the bubble during the bubble motion given the condition in Figure 4. In a sudden contractive channel, the deformation of the bubble is primarily affected by the horizontal wall of the contraction above the bubble and the vertical wall in the contractive channel. When the bubble is close to the contractive part of the channel, the bubble is primarily affected by the horizontal wall at the top of the bubble. When the bubble enters into the contractive portion, it is primarily affected by the vertical wall on both sides of the bubble.

When the contractive ratio is 1.18 and 1.45 and the bubble is near the contractive portion, because the horizontal

wall above the bubble is small, there is a slight effect on the shape of the bubble, and there is only a slight increase in the aspect ratio. When the bubbles remain in the contractive part, the aspect ratio of the bubble is smaller because of the effect of the vertical wall.

When the contractive ratio is 1.88, 2.2, 2.67, and 4.57 and the bubbles are close to the contractive part, the bubbles are primarily affected by the horizontal wall above the bubble. Therefore, when the aspect ratio of the bubble is compared with the motion in the noncontractive channel, the aspect ratio of the bubble is greater, and with an increase in the contractive degree, a larger horizontal wall area results in a stronger effect. For example, when the contractive ratio is 4.57, the aspect ratio achieved the maximum value of 5.2, which is 1.85 times greater than the motion of the bubbles in the noncontractive channel at the same time. When the bubbles enter the contractive portion, the shape of the bubble will be affected by the vertical wall on both sides of the channel, and the aspect ratio of the bubble becomes smaller. When the bubbles come out from the contractive portion, the aspect ratio of the bubble will become larger.

When the contractive ratio is 16, because the contractive degree of the channel is too large, the channel is too narrow and the bubbles cannot enter the contractive portion. The bubble is primarily affected by the horizontal wall on the top of the bubble. The aspect ratio of the bubble increases constantly, and the maximum aspect ratio is close to 8 and would then decrease, but the bubble still cannot pass through the channel.

5. Effect of the Symmetric Contractive Channel on the Velocity of the Bubbles

When the bubbles move upward from the bottom under the action of gravity, the channel which contracted suddenly will affect the speed of the bubbles, and this effect is primarily influenced by Eo and Re . In this paper, we only analyze the situation in which the bubbles can pass through the contractive channel, and we do not analyze the situation in which the bubble cannot pass through the channel when the contractive ratio is too large, as shown in Figure 4 ($E = 16$). In this section, we study the case which the contractive ratio is 2.2, because in this case the effect of the wall becomes obvious and the bubble can go through the channel smoothly. We compared the motion of the bubble with that of the noncontractive channel. To react to the speed and the deformation of the bubble, this paper analyzed the bottom and the top velocity of the bubble.

The influence of the contractive channel on the velocity of the bubble was primarily related to Re and Eo . Figure 6 is the change chart for the bottom and the top velocity of the bubble in the case of $Re = 70$ and $Eo = 8$, and Figure 7 is in the case of $Re = 70$ and $Eo = 3.2$.

As Figure 6 shows, during the early process of the bubble rising, the bubble was far away from the section of the contraction. The velocity of the bubble was less affected, so the speed of the bubble in the contraction channel was the same as the speed in the noncontractive channel. When the bubble was close to the contractive channel, it was affected by the

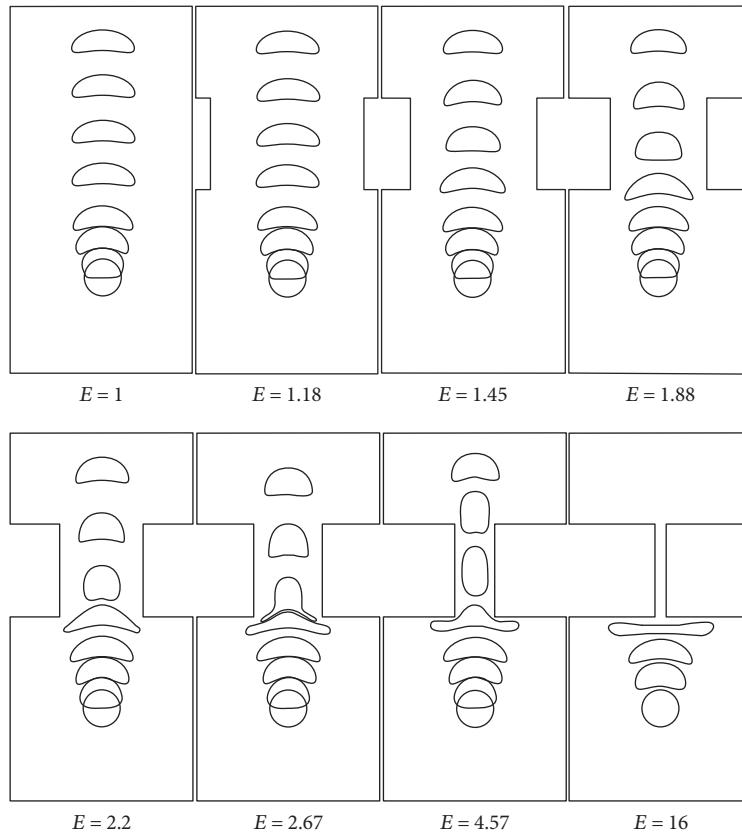


FIGURE 4: Free rise of the bubbles in different contractive channels ($Re = 28.2$, $Eo = 16$, and $Mo = 0.01$).

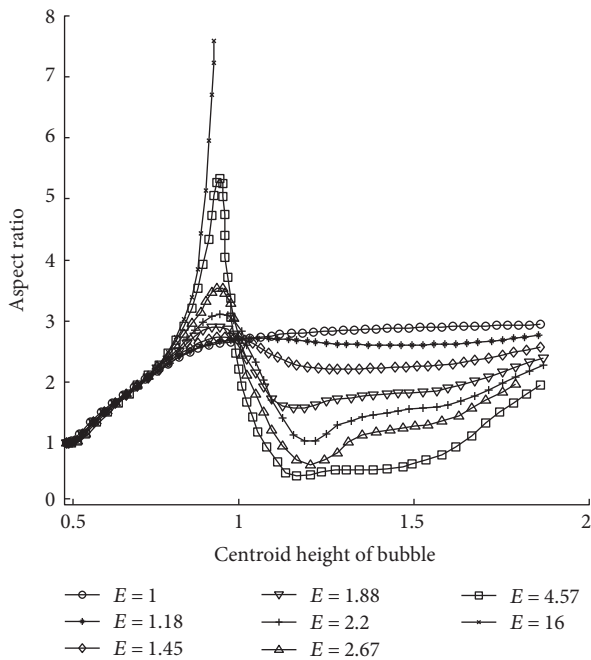


FIGURE 5: Aspect ratio of the bubbles with different contractive ratios ($Re = 28.2$, $Eo = 16$, and $Mo = 0.01$).

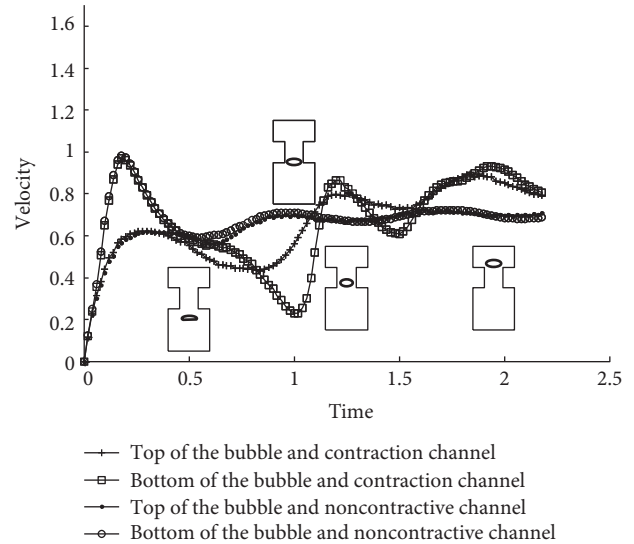


FIGURE 6: The free rising velocity of bubbles in the contractive and noncontractive channels ($Re = 70$, $Mo = 8 \times 10^{-5}$, and $Eo = 8$).

horizontal wall. Therefore, the aspect ratio of the bubble becomes greater, the resistance to the bubble rising becomes greater, and the velocity of the bubble becomes smaller. When the bubble enters into the contraction, the aspect ratio

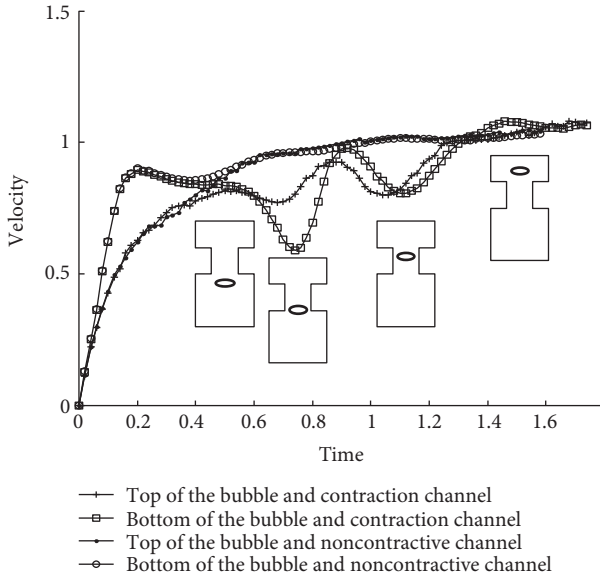


FIGURE 7: The velocity of the bubbles in the contractive and noncontractive channels ($Re = 70$, $Mo = 8 \times 10^{-5}$, and $Eo = 3.2$).

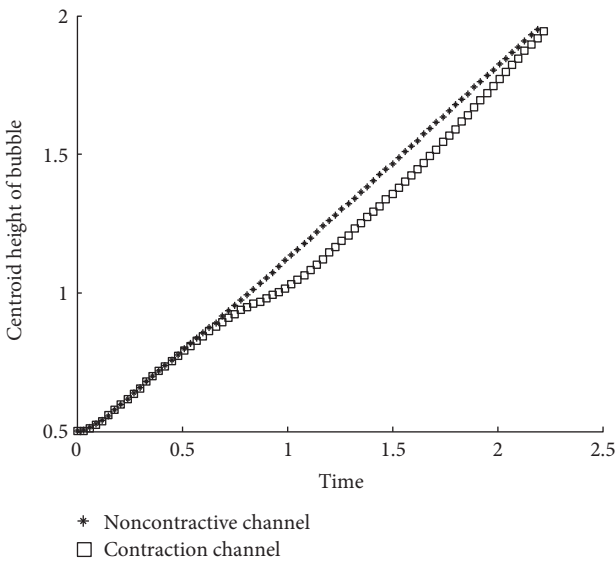


FIGURE 8: The centroid height of the bubble in the contractive and noncontractive channels ($Re = 70$, $Mo = 8 \times 10^{-5}$, and $Eo = 8$).

of the bubble decreases, the resistance to the bubble rising was also reduced, and the velocity of the bubble increased. When the bubble was coming out of the contractive portion, the velocity of the bubble decreases.

When the bubble is located near the contractive part, the contractive channel decelerates the bubble, and when the bubble enters the contraction, the contraction accelerates the bubble. Figure 8 shows the height-time diagrams of the bubble from which we can observe the influence of the contraction clearly under the combined influence of the “deceleration” and the “acceleration.” The time it takes the bubble to go through the contractive and noncontractive channels is approximately the same.

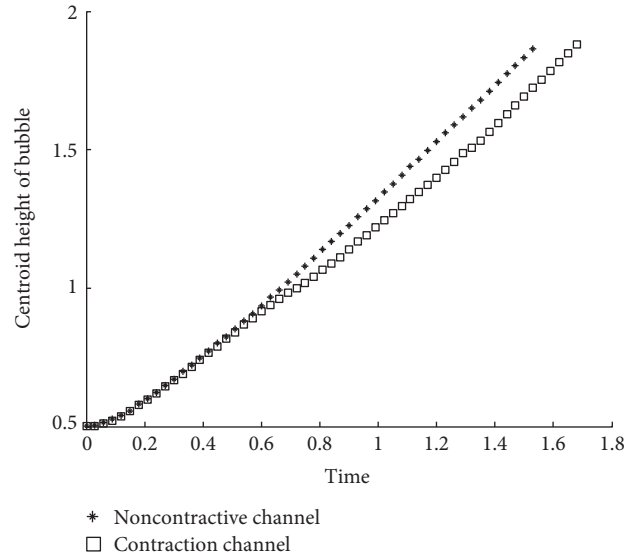


FIGURE 9: The centroid height of the bubble in the contractive and noncontractive channels ($Re = 70$, $Mo = 1 \times 10^{-5}$, and $Eo = 3.2$).

It can be observed from Figure 7, in the case of a larger Eo value, the contractive channel also has the effect of “decelerating” and “accelerating” the bubbles compared with the front situation. The contractive channel had a weak influence on the acceleration of the bubbles. Therefore, as shown in Figure 9, it takes the bubble a longer time to pass through the contractive channel compared with the bubble going through the noncontractive channel.

The first case shows the influence of the contractive channel on the velocity of the bubble for the two different values of Eo . This influence on the velocity is strongly affected by Eo and Re . According to the analysis above and due to the influences of the contractive channel, the velocity of the bubbles decreased when the bubble nears the section of the contractive channel, and then when the bubble enters the contraction, the velocity of the bubble increased. To measure the comprehensive influence of the contraction channel on the velocity of the bubble, we defined the average velocity ratio as, in the same case, the average velocity of a bubble that is completely through the channel; the contraction channel has a constant cross-sectional area. Figure 10 shows the distribution of the average velocity ratio of the bubbles when Re and Eo are different.

As seen in Figure 10, with an increase in Re , the ratio of the average velocity increased given the same value of Eo . According to the research from Clift [1], with an increase in Re , the shape of the bubbles has the tendency to become more flat. A flat bubble shape results in a greater resistance to rising. However, when the bubbles pass through the contraction channel, the bubbles are squeezed due to the effect of the wall making the aspect ratio of the bubble decrease, and the resistance of the bubble to rise has a decreasing trend. Therefore, the ratio of the average velocity increases with an increase in Re . Figure 10 shows that a decrease in Eo results in the average velocity ratio of the bubble being reduced. A smaller Eo results

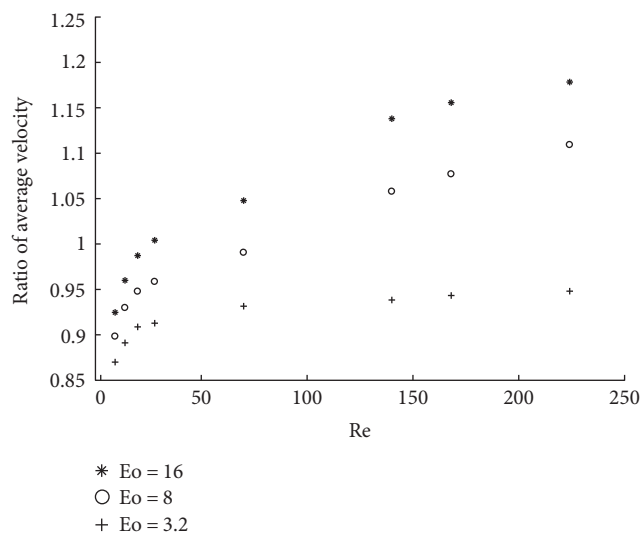


FIGURE 10: Relationship between the ratio of average velocity and Re and Eo.

in a more difficult deformation of the bubble, so the effect that the vertical wall makes the aspect ratio of the bubble become smaller is not obvious. That is, the resistance of the bubble to rise is not obvious. A smaller Eo results in the bubble having a smaller average velocity ratio.

6. Conclusion

- (1) The bubble rises freely in a symmetric contractive channel when the distance between the bubbles and the contractive part of the channel is considerable, and the deformation of the bubble is similar to the situation in which the bubbles move in a noncontractive channel. When the bubble is close to the contractive channel, due to the effect of the wall, the shape of the bubbles will be more flat; that is, the aspect ratio becomes greater. When the bubbles enter the contractive part of the channel, the shape of bubbles will not be as flat as before, and the aspect ratio becomes small. A greater contractive degree of the channel results in the effect becoming more obvious.
- (2) Compared with the noncontractive channel, when the bubble rises freely in a symmetric contractive channel, the contractive channel causes the velocity of the bubble to decrease at first and then increase combining both “deceleration” and “acceleration.” The average velocity of the bubble in the contractive channel may be greater than in the noncontractive channel or it may be smaller. The main influential factors are Re and Eo, and when Re or Eo is greater, the bubble will have an accelerating trend.

Conflicts of Interest

The authors declare that they have no conflicts of interest.

Acknowledgments

The research is supported by the National Natural Science Foundation of China (11562011), the Natural Science Foundation of Jiangxi Province (20151BAB202002), and the funds from Hundred Sail Away Project in 2015 provided by Jiangxi Provincial Party Committee Organization Department and Jiangxi Association for Science and Technology.

References

- [1] P. G. Vicente, A. Garcia, and A. Viedma, “Experimental investigation on heat transfer and frictional characteristics of spirally corrugated tubes in turbulent flow at different Prandtl numbers,” *International Journal of Heat and Mass Transfer*, vol. 47, no. 4, pp. 671–681, 2004.
- [2] A. García, J. P. Solano, P. G. Vicente, and A. Viedma, “The influence of artificial roughness shape on heat transfer enhancement: corrugated tubes, dimpled tubes and wire coils,” *Applied Thermal Engineering*, vol. 35, no. 1, pp. 196–201, 2012.
- [3] S. K. Saha, “Thermal and friction characteristics of turbulent flow through rectangular and square ducts with transverse ribs and wire-coil inserts,” *Experimental Thermal and Fluid Science*, vol. 34, no. 5, pp. 575–589, 2010.
- [4] S. Pethkool, S. Eiamsa-Ard, S. Kwankaomeng, and P. Promvong, “Turbulent heat transfer enhancement in a heat exchanger using helically corrugated tube,” *International Communications in Heat and Mass Transfer*, vol. 38, no. 3, pp. 340–347, 2011.
- [5] Z. S. Kareem, S. Abdullah, T. M. Lazim, M. M. Jaafar, and A. F. Wahid, “Heat transfer enhancement in three-start spirally corrugated tube: experimental and numerical study,” *Chemical Engineering Science*, vol. 134, pp. 746–757, 2015.
- [6] I. Chakraborty, G. Biswas, and P. S. Ghoshdastidar, “A coupled level-set and volume-of-fluid method for the buoyant rise of gas bubbles in liquids,” *International Journal of Heat and Mass Transfer*, vol. 58, no. 1-2, pp. 240–259, 2013.
- [7] K. Szwec, J. Pozorski, and J. P. Minier, “Simulations of single bubbles rising through viscous liquids using smoothed particle hydrodynamics,” *International Journal of Multiphase Flow*, vol. 50, no. 50, pp. 98–105, 2013.
- [8] A. M. Zhang, “The law of the underwater explosion bubble motion near free surface,” *Acta Physica Sinica*, vol. 57, no. 1, pp. 339–353, 2008.
- [9] Y. Y. Yan, Y. Q. Zu, and B. Dong, “LBM, a useful tool for meso-scale modelling of single-phase and multiphase flow,” *Applied Thermal Engineering*, vol. 31, no. 5, pp. 649–655, 2011.
- [10] L. Amaya-Bower and T. Lee, “Single bubble rising dynamics for moderate Reynolds number using Lattice Boltzmann method,” *Computers & Fluids*, vol. 39, no. 7, pp. 1191–1207, 2010.
- [11] Q. Dai and L. Yang, “LBM numerical study on oscillating flow and heat transfer in porous media,” *Applied Thermal Engineering*, vol. 54, no. 1, pp. 16–25, 2013.
- [12] J. Hua and J. Lou, “Numerical simulation of bubble rising in viscous liquid,” *Journal of Computational Physics*, vol. 222, no. 2, pp. 769–795, 2007.
- [13] K. L. Pan and Z. J. Chen, “Simulation of bubble dynamics in a microchannel using a front-tracking method,” *Computers and Mathematics with Applications*, vol. 67, no. 2, pp. 290–306, 2014.

- [14] G. Tryggvason, B. Bunner, A. Esmaeeli et al., "A front-tracking method for the computations of multiphase flow," *Journal of Computational Physics*, vol. 169, no. 2, pp. 708–759, 2001.
- [15] J. U. Brackbill, D. B. Kothe, and C. Zemach, "A continuum method for modeling surface tension," *Journal of Computational Physics*, vol. 100, no. 2, pp. 335–354, 1992.
- [16] D. Bhaga and M. E. Weber, "Bubbles in viscous liquids: shapes, wakes and velocities," *Journal of Fluid Mechanics*, vol. 105, no. 1, pp. 61–85, 1981.

Research Article

Study on the Instability of Two-Phase Flow in the Heat-Absorbing Tube of Trough Solar Collector

Ying Zhang,¹ Peiyao Liu,¹ Peisheng Li,^{1,2} Yue Chen,¹ and Yanni Pan¹

¹School of Mechanical and Electrical Engineering, Nanchang University, Nanchang, Jiangxi 330031, China

²Shangrao Normal College, Shangrao, Jiangxi 334001, China

Correspondence should be addressed to Peisheng Li; ncudns1995z@163.com

Received 26 July 2017; Accepted 30 August 2017; Published 23 October 2017

Academic Editor: Ben Xu

Copyright © 2017 Ying Zhang et al. This is an open access article distributed under the Creative Commons Attribution License, which permits unrestricted use, distribution, and reproduction in any medium, provided the original work is properly cited.

The Marangoni effect and Rayleigh-Benard effect in the two-phase region of solar trough heat-absorbing tube are simulated by FTM (front tracking method). Considering the Marangoni effect alone, although surface tension gradient and surface tension affect the interface wave, the two effects have different characteristics. The surface tension gradient caused by the temperature gradient is one of the factors that swing the interface. The amplitude attenuation of the interface wave decreases with the increase of the Marangoni number (Ma). In general, the surface tension gradient enhances the convection opposite to the temperature gradient. Under the gravity field, the Rayleigh-Benard effect influences the development of the vortex structure in the flow field, which in turn affects the velocity gradient near the interface to influence the evolution of the interface fluctuation. In a small Rayleigh number (Ra), the buoyancy convection reduces the velocity gradient, thus suppressing the evolution of the interfacial wave. In the range of $Ra < 4.0E4$, the larger the Ra, the stronger the inhibitory effect. However, when the Ra number is large ($Ra > 4.0E4$), the situation is just the opposite. The larger the Ra is, the stronger the promoting effect is.

1. Introduction

Heat-absorbing tube, the primary part of the solar thermal system, is a device used to convert solar energy to heat energy. Its stability and heat transfer efficiency inside have a direct impact on the operation of the whole system. A lot of researchers have studied its aspects. By numerical calculation, Muñoz and Abánades [1] and Kumar and Reddy [2] obtained results showing that changing the geometrical parameters can enhance the heat transfer and reduce the temperature gradient in the tube like adding a porous disk and using helical internal fins, thereby reducing heat loss. Flores and Almanza [3] designed a copper-steel composite bimetallic heat pipe which is helpful to reduce the circumferential temperature difference. Agrafiotis et al. [4] pointed out that the use of good thermal shock resistance of the ceramic material can effectively overcome the damage caused by temperature gradient. It is obvious to find that the temperature gradient inside is always harmful, which is too easy to cause the pipe bending, heat loss increase,

and a series of problems. However, scholars are more concentrated on the pipe material, structure or other external factors, and the effect of the radial temperature gradient on the flow in the tube, and the resulting heat loss had few analyses.

Poor radial temperature distributions create Marangoni and Rayleigh-Benard effects. The Marangoni effect and the Rayleigh-Benard effect cover large areas [5–7], included covering slags, contaminant transport, hypermonotectic alloy etc. Two effects were discovered very early [8, 9], but in recent years, scholars paid close attention to it again because this seemingly insignificant perturbation has a significant impact on fluid flow instability, heat transfer, and mass transfer [10–12]. The study for the two effects is mainly focused on the causes of convection and the effect of heat transfer and mass transfer on convections [13, 14]; however, little attention has been paid to the change of interface motion caused by the convective process.

As mentioned above, the Marangoni effect and Rayleigh-Benard effect in heat-absorbing tube have been studied

extensively, but the influence of the two effects on the interface fluctuation has not been explored thoroughly, due to the high-precision demand for interface tracking. Therefore, in order to study the interfacial fluctuation under the effect of convection caused by temperature gradient, this paper adopts a numerical method (FTM) with high interfacial numerical accuracy [15, 16], a numerical simulation of interface fluctuation within a two-phase region in a heat-absorbing tube is carried out, and some characteristics of Marangoni and Rayleigh-Benard effects on the variation of the interfacial fluctuation are found, which are expected to improve the internal working environment and to develop higher efficiency heat-absorption.

2. Mathematical Model and Numerical Method

2.1. Phase-Interface Tracking N-S Equation and Energy Equation

Assumptions. The fluid is incompressible Newtonian fluid, and the fluid density change satisfied the Boussinesq approximation without heat source; its two-dimensional flow momentum equation and energy equation can be written as follows:

$$\begin{aligned} \rho \frac{\partial u}{\partial t} + \rho \nabla \cdot uu &= -\nabla p + \rho g \beta (T - T_L) + \mu \nabla^2 u + f, \\ \frac{\partial \rho c_p T}{\partial t} + \nabla \cdot (\rho c_p T u) &= \nabla \cdot (k \nabla T). \end{aligned} \quad (1)$$

These equations are valid for the whole flow field, and the various fluids can be identified by a step (Heaviside) function H , which is written in Section 2.4, where u is velocity, p is pressure, ρ is the fluid density, μ is viscosity, g is acceleration of gravity, k is the thermal conductivity, c_p is the heat capacity at constant pressure, T is the temperature, f is the volumetric forces at the interface regardless of gravity, β is the thermal expansion coefficient, and T_L is the reference temperature in the Boussinesq model, which is the temperature of the cold wall.

2.2. The Surface Tension. Using the CSF (continuous-surface-force) method, the expression is

$$F_\sigma = \int_s \left[\sigma(T) kn + \frac{\partial \sigma(T)}{\partial (s)} t \right] \delta(x - x^f) ds, \quad (2)$$

where $\delta(x - x^f)$ is a Dirac function that when on the interface shows 1 and if not shows 0.

The surface tension is assumed to vary linearly with temperature, and the expression is as follows:

$$\sigma(T) = \sigma_0 + \gamma(T - T^*), \quad (3)$$

where γ is the temperature coefficient, in general, which has a negative value, T^* is the initial average temperature of the interface, and the temperature of the interface point is obtained from the fixed grid by bilinear interpolation.

2.3. Moving the Interface. The interface is usually combined with a fixed grid; the exchange of information between the interface and the grid is achieved through the area weight function. After the bilinear interpolation is performed, the moving speed of the interface can be obtained (well, the interface is always moving without the need of calculating the speed). Using a simple first-order explicit time integral, we can get the interface position in the next time step.

$$x_f^{(n+1)} = x_f^n + \Delta t u_f^n, \quad (4)$$

where $x_f^{(n+1)}$ and x_f^n are the position of the interface at time $n + 1$ and n , respectively, Δt is the time step, and u_f^n is the velocity of the interface at time n .

2.4. Reconstruction of Physical Field. For immiscible and incompressible fluid, fluid holds its characteristics, respectively, at both sides of the interface. When the interface moves, the distribution of interfacial parameter also changes, so we use the Heaviside function to characterize this change:

$$H(\varphi) = \begin{cases} 1, & \varphi > \alpha \\ \frac{1}{2} \left(1 + \frac{\varphi}{\alpha} + \frac{1}{\pi} \left(\frac{\pi \varphi}{\alpha} \right) \right), & \|\varphi\| \leq \alpha \\ 0, & \varphi < -\alpha, \end{cases} \quad (5)$$

where φ is the distance to the interface of a given point and 2α is the thickness of the transition region between the absolute value of the two fluids. Therefore, the distribution of density, viscosity, thermal conductivity, and constant pressure heat capacity is obtained by using the abovementioned instruction function.

2.5. The Physical Model. As shown in Figure 1(a), the heat-absorbing tubes are placed horizontally and there are three sections. The second zone of the steam-water two-phase zone is taken as the research object as shown in Figure 1(b). T_H and T_L are the radiation surface temperature (high temperature) and the back radiation surface temperature (low temperature), respectively. The temperature difference of the high and low temperature wall is set to 100; all the physical quantities used in this article have been nondimensionalized. The calculated domain size is $L \times L = 1 \times 1$, the grid number is 600×600 , where h is the grid spacing, $\Delta t = 0.06h$, and an initial disturbance of 0.1 at $Y = 0.5$ was provided, due to the existence of relative movement between the upper and lower layers of fluid; therefore, an initial shear field [17] can be set as follows:

$$I(x, y) = \tan h \left[\frac{y - 0.5 - 0.01 \sin(2\pi x)}{0.02} \right]. \quad (6)$$

The fluid's initial speed is defined as follows:

$$\begin{aligned} u(x, y, 0) &= \theta I(x, y), \\ v(x, y, 0) &= 0, \end{aligned} \quad (7)$$

where θ is the velocity coefficient.

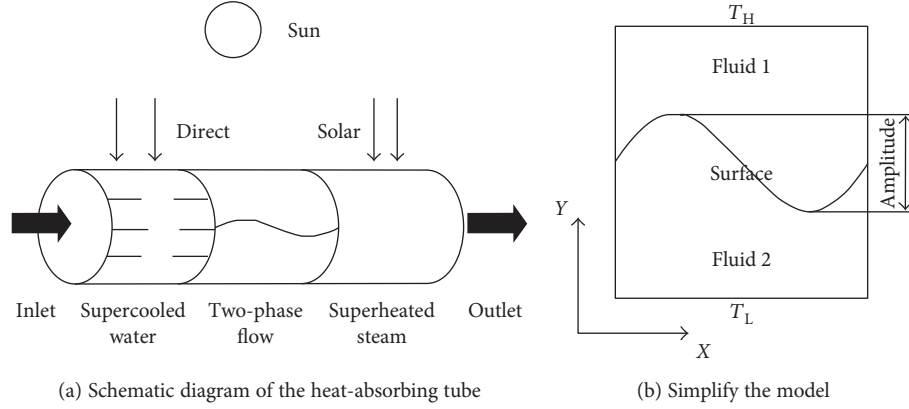


FIGURE 1: Physical model.

2.6. Model Verification. Where there is large shear force across an initial amplitude between two-component fluids, the interface is unstable, which is called Kelvin-Helmholtz instability. According to the results from Lee and Kim [17]. When we set $h = 1/256$, $\Delta t = 0.064h$, $Re = 5000$, and $g = \sigma = 0$, the analytical nondimensional growth rate γ_e can be written as follows:

$$\gamma_e = \frac{4\pi\sqrt{r}}{1+r}. \quad (8)$$

r is the density ratio between two fluids.

The numerical growth rate γ_n can be written as

$$\gamma_n = \frac{A(t)/(A_0 - 1)}{t}, \quad (9)$$

where A_0 is the initial amplitude.

In this paper, a model verification was provided by comparing with the numerical results from analytical results as shown in Figure 2. It depicts that two results are in good agreement. The conclusion shows that the numerical method of this paper can realize the description of the interface instability process well.

2.7. Dimensionless Definition. The Marangoni number was defined as

$$Ma = \frac{\gamma|\nabla T|d}{\mu_2 a_2}. \quad (10)$$

The Reynolds number was defined as

$$Re = \frac{\rho_2 u_0 d}{\mu_2}, \quad (11)$$

where u_0 is the initial velocity of the fluid in the gravity field defined as $u_0 = g\rho_2 d^2 / 2\mu_2$.

The Rayleigh number was defined as

$$Ra = \frac{\beta\rho_2 g \nabla T d^3}{\mu_2 a_2}. \quad (12)$$

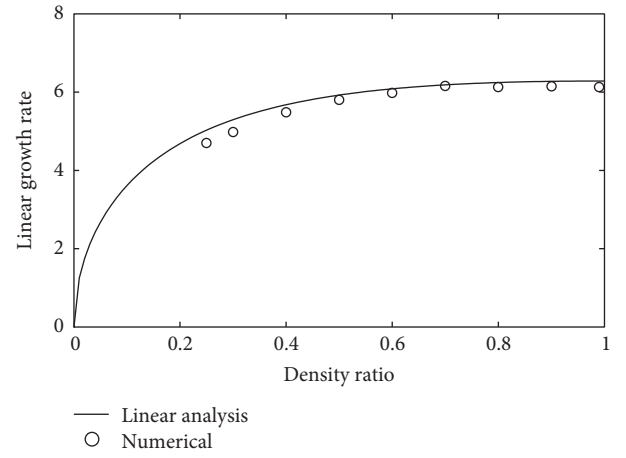


FIGURE 2: Comparison of simulation results with analytical results.

3. Result and Discussion

3.1. Marangoni Effect on Liquid Membrane Flow. In microgravity or zero gravity, the Rayleigh-Benard effect is very weak; in order to highlight the effects of the Marangoni effect, gravity is not considered here. Considering that the velocity of the two-phase zone in the heat-absorbing tube is small, when the Reynolds number is small, the fluid instability will not continue to develop but will be restored due to the smaller shear force at the interface. At the same time, due to the smaller size of convective heat transfer in the flow field, a vertical downward temperature gradient can still be formed near the interface. There will be two effects at this point; on the one hand, as the temperature changes, the surface tension coefficient accordingly. As shown in Figures 3(a), 3(b), and 3(c), in the initial stage ($t = 0.03$), the pressure produced by the interface varies obviously due to the different coefficients of surface tension. The larger the Ma number is, the lower the pressure difference at the wave crest (high temperature) is, and the greater the pressure difference at the trough (low temperature) is. In addition, it can be found in Figure 3(a) that the internal and external pressures are approximately symmetrical, but Figures 3(b) and 3(c), Ma is not zero. Due to the effect of the tangential surface tension, the internal

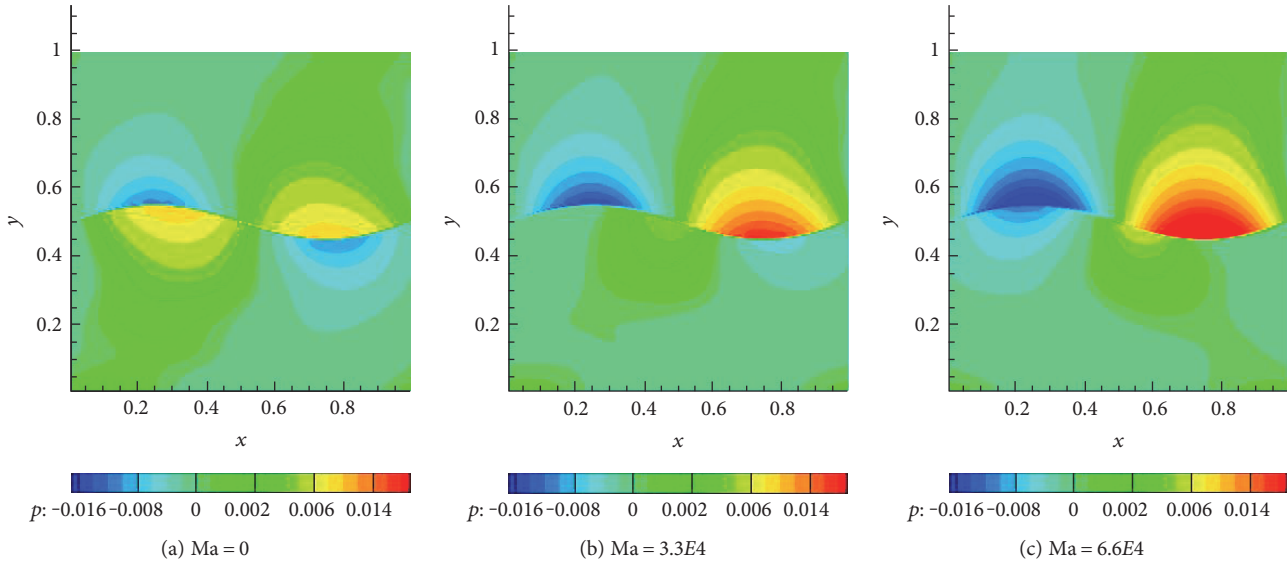


FIGURE 3: The pressure distribution of the interface at $T=0.03$ time, $Re = 12.5$.

and external pressures at the crest and trough interface become asymmetrical.

On the other hand, the surface tension gradient caused by the temperature gradient affects the motion of the interface, which inhibits perturbations moving in the same direction of the temperature gradient and promotes perturbations moving in the opposite direction of the temperature gradient. The numerical value of the surface tension affects the normal surface tension, while the surface tension gradient affects the tangential surface tension. In order to distinguish the difference between the normal surface tension and the tangential surface tension, Figure 4 depicts the time dependent curves of the peaks and troughs of the interface when the coefficient of surface tension and the number of Ma are changed, respectively. As can be seen from the figure, the wave crests and troughs are symmetrically changed under the same conditions. In further analysis, comparing the curves of $Ma=0$, σ (surface tension coefficient)=0.01, and $Ma=0$, $\sigma=0.02$ in Figure 4, increasing the surface tension coefficient reduces the fluctuation period, and when the number of fluctuations is the same, the fluctuation range of the crest and trough increases. But comparing the curves of $\sigma=0.01$, $Ma=0$ and $\sigma=0.01$, $Ma=3.33E4$, at the crest of the latter, the surface tension decreases due to the influence of temperature, and only from this point of view, the wave period of crest should be increased. However, the reaction in the curve is not the case because the surface tension gradient is downward, and the period of wave crest decreases at the trough; the surface tension coefficient is greater than the average because the temperature is lower; if only the increase of the coefficient of surface tension is considered, the magnitude of the trough recovery should be increased. Because of the downward surface tension gradient, the upward recovery movement is suppressed, and the upper pole of the first movement of $Ma=3.33E4$ is smaller than that of $Ma=0$; comparing the curves of $\sigma=0.01$, $Ma=1.33E4$ and $\sigma=0.01$, $Ma=3.33E4$, respectively, from the two sets

of curves, we can see that the difference of peaks and troughs due to the surface tension gradient increases with the increase in the Ma numbers. At the later stage of the motion, the disturbance amplitude is gradually smaller, and the repeated fluctuation make the single temperature gradient near the interface gradually disappear, and the disturbance fluctuation gradually becomes symmetrical. On the whole, in the Marangoni system, the existence of the surface tension gradient increases the unstable factors, and the larger the Ma number is, the longer is the time required for the interface disturbance to recover.

Because of the gradient of surface tension, the flow field is strengthened in the direction of temperature gradient and the temperature change near the bottom of the interface is affected. This change fluctuates with the fluctuation of the interface, and the fluctuation is similar. Figure 5 shows the change of the average temperature between 0.2 and 0.4 in the longitudinal direction of the flow field (y -axis). When the number of Ma is zero, the bottom temperature changes with a very symmetrical periodic change, while the number of Ma is not equal to zero. The temperature fluctuation amplitude is greatly enhanced. At the beginning of the movement, as the deformation of the interface begins to recover, the bottom temperature begins to decrease, but the surface tension gradient promotes downward convection; the larger the Ma number is, the smaller the temperature drop is and the faster the temperature rise is. In addition, the increase of the Ma number increases the magnitude of the temperature rise.

3.2. The Effect of Rayleigh-Benard Effect on the Stability of Fluid Interface under Gravity. In the normal gravity field, the Marangoni effect is almost negligible compared with the Rayleigh-Benard effect. Therefore, the influence of the Rayleigh-Benard effect on the flow field of the fluid interface is studied by setting the upper fluid in the opposite direction to the underlying fluid; the influence of the Marangoni effect

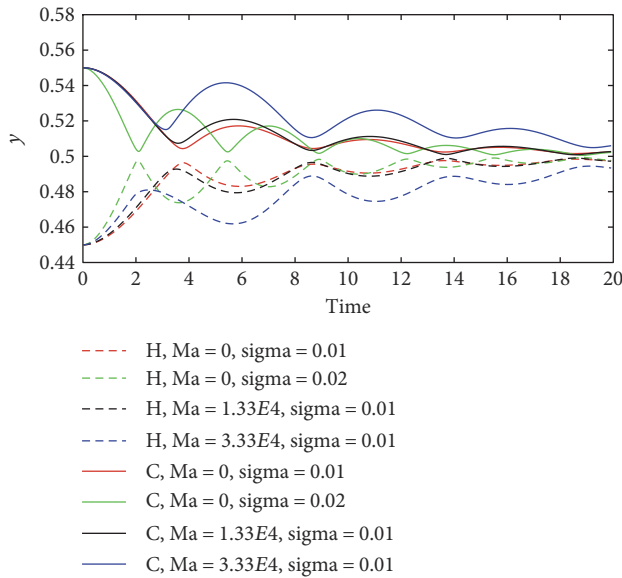


FIGURE 4: Curve of the position of wave crest and trough with time. H is the trough, C is the crest, $Re = 12.5$.

is ignored. Figure 6 shows the streamline with $Ra = 0, 1.25E4$, and $6.25E4$ and with $T = 0.09, 1.99$, and 4.44 , respectively. In order to observe it better, a separate color note was used each time. As shown in Figure 6, the vortices generated by the Rayleigh-Benard effect interacts with the original vortices. When the Ra number is small ($Ra = 1.25E4$, Figures 5(b), 5(e), and 5(h)), the center of the flow field generates a vortex with a larger vortex velocity. When the Ra number is large ($Ra = 6.25E4$, Figures 5(c), 5(f), and 5(i)), the eddy current in the center of the flow field does not change significantly in the X direction, but the velocity of turbulence increases obviously on both sides. When $t = 1.99$ and $Ra = 0$, the vortex develops only near the interface, and in the case of $Ra = 1.25E4$, the range of the vortex becomes larger and is almost filled with the half of area. And two plume vorticities are produced in the lower left corner and the lower right corner. The kinetic energy is constantly dissipated in the rotary motion, so the velocity of the fluid decreases gradually. In the case of $Ra = 6.25E4$, the distribution of vortices is similar to that of $Ra = 0$, only at the vicinity of the interface, and the velocity of the upper fluid becomes larger. By the influence of the Rayleigh-Benard effect, when Ra is not zero, the flow rate of the lower fluid decreases. Moreover, the speed at $Ra = 1.25E4$ decreases by a greater magnitude than that of $Ra = 6.25E4$. The flow rate of the upper fluid is different from that of the lower fluid. At $Ra = 1.25E4$, the flow rate of the upper fluid decreases, while when $Ra = 6.25E4$, the flow rate of the upper fluid increases significantly. In general, when $Ra = 1.25E4$, the difference of velocity between fluids decreases; when $Ra = 6.25E4$, it suggests the opposite. Another big difference is the vortex structure in later stage, when $Ra = 0$, it almost disappears; in the case when Ra is not zero, there is always a vortex at the center of the flow field.

Figure 7 shows the time-dependent curves of amplitude in different Ra number. At $Ra = 0$, the velocity gradient

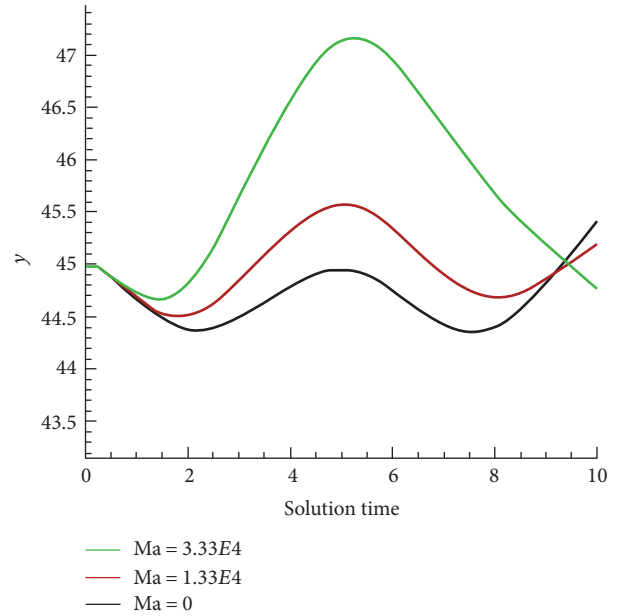


FIGURE 5: Temperature changes of bottom.

between fluids is so large that the surface tension can no longer overcome the shear force and maintain the original state, which results in the appearance of the fingers at the interface; this phenomenon has been mentioned by [18]. When $Ra = 1.25E4$, the Rayleigh-Benard effect reduces the velocity difference, and the disturbance does not produce the finger-like protrusions, but the amplitude of interface decreases gradually. When $Ra = 6.25E4$, the difference increases and the amplitude increases. In addition, the interface development does not monotonically because of the existence of vortices, and by the same reason, tremors becomes unstable after $T = 5$ in the case of $Ra = 6.25E4$ and $Ra = 0$.

So the influence of the Rayleigh-Benard effect on the interface perturbation is found to have two opposite effects when the Ra number is small and the Ra number is large. As shown in Figure 7, since the phase of the interface wave is different in different cases, the second trough of the curve in Figure 7 is taken as a form. It can be seen from Figure 8 that in the range of $1.0E4 < Ra < 4.00E4$, the amplitude of the interface wave decreases with the increase of Ra number, that is, with the increase of Ra number, the inhibition of buoyancy convection on the interfacial wave instability is increasingly strong, which is opposite to the case of $4.0E4 < Ra < 6E.04$.

4. Conclusions

In this paper, we consider the flow effect caused by the uneven temperature distribution in the basic FTM model and simulate the evolution process of the interface wave at the shear field with or without gravity, providing a theoretical basis for the optimization design of the heat-absorbing tube. The specific research results are as follows:

- (1) In the shear field, when only the Marangoni effect is considered, the interface evolution is affected by

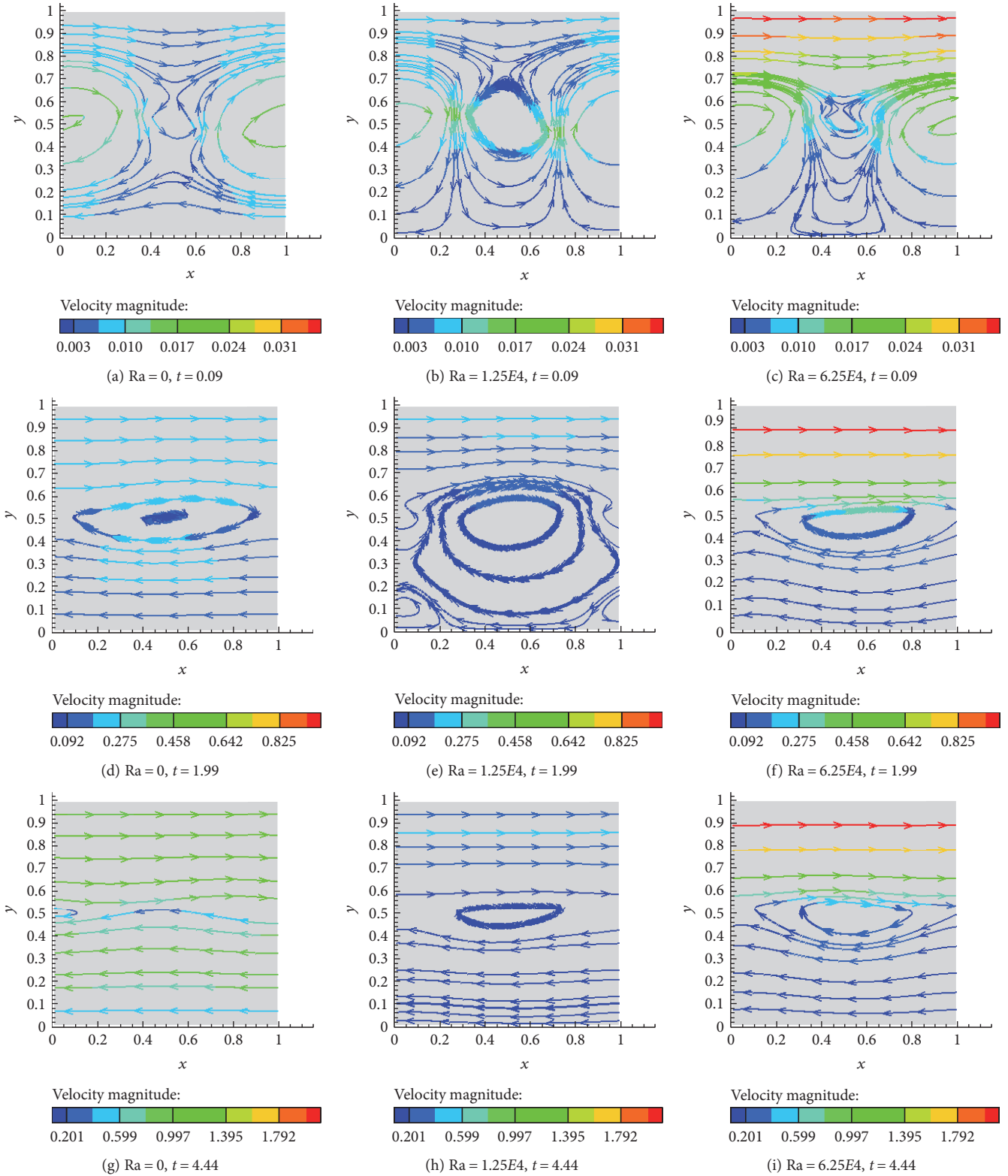


FIGURE 6: Streamlines in different Ra numbers.

both surface tension and the gradient of surface tension. When the motion direction of the interface is the same as that of the surface tension gradient, the motion is promoted. As a whole, the

surface tension gradient increases the instability due to the temperature change, and the attenuation of the amplitude becomes slower. Therefore, the choice of large temperature coefficient of the

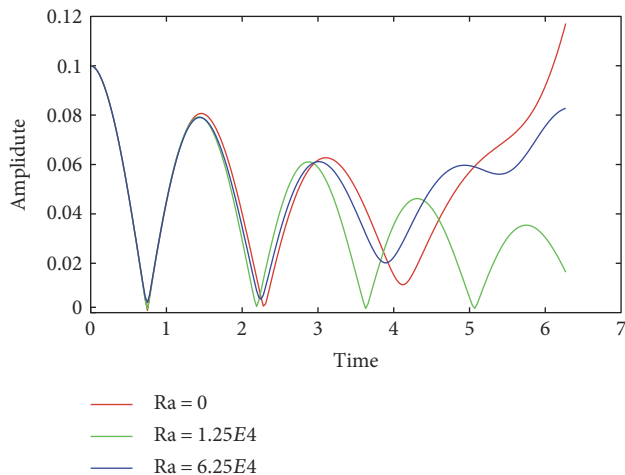


FIGURE 7: Curves of interface amplitude versus time when $Ra = 0$, $1.25E4$, $6.25E4$.

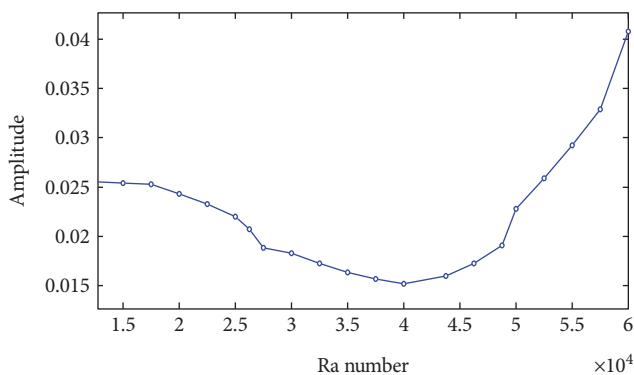


FIGURE 8: Disturbance amplitude in different Ra number when at $T = 6$ times.

fluid can enhance the heat transfer in the heat-absorbing tube.

- (2) In the gravitational field, the Marangoni effect and the Rayleigh-Benard effect work together, but compared with the Marangoni effect, the Rayleigh-Benard effect dominates and does not have obvious directionality; at first, it affects the development of the flow field vortex structure, and then the change of the velocity gradient near the interface affects the evolution of the interfacial fluctuations. When the Ra number is small, the buoyancy convection causes the velocity gradient to decrease and suppress the evolution of the interface wave, and the function is stronger in no other Ra number than $4.0E4$. However, when the Ra number is large, the situation is exactly the opposite to the small one. From what has been discussed above, it is better to let the Ra number stay away from $4.0E4$ by some means such as the fluid's density, viscosity and thermal expansion coefficient, which make the flow field vortex movement most violently, and is the most favorable for heat transfer.

Conflicts of Interest

The authors declare that there is no conflict of interest regarding the publication of this paper.

Acknowledgments

The authors gratefully acknowledge the support under the National Natural Science Foundation of China (Grant no. 11562011) and the funds from Hundred Sail Away Project in 2015 provided by Jiangxi Provincial Party Committee Organization Department and Jiangxi Association for Science and Technology.

References

- [1] J. Muñoz and A. Abánades, "A technical note on application of internally finned tubes in solar parabolic trough absorber pipes," *Solar Energy*, vol. 85, no. 3, pp. 609–612, 2011.
- [2] K. R. Kumar and K. S. Reddy, "Thermal analysis of solar parabolic trough with porous disc receiver," *Applied Energy*, vol. 86, no. 9, pp. 1804–1812, 2009.
- [3] V. Flores and R. Almanza, "Behavior of the compound wall copper-steel receiver with stratified two-phase flow regimen in transient states when solar irradiance is arriving on one side of receiver," *Solar Energy*, vol. 76, no. 1–3, pp. 195–198, 2004.
- [4] C. C. Agrafiotis, I. Mavroidis, A. G. Konstandopoulos et al., "Evaluation of porous silicon carbide monolithic honeycombs as volumetric receivers/collectors of concentrated solar radiation," *Solar Energy Materials and Solar Cells*, vol. 91, no. 6, pp. 474–488, 2007.
- [5] Y. Ueshima, "Evaluation of local dissolution rates and wetting behaviors of solid alumina in liquid slag with the Marangoni number," *ISIJ International*, vol. 56, no. 8, pp. 1506–1508, 2016.
- [6] P. Lakshmanan and P. Ehrhard, "Marangoni effects caused by contaminants adsorbed on bubble surfaces," *Journal of Fluid Mechanics*, vol. 647, no. 9, pp. 143–161, 2010.
- [7] H. B. Cui, C. Y. Li, K. F. Wang, G. F. Mi, J. J. Guo, and Y. Q. Su, "Effect of Marangoni convection on microstructure evolution of Cu-Pb hypermonotectic alloy by phase field simulation," *Foundry*, vol. 57, no. 11, pp. 1176–1180, 2008.
- [8] K. Mukai, "Recent studies on the interfacial phenomena in which Marangoni effect participates," *Tetsu-to-Hagané*, vol. 71, no. 11, pp. 1435–1440, 1985.
- [9] E. Bodenschatz, W. Pesch, and G. Ahlers, "Recent developments in Rayleigh-Bénard convection," *Annual Review of Fluid Mechanics*, vol. 32, no. 1, pp. 709–778, 2000.
- [10] Z. Alloui and P. Vasseur, "Onset of Marangoni convection and multiple solutions in a power-law fluid layer under a zero gravity environment," *International Journal of Heat and Mass Transfer*, vol. 58, no. 1–2, pp. 43–52, 2013.
- [11] T. P. Lyubimova, D. V. Lyubimov, and Y. N. Parshakova, "Implications of the Marangoni effect on the onset of Rayleigh-Bénard convection in a two-layer system with a deformable interface," *The European Physical Journal Special Topics*, vol. 224, no. 2, pp. 249–259, 2015.
- [12] L. V. Matveev, "Impurity transport in developed Rayleigh-Bénard convection," *International Journal of Heat and Mass Transfer*, vol. 95, pp. 15–21, 2016.

- [13] P. G. Siddheshwar, V. Ramachandramurthy, and D. Uma, "Rayleigh-Bénard and Marangoni magnetoconvection in Newtonian liquid with thermorheological effects," *International Journal of Engineering Science*, vol. 49, no. 10, pp. 1078–1094, 2011.
- [14] A. B. Pieri, F. Falasca, J. von Hardenberg, and A. Provenzale, "Plume dynamics in rotating Rayleigh-Bénard convection," *Physics Letters A*, vol. 380, no. 14, pp. 1363–1367, 2016.
- [15] W. Tauber, S. O. Unverdi, and G. Tryggvason, "The nonlinear behavior of a sheared immiscible fluid interface," *Physics of Fluids*, vol. 14, no. 8, pp. 2871–2885, 2002.
- [16] J. Zhang, D. M. Eckmann, and P. S. Ayyaswamy, "A front tracking method for a deformable intravascular bubble in a tube with soluble surfactant transport," *Journal of Computational Physics*, vol. 214, no. 1, pp. 366–396, 2006.
- [17] H. G. Lee and J. Kim, "Two-dimensional Kelvin-Helmholtz instabilities of multi-component fluids," *European Journal of Mechanics - B/Fluids*, vol. 49, pp. 77–88, 2015.
- [18] X. M. Ye, Y. Zhang, S. L. Wang, and C. X. Li, "Investigation on stability of sheared wavy liquid films," *Proceedings of the Chinese Society of Electrical Engineering*, vol. 27, no. 20, pp. 103–106, 2007.

Research Article

Predictive Power of Machine Learning for Optimizing Solar Water Heater Performance: The Potential Application of High-Throughput Screening

Hao Li,^{1,2} Zhijian Liu,³ Kejun Liu,⁴ and Zhien Zhang⁵

¹Department of Chemistry, The University of Texas at Austin, 105 E. 24th Street, Stop A5300, Austin, TX 78712, USA

²Institute for Computational and Engineering Sciences, The University of Texas at Austin, 105 E. 24th Street, Stop A5300, Austin, TX 78712, USA

³Department of Power Engineering, School of Energy, Power and Mechanical Engineering, North China Electric Power University, Baoding 071003, China

⁴Department of Computer Science, Rice University, 6100 Main Street, Houston, TX 77005-1827, USA

⁵School of Chemistry and Chemical Engineering, Chongqing University of Technology, Chongqing 400054, China

Correspondence should be addressed to Hao Li; lihao@utexas.edu

Received 12 July 2017; Revised 6 August 2017; Accepted 5 September 2017; Published 24 September 2017

Academic Editor: Zhonghao Rao

Copyright © 2017 Hao Li et al. This is an open access article distributed under the Creative Commons Attribution License, which permits unrestricted use, distribution, and reproduction in any medium, provided the original work is properly cited.

Predicting the performance of solar water heater (SWH) is challenging due to the complexity of the system. Fortunately, knowledge-based machine learning can provide a fast and precise prediction method for SWH performance. With the predictive power of machine learning models, we can further solve a more challenging question: how to cost-effectively design a high-performance SWH? Here, we summarize our recent studies and propose a general framework of SWH design using a machine learning-based high-throughput screening (HTS) method. Design of water-in-glass evacuated tube solar water heater (WGET-SWH) is selected as a case study to show the potential application of machine learning-based HTS to the design and optimization of solar energy systems.

1. Introduction

How to cost-effectively design a high-performance solar energy conversion system has long been a challenge. Solar water heater (SWH), as a typical solar energy conversion system, has complicated heat transfer and storage properties that are not easy to be measured and predicted by conventional ways. In general, an SWH system uses solar collectors and concentrators to gather, store, and use solar radiation to heat air or water in domestic, commercial, or industrial plants [1]. For the design of high-performance SWH, the knowledge about correlations between the external settings and coefficients of thermal performance (CTP) is required. However, some of the correlations are hard to know for the following reasons: (i) measurements are time-consuming [2]; (ii) control experiments are usually difficult to perform; and (iii) there is no current physical model that can precisely

connect the relationships between external settings and intrinsic properties for SWH. Currently, there are some state-of-the-art methods for the estimation of energy system properties [3–5] and for the optimization of performances [6–11]. However, most of them are not suitable for the solar energy system. These problems, together with the economic concerns, significantly hinder the rational design of high-performance SWH.

Fortunately, machine learning, as a powerful technique for nonlinear fitting, is able to help us precisely acquire the values of CTP with the knowledge of some easy-measured independent variables. With a sufficiently large database, a machine learning technique with appropriate algorithms can “learn” from the numerical correlations hidden in the dataset via a nonlinear fitting process and perform precise predictions. With such a technique, we do not need to exactly find out the physical models for each CTP and can directly

acquire a precise prediction with a well-developed predictive model. During the past decades, Kalogirou et al. have done a large number of machine learning-based numerical predictions of some important CTPs for solar energy systems [12–19]. Their results show that there is a huge potential application of machine learning techniques to energy systems. Based on their successful works, we recently developed a series of machine learning models for the predictions of heat collection rates (daily heat collection per square meter of a solar water system, MJ/m²) and heat loss coefficients (the average heat loss per unit, W/(m³K)) to a water-in-glass evacuated tube solar water heater (WGET-SWH) system [2, 20, 21]. Our results show that with some easy-measured independent variables (e.g., number of tubes and tube length), both heat collection rates and heat loss coefficients can be precisely predicted after some proper trainings from the datasets, with proper algorithms (e.g., artificial neural networks (ANNs) [2, 20], support vector machine (SVM) [2], and extreme learning machine (ELM) [21]). An ANN-based user-friendly software was also developed for quick measurements [20]. These novel machine learning-assisted measurements dramatically shorten the measurement period from weeks to seconds, which has good industrial benefits. However, all the machine learning studies mentioned here are only the predictions and/or measurements. So far, very few industries really put these methods into practical applications. To the best of our knowledge, very few references concern about the optimization of thermal performance of energy systems using such a powerful knowledge-based technique [22]. To address this challenge, we recently used a high-throughput screening (HTS) method combined with a well-trained ANN model to screen 3.5×10^8 possible designs of new WGET-SWH settings, in good agreement with the subsequent experimental validations [23]. This is so far the first trial of HTS to a solar energy system design. The HTS method (roughly defined as the screening of the candidates with the best target properties using advanced high-throughput experimental and/or computational techniques) has already been widely used in biological [24–28] and computational [29–31] areas. With the basic concept that screening thousands or even millions of possible cases to discover the candidates with the best target functions or performances, HTS helps people dramatically reduce the required regular experiments, saving much economic cost and manpower.

In this paper, we aim to propose an HTS framework for optimizing a solar energy system. Picking SWH as a case study, we show how this optimization strategy can be applied to a novel solar energy system design. Different from the study by Liu et al. [23], this paper shows the predictive power of machine learning and the development of a general HTS framework. Instead of listing tedious mathematical works, in this paper, we provide vital details about the general modeling and HTS process. Since tube solar collectors have a substantially lower heat loss coefficient than other types of collectors [12, 32], WGET-SWHs gradually become popular during the past decades [33–35], with the advantages of excellent thermal performance and easy transportability [36, 37]. With this reason, we chose the WGET-SWH system

as a typical SWH, to show how a well-developed ANN model can be used to cost-effectively optimize the thermal performance of an SWH system, using an HTS method.

2. Machine Learning Methods

2.1. Principles of an ANN. There are various machine learning algorithms that have been effectively applied to the prediction of properties for energy systems, such as ANN [12, 13, 17, 18, 20, 38], SVM [20, 39, 40], and ELM [21, 41]. Because the ANN method is the most popular algorithm for numerical predictions [42], we only introduce the basic principle of ANN here. A general schematic ANN structure is shown in Figure 1, with the input, hidden, and output layers constructed by certain numbers of “neurons.” Each neuron (also called a “node”) in the input layer, respectively, represents a specific independent variable. The neuron in the output layer represents the dependent variable that is needed to be predicted. Usually, the independent variables should be the easy-measured variables that have a potential relationship with the dependent variable. The dependent variable is usually the variable that is hard to be detected from experiments and is expected to be precisely predicted. The layer between the input and output layers shown in Figure 1 is the hidden layer. The optimal number of neurons in the hidden layer depends on the study object and the scale of the dataset. Each neuron connects to all the neurons in the adjacent layer, with the connection called the weight (usually represented as w), which directly decides the predictive performance of the ANN, using the activation functions. For the training of an ANN, the initial weights will be first selected randomly, and then following iterations would help find out the optimal weight values that fulfill the prediction criterions. All the data move only in the same direction (from left to right, as shown in Figure 1). A well-trained ANN should consist of the optimal numbers of hidden layer neurons, hidden layer(s), and weight values, which sufficiently avoid the risk of either under- or overfitting. In practical applications, there is a large number of neural networks with modified algorithms, such as ELM [43–45], back-propagation neural network (BPNN) [46–48], and general regression neural network (GRNN) [49–51]. Though there are various network models, the basic principles for model training are similar.

2.2. Training of an ANN. To train a robust ANN, several factors should be considered: (i) percentages of the training and testing sets; (ii) number of hidden neurons; (iii) number of hidden layers; and (iv) required time for training. When training a practical ANN for real applications, a large training set is recommended. For predicting the heat collection rates of WGET-SWHs, we found that with a relatively large dataset (>900 data groups), the training set higher than 85% could help acquire a model with good predictive performance in the testing set [2]. Another reason to use a large training set is that if the training set percentage is small, it would be a waste of data for practical applications. The reason is simple: more data groups for training would usually lead to a better predictive performance. For the selection of the number of

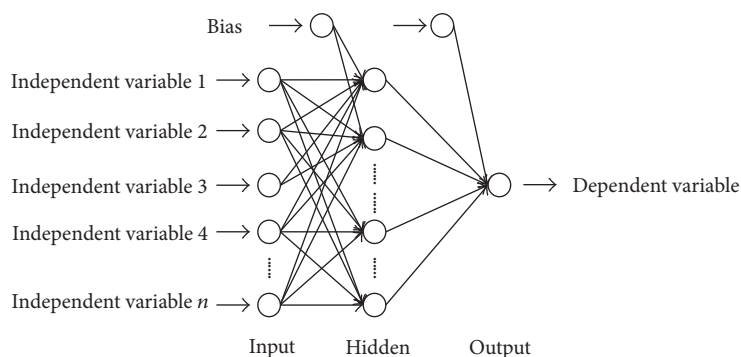


FIGURE 1: Schematic structure of a typical ANN. Circles represent the neurons in the algorithm.

hidden neurons, it is quite important to try the neuron numbers from low to high. If the number of hidden neurons is not enough, there would be a risk of underfitting; if it is too many, there would be a risk of overfitting and time-consuming. Therefore, finding the best number of neurons by comparison is particularly important. It should be noted that in some special neural network methods (e.g., GRNN), the number of hidden neurons can be a fixed value once the dataset is defined in some software packages. Under this circumstance, it is no longer necessary to worry about the hidden neuron settings. In addition to the hidden neuron numbers, same tests should be done on the number of layers, in order to avoid either under- or overfitting. The last factor we need to consider is the training time. According to the basic principle of an ANN (Figure 1), the interconnection among neurons would become more complicated with higher numbers of neuron. Therefore, with larger database and larger numbers of independent variables and hidden neurons, the training time would be longer. This means that sometimes an ordinary personal computer (PC) cannot sustain a tedious cross-validation test. From our previous studies with an ANN training [2, 51], we found that if the database was sufficiently large, repeated training and/or cross-validation training would lead to insignificant fluctuation. In other words, for practical applications, the ANN training and testing results would be robust if the database is large, and so a cross-validation process can be rationally skipped after a simple sensitivity test, in order to save computational cost.

2.3. Testing of an ANN. Using a testing result with an ANN for the prediction of heat collection rate as an example (Figure 2), we can see that a well-trained ANN can precisely predict the heat collection rates of the data in the testing set, with relatively low absolute residual values. Though there are still deviations exist in some predicted points, the overall accuracy is still relatively high and acceptable to practical applications. It should be noted that for a solar energy system, the independent variables for modeling should always include some environmental variables, such as solar radiation intensity and ambient temperature [2]. These variables are highly dependent to the external temperature, location, and season. That is to say, the external conditions of the predicted data should be in the similar environmental

conditions as the data used for the model training. Otherwise, the ANN may not perform good predictive performance. In all of our recent studies, all the data measurements were performed in very similar season, temperature, and location, which can sufficiently ensure precise predicted results in both the testing set and subsequent experimental validation.

3. High-Throughput Screening (HTS)

The basic idea of computational HTS is simple: the calculations of all possible systems in a certain time period (using fast algorithms) and the screening of the candidates with target performances. Previously, Greeley et al. used density functional theory (DFT) calculations to screen and design high-performance metallic catalysts for hydrogen evolution reaction via an HTS method, in good agreement with experimental validations [29]. Hautier et al. combined DFT calculations, machine learning, and HTS methods to predict the missing ternary oxide compounds in nature and develop a completed ternary oxide database [31], which shows that a machine learning-assisted HTS process can be precisely used for new material prediction and discovery. However, though the HTS method has been widely used in many areas, its conceptual applications to energy system optimization is not reported during the past decade.

Very recently, our studies show that the machine learning-assisted HTS process can be effectively performed on the optimization of solar energy system [23]. Choosing WGET-SWH as a case study, our results show that an HTS process with a well-trained ANN model can be used for the optimization of heat collection rate of SWH. The first step was to generate an extremely large number of independent variable combinations (3.5×10^8 possible design combinations) as the input of a well-trained ANN model. The heat collection rates of all these combinations were then, respectively, predicted by the ANN. After that, the new designs with high predicted heat collection rates were recorded as the candidate database. For validation, we installed two screened cases and performed rigorous measurements. The experimental results showed that the two selected cases had higher average heat collection rates than all the existing cases in our previous measurement database. Being similar to a previous chemical HTS concept proposed by Pyzer-Knapp et al. [52], we reconstruct the process of this

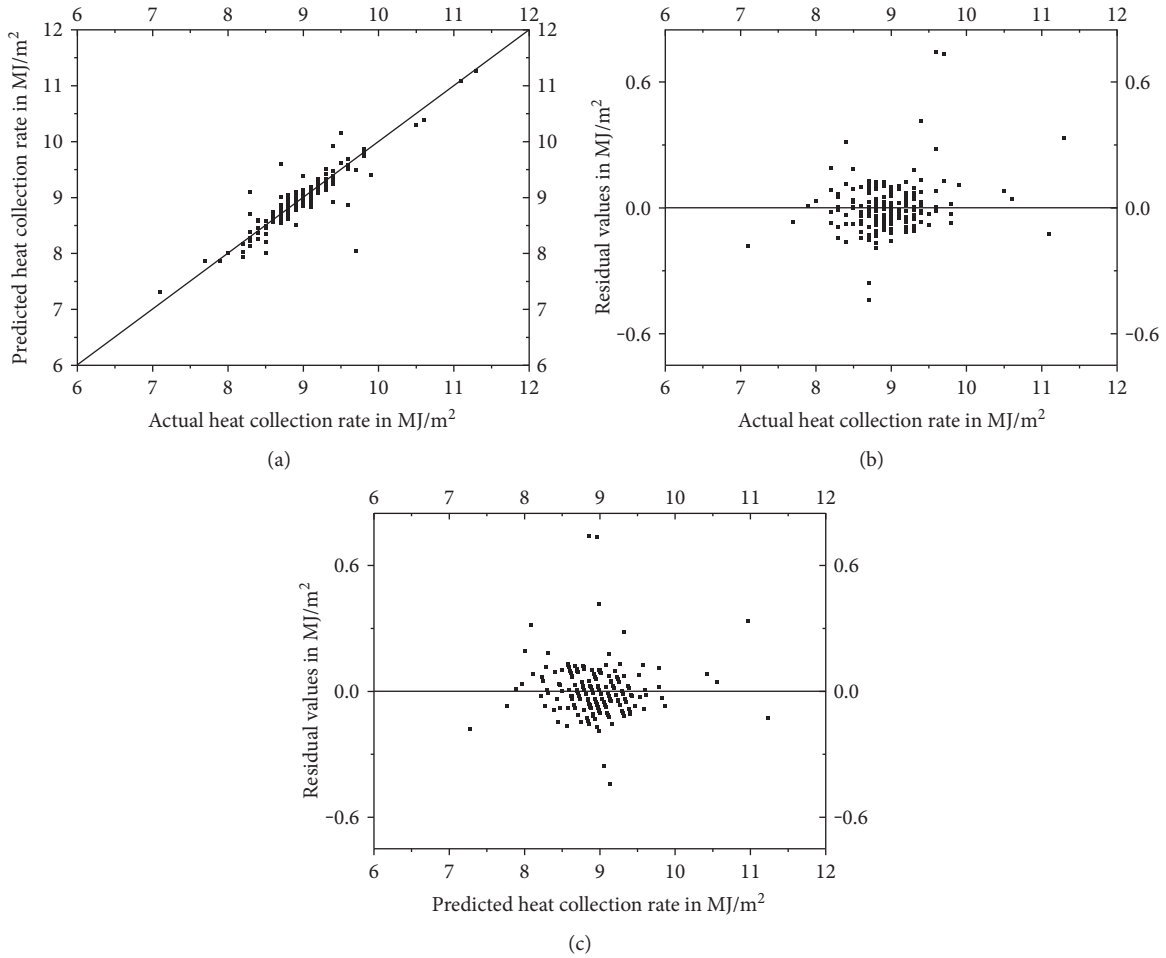


FIGURE 2: Testing results using an ANN model for the prediction of heat collection rate for WGET-SWHs. (a) Predicted values versus actual values; (b) residual values versus actual values; and (c) residual values versus predicted values. Reproduced with permission from Liu et al. [2].

optimization method, as shown in Figure 3. More modeling and experimental details can be found in [23].

4. HTS-Based Optimization Framework

Based on the recent trials on the HTS-based optimization method to the SWH system, here, we propose a framework for the design and optimization of solar energy systems. Though the machine learning-based HTS method is a quick design strategy, the preconditions should be fulfilled rigorously. That means, two vital conditions should be fulfilled, including (i) a well-trained machine learning model and (ii) a rational generation of possible inputs.

4.1. A Well-Trained Machine Learning Model. To acquire a well-trained machine learning model, in addition to the regular training and testing processes as shown in Sections 2.2 and 2.3, another key step is to define the independent variables for training. Since the dependent variable is usually the quantified performance of the energy system, the selection of an independent variable which has potential relationships with the dependent variable would directly decide the predictive precision of the model. In our previous case [23],

we chose seven independent variables as the inputs, including tube length, number of tubes, tube center distance, tank volume, collector area, final temperature, and tilting angle (the angle between tubes and the ground). A 3-D schematic design of a WGET-SWH system is shown in Figure 4 [23], which shows that only with these independent variables can we reconstruct a WGET-SWH system quickly with some other minor empirical settings. Unlike a physical model (which requires rigorous mathematical deduction and hypothesis), machine learning does not require the user to know exactly about the potential relationships between the independent and dependent variables. This feature also leads to the fact that machine learning prediction method is more flexible than conventional methods. From these seven inputs, we can see that except for the final temperature, all the other six variables are the important parameters of a WGET-SWH. In terms of the final temperature, we found that this is extremely important to ensure a precise model for heat collection rate prediction. The reason is simple: the heat collection performance of a WGET-SWH is not only decided by the mechanical settings of the system but also depends on the environmental conditions such as solar radiation intensity, ambient temperature, and the final temperature. Since

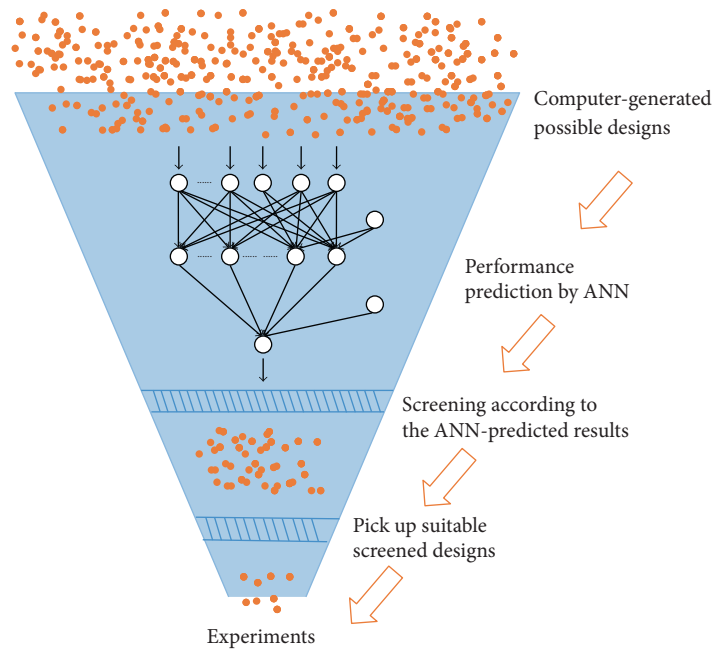


FIGURE 3: An HTS process for solar energy system optimization. Each orange circle represents a possible design.

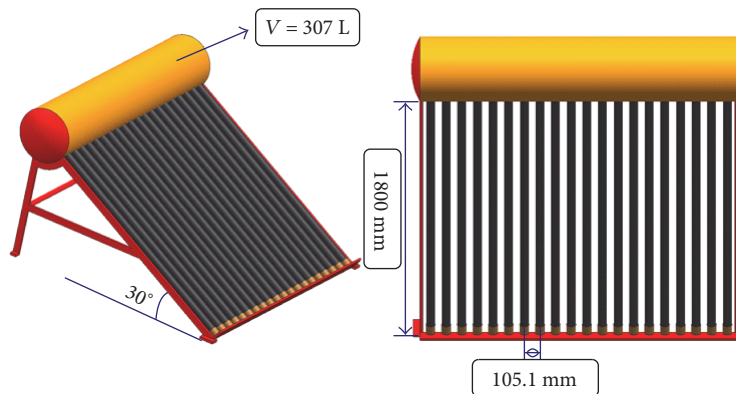


FIGURE 4: A 3-D schematic design for WGET-SWH installation. Reproduced with permission from Liu et al. [23].

the solar radiation intensity correlates well with the final temperature in a nonphotovoltaic heat transfer system, and it is not easy to be measured, we did not consider this as a variable for model training. Also, because the ambient temperatures are very similar during the measurements of all the SWHs in our database (we performed all the measurements in the similar months and locations), we also removed it from the variable list. It should be noted that for the measurements gathered from various seasons and unstable weathers, the ambient temperature sometimes is important and should not be neglected for modeling. Results show that without the solar radiation intensity and ambient temperature, our predictive models were still precise and robust enough [2]. Reducing the number of independent variables like these not only helps us dramatically reduce the required time for model training but also simplifies the input generation process at the following

HTS application. Another vital step is the scale and size of the database. Due to the complexity of the energy collection and transfer system, there are usually a large number of independent variables. To ensure a good training, a large and wide database should be used. If the size of the database for training is too small, it would generate high error rates during fittings; if the range of database is too narrow, the trained model would only have good performance in a very local data range, sacrificing the precision of the data in a relatively remote region. In many previous cases, we can see that a large and wide database is crucial to ensure a good practical prediction [53]. In our case study, the ranges of the independent variables were wide enough to ensure a good predictive performance of the ANN [2]. Detailed descriptive statistics (maximum, minimum, data range, average value, and standard deviation) of the WGET-SWH database we used for training are shown in Table 1.

TABLE 1: Descriptive statistics of the variables for 915 samples of in service WGET-SWHs. Reproduced with permission from Liu et al. [2].

Items	Tube length (mm)	Number of tubes	TCD (mm)	Tank volume (kg)	Collector area (m ²)	Angle (°)	Final temp. (°C)	HCR
Maximum	2200	64	151	403	8.24	85	62	11.3
Minimum	1600	5	60	70	1.27	30	46	6.7
Data range	600	59	91	333	6.97	55	16	4.6
Average value	1811	21	76.2	172	2.69	46	53	8.9
Standard deviation	87.8	5.8	5.11	47.0	0.73	3.89	2.0	0.48

TCD: tube center distance; final temp.: final temperature; HCR: heat collection rate (MJ/m²). Tank volume was defined as the maximum mass of water in tank (kg).

TABLE 2: Number of selected values of different independent variables (extrinsic properties). Reproduced with permission from Liu et al. [23].

	Tube length (mm)	Number of tubes	TCD (mm)	Tank volume (kg)	Collector area (m ²)	Angle (°)	Final temp. (°C)
Number of selected values	5	30	5	111	50	5	17

TCD: tube center distance; final temp.: final temperature.

TABLE 3: Input variables of two newly designed WGET-SWHs. Reproduced with permission from Liu et al. [23].

	Tube length (mm)	Number of tubes	TCD (mm)	Tank volume (kg)	Collector area (m ²)	Angle (°)	Final temp. (°C)
Design A	1800	18	105.5	163	1.27	30	52–62
Design B	1800	20	105.5	307	1.27	30	52–62

TCD: tube center distance; final temp.: final temperature.

TABLE 4: Measured heat collection rates (MJ/m²) of the two novel designs. All the measurements were performed under the environmental conditions similar to those of the measurements for the previous database (Table 1). Reproduced with permission from Liu et al. [23].

	Day 1	Day 2	Day 3	Day 4	Average	Predicted	Error rate
Design A	11.38	11.26	11.34	11.29	11.32	11.47	1.35%
Design B	11.47	11.43	11.42	11.45	11.44	11.66	1.90%

4.2. A Rational Generation of Possible Inputs. A rational generation of inputs of the ANN during the HTS process is also crucial to ensure a quick HTS with less time consumption. Without a rational criterion, there will be infinite possible combinations, which will lead to infinite computational cost. In our current study, we found that a quick way is to generate the inputs according to the trained weights of each independent variables: the independent variable with a higher numerical weight of the model will be assigned more possible values as the input of ANN during prediction. The basic assumption is that a larger value of weight will lead to a more significant change to the predicted results. In Liu et al. [23], we show that the tank volume has the highest weight to determine the heat collection rate, which also qualitatively agreed with the empirical knowledge. Thus, we generated more inputs of tank volume with different numerical values for the HTS

process. Table 2 shows the numbers of selected values of independent variables for screening the optimized WGET-SWHs via an HTS process [23]. Except for the final temperature, the number of values of all the independent variables was assigned according to their sequences of weight after a typical and robust ANN training. In terms of the inputs of final temperature, since it is not a part of the SWH installation, we consider all its possible integers shown in the database (Table 1) as the inputs for HTS. It should be noted that the weight values of a trained ANN do not contain exact physical meanings because the initial weights for an ANN training were usually selected randomly. Multiple trainings of ANN will lead to different final weight values. Thus, in addition to referring to the trained weight values, sometimes we should artificially assign more possible input values for the independent variables that are physically more influential to the predicted results. For other weight-free algorithms (e.g., SVM), artificial choices for inputs are particularly important.

4.3. Experimental Validation. With the inputs of the generated independent variable values, the machine learning model is able to output their predicted heat collection rates in an extremely short timescale. After screening, those designs with high predicted heat collection rates can be recorded as the candidates for future applications. In our recent studies, two typical designs after an HTS process were selected for experimental installations, with their independent variables summarized in Table 3.

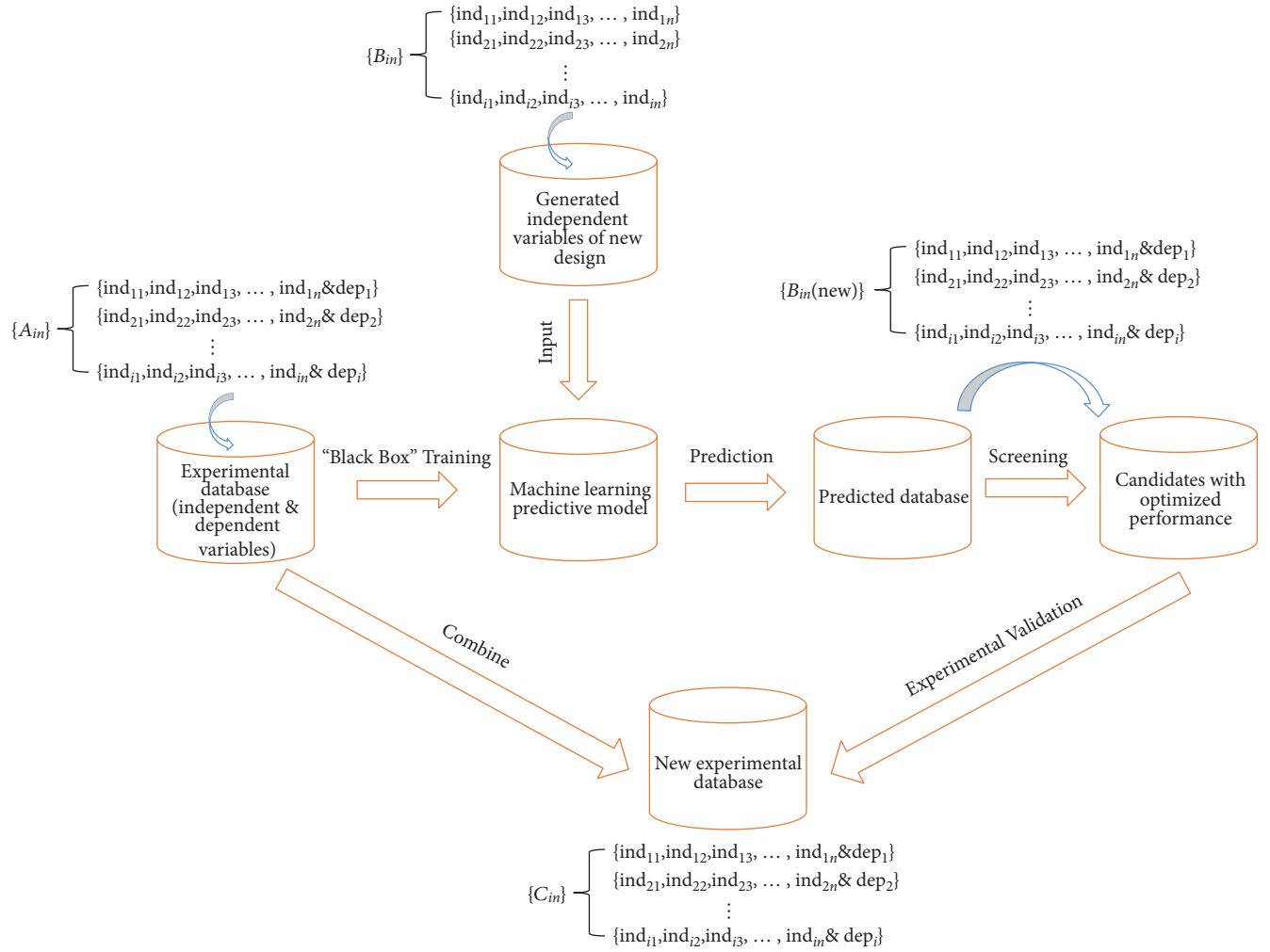


FIGURE 5: A proposed framework of machine learning-assisted HTS process for target performance optimization. Independent variables are assigned as "ind." Dependent variables are assigned as "dep." $\{A_{in}\}$ represents the original experimental database. $\{B_{in}\}$ represents the generated independent variables as the inputs. $\{B_{in}(new)\}$ represents the generated independent variables and their predicted dependent variables. $\{C_{in}\}$ represents the new experimental database combining the original experimental database and the experimental validation results of the screened candidates.

Rigorous experimental measurements on these two new designs validated that both of them outperformed all our 915 WGET-SWHs in the previous database under similar environmental conditions (Table 4). More comparative results are shown in [23].

4.4. A Framework for HTS-Based Optimization. The proposed framework for HTS-based optimization mainly consists of two parts: (i) developing a predictive model and (ii) screening possible candidates. The machine learning model is described as a "black box" in this framework since we do not need to know what really happens inside the training for real applications (and usually we care more about the fitting results). The concrete algorithmic and experimental processes of the proposed framework can be summarized as follows:

Step 1: Select the independent and dependent variables for the machine learning model.

Step 2: Train and test a predictive machine learning model with a proper experimental database.

Step 3: Generate a large number of the combinations of independent variable values.

Step 4: Input the generated independent variables into the well-trained predictive model.

Step 5: Screen and record the outputted dependent variable values and their corresponding independent variable values that fulfill all the screening criterions.

Step 6: Select the candidates from the results of Step 5 for experimental validation.

Step 7: Record the experimental results from Step 6.

To sum up, the proposed framework is shown in Figure 5. It can be seen that once all the preconditions of the

“cylinders” discussed above are fulfilled, a completed machine learning-assisted process can be achieved. The ultimate goal of the screening is to find out better candidates with optimized target performance. These candidates will have the independent variables different (or partially different) from the previous experimental database. Combining the previous experimental database with the experimental validation on new designed candidates, we can construct a new experimental database with more informative knowledge for future applications. It should be noted that this framework not only works for solar energy systems but also works for the optimization cases of other devices. We expect that this framework can be expanded to other optimization demands in the future.

5. Conclusions

In this paper, we have summarized our recent studies on the predictive performance of machine learning on an energy system and proposed a framework of SWH design using a machine learning-based HTS method. This framework consists of (i) developing a predictive model and (ii) screening possible candidates. A combined computational and experimental case study on WGET-SWH shows that this framework can help efficiently design new WGET-SWH with optimized performance without knowing the complicated knowledge of the physical relationship between the SWH settings and the target performances. We expect that this study can fill the blank of the HTS applications on optimizing energy systems and provide new insight on the design of high-performance energy systems.

Conflicts of Interest

The authors declare no conflict of interest.

Authors' Contributions

Hao Li proposed and studied the overall HTS framework and wrote the manuscript. Zhijian Liu provided the experimental and financial supports. Kejun Liu provided relevant programming supports. Zhien Zhang participated in the discussions and revised the manuscript.

Acknowledgments

This work was supported by the Major Basic Research Development and Transformation Program of Qinghai province (no. 2016-NN-141) and Natural Science Foundation of Hebei (no. E2017502051).

References

- [1] S. Mekhilef, R. Saidur, and A. Safari, “A review on solar energy use in industries,” *Renewable and Sustainable Energy Reviews*, vol. 15, pp. 1777–1790, 2011.
- [2] Z. Liu, H. Li, X. Zhang, G. Jin, and K. Cheng, “Novel method for measuring the heat collection rate and heat loss coefficient of water-in-glass evacuated tube solar water heaters based on artificial neural networks and support vector machine,” *Energies*, vol. 8, pp. 8814–8834, 2015.
- [3] Z. Wei, T. M. Lim, M. Skyllas-Kazacos, N. Wai, and K. J. Tseng, “Online state of charge and model parameter co-estimation based on a novel multi-timescale estimator for vanadium redox flow battery,” *Applied Energy*, vol. 172, pp. 169–179, 2016.
- [4] Z. Wei, K. J. Tseng, N. Wai, T. M. Lim, and M. Skyllas-Kazacos, “Adaptive estimation of state of charge and capacity with online identified battery model for vanadium redox flow battery,” *Journal of Power Sources*, vol. 332, pp. 389–398, 2016.
- [5] Z. Wei, S. Meng, K. J. Tseng, T. M. Lim, B. H. Soong, and M. Skyllas-Kazacos, “An adaptive model for vanadium redox flow battery and its application for online peak power estimation,” *Journal of Power Sources*, vol. 344, pp. 195–207, 2017.
- [6] Z. Wang and Y. Li, “Layer pattern thermal design and optimization for multistream plate-fin heat exchangers—a review,” *Renewable and Sustainable Energy Reviews*, vol. 53, pp. 500–514, 2016.
- [7] Z. Wang, B. Sundén, and Y. Li, “A novel optimization framework for designing multi-stream compact heat exchangers and associated network,” *Applied Thermal Engineering*, vol. 116, pp. 110–125, 2017.
- [8] Z. Wang and Y. Li, “Irreversibility analysis for optimization design of plate fin heat exchangers using a multi-objective cuckoo search algorithm,” *Energy Conversion and Management*, vol. 101, pp. 126–135, 2015.
- [9] J. Xu and J. Tang, “Modeling and analysis of piezoelectric cantilever-pendulum system for multi-directional energy harvesting,” *Journal of Intelligent Material Systems and Structures*, vol. 28, pp. 323–338, 2017.
- [10] J. Xu and J. Tang, “Linear stiffness compensation using magnetic effect to improve electro-mechanical coupling for piezoelectric energy harvesting,” *Sensors and Actuators A: Physical*, vol. 235, pp. 80–94, 2015.
- [11] J. W. Xu, Y. B. Liu, W. W. Shao, and Z. Feng, “Optimization of a right-angle piezoelectric cantilever using auxiliary beams with different stiffness levels for vibration energy harvesting,” *Smart Materials and Structures*, vol. 21, p. 65017, 2012.
- [12] S. Kalogirou, “The potential of solar industrial process heat applications,” *Applied Energy*, vol. 76, pp. 337–361, 2003.
- [13] S. A. Kalogirou, S. Panteliou, and A. Dentsoras, “Artificial neural networks used for the performance prediction of a thermosiphon solar water heater,” *Renewable Energy*, vol. 18, pp. 87–99, 1999.
- [14] S. A. Kalogirou, “Artificial neural networks and genetic algorithms in energy applications in buildings,” *Advances in Building Energy Research*, vol. 3, pp. 83–119, 2009.
- [15] S. A. Kalogirou, “Applications of artificial neural-networks for energy systems,” *Applied Energy*, vol. 67, pp. 17–35, 2000.
- [16] S. A. Kalogirou, “Solar thermal collectors and applications,” *Progress in Energy and Combustion Science*, vol. 30, pp. 231–295, 2004.
- [17] S. Kalogirou, “Artificial neural networks for the prediction of the energy consumption of a passive solar building,” *Energy*, vol. 25, pp. 479–491, 2000.
- [18] S. A. Kalogirou, E. Mathioulakis, and V. Belessiotis, “Artificial neural networks for the performance prediction of large solar systems,” *Renewable Energy*, vol. 63, pp. 90–97, 2014.

- [19] S. Kalogirou, A. Designing, and Modeling Solar Energy Systems, *Solar Energy Engineering*, pp. 583–699, Elsevier, Oxford, UK, 2014.
- [20] Z. Liu, K. Liu, H. Li, X. Zhang, G. Jin, and K. Cheng, “Artificial neural networks-based software for measuring heat collection rate and heat loss coefficient of water-in-glass evacuated tube solar water heaters,” *PLoS One*, vol. 10, article e0143624, 2015.
- [21] Z. Liu, H. Li, X. Tang, X. Zhang, F. Lin, and K. Cheng, “Extreme learning machine: a new alternative for measuring heat collection rate and heat loss coefficient of water-in-glass evacuated tube solar water heaters,” *SpringerPlus*, vol. 5, 2016.
- [22] H. Peng and X. Ling, “Optimal design approach for the plate-fin heat exchangers using neural networks cooperated with genetic algorithms,” *Applied Thermal Engineering*, vol. 28, pp. 642–650, 2008.
- [23] Z. Liu, H. Li, K. Liu, H. Yu, and K. Cheng, “Design of high-performance water-in-glass evacuated tube solar water heaters by a high-throughput screening based on machine learning: a combined modeling and experimental study,” *Solar Energy*, vol. 142, pp. 61–67, 2017.
- [24] W. F. An and N. Tolliday, “Cell-based assays for high-throughput screening,” *Molecular Biotechnology*, vol. 45, pp. 180–186, 2010.
- [25] T. Colbert, “High-throughput screening for induced point mutations,” *Plant Physiology*, vol. 126, pp. 480–484, 2001.
- [26] J. Bajorath, “Integration of virtual and high-throughput screening,” *Nature Reviews Drug Discovery*, vol. 1, pp. 882–894, 2002.
- [27] D. Wahler and J. L. Reymond, “High-throughput screening for biocatalysts,” *Current Opinion in Biotechnology*, vol. 12, pp. 535–544, 2001.
- [28] R. P. Hertzberg and A. J. Pope, “High-throughput screening: new technology for the 21st century,” *Current Opinion in Chemical Biology*, vol. 4, pp. 445–451, 2000.
- [29] J. Greeley, T. F. Jaramillo, J. Bonde, I. B. Chorkendorff, and J. K. Nørskov, “Computational high-throughput screening of electrocatalytic materials for hydrogen evolution,” *Nature Materials*, vol. 5, pp. 909–913, 2006.
- [30] J. Greeley and J. K. Nørskov, “Combinatorial density functional theory-based screening of surface alloys for the oxygen reduction reaction,” *Journal of Physical Chemistry C*, vol. 113, pp. 4932–4939, 2009.
- [31] G. Hautier, C. C. Fischer, A. Jain, T. Mueller, and G. Ceder, “Finding natures missing ternary oxide compounds using machine learning and density functional theory,” *Chemistry of Materials*, vol. 22, pp. 3762–3767, 2010.
- [32] G. L. Morrison, N. H. Tran, D. R. McKenzie, I. C. Onley, G. L. Harding, and R. E. Collins, “Long term performance of evacuated tubular solar water heaters in Sydney, Australia,” *Solar Energy*, vol. 32, pp. 785–791, 1984.
- [33] R. Tang, Z. Li, H. Zhong, and Q. Lan, “Assessment of uncertainty in mean heat loss coefficient of all glass evacuated solar collector tube testing,” *Energy Conversion and Management*, vol. 47, pp. 60–67, 2006.
- [34] Y. M. Liu, K. M. Chung, K. C. Chang, and T. S. Lee, “Performance of thermosyphon solar water heaters in series,” *Energies*, vol. 5, pp. 3266–3278, 2012.
- [35] G. L. Morrison, I. Budihardjo, and M. Behnia, “Water-in-glass evacuated tube solar water heaters,” *Solar Energy*, vol. 76, pp. 135–140, 2004.
- [36] L. J. Shah and S. Furbo, “Theoretical flow investigations of an all glass evacuated tubular collector,” *Solar Energy*, vol. 81, pp. 822–828, 2007.
- [37] Z. H. Liu, R. L. Hu, L. Lu, F. Zhao, and H. S. Xiao, “Thermal performance of an open thermosyphon using nanofluid for evacuated tubular high temperature air solar collector,” *Energy Conversion and Management*, vol. 73, pp. 135–143, 2013.
- [38] M. Souliotis, S. Kalogirou, and Y. Tripanagnostopoulos, “Modelling of an ICS solar water heater using artificial neural networks and TRNSYS,” *Renewable Energy*, vol. 34, pp. 1333–1339, 2009.
- [39] W. Sun, Y. He, and H. Chang, “Forecasting fossil fuel energy consumption for power generation using QHSA-based LSSVM model,” *Energies*, vol. 8, pp. 939–959, 2015.
- [40] H. C. Jung, J. S. Kim, and H. Heo, “Prediction of building energy consumption using an improved real coded genetic algorithm based least squares support vector machine approach,” *Energy and Buildings*, vol. 90, pp. 76–84, 2015.
- [41] K. Mohammadi, S. Shamsirband, P. L. Yee, D. Petković, M. Zamani, and S. Ch, “Predicting the wind power density based upon extreme learning machine,” *Energy*, vol. 86, pp. 232–239, 2015.
- [42] S. Kalogirou, “Applications of artificial neural networks in energy systems,” *Energy Conversion and Management*, vol. 40, pp. 1073–1087, 1999.
- [43] G.-B. Huang, Q.-Y. Zhu, and C.-K. Siew, “Extreme learning machine: theory and applications,” *Neurocomputing*, vol. 70, pp. 489–501, 2006.
- [44] G.-B. Huang, H. Zhou, X. Ding, and R. Zhang, “Extreme learning machine for regression and multiclass classification,” *IEEE Transactions on Systems Man and Cybernetics, Part B (Cybernetics)*, vol. 42, pp. 513–529, 2012.
- [45] G. Huang, G. B. Huang, S. Song, and K. You, “Trends in extreme learning machines: a review,” *Neural Networks*, vol. 61, pp. 32–48, 2015.
- [46] M.-C. Lee and C. To, “Comparison of support vector machine and back propagation neural network in evaluating the enterprise financial distress,” *International Journal of Artificial Intelligence & Applications*, vol. 1, pp. 31–43, 2010.
- [47] J. Z. Wang, J. J. Wang, Z. G. Zhang, and S. P. Guo, “Forecasting stock indices with back propagation neural network,” *Expert Systems with Applications*, vol. 38, pp. 14346–14355, 2011.
- [48] N. M. Nawi, A. Khan, and M. Z. Rehman, “A new back-propagation neural network optimized,” *ICCSA 2013*, pp. 413–426, 2013.
- [49] D. F. Specht, “A general regression neural network,” *IEEE Transactions on Neural Networks*, vol. 2, pp. 568–576, 1991.
- [50] C.-M. Hong, F.-S. Cheng, and C.-H. Chen, “Optimal control for variable-speed wind generation systems using general regression neural network,” *International Journal of Electrical Power & Energy Systems*, vol. 60, pp. 14–23, 2014.
- [51] H. Li, X. Tang, R. Wang, F. Lin, Z. Liu, and K. Cheng, “Comparative study on theoretical and machine learning methods for acquiring compressed liquid densities of 1,1,1,2,3,3,3-heptafluoropropane (R227ea) via song and Mason equation, support vector machine, and artificial neural networks,” *Applied Sciences*, vol. 6, p. 25, 2016.

- [52] E. O. Pyzer-Knapp, C. Suh, R. Gómez-Bombarelli, J. Aguilera-Iparraguirre, and A. Aspuru-Guzik, "What is high-throughput virtual screening? A perspective from organic materials discovery," *Annual Review of Materials Research*, vol. 45, pp. 195–216, 2015.
- [53] S. A. Kalogirou, "Artificial neural networks in renewable energy systems applications: a review," *Renewable and Sustainable Energy Reviews*, vol. 5, 2000.

Research Article

Determination of Performance Measuring Parameters of an Improved Dual Paraboloid Solar Cooker

Suhail Zaki Farooqui^{1,2}

¹US-Pakistan Center for Advanced Studies in Energy, University of Engineering & Technology, Peshawar, Pakistan

²Faculty of Engineering Sciences, PNEC, National University of Sciences & Technology, Islamabad, H.I. Rahamatullah Road, Karachi 75350, Pakistan

Correspondence should be addressed to Suhail Zaki Farooqui; drsuzaki@hotmail.com

Received 9 May 2017; Revised 15 June 2017; Accepted 20 June 2017; Published 7 August 2017

Academic Editor: Xinhai Xu

Copyright © 2017 Suhail Zaki Farooqui. This is an open access article distributed under the Creative Commons Attribution License, which permits unrestricted use, distribution, and reproduction in any medium, provided the original work is properly cited.

An experimental investigation into the performance evaluation of an improved dual reflector foldable paraboloid solar cooker has been reported, along with its energy and exergy analysis. The best attribute of this lightweight and low-cost solar cooker is its high performance coupled with the ease of handling. The cooker utilizes two paraboloid reflectors made out of Mylar-coated fiberglass dishes, each having a diameter of 90 cm and focal length of 105 cm. The total intercepted radiation energy is 1.08 kW under standard test conditions. Stagnation temperatures of up to 330°C and cooking temperatures of up to 290°C have been attained with load. Altogether, 9 experiments have been performed with and without load. Loaded tests have been conducted with water and vegetable oil. Results indicate an average cooking power of 485 W, peak exergy gain of 60.53 W, quality factor of 0.077, and a high product of temperature difference gap at half peak power to peak power of 4364.33 W·K. The maximum exergy output power attained was 70 W, while maximum exergy efficiency was 8–10%. All performance measuring parameters indicate that it is a high performance solar cooker for rural and urban communities and is suitable for all types of oil- and water-based cooking.

1. Introduction

Development of more efficient and user friendly solar cookers is a high priority area, as cooking of food accounts for a substantially large chunk of the total fuel consumption on Earth. In case of the developing countries, this activity accounts to over one-third of the total primary fuel consumption [1, 2]. Conversion of cooking to renewables has the potential of substantially reducing the fuel bills of many energy-deficient countries of the world, as well as reducing the greenhouse gas emissions. Three broad types of solar cookers have been reported in the literature during the last over half a century. Box-type solar cookers utilizing the greenhouse effect to acquire the cooking temperatures are so far the most popular ones, due mainly to their simplicity and lower costs. However, they suffer from the main disadvantage of approaching the maximum temperatures of around 120°C. Therefore, they are suitable only for water-based low temperature cooking [3, 4]. Oil-based high temperature cooking is not possible with these cookers. Parabolic

types are the second most common solar cookers. Typically, they utilize a parabolic reflector mounted near the ground, which focuses the reflected solar radiation onto a cooking pan placed at a height. Generally, these cookers acquire high cooking temperatures suitable for cooking all types of food. However, they suffer from a number of issues, including the requirement of frequent solar tracking, lack of maneuverability due to larger sizes and weights, and the splashes of oil and curry falling onto the reflector, requiring frequent cleaning and adversely affecting its reflectivity. The third main type of solar cookers are the vacuum tube-based cookers, as presented by various authors [1, 3–7]. Though these cookers acquire high temperatures and are very efficient, they are complex to operate and expensive to manufacture.

Parabolic-type solar cookers have been offered in several versions by a number of authors. Typically, these cookers acquire concentration ratios of up to 50 and temperatures of up to 300°C [8]. With a spherical reflector, the first design was proposed by Stam in 1961 [2]. It was the simplest type of reflector, allowing the cooking vessel to be hung

from a tripod at a suitable focal point. However, due to the spherical shape of the reflector, the focus was not very good. A parabolic reflector-type cooker named as SK-14 was invented by Dr. Dieter Seifert [9, 10]. The focus of this cooker was much better and sharper than the previous one. However, it is very sensitive to even a slight change in the position of the sun and hence it requires constant tracking. Due to its deeply curved parabolic reflectors, the focal point lies inside the dish [11, 12]. Further, due to the usage of a single large dish, it occupies more space, making it difficult to carry from one place to the other. Also, the frequent oil and curry splashes spoil the reflector surface, as the cooking utensils are placed above the parabolic reflector. Making this type of cooker requires advanced manufacturing facilities available only to large companies.

The Sheffler community solar cooker was invented by Wolfgang Sheffler in 1986 [13, 14]. The Sheffler-type solar cookers utilize large flexible parabolic mirrors to concentrate the solar radiation inside a kitchen on a fixed point through a North-facing window, where high temperatures of up to 1000°C are attainable to cook all types of food. The polar directional controls of the parabolic mirrors are carried out through clockwork rotation at the rate of one revolution per day. The reflector is made to change the shape of its entire surface every few days to adapt itself to the changing declination angles of the sun. For these reasons, its design, manufacturing, and installation are complex. Further, it requires heavy and robust permanent structure for its support and installation needs shadow-free area throughout the year in the south direction. The requirement for capital investment is also high. Some authors have also evaluated the compound parabolic reflectors which do not require solar tracking for a few hours [15, 16]. However, these are not suitable for use with solar cookers due to their bulky size, complex construction, and use of large quantities of thermal fluids, causing delayed heating.

In this paper, the design and working scheme of a dual reflector parabolic cooker has been described and experimentally tested with an aim to address the abovementioned deficiencies noted in this class of cookers. A lightweight cooker with two foldable fiberglass parabolic reflectors coated with Mylar sheet has been introduced. These attributes make it convenient to move the cooker from one place to the other, operate at any desired place, and easily store inside the home when not in use. A number of simple controls have been provided to change the inclination of each individual reflector, as well as the collective inclination of both the reflectors, in order to maintain the focused radiation from both the reflectors onto the cooking pan, with changing positions of the sun on the sky. Further, sufficient separation has been provided between the two reflectors to allow any oil and curry splashed from the cooking pan to fall onto the ground, rather than damaging the reflector surfaces. Support for the cooking pan has been kept separate to allow easy maneuverability of the cooker and to prevent shaking of the cooking utensils, while the reflective mirrors are adjusted.

Several experiments have been conducted without load and with load of 4 kg of water, as well as vegetable oil to extract the various performance measuring parameters. The

experimental results are analyzed in each case for determining the first and second figures of merit, cooking power, energy and exergy efficiencies, and the quality factor of the cooker.

The first figure of merit F_1 measures the optical efficiency of the cooker per unit heat loss factor. This is measured by dividing the difference of the maximum temperature attained by the unloaded bottom of the cooker with the ambient air temperature to the average solar radiation intensity during experiment. The second figure of merit F_2 gives an indication of heat transfer from the absorbing base to the water inside the cooker. It is evaluated in the presence of full load, as the product of heat gained by water and F_1 per unit aperture area per unit time per unit temperature. The cooking power is the heat gained by the water inside the cooker per unit time. Energy efficiency of the cooker is evaluated as the heat gained by the water inside the cooker divided by the solar radiation energy intercepted by the cooker collector during a given time. The exergy efficiency measures the potential of the cooker to extract the solar radiation energy. This is obtained by dividing the exergy output of the cooker by the exergy input. The exergy input and output are evaluated by recording the ambient air and water temperatures and solar radiation intensity after periodic intervals of time, while considering the water content, aperture area of the cooker, and the temperature of the surface of the sun, using formulas described in (4) and (5). The quality factor of the cooker is determined by dividing the peak exergy gain of the cooker with the exergy loss (the difference between exergy input and output) at that instant of time. The peak exergy gain is obtained by plotting the exergy output versus the temperature difference of water with the ambient air. The curve is fitted with a second order polynomial, and peak is determined.

2. The Optical Scheme of the Dual Paraboloid Reflector

A paraboloid reflector is defined to provide a sharp focus to the rays of light reflected from its surface, when the incident light consists of rays parallel to the axis of the paraboloid. If the incident light is not parallel to the axis of the paraboloid, the reflected light does not make a sharp focus at the focal point, but rather a dispersed focus at a point other than the focal point, as shown in Figure 1 [17].

Since the cooking pan has finite dimensions, the need for a sharp focus is not quite critical and the cooker can benefit even from a dispersed focus of the incident light reflected from the two paraboloids placed at a distance from each other, without much significant loss of performance. This feature enables the two paraboloids to get folded when not in use, making it handy to allow easy movement and storage of the cooker. Further, it allows the oil and curry splashes to mostly fall on the ground, rather than spoiling the central part of the reflective surface. The paraboloids used in the above scheme have a focal length of 105 cm and a radius of 45 cm. The distance between the rims of the two paraboloids is 20 cm. Therefore, the angle of incidence of the solar radiation to the axis of each paraboloid is

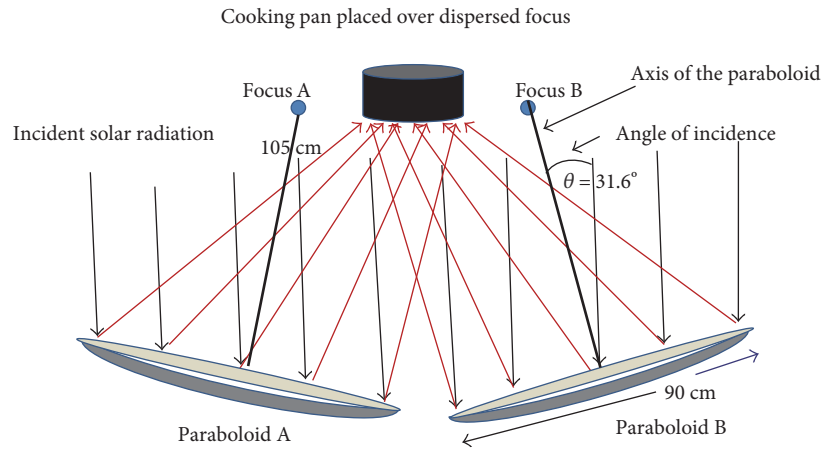


FIGURE 1: Optical scheme of the light reflected from a dual paraboloid reflecting system defining a dispersed focus.

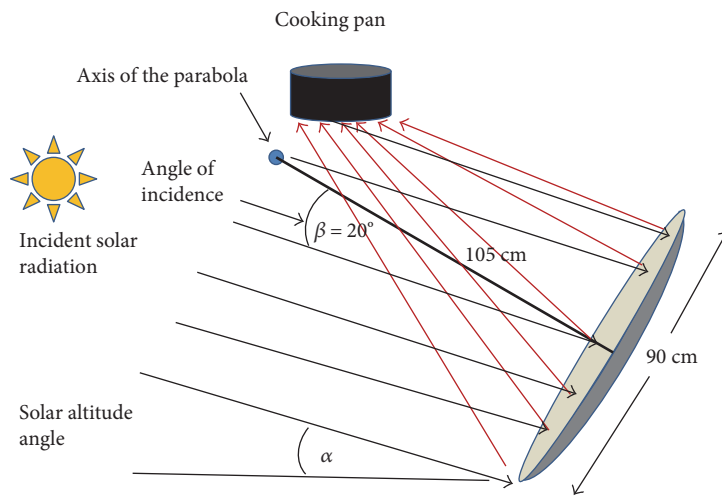


FIGURE 2: Operational scheme of the dual paraboloid reflector to cater for the changing altitude angle of the sun.

$\sin^{-1}(55/105) = 31.6^\circ$. Further, the altitude angle of the two paraboloids would not, in general, be the same during operation as that of the sun at any instant of time, since the height of the cooking pan is held fixed during operation while the altitude angle of the sun changes. The cooking pan is not placed vertically above the reflectors, as shown in Figure 2. Normally, there would be a difference of nearly $10\text{--}20^\circ$ between the two angles during 9:00 to 15:00 hours, depending upon the season. The total maximum cosine losses due to the difference between the angle of incidence of the solar radiation and the axes of the paraboloids are therefore $\leq [1 - \cos(31.6^\circ) \cdot \cos(20^\circ)] = 20\%$.

3. The Dual Paraboloid Reflector Solar Cooker

The complete dual parabolic reflector solar cooker has been constructed in five pieces. Four of them are connected together to make one piece, while the fifth piece is kept separate to make the handling of the cooker easier. Two identical paraboloids made out of fiberglass having diameter of 90 cm and focal length of 105 cm each have been used. The

inner surfaces of the paraboloids have been coated with highly reflective Mylar sheet. The sheet has a reflectivity of 94% and can withstand temperatures of up to 200°C [18]. Two pipe frames A and B are constructed as shown in Figure 3. Two steel pipes are bent in circles of diameter 75 cm each. Two small pieces of pipes “a1” are welded with frame A on one side, while another 17.5 cm long pipe “a2” is perpendicularly welded to them on the other side. A small rod passing through a small piece of pipe attached to an eye is welded between the small pieces of pipes, so that the pipe containing the eye can easily rotate with respect to the rod. The eye contains a threaded nut that allows a bolt to pass through. The bolt pressing against a closed ended U-channel on another frame provides a simple control for changing the orientation of the parabolic reflector, while in operation. The frame B is also similarly constructed with different distance between the pipes “b1.” Whole scheme is illustrated in Figure 3.

The parabolic reflector frames A and B are then mounted on another frame through a rotational axis rod, as shown in Figure 4. The rotational axis rod passes through the pipes

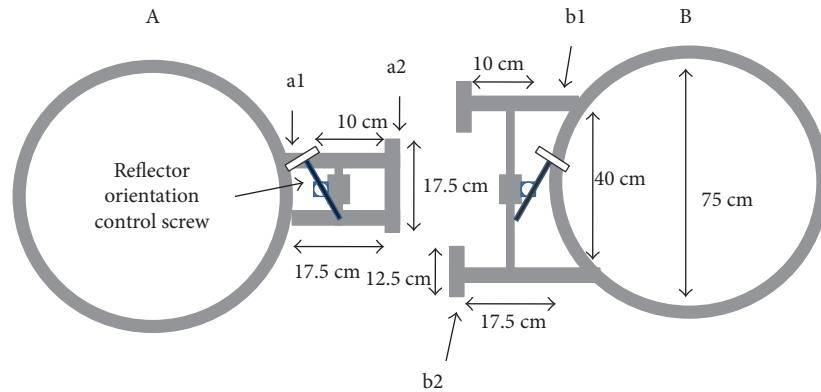


FIGURE 3: Schematic diagram of the dual parabolic reflector support system with dimensions.

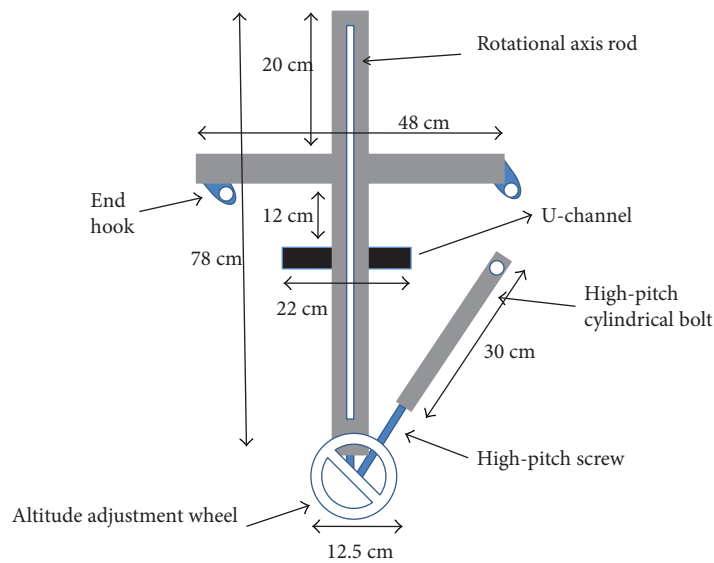


FIGURE 4: Schematic diagram of the frame allowing the orientation control of the parabolic reflectors along the altitude.

“a2” and “b2” of frames “A” and “B” and allows both frames to rotate with respect to it. This allows both reflectors to be adjusted, such that the reflected solar radiation gets focused below the coking pan, within an area equal to the diameter of the pan.

The frame shown in Figure 4 consists of a 78 cm long rectangular pipe, cross welded with another piece of 48 cm long pipe and a 22 cm long closed end U-channel. The 48 cm long pipe contains one strut with an eye hole at each end. The whole frame can rotate with respect to a rod passing through these struts. The rear end of this frame is connected to an altitude adjustment wheel, which can drive a high-pitch screw into a similarly pitched 30 cm long bolt. The next end of this bolt is connected to another frame, such that rotating the altitude adjustment wheel allows the whole frame to change its orientation with respect to the rod passing through the abovementioned two struts. This rod is welded onto the frame shown in Figure 5.

The Y-shaped frame shown in Figure 5 is made out of four rectangular pipe sections. Five wheels are connected at the ends of the frame. The frame in Figure 4 is connected

to this frame through the 53 cm long welded rod and a hook, as shown. This frame supports the entire structure of the cooker and can be easily moved across over a flat surface. The total weight of the entire structure with fiberglass dishes is 12 kg.

The last part of the cooker is the cooking pan holder. The holder frame made out of angle iron, shown in Figure 6, is 125 cm high, 60 cm long, and 37.5 cm wide and provides a structurally stable support for the cooking pan. The bottom of this frame is slipped between the two front wheels of the frame shown in Figure 5, such that any movement of the reflector frame does not cause any vibrations onto the cooking frame.

The complete dual parabolic reflector cooker in operation is shown in Figure 7.

4. Performance Measuring Experiments

Several experiments had been performed on carefully selected calm and clear days at 33.73° N latitude and 73.09° E longitude test location (Islamabad, Pakistan), during the

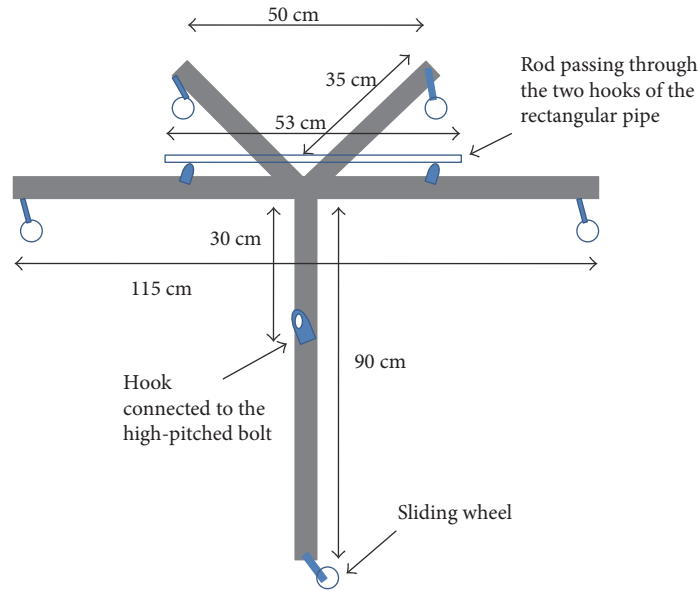


FIGURE 5: Schematic diagram of the Y-shaped support frame, placed on a level surface.

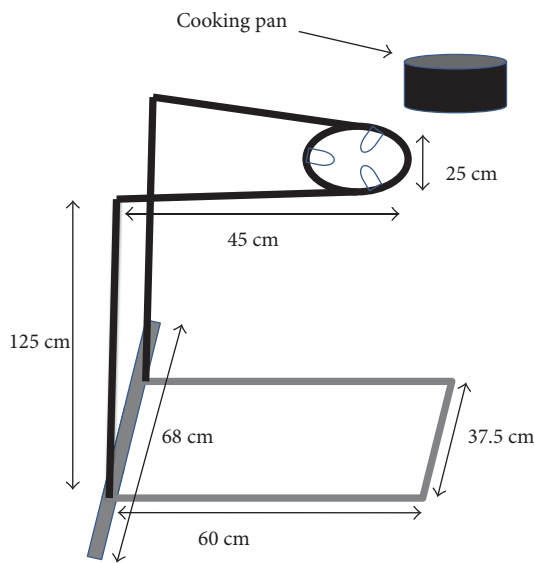


FIGURE 6: Cooking pan holding frame.



FIGURE 7: The dual parabolic reflector solar cooker in operation.

months of April and May 2016, to assess the performance measuring parameters of the dual parabolic reflector solar cooker, described in the previous section. Three experiments were performed on different days without load to determine the maximum plate stagnation temperature and the first figure of merit F_1 . Three more experiments were performed with 4 kg of water load each, to determine the energy and exergy efficiencies of the cooker, the second figure of merit F_2 , cooking power, and the quality factor of the cooker. Further, three experiments were performed with cooking oil load to determine the maximum achievable temperatures with load, as shown in Table 1. The recorded data included the ambient temperature T_a , plate temperature T_p , load temperature T_l , and the solar radiation intensity I_h on the

horizontal surface. The maximum available power to the cooker through two reflectors (diameter 90 cm each) under standard solar insolation conditions of 1000 W/m^2 , while taking into account the cosine losses, is 1.08 kW. The cooking pot had a diameter of 25 cm and could accommodate up to 7 liters of liquid load. It was surrounded from all sides with a 5 cm thick glass wool insulation. The lid at the top was also covered with a 5 cm thick layer of glass wool. The insulation-free bottom of the pot was exposed to the ambient air and was sprayed with dull black deco paint. Nine experiments had been performed with corresponding conditions as outlined in Table 1.

The first set of experiments was performed without load on the cooker. The base plate temperature of the cooker, the ambient temperature, and the solar radiation intensity on a horizontal surface were measured and recorded every two minutes, while cooker tracking adjustments were

TABLE 1: Test conditions of nine experiments.

Exp. number	Date of experiment	Experiment start solar time (H:M)	Experiment end solar time (H:M)	Load (gm)	Max. temp. attained (°C)
1	April 13, 2016	09:40	10:30	Nil	233
2	April 13, 2016	12:18	12:46	Nil	258
3	April 22, 2016	11:26	12:18	Nil	331
4	April 14, 2016	13:46	14:14	4000 (water)	100
5	May 02, 2016	12:16	13:04	4000 (water)	100
6	May 18, 2016	12:24	12:58	4000 (water)	100
7	April 22, 2016	12:06	12:44	850 (oil)	294
8	April 27, 2016	10:56	12:00	850 (oil)	262
9	April 29, 2016	11:04	12:00	850 (oil)	285

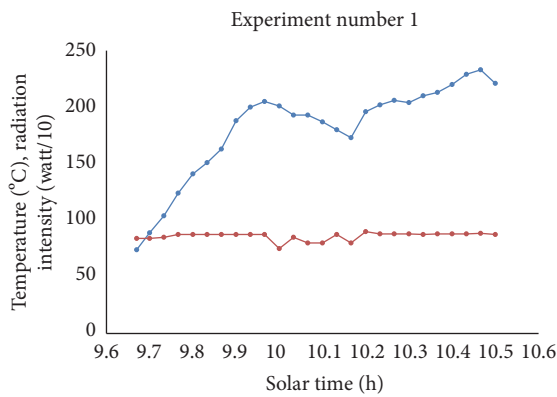


FIGURE 8: Plot of temperature (blue) and solar radiation intensity (red) versus time for the first unloaded experiment. Radiation intensity is divided by 10 to fit the scale.

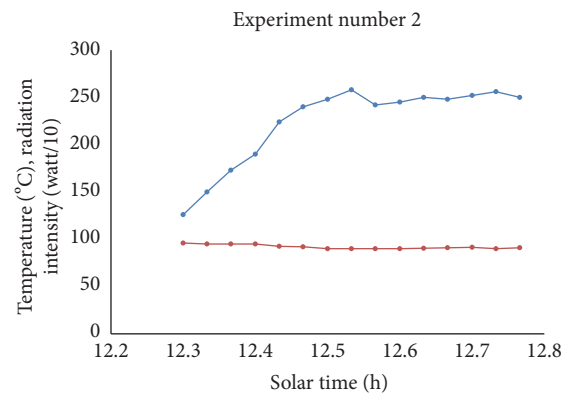


FIGURE 9: Plot of temperature (blue) and solar radiation intensity (red) versus time for the second unloaded experiment. Radiation intensity is divided by 10 to fit the scale.

performed every five minutes. Digital thermometers UT33 series, prepared by Uni-Trend Group Ltd., China, were used for temperature measurement, while Apogee SP110 pyranometer was used for the measurement of solar radiation intensity. The data plotted in Figures 8, 9, and 10 indicates the stagnation temperatures attained in each case.

The blue curves in Figures 8, 9, and 10 show that the maximum temperatures attained during the three unloaded experiments were 233°C, 258°C, and 331°C, respectively. A comparison of these figures shows that the maximum plate temperature depends heavily on the existing intensity of the solar radiation.

The second set of experiments was conducted with a load of 4 kg of water each time, on April 14, May 2, and May 18, 2016, as per the recommended test load for solar cookers per unit aperture area per unit concentration ratio [19]. As shown in Figures 11, 12, and 13, 4 kg of water load was brought to a boil in 28 minutes, 48 minutes, and 34 minutes from starting temperatures of 42°C, 39°C, and 36°C, respectively.

The last set of experiments was conducted with one liter (850 gm) of vegetable oil load each time, on April 22, 27, and 29, 2016. As shown in Figures 14, 15, and 16, the vegetable oil attained maximum temperatures of 294°C, 262°C, and

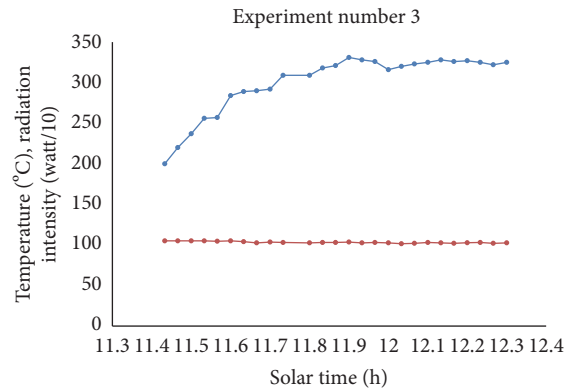


FIGURE 10: Plot of temperature (blue) and solar radiation intensity (red) versus time for the third unloaded experiment. Radiation intensity is divided by 10 to fit the scale.

285°C in 38 minutes, 64 minutes, and 56 minutes from starting temperatures of 101°C, 60°C, and 53°C, respectively.

Results of three sets of three experiments each have been shown in the foregoing, with dual parabolic reflector solar cooker, during the months of April and May 2016. The experiments with no load on the cooker indicate that under

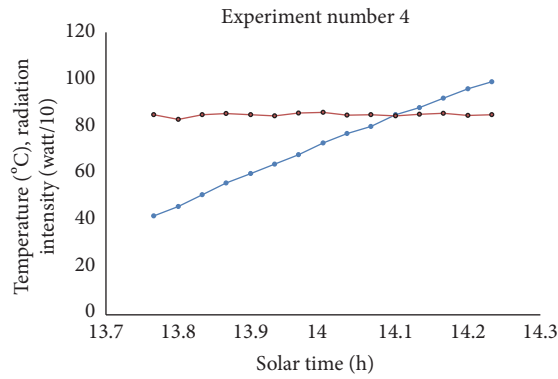


FIGURE 11: Plot of temperature (blue) and solar radiation intensity (red) versus time for the first experiment with 4 kg of water load. Radiation intensity is divided by 10 to fit the scale.

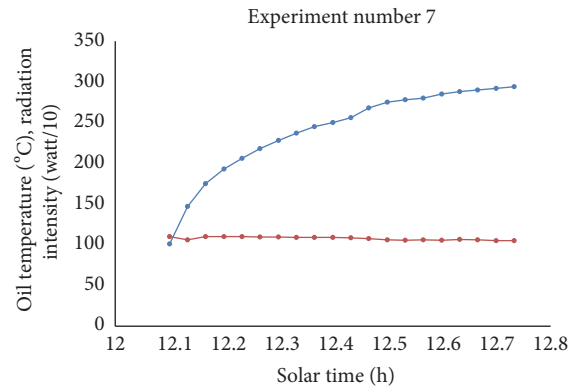


FIGURE 14: Plot of temperature (blue) and solar radiation intensity (red) versus time for the first experiment with 850 gm of vegetable oil load. Radiation intensity is divided by 10 to fit the scale.

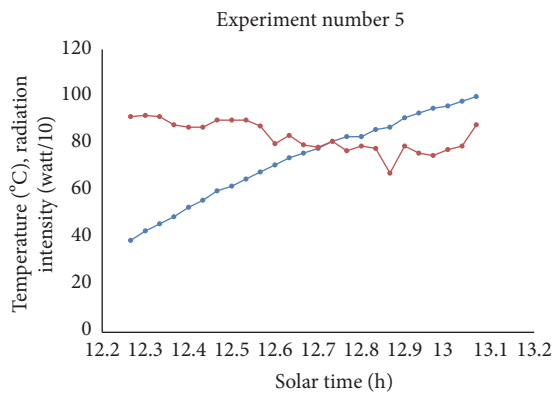


FIGURE 12: Plot of temperature (blue) and solar radiation intensity (red) versus time for the second experiment with 4 kg of water load. Radiation intensity is divided by 10 to fit the scale.

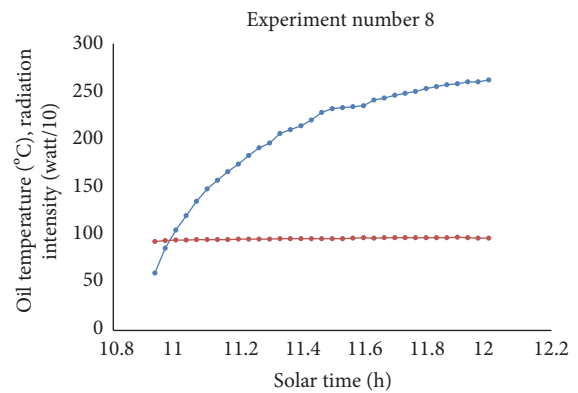


FIGURE 15: Plot of temperature (blue) and solar radiation intensity (red) versus time for the second experiment with 850 gm of vegetable oil load. Radiation intensity is divided by 10 to fit the scale.

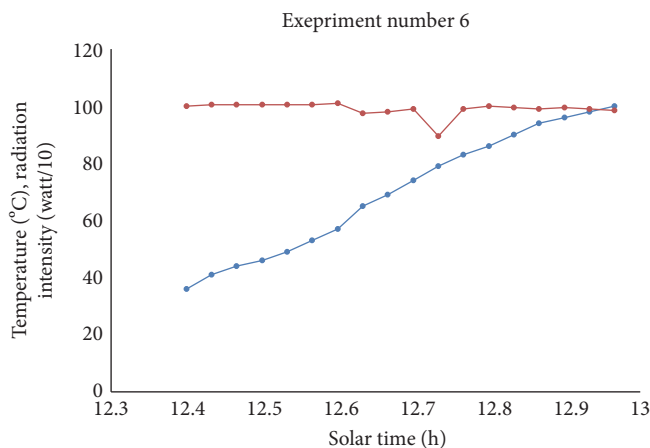


FIGURE 13: Plot of temperature (blue) and solar radiation intensity (red) versus time for the third experiment with 4 kg of water load. Radiation intensity is divided by 10 to fit the scale.

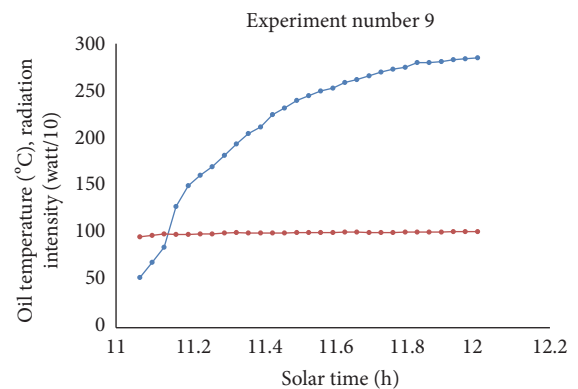


FIGURE 16: Plot of temperature (blue) and solar radiation intensity (red) versus time for the third experiment with 850 gm of vegetable oil load. Radiation intensity is divided by 10 to fit the scale.

clear sky conditions, maximum plate temperatures as high as 330°C may be attained in 30 to 40 minutes duration. Experiments with 4 kg of water load indicate that starting from the

ambient temperatures, it boils in 28 to 48 minutes, depending upon the radiation intensity. The last set of experiments with vegetable oil load indicates the maximum attainable cooking temperatures with load. Temperatures as high as 294°C have been attained this way, with the average attained temperature

of about 280°C in 53 minutes. All these results indicate that the cooker presented in this paper is most suitable for fulfilling the oil-based high-temperature cooking needs of the public, while being user friendly, lightweight, and low cost.

The detailed performance measuring parameters of the cooker have been evaluated in the following sections.

5. Determination of the First and Second Figures of Merit

In order to test the performance of solar cookers, two figures of merit (FOM) are normally recommended. These are defined as F_1 and F_2 [20, 21]. F_1 (measured in $\text{m}^2 \text{K/W}$) is the ratio of optical efficiency to the heat loss factor by the bottom absorbing plate and is a measure of the differential temperature gained by it at a particular level of solar insolation. F_2 gives an indication of heat transfer from the absorbing base to the water inside the cooker.

Mathematically, they are defined as

$$F_1 = \frac{T_{ps} - T_a}{H_s}, \quad (1)$$

where T_{ps} is the plate (tray) stagnation temperature, H_s is the solar insolation on the horizontal surface, and T_a is the ambient temperature.

$$F_2 = \frac{F_1(M \cdot C)_w \ln \left[\frac{1 - (T_{wi} - T_{av})/(F_1 \cdot H_{av})}{1 - (T_{wf} - T_{av})/(F_1 \cdot H_{av})} \right]}{A \cdot \tau}, \quad (2)$$

where $(M \cdot C)_w$ indicates the mass of the water in the pot multiplied to its heat capacity, A stands for the aperture area of the cooker, τ is the time difference during which water was heated from an initial temperature T_{wi} to the final temperature T_{wf} , H_{av} is the average solar radiation on a horizontal surface, and T_{av} is the average ambient temperature during the experiment. F_1 is evaluated in the absence of any load on the solar cooker while F_2 is evaluated in the presence of full load.

The cooking power of a cooker can be calculated as [21]

$$P = (M \cdot C)_w \left[\frac{\Delta T_w}{\Delta t} \right], \quad (3)$$

where ΔT_w is the temperature difference of water acquired in time Δt .

For the unloaded solar cooker described in this paper, three experiments were conducted on April 13 and April 22, 2016. The F_1 calculation results are summarized in Table 2.

For the fully loaded (4 kg of water load) cooker, data were collected on April 14, May 2, and May 18, 2016. For analysis, data are used for the water temperatures between 60 and 90°C, for each experiment. The results are summarized in Table 3.

From the results in Tables 2 and 3, it is concluded that the average value of the first figure of merit F_1 is 0.2578, while that of the second figure of merit F_2 is 0.567. The average cooking power of the solar cooker is 485 W. For comparison, the typical value of F_1 is 0.103, F_2 is 0.309, and the cooking

TABLE 2: Calculation of the first figure of merit for the dual parabolic reflector solar cooker during experiment numbers 1, 2, and 3.

Exp. number	T_{as} (°C)	T_{ps} (°C)	H_s (W/m ²)	F_1 (m ² K/W)
1	29.3	233	885	0.2302
2	30.5	258	900	0.2528
3	30.3	331	1035	0.2905

power is 30 W for typical box-type solar cookers [4], while F_1 is 0.395 and F_2 is 0.654 for SK-14-type solar cooker with 1.54 m² aperture area [12]. These parameters indicate that the dual parabolic cooker performance is comparable to that of SK-14 solar cooker.

6. Determination of Exergy Efficiency and Quality Factor

Exergy efficiency is often measured and reported for a given solar energy device as a measure of its potential for extracting heat from its surrounding environment [19, 22]. As per definition, the exergy approaches zero as the device approaches an equilibrium state with the environment. Exergy of the solar radiation describes the exergy input to the solar energy device and is determined by measuring the solar radiation flux ($I^\circ A \Delta t$) during the experiment and using the relation [23, 24]:

$$E_{Xi} = I^\circ A \Delta t \left[1 + \left(\frac{T_a}{T_s} \right)^4 \left(\frac{1}{3} \right) - \left(\frac{4}{3} \right) \left(\frac{T_a}{T_s} \right) \right], \quad (4)$$

where T_a and T_s , respectively, indicate the ambient air temperature during the experiment and the surface temperature of the sun, I° represents the measured solar radiation intensity perpendicular to the collector at a given instant, Δt is the time interval between two readings, and A indicates the aperture area of the solar collector under investigation. The exergy output power of the device can be evaluated as [23]

$$E_{xo} = E_{out} - M \cdot C \cdot T_a \ln \left[\frac{T_{wf}}{T_{wi}} \right], \quad (5)$$

where T_{wi} is the initial and T_{wf} is the final temperature of water (or any other material) placed inside the device. M and C , respectively, represent the mass and the specific heat capacity of the material.

The exergy efficiency may therefore be evaluated as

$$\psi = \frac{(M \cdot C) \cdot [(T_{wf} - T_{wi}) - T_a \ln(T_{wf}/T_{wi})] / \Delta t}{I^\circ \left[1 + 1/3(T_a/T_s)^4 - 4/3(T_a/T_s) \right] A}. \quad (6)$$

Another important parameter is the exergy loss coefficient, which is determined by measuring the difference between exergy input and output and the temperature difference δT between the water and the ambient air, defined as

$$E_{X_{loss}} = \frac{E_{xi} - E_{xo}}{A \cdot \Delta t \cdot \delta T} \quad (\text{W/m}^2 \text{K}). \quad (7)$$

TABLE 3: Calculation of the second figure of merit and the cooking power for the dual parabolic reflector solar cooker for experiment numbers 4, 5, and 6.

Exp. number	Effective aperture area (m ²)	T _{wi} (°C)	T _{wf} (°C)	T _{av} (°C)	H _{av} (W/m ²)	Duration τ (seconds)	(M·C) _w (J/K)	F ₂	P (W)
4	1.08	60	92	36.6	852.4	960	16,800	0.638	560
5	1.08	60	91	41.8	814.6	1560	16,800	0.453	333.8
6	1.08	65	91	42.8	990.2	780	16,800	0.610	560

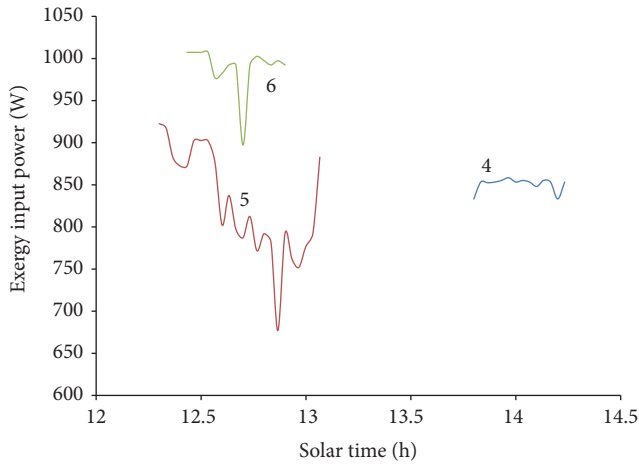


FIGURE 17: Exergy input power during the three experiments with 4 kg of water load. Curves are labeled according to the experiment number.

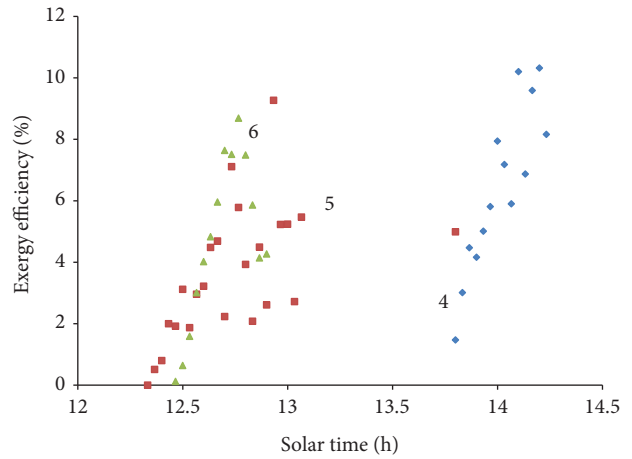


FIGURE 19: Efficiency of the exergy output power during the three experiments with 4 kg water load. Blue points correspond to experiment number 4, red to experiment number 5, and green to experiment number 6.

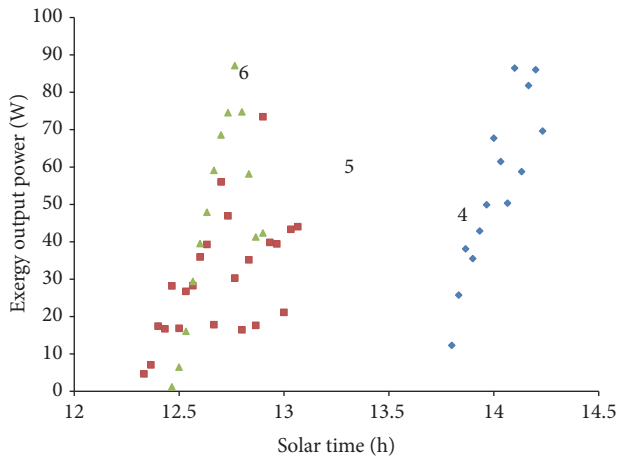


FIGURE 18: Exergy output power during the three experiments with 4 kg of water load. Blue points correspond to experiment number 4, red to experiment number 5, and green to experiment number 6.

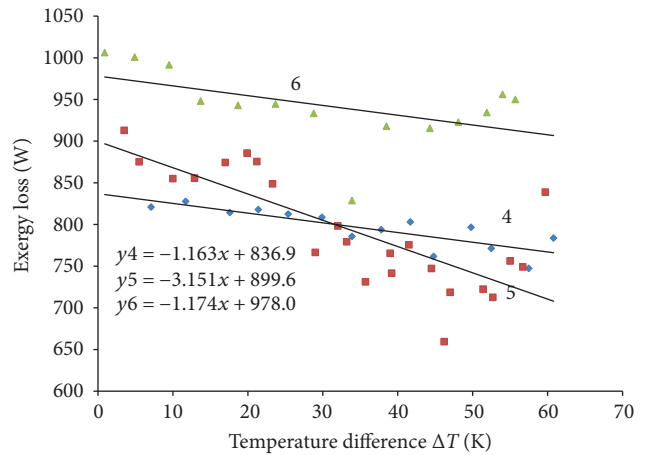


FIGURE 20: Least-squares fit to the exergy loss data for experiment numbers 4, 5, and 6.

A plot of the exergy loss ($E_{xi} - E_{xo}$) versus δT can provide the overall heat loss coefficient of the cooker. Further, it has been proposed that a plot between the exergy output power and δT , fitted with a second order polynomial, can be used to infer the peak exergy power of the device during a particular experiment [25]. The plot may also be used to infer the temperature difference gap between

the temperatures corresponding to half exergy power points, on either side of the peak power point.

The exergy input power during the three experiments, as derived from (4), is shown in Figure 17.

The exergy output power during the three experiments, as extracted using 5 and fitted to a least-squares curve to show the trend with time, is shown in Figure 18, while the exergy efficiency is plotted in Figure 19.

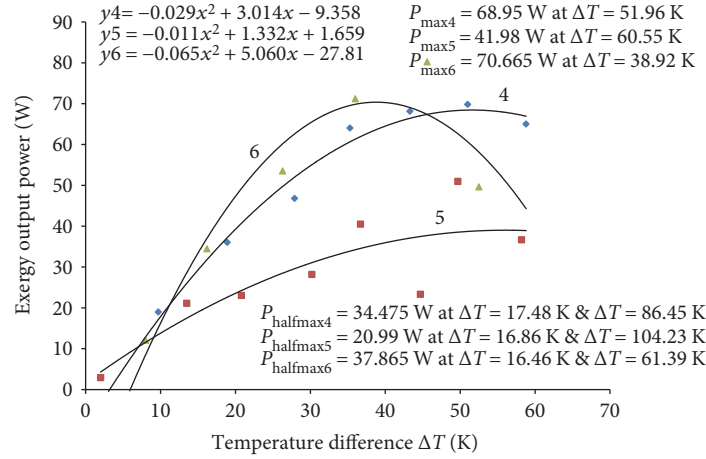


FIGURE 21: Exergy output power versus the temperature difference. Data are fitted with second order polynomials. Curves are labeled according to the experiment number.

TABLE 4: Various exergy-based performance measuring parameters for three types of solar cookers.

Cooker parameter	Dual parabolic	SK-14	Sheffler type	Box type	Vacuum tube type
Slope of exergy loss curve (W/K)	1.828	5.407	19.485	0.577	2.63
Aperture area (m ²)	0.049	1.47	8.21	0.4326	0.107
Heat loss coefficient (W/K m ²)	37.31	40.35	54.125	1.334	24.58
Specific heat loss coefficient (W/K kg m ²)	9.326	8.07	2.706	0.417	4.916
Peak exergy gain (W)	60.53	18.21	55.75	48.39	55.6
Exergy lost at peak exergy gain (W)	805.87	171.79	560.606	377.90	1323.8
Quality factor	0.077	0.106	0.099	0.1281	0.042
Temperature difference at peak power (K)	50.48	30.33	29.165	31.64	55.2
Temperature difference gap at half power (K)	72.1	40.374	39.62	41.76	38.75
Product of temperature difference gap at half power to peak power (W·K)	4364.33	735.3	2208.815	2020.77	2154.5

The exergy loss data ($E_{X_i} - E_{X_o}$) is plotted versus the temperature difference δT in Figure 20, corresponding to experiment numbers 4, 5, and 6. The data are fitted with linear curves. Heat loss coefficient (W/K m²) of the cooker is extracted by dividing the slopes of these curves by the aperture area of the cooker, while the specific heat loss coefficient (W/K kg m²) is obtained by further division by the amount of water. The quality factor of the solar cooker may be evaluated by dividing the peak exergy gained to the exergy lost at that instant [25].

Figure 21 shows the graphs between the output exergy power E_{X_o} and the temperature difference δT . The data are fitted to a second order polynomial, for all three experiments. The peak value of the exergy power and the temperature difference gaps corresponding to half peak power points have been extracted in each case.

The top three lines in the left of Figure 21 show the equations of the polynomial fits to the data for the three experiments. The bottom set of three lines shows the peak exergy power attained during each of the three experiments at a specific temperature difference. The third set

of three lines at the right top of Figure 21 provides the temperature difference gaps at half peak exergy power points. The temperature difference gaps are 68.96, 102.43, and 44.93 K, respectively.

The average value of the peak exergy power for the three experiments is 60.53 W, while the average temperature difference gap at half peak power is 72.1 K. The product of the peak power with the temperature difference gap is therefore 4364.33 W·K. This value is by far the highest reported in literature, for any solar cooker. Table 4 summarizes the various exergy-based performance measuring parameters for these experiments and provides comparison of these parameters with those of other types of solar cookers [1, 3, 4, 25].

From Table 4, it may be concluded that the specific heat loss coefficient for parabolic-type solar cooker is comparable to that of SK-14. The quality factor of this cooker is higher than that of vacuum tube-type cooker and comparable to those of Scheffler and SK-14 types. However, the peak exergy gain, which determines the actual useful energy, is quite high, as compared to other types of solar cookers. Further, the temperature difference gap at half peak power and its product

with the peak exergy gain are substantially higher compared to any other solar cooker reported so far. The average energy efficiency during the three experiments was 46.3%, 39.9%, and 49.38%, respectively. Due to design improvements in the present cooker, the maximum energy (49.38%) and exergy (8–10% from Figure 19) efficiencies have substantially improved compared to the results reported for a single parabolic trough cooker, where maximum energy efficiency was 15.7% and maximum exergy efficiency was 1.25% [23]. Similarly, these parameters are substantial improvements over SK-14 and Scheffler-type parabolic solar cookers [25].

7. Conclusions

This paper presents the results of an experimental investigation of an improved dual parabolic reflector solar cooker along with its construction details. The cooker has been explicitly designed from the point of view of a common user in terms of its usefulness and ease of transportation and handling, while addressing several other issues prevalent with such cookers. The cooker has been extensively tested under different load conditions and without load. All test results support it as a substantial improvement over other solar cookers in terms of its capacity of cooking all types of food as well as faster cooking with a view to its portability and lightweightness. The various standard performance measuring parameters have been evaluated at a test load of 4 kg of water. The average cooking power of the cooker has been found to be 485 W, while the maximum attainable temperatures with load approached 290°C. Many cooking experiments like frying of eggs and French fries and making of bread have been conducted several times with great ease. The cooker has high exergy gain of up to 70 W, with 8–10% maximum efficiency, while the thermal efficiency of the cooker is up to 49.4%. The product of peak exergy power to the temperature difference gap, which is an important parameter for comparing the performance of solar cookers, has been found to be 4364.33 W·K, which is by far the highest reported in the literature, for any solar cooker. The cooker is low cost (around US\$ 100) and easy to manufacture. It is quite ready for large scale dissemination.

Conflicts of Interest

The author declares that he has no conflicts of interest.

Acknowledgments

This work has been conducted at the Pakistan Council of Renewable Energy Technologies, Islamabad. The author is grateful to the council for extending its funds, facilities, and manpower for carrying out this study.

References

- [1] S. Z. Farooqui, "A review of vacuum tube based solar cookers with the experimental determination of energy and exergy efficiencies of a single vacuum tube based prototype," *Renewable and Sustainable Energy Reviews*, vol. 31, pp. 439–445, 2014.
- [2] R. M. Muthusivagami, R. Velraj, and R. Sethumadhavan, "Solar cookers with and without thermal storage—a review," *Renewable and Sustainable Energy Reviews*, vol. 14, no. 2, pp. 691–701, 2010.
- [3] S. Z. Farooqui, "Impact of load variation on the energy and exergy efficiencies of a single vacuum tube based solar cooker," *Renewable Energy*, vol. 77, pp. 152–158, 2015.
- [4] S. Z. Farooqui, "Angular optimization of dual booster mirror solar cookers – tracking free experiments with three different aspect ratios," *Solar Energy*, vol. 114, pp. 337–348, 2015.
- [5] A. Balzar, P. Stumpf, S. Eckhoff, H. Ackermann, and M. Grupp, "A solar cooker using vacuum-tube collectors with integrated heat pipes," *Solar Energy*, vol. 58, no. 1–3, pp. 63–68, 1996.
- [6] S. Z. Farooqui, "A vacuum tube based improved solar cooker," *Sustainable Energy Technologies and Assessments*, vol. 3, pp. 33–39, 2013.
- [7] R. Kumar, R. S. Adhikari, H. P. Garg, and A. Kumar, "Thermal performance of a pressure cooker based on evacuated tube solar collector," *Applied Thermal Engineering*, vol. 21, pp. 1699–1706, 2001.
- [8] K. Ashok, "A review of solar cooker designs, TIDE (TERI information digest on energy)," vol. 8, no. 1, pp. 1–37, 1998.
- [9] S. C. Mullick, T. C. Kandpal, and S. Kumar, "Thermal test procedure for a paraboloid concentrator solar cooker," *Solar Energy*, vol. 46, no. 3, pp. 139–144, 1991.
- [10] M. M. Rathore and R. M. Warkhedkar, "A review of solar cookers, international journal of modern trends in engineering and research, special issue of ICRTET'2015," vol. 2, no. 7, pp. 1997–2004, 2015.
- [11] A. S. Ahmed, N. S. P. Rao, P. L. S. Murthy, and B. P. Terani, "Detail study of parabolic solar cooker SK-14," *International Research Journal of Engineering and Technology*, vol. 2, no. 4, pp. 24–27, 2015.
- [12] A. Chandak, S. K. Somani, and P. M. Suryaji, "Comparative analysis of SK-14 and PRINCE-15 solar concentrators," in *Proceedings of the World Congress on Engineering 2011 Vol III WCE 2011*, London, UK, July 6–8, 2011.
- [13] W. Scheffler, "Introduction to the revolutionary Design of Scheffler Reflectors," *Germany*, November 2016, <http://www.solare-bruecke.org>.
- [14] W. Scheffler, "The Scheffler reflector, Solare Bruecke," November 2016, <http://www.solare-bruecke.org/index.php/en/die-scheffler-reflektoren>.
- [15] C. Reichl, F. Hengstberger, and C. Zauner, "Heat transfer mechanisms in a compound parabolic concentrator: comparison of computational fluid dynamics simulations to particle image velocimetry and local temperature measurements," *Solar Energy*, vol. 97, pp. 436–446, 2013.
- [16] Y. Yoshiki Nishi and T. Sema, "Estimation of exergy efficiency of compound parabolic concentrator under time-varying cloud cover condition," *Solar Energy*, vol. 98, pp. 341–348, 2013.
- [17] W. B. Stine and M. Geyer, "Power from the sun", J.T. Lyle Center for Regenerative Studies, *John Wiley and Sons, Incorporated*, 2001.
- [18] Mylar, "All you need to know about," October 2016, <https://www.mjguide.com/tutorials/Lighting/1568.htm>.
- [19] P. A. Funk, "Evaluating the international standard procedure for testing solar cookers and reporting performance," *Solar Energy*, vol. 68, pp. 1–7, 2000.

- [20] S. C. Mullick and S. K. Kandpal, "Testing of box type solar cookers: second figure of merit - F2 and its variation with load and number of pots," *Solar Energy*, pp. 409–413, 1996.
- [21] G. N. Tiwari, "Solar energy: fundamentals, design, modeling and applications," *Alpha Science International*, 2002.
- [22] R. Petela, "Exergy of undiluted thermal radiation," *Solar Energy*, vol. 74, pp. 469–488, 2003.
- [23] H. H. Ozturk, "Experimental determination of energy and exergy efficiency of the solar parabolic-cooker," *Solar Energy*, vol. 77, pp. 67–71, 2004.
- [24] R. Petela, *Engineering Thermodynamics of Thermal Radiation for Solar Power Utilization*, McGraw-Hill, New York, 2010.
- [25] N. Kumar, G. Vishwanath, and A. Gupta, "An exergy based unified test protocol for solar cookers of different geometries," *Renewable Energy*, vol. 44, pp. 457–462, 2012.